Universiteit
Antwerpen

Faculteit Wetenschappen
Departement Fysica

Vibrational properties of graphene nano-flakes and thermo-mechanical properties of graphene-like materials

---

Vibrationele eigenschappen van grafeen nano-vlokken en thermo-mechanische eigenschappen van grafeen-achtige materialen

---

Proefschrift voorgelegd tot het behalen van de graad van doctor in de wetenschappen aan de Universiteit Antwerpen te verdedigen door

Sandeep Kumar Singh

Promotor: Prof. Dr. F. M. Peeters
Co-promotor: Prof. Dr. M. Neek-amal

Antwerpen 2014

Members of the Jury:

Chairman
Prof. Dr. Pierre Van Mechelen, Universiteit Antwerpen, Belgium

Supervisor
Prof. Dr. François Peeters, Universiteit Antwerpen, Belgium
Prof. Dr. M. Neek-amal, Shahid Rajaee Teacher Training University, Tehran, Iran.

Members
Prof. Dr. Gustaaf Van Tendeloo, Universiteit Antwerpen, Belgium,
Prof. Dr. Erik Neyts, Universiteit Antwerpen, Belgium,
Prof. Dr. Patrick Wagner, University of Hasselt, Belgium,
Prof. Dr. Joao Milton Pereira, Universidade Federal do Ceará, Fortaleza, Brazil.

Contact Information

Sandeep Kumar Singh
G.U. 206
Groenenborgerlaan 171
2020 Antwerpen
Belgium
san2007iit@gmail.com

Acknowledgement

This research work could not have been done without the support and encouragement from numerous individuals.

First of all, I am indebted to my supervisor, Prof. Francois Peeters for his guidance, patience, motivation, and enthusiasm during my PhD study. He has given me an opportunity and complete freedom to work on interesting research topics. It is my privilege to be his student. I would like to express my gratitude to my collaborators Prof. Mehdi Neek-Amal, Dr. Seba Costamagna and Prof. Karl Michel who have been a significant support throughout my PhD work. I would like to thank to my thesis committee: Prof. Pierre Van Mechelen, Prof. Gustaaf Van Tendeloo, Prof. Erik Neyts, Prof. Patrick Wagner, and Prof. Joao Milton Pereira for reviewing my thesis and giving their insightful comments.

I would like to thank to all the CMT group members and our secretary Ms. Evans Hilde, an incredibly nice person for all her administrative support.

I would also like to thank especially Gaurav, Shweta, Nissy, Amit, Hemant, Kumud, Ravi Kishore and all Indian student community for being such nice friends.

Last but not least, I want to give my deepest appreciation to my whole family and friends in India for their support and love. I would like to especially thank the ones who brings joy and happiness every day of my life: my wife Khushbu Kushwaha.

Finally, I thank the Flemish Science Foundation (FWO-Vl), the European Science Foundation (ESF)- EuroGRAPHENE (project CONGRAN), and the Methusalem foundation of the Flemish Government for funding my research.

Sandeep Kumar Singh

Contents

List of Abbreviations

0D	Zero dimensional
1D	One dimensional
2D	Two dimensional
3D	Three dimensional
GE	Graphene
h-BN	Hexagonal boron nitride
FG	Fluorographene
MD	Molecular dynamics
CVD	Chemical vapor deposition
DFT	Density functional theory
DOS	Density of states
CNT	Carbon nano-tube
GNF	Graphene nano-flake
LEEM	Low-energy electron microscopy
EEM	Electronegativity Equalization Method
$\mathbf{N}_f$	Total number of degrees of freedom

CHAPTER 1

Introduction

1.1 Graphene

One of the most fascinating property of carbon (a Group IV element) is its unique chemical bonding flexibility which is able to produce many different molecular compounds and crystalline solids. Carbon has four valence electrons which tend to interact with each other to produce various kinds of carbon allotropes. Therefore, the allotropes of carbon span all three spatial dimensions from 0D fullerenes, 1D carbon nanotubes, 2D graphene to 3D graphite and diamond with very different physical properties, e.g. graphite is an insulator while diamond is a conductor. Some of these different allotropes of carbon are shown in Fig. 1.1.

Since the first experimental isolation in 2004, graphene [1], a single planar layer of carbon atoms arranged in a two-dimensional (2D) honeycomb lattice has generated an enormous amount of interest in the solid state community. The planar honeycomb structure of graphene has been observed experimentally (see Fig. 1.2). Many extraordinary properties, such as its electronic spectrum [2], electronic transport [3], high Young's modulus [4] and excellent thermal conductivity [5], have all been reported. Because of its remarkable properties [6, 7], applications using graphene in a wide range of areas, including high-speed electronics [8], optical devices [9], energy generation and storage [9–11], and hybrid materials [12], have all been explored. Andre Geim and Konstantin Novoselov from the University of Manchester won the Nobel Prize in Physics 2010 *for groundbreaking experiments regarding the two-dimensional material graphene*. Graphene is a basic

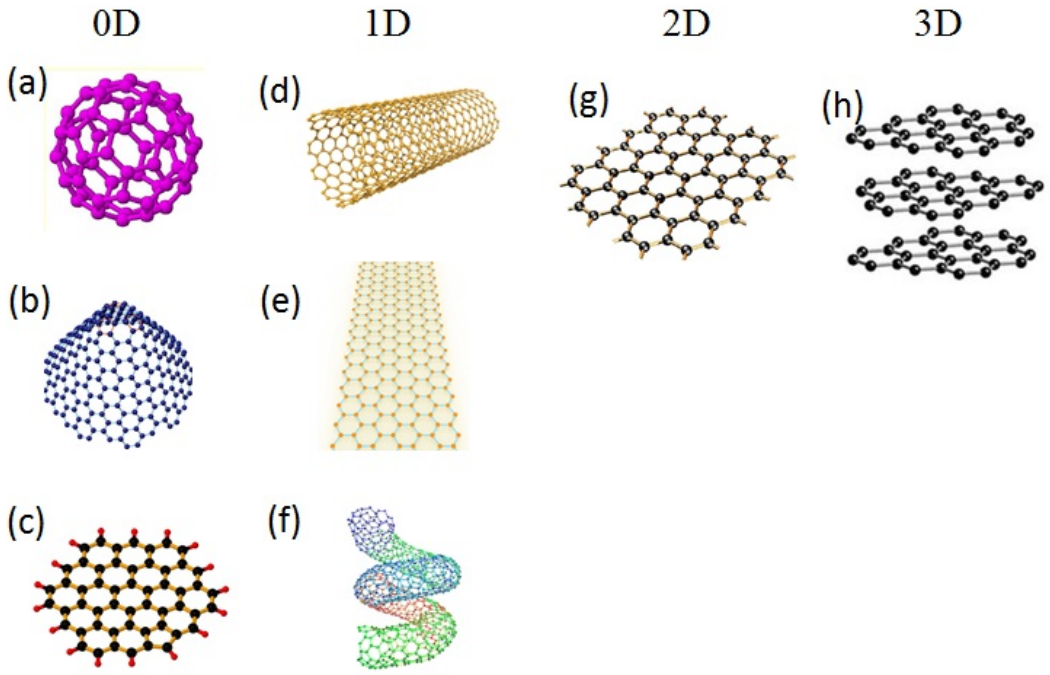

Figure 1.1: Allotropes of carbon in different dimensions [13]. Fullerene (a), nanocone (nanohorn) (b), graphene nano-flake (c), carbon nanotube (d), graphene nanoribbon (e), helicoidal carbon nanotube (f), graphene (g), and graphite (h).

building block for graphitic materials. As demonstrated in Fig. 1.3, it can be wrapped up into 0D fullerenes, rolled into 1D nanotubes or stacked into 3D graphite. Furthermore, graphene can also be cut in 1D small ribbons called nanoribbons.

More than 70 years ago, Peierls [14, 15], Landau [16, 17] and later Mermin and Wagner [18, 19] showed theoretically that, in the standard harmonic approximation, thermal fluctuations should destroy long range order resulting in melting of a 2D lattice at any finite temperature. This theoretical prediction was strongly supported by various experimental investigations with thin films in which the samples became unstable as their thickness was reduced. But, the 2D graphene crystal remains intact because of the anharmonic coupling between its bending and stretching modes [20]. In 1947, P. R. Wallace [21] performed the first band structure calculations for a single graphite layer using a tight-binding approximation in order to understand the band structure of graphite. As a first approximation, he assumed that the interlayer coupling was negligible, thereby indirectly computing the band structure of single layer graphene. In 1984, Gordon Semenoff [22] made the strik-

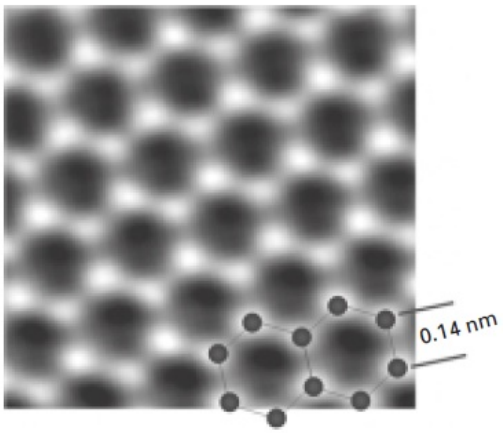

Figure 1.2: Remarkable transmission electron aberration-corrected microscope (TEAM) image of graphene vividly showing the carbon atoms and bonds in the honeycomb structure (courtesy of Berkeley's TEAM05, 2009) [25]

.

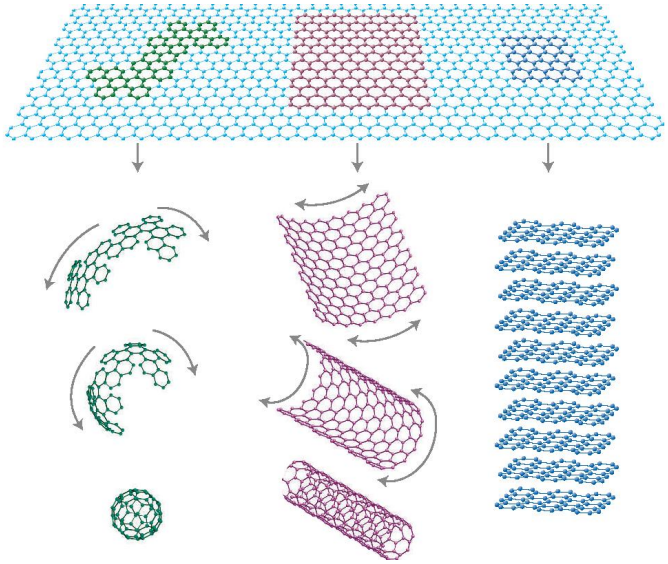

Figure 1.3: Graphene forms the basis of the other graphitic carbon allotropes; from left to right: fullerenes (C_{60}), carbon nanotubes, and graphite. (Taken from ref. [6].)

ing theoretical observation that the low energy excitations of graphene, which was still hypothetical at the time, served as a condensed matter analogue to (2+1)D quantum electrodynamics. He showed that the Hamiltonian at low energy consists of two decoupled copies of the Dirac equation, which are related by time reversal. It was finally in 2005 that two papers appeared in Nature that confirmed the existence of Dirac fermions in single layer graphene [23, 24].

The direct lattice of graphene: Graphene, a honeycomb lattice of carbon atoms is shown in Fig. 1.4(a). The primitive cell of graphene is composed of two non-equivalent atoms, A and B. The carbon-carbon bond length a_{C-C} is approximately 1.42 Å. The positions of type A (or B) atoms can be generated using a linear combination of basis vectors

$$A(n_1, n_2) = n_1\mathbf{a}_1 + n_2\mathbf{a}_2, \tag{1.1}$$

with lattice vectors $\mathbf{a}_1$ and $\mathbf{a}_2$ given by (see Fig. 1.4(a))

$$\mathbf{a}_1 = \left(\frac{\sqrt{3}a}{2}, \frac{a}{2}\right), \mathbf{a}_2 = \left(\frac{\sqrt{3}a}{2}, \frac{-a}{2}\right) \tag{1.2}$$

with $|\mathbf{a}_1| = |\mathbf{a}_2| =$a and n_1, n_2 are two arbitrary integer numbers. In graphene, each carbon atom (A or B) is covalently bonded to its three nearest neighbors and the separation between type A (B) and the nearest type B (A) atoms are

$$\mathbf{R}_1 = \left(\frac{a}{\sqrt{3}}, 0\right), \mathbf{R}_2 = \left(\frac{-a}{2\sqrt{3}}, \frac{-a}{2}\right), \mathbf{R}_3 = \left(\frac{-a}{2\sqrt{3}}, \frac{a}{2}\right) \tag{1.3}$$

with $|\mathbf{R}_1| = |\mathbf{R}_2| = |\mathbf{R}_3| =a_{C-C}$.

The reciprocal lattice: The reciprocal lattice of graphene is also a hexagonal lattice (see Fig. 1.4(b)) with the reciprocal vectors given by

$$\mathbf{b}_1 = \left(\frac{2\pi}{\sqrt{3}a}, \frac{2\pi}{a}\right), \mathbf{b}_2 = \left(\frac{2\pi}{\sqrt{3}a}, \frac{-2\pi}{a}\right) \tag{1.4}$$

with $|\mathbf{b}_1| = |\mathbf{b}_2| = 4\pi/\sqrt{3}$a. The first Brillouin zone is shown by the shaded area in Fig. 1.4(b) and has sides of length $b_{BZ} = |\mathbf{b}_1|/\sqrt{3} = 4\pi/3a$. The Γ-point is at the center of the Brillouin zone, and the vectors describing the location of the other high symmetric points with respect to the zone center are

$$\mathbf{\Gamma M} = \left(\frac{2\pi}{\sqrt{3}a}, 0\right), \mathbf{\Gamma K} = \left(\frac{2\pi}{\sqrt{3}a}, \frac{2\pi}{3a}\right). \tag{1.5}$$

There are six K-points and six M-points within the Brillouin zone.

In the next section, I will discuss the very interesting 0D form of graphene also called graphene nano-flakes.

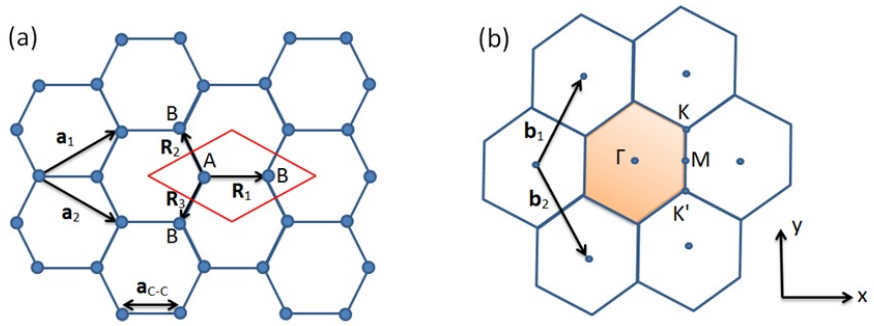

Figure 1.4: (a) The honeycomb lattice of graphene. The unit cell contains two atoms denoted as A and B. (b) The reciprocal lattice of graphene. The first Brillouin zone is the shaded hexagon with the high symmetry points labeled as Γ, M, and K located at the center, midpoint of the side, and corner of the hexagon respectively (taken from Ref. [25]).

1.2 Graphene nano-flakes

Graphene nano-flakes which are the 0D form of graphene, have great potential for a variety of applications specially in electronic and magnetic devices which differ from those of 2D and 1D (e.g. nano-ribbons) graphene. GNFs can be made by bottom-up and top-down approaches. In the bottom-up method, small molecular units are fused to form large aromatic hydrocarbons by a large variety of chemical reactions [26,27] while in the top-down approach, GNFs are directly cut from a large piece of graphene sheet. Large graphene sheets are produced by a variety of methods, micromechanical cleavable of a graphite single crystal [1], by chemical "unzipping" carbon nanotubes (CNTs) [28], etc. An alternative procedure to make GNFs is to confine a region of bulk material by using an electrostatic potential. Since the relativistic nature of electronic excitations in graphene and its zero energy gap leads to Klein tunneling, therefore electrons can tunnel unimpeded through such barriers. To overcome this problem, new approaches have to be developed which includes, creating a confinement potential within the graphene layer to trap an electron for a finite time, the introduction of a finite gap by coupling with the substrate or by using a bilayer [29], or the use of a magnetic confinement potential [30, 31]. Edges of GNFs play a very important role in determining their electronic and magnetic properties. Therefore, density functional theory was performed to study the thermal stability and reconstruction of un-terminated edges of GNFs (n=24, 32, 128) for temperature up to 2400 K [32]. In addition to edges and corners, the effect of defects are also important as they often degrade the properties of GNFs, but may introduce new properties such as magnetism. Because of the finite size of GNFs, defects can dominate the structure and its properties, depending on defect size and defect density. Functional groups attached to the GNFs also open

new opportunities for technological applications. Density functional theory was used to investigate rectangular graphene nanodots (having both armchair and zigzag edges) with different edge chemical modifications [33]. The saturation with different atoms or molecular groups on the zigzag edges leads to a spin-polarized ground state with magnetic moment, spin density, and electronic energy gap which strongly depend on the atomic groups used to passivate the dangling bonds. First-principles calculations were used to investigate the magnetic properties of graphene fragments with arbirary shape, showing that the net total electron spin of a graphene nanoflake depends strongly on its shape due to the topological frustration of π bonds [34, 35]. Graphene quantum dots have been studied through ab-initio electronic calculations, being proposed as structures that can serve as the fundamental logic gates of high-density ultrafast spintronics devices [36]. This leads to the expectation that they may be extremely useful in areas such as spintronics, sensors and transistors. Vibrational states which lead to Raman and/or infrared spectra are very useful in identifying the structure of GNFs. Few layer GNFs have also been the subject of theoretical and experimental interest, e.g. bilayer GNFs have a different band gap than single layer GNFs and electrons in such structures may be confined with potential barriers in contrast to single layer GNFs [30]. GNFs also show interesting optical properties when functionalized. For more details, I refer the readers to chapter 13 of Ref. [37].

1.3 Graphene-like materials

Since the discovery of extraordinary properties of graphene, 2D layered materials such as boron-nitride, fluorographene, metal chalcogenides, transition metal oxides, and other 2D compounds have gained tremendous interest for their particular electronic structure that ranges from insulator to metal to superconductor. A large variety of layered crystals with strong in-plane bonds and weak van der Waals-like inter-plane bonds exists which could potentially be exfoliated into 2D materials. These have various properties including the topological insulator effect [38, 39], superconductivity [40], and thermoelectricity [41]. Furthermore, a strong interest in group-IV graphene-like 2D buckled nanosheets has recently emerged. Silicene and germanene, the silicon- or germanium-based counterparts of graphene, have progressed from theoretical predictions [42] to experimental observations [43] only within a few years. Theoretical calculations have shown that they exhibit electronic characteristics similar to graphene [44].

In contrast to the zero band gap of pristine graphene itself and the electric field induced band gap (a few hundred meV) introduced in bilayer graphene, a single layer MoS_2 is a direct band gap semiconductor. The current on/off ratio of single-layer MoS_2 transistors exceeds 10^8 at room temperature [45], much higher than for graphene transistors [1]. There-

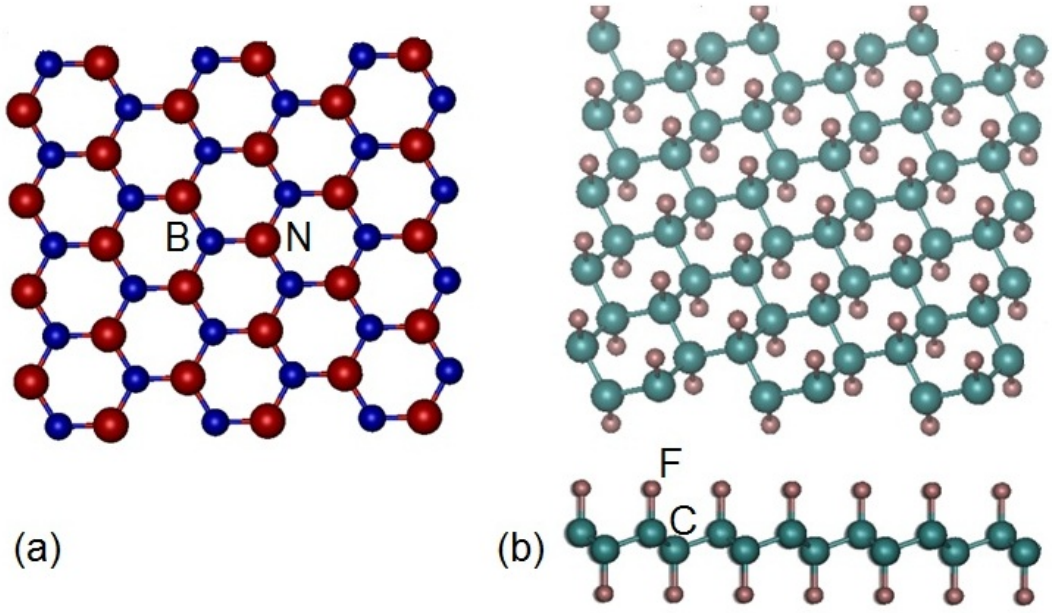

Figure 1.5: (a) Top view of hexagobal boron-nitride (h-BN). The boron and nitrogen atoms are in blue and red colors, respectively. (b) Top and side view of fluorographene. The carbon atoms are in cyan color and the fluorine atoms are in pink.

fore, MoS_2 is a potential material for digital circuits and light-emitting diodes. Graphene-like silicene-based technologies might have the major advantage of easy integration into existing electronics industry.

In the present thesis, I studied a monolayer of hexagonal boron-nitride and fluorographene that are graphene-like 2D materials which have been experimentally investigated and found to be stable materials at room temperature.

1.3.1 Hexagonal Boron-nitride (h-BN)

Hexagonal boron-nitride (h-BN) are composed of alternating boron and nitrogen atoms in a honeycomb arrangement similar to graphene (see Fig. 1.5(a)). After the discovery of graphene [1], free-standing 2D BN flakes were peeled off from a BN crystal in 2005 [46]. Chemical bonds are covalent with some important ionic contribution. The ionic character is a consequence of the charge transfer of ≈ 0.43 electrons from B to N [47]. The phonon spectrum of h-BN includes three acoustic and three optical modes [47, 48]. Theoretical calculations have shown that h-BN is mechanically a softer material than graphene [49]. H-BN is an insulator (or a wide-band semiconductor) with a band gap of about 5.9 eV [50].

The theoretical analysis of the electronic properties of boron-nitride nanotubes (BNNTs) and nanosheets reviewed by Arenal et al [51] showed their bandgap to be direct independent of the details of the atomic structure. This insulating behavior of BN nanostructure encourages their applications as a protective shield encapsulating nanomaterials [52]. With a similar lattice constant to graphene and the same hexagonal structure, h-BN offers one of the best and most advanced platforms for future graphene electronics by enhancing the graphene stability and quality [53]. Deposition of graphene on h-BN is found to improve the transport properties of graphene, possibly due to the suppression of scattering from out-of-plane ripples [54]. Numerical calculations of h-BN with single boron or nitrogen vacancies showed that the magnetic moment of the unit cell in the defect network approaches a value of 1 μ_B. Hexagonal boron-nitride (h-BN) can be made magnetic also by doping with Be, O, Al, C or Si [55, 56].

1.3.2 Fluorographene (FG)

Fluorinated graphene also called fluorographene represents a type of chemically modified graphene (see Fig. 1.5(b)). Fluorographene was prepared experimentally [57, 58] by chemical and mechanical exfoliation of graphite fluoride in 2010. Although bulk graphite fluoride has been used as a lubricant for nearly 100 years and has also been exploited as an excellent electrode material in primary lithium batteries, graphene fluoride was not experimentally realized until 2010. Alternative ways of preparing fluorinated graphene by cold plasma was developed simultaneously. However this approach often generates non-stoichiometric fluorinated graphenes (C_1F_a, a$<$1). The attachment of fluorine atoms to sp^2 carbon changes the hybridization state to sp^3, which significantly affects the electronic properties and local structure of the materials but preserves the 2D hexagonal symmetry. Such changes in the type of bonding induce an opening of the band gap at the K point. Experimental studies have shown that fluorographene is a wide band gap semiconductor (band gap ranges from 3.1 to 3.8 eV [57, 59]) with high resistance and mechanical strength, viz., Young's modulus of fluorographene (0.3 TPa) is much lower than that of pristine graphene, although 1.5 times higher than that of steel. Fluorographene has turned out to exhibit good structural, chemical properties and thermal stability up to $400\,^{\circ}\mathrm{C}$. This makes fluorographene a candidate to replace Teflon in various protective coatings. Also, the luminescent and optical properties of fluorographene are similar to those of diamond and make it an attractive material for optoelectronics [60]. A number of specimens of formal stoichiometry $C_2F_x(x \leq 1)$ exhibited magnetism [61]. The electronic and phonon spectra of partially [62,63] and fully covered fluorographene [64,65] were calculated. The formation of quantum dot like structures [65] and specific features of the magnetic and electronic states of CF_x nanoribbons were investigated theoretically [66]. The electronic

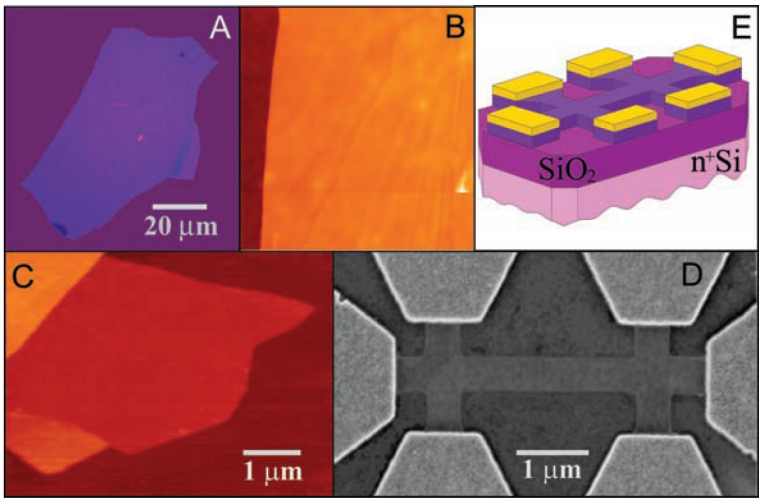

Figure 1.6: Graphene films obtained by mechanical exfoliation. (A) Photograph of a graphene flake with thickness 3 nm on top of an oxidized Si wafer. (B) Atomic force microscope (AFM) image of $2 \times 2\ \mu m^2$ area of the flake near its edge. Colors: dark brown is the SiO_2 surface while orange is the 3 nm height above the SiO_2 surface. (C) AFM image of single layer graphene. Colors: brown-red (central area). (D) Scanning electron microscope image of a few layer, graphene Hall device. (E) Schematic view of the device in (D). (Taken from ref. [1].)

and structural properties of fluorographene upon adsorption of various metal atoms (K, Li, Au) were studied [67] and models for a hypothetical graphane-fluorographene (CH_xF_y) hybrid material, i.e., the graphene sheet with fluorine and hydrogen adatoms, were proposed [67, 68]. It is predicted that fluorographene is the most stable system among the possible isoelectronic analogues, namely, graphene bromide, chloride and iodide [69].

1.4 Synthesis of Graphene

The first isolation of monolayer graphene was done using the famous Scotch tape method to peel off carbon layer-by-layer from graphite in 2004 [1]. To date, many other experimental processes have been developed for synthesis of single to many layers of graphene of various dimensions, shapes and quality. Here, I will discuss some of the most important synthesis methods.

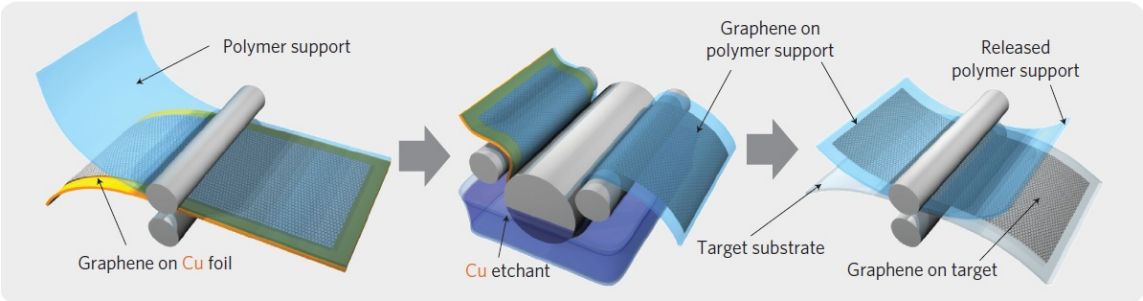

Figure 1.7: Schematic of the roll-based production of graphene films grown on a copper foil. The process includes adhesion of polymer supports, copper etching (rinsing) and dry transfer-printing on a target substrate. A wet-chemical doping can be carried out using a set-up similar to that used for etching. (Taken from ref. [71].)

1.4.1 Mechanical Exfoliation

Novoselov and Geim prepared graphene films by mechanical exfoliation of small mesas of highly oriented pyrolytic graphite (HOPG). Using dry etching in oxygen plasma, 5 mm-deep mesas on top of the platelets (mesas were squares of various sizes from 20 mm to 2 mm) were created and then pressed against a 1-mm-thick layer of a fresh wet photoresist spun over a glass substrate. After baking, the mesas became attached to the photoresist layer, which allowed us to cleave them off the rest of the HOPG sample. Scotch tape was used to repeatedly peel flakes of graphite from the mesas. These thin films were then released in acetone and captured on the surface of a Si/SiO_2 wafer surface. After this, ultrasound cleaning propanol was used to remove mostly thick flakes. Thin flakes (d < 10 nm) were found to attach strongly to SiO2 due to van der Waals forces [1].

These few-layer graphene (FLG) flakes were identified using the contrast difference in an optical microscope and single layers using an SEM. Using this technique, Geim and Novoselov were able to generate few- and single-layer graphene flakes with dimension up to 10 μm as shown in Figure 1.6. The scotch tape method can generate flakes with size of up to 1 mm in length, of excellent quality and well suited for fundamental research. However, the process is limited to small size and cannot be scaled for industrial production [7](a).

1.4.2 Chemical Vapour Deposition

In this method, carbon is supplied in the gas form and a metal used as both catalyst and substrate to grow the graphene layer. Li et al. used the CVD method to produce large-area uniform polycrystalline graphene films on copper foils and films, and showed promise

for many applications [70]. Raman spectroscopy and SEM imaging confirm that the graphene is primarily monolayer independent of growth time. Despite the fact that the complete process typically requires transfer from the copper support to a dielectric surface or other substrate of interest, the production of square metres of graphene has already been achieved [71].

Recently, Lee et al. [72] have demonstrated a technique to produce uniform bilayer graphene by CVD on copper using a similar process but using modified growth conditions. Despite the presence of defects, grain boundaries, inclusions of thicker layers, and so on, such films can readily be used in transparent conductive coating applications (such as touch screens).

A number of issues related to gaining control of the domain (grain) size, ripples, doping level and the number of layers need to be resolved. The transfer process should be optimized with the objective of minimizing the damage to graphene. The future goal would be the development of graphene growth on arbitrary surfaces and/or at low temperature (for example, using plasma-enhanced CVD or other methods) with a minimal number of defects.

1.4.3 Thermal Decomposition of SiC

In this technique, SiC is heated in ulta-high-vacuum (UHV) to temperatures between 1000 °C and 1500 °C. Graphitic layers can be grown either on the silicon or carbon faces of a SiC wafer by sublimating Si atoms and leave behind a carbon-rich surface [73]. Initially, Berger and de Heer produced few layer randomly oriented graphene layers using the C-terminated face of SiC [74], but now the number of graphene layers grown can be controlled [75].

The major drawbacks of this method are the high cost of the SiC wafers, the high temperature required for growth, an increase in size of the crystallites and control of unintentional doping from the substrate and buffer layers.

1.5 Applications of Graphene

Graphene has some outstanding physical properties that makes it extremely appealing for applications i.e. room-temperature electron mobility $> 1.0\times10^5$ $\mathrm{cm^2V^{-1}s^{-1}}$ [76], a Young's modulus of 1TPa and intrinsic strength of 130 GPa [4], very high thermal conductivity (about 3,000 $\mathrm{Wm^{-1}K^{-1}}$) [5], optical absorption of exactly $\pi\alpha \approx 2.3\%$ (in the infrared limit, where α is the fine structure constant) [77], complete impermeability to any gases [78], ability to sustain extremely high densities of electric currents (a million

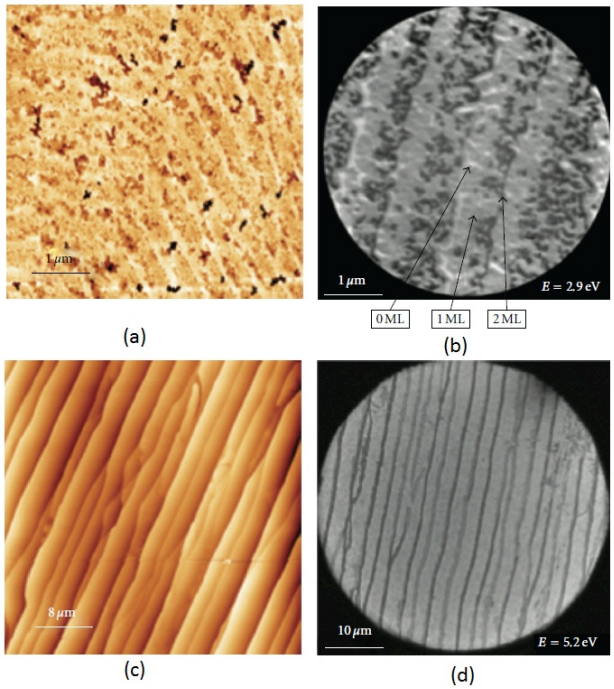

Figure 1.8: Graphene obtained by thermal decomposition of SiC. (a) Atomic force microscopy (AFM) image of graphene growth on SiC annealed at UHV. (b) LEEM image of UHV grown graphene film. (c) AFM image of graphene annealed in Ar at 900 mbar. (d) LEEM image of graphene on Ar annealed SiC substrate showing terraces up to 50 μm in length. (Taken from ref. [79].)

times higher than copper) [80]. I will mention some areas where graphene may be used for future devices.

1.5.1 Flexible electronics

Transparent conductive coatings are highly demanded in transparent electronics such as touch screen displays, electronic paper (e-paper) and organic light-emitting diodes (OLEDs). These devices require a low sheet resistance with high transmittance. Due to outstanding mechanical flexibility, chemical durability, electrical and optical characteristic (excellent transmittance of 97.7% per layer [77]), graphene is a potential candidate for flexible electronic devices where traditionally used indium tin oxide (ITO) usually fails. The fracture strain of graphene is found ten times higher [4] than that of ITO, making graphene an ideal candidate to bendable and rollable devices as shown in Fig. 1.9.

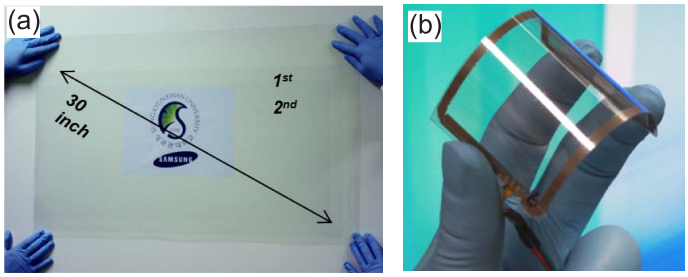

Figure 1.9: (a) A large continuous display based on few-layer graphene deposited on a polymer substrate, fabricated by Samsung company (Taken from Ref. [71]). (b) A flexible graphene screen.

1.5.2 Logic transistor

In recent years, many methods are tried to open a bandgap in graphene: nanoribbons [81, 82], single electron transistor [83, 84] formation, bilayer [29, 75, 85] and chemically modified graphene [57, 86]. Except for chemical modified graphene, other methods are unable to open a band gap of more than 360 meV, limiting the transistor on/off ratio to about 10^3 which is much less than the required 10^6. This issue of the low on/off ratio can be solve by introducing the new vertical transistor design [52] allowing on/off ratios of $> 10^6$.

1.5.3 High-frequency transistors

Even the lack of a band-gap in graphene that does not support its use in digital electronics, graphene has been considered as a potential candidate for high-frequency transistor or analog applications, such as amplifiers and transmitters [8](Fig. 1.10). The outstanding carrier mobility, the high transconductance (the crucial parameter when considering an amplifiers performance), the ultimate thinness and stability make graphene devices an excellent candidate for fast analog electronics. A further important parameter in the radio frequency (RF) field is the frequency cutoff f_T; the frequency at which the current gain for the device is reduced to one, and is thus the limiting frequency at which a signal will be carried through. Recently, a value of f_T as high as 300 GHz was found experimentally [87] which theoretically was predicted to be extended to 1 THz [88].

1.5.4 Graphene for sensors and metrology

The large surface area and easily dopable nature of graphene makes it extremely sensitive to the environment, hence, a promising potential candidate for the use in sensor applications [89]. Interactions of various gas molecules with graphene affects its electronic prop-

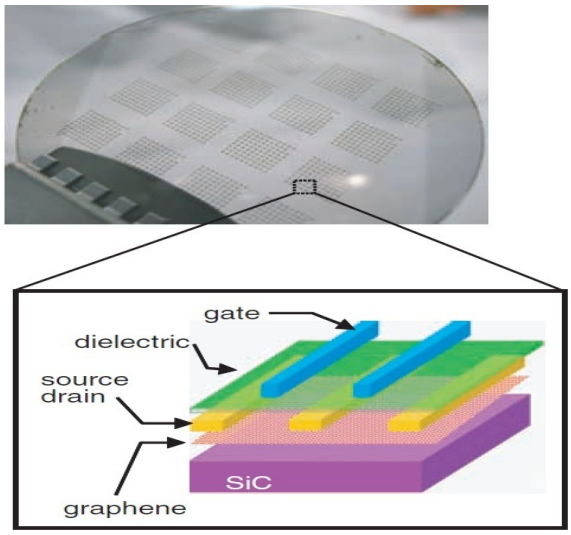

Figure 1.10: Image of devices fabricated on a 2-inch graphene wafer and schematic cross-sectional view of a top-gated graphene FET (Taken from Ref. [8]).

erties in a measurable way [90]. In fact, it is possible to detect individual gas molecules bonded to graphene due to graphene's low-electronic noise characteristic [91].

The quantum Hall effect (QHE) is a quantisation of resistance, occurring in two-dimensional electronic systems and relates the resistance quantum, h/e^2 where e is the electron charge and h is Planck′s constant. The QHE has been observed only at liquid-helium temperatures, but in graphene, the QHE can be measured even at room temperature. Thus it is possible that QHE resistance standards will be available to a broader community, outside a few national institutions [92]. Epitaxially grown graphene on silicon carbide is the best Hall device yet that reported Hall resistances accurate to a few parts per billion [93]. Janssen et al. [94] demonstrated the universality of the QHE in this fundamentally different material system.

1.5.5 Energy generation and storage

As the global energy demand is increasing, nowadays most efforts are concentrated on solar cells. The outstanding electron transport, high carrier mobility and transparency make graphene a potential candidate for photovoltaic devices. Due to the low intrinsic optical absorption of graphene [77], the power conversion efficiency is insuffient for practical purposes. Therefore, such devices would require complex plasmonic enhancement structures to achieve the desired responsivity. Instead, graphene's potential to serve as a transpar-

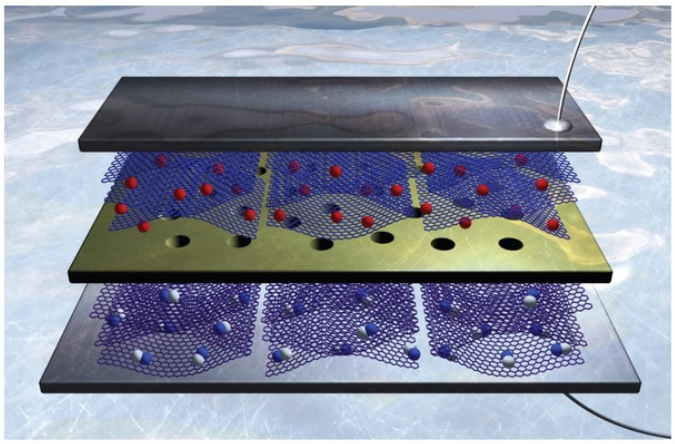

Figure 1.11: In a supercapacitor device two high-surface-area graphene-based electrodes (blue and purple hexagonal planes) are separated by a membrane (yellow). Upon charging, (white and blue merged spheres) and cations (red spheres) of the electrolyte accumulate at the vicinity of the graphene surface. The ions are electrically isolated from the carbon material by the electrochemical double layer that is serving as a molecular dielectric (Taken from Ref. [7]).

ent electrode in either quantum dots or dye-sensitized solar cells has been demonstrated recently.

Lithium-ion batteries are currently widely used for portable electronic devices. In such a battery, the storage of electrochemical energy is done by the intercalation and deintercalation of lithium ions such that upon charging lithium ions are taken from the cathode and introduced to the anode. In general poor electrical conductivity of the cathode can be overcome by the addition of graphene. Graphene would not only act as an advanced conductive filler but may also give rise to novel core-shell or sandwich-type nanocomposite structures. The presence of the oxygen-containing functional groups increase the interlayer spacing between the graphene sheets to maximise the available surface for Li insertion [95]. The significant amount of heat generated within the battery can also be removed by graphene due to its high thermal conductivity.

The principle behind supercapacitors (see Fig.1.11) is the storage and delivery of energy within electrochemical double-layer capacitors [96] with high discharge rates, hence, can be used as the primary power source or with the combination of fuel cells or batteries. Graphene with its high-surface-area, high electrical conductivity, an accessible and defined pore structure, good resistance to oxidative processes and high temperature stability makes it an ideal candidate for supercapacitor application. Performance of these devices

Figure 1.12: Illustration for the strongest material ever measured. (Taken from ref. [97].)

can be improved in the future by modifying the surface by the attachment of functional groups, and by forming graphene/ metal oxide composites.

1.5.6 Paints and composite materials

Graphene-derived paints can be used for conductive ink, electromagnetic-interference shielding, and gas barrier applications. It can also be used as a corrosion barrier against water, oxygen diffusion, moisture barrier properties, electrical and thermal conductivity. Due to its high melting temperature and outstanding mechanical strength, graphene can significantly enhance the operating temperature level of composites and improve composite compressive strength. But, a high concentration of graphene nanoplatelets may start the formation of clusters (due to platelet agglomeration) which can lead to nonuniform distribution of the reinforcement in nanocomposite [98].

Due to the recent involvement of companies in graphene business, the production

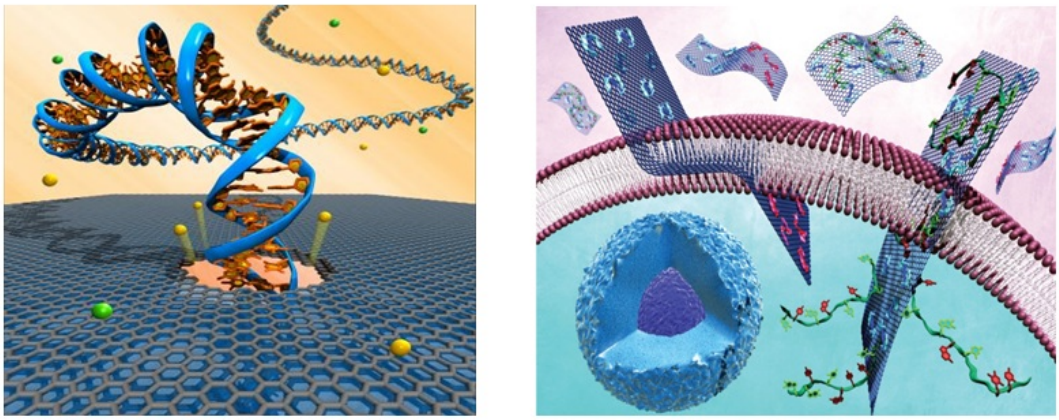

Figure 1.13: (a) Researchers of Pennsylvania developed a graphene-based platform to sequence a single DNA molecule. (photo: Robert Johnson, Temple University [99]). (b) Manipulating the hydrophilic-lipophilic properties of graphene (blue hexagonal planes) through chemical modification would allow interactions with biological membranes (purple-white double layer), such as drug delivery into the interior of a cell (blue region). (Taken from ref. [7].)

of graphene and graphene oxide has become competitive. Therefore, it is expected that graphene flakes over 10 μm in size (required to take full advantage of the high Young's modulus of graphene) will appear on the market within a few years. Also graphene is the second strongest material ever measured, some 200 times stronger than structural steel [97], even with defects [100].

1.5.7 Bio applications

Graphene has a number of unique mechanical, electronic, and optical properties that are very important in order to develop novel electronic materials. Graphene's unique properties make it potentially promising for bio applications such as precise biosensing through graphene-quenched fluorescence, graphene enhanced cell differentiation and growth, disinfecting hospitals, detecting tumors, delivering drugs and sequencing DNA.

For graphene-based DNA sequencing, one starts with a membrane from the material immerse in a conductive fluid, and apply a voltage to one end so DNA can be drawn through mini pores in the graphene. In this method which is called nanopore sequencing, graphene can interact strongly with nucleotides through π-stacking interaction, therefore

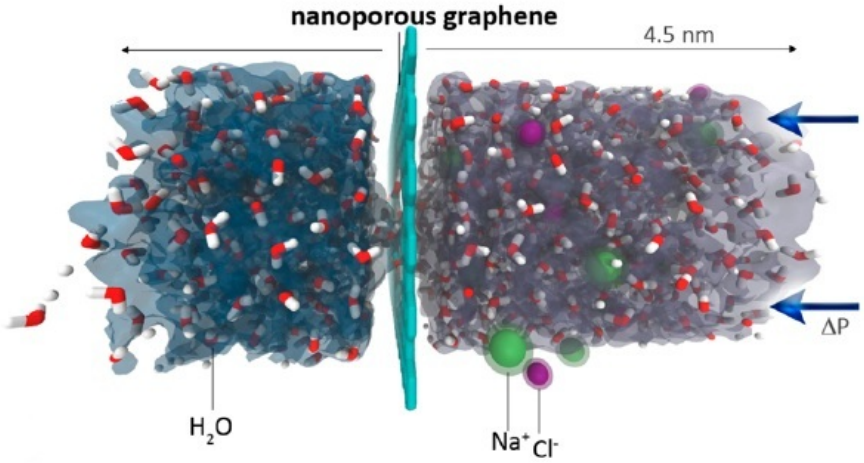

Figure 1.14: Illustration of the side view of the computational system investigated. Sodium and chlorine ions (green and purple) in saltwater are blocked while only water molecules (red and white) are passed through by the porous graphene membrane. (Taken from ref. [101].)

it would allow DNA to be analysed one nucleotide at a time.

Graphene can be utilised as nanocarriers for drug delivery, gene delivery and nanomedicine for cancer therapies. Graphene lipophilic properties which might help in membrane barrier penetration, can be used to carry genes to specific location (see Fig. 1.13(b)). The nanotoxicity of graphene and its derivatives (e.g., graphene oxide) is closely associated with its biocompatible functionalization, size distribution, concentration and shape, which need detailed investigations [102].

1.5.8 Water Desalination

Today, oceans and seas contain about 97% of worlds water. But, clean water supply is a challenge in developing nations. To solve this problem, desalination techniques should become more energy-efficient and less expensive. Recently, Cohen-Tanugi and Grossman from MIT have shown in computer simulations that nanoporous graphene membranes are able to filter salt ions from ocean water at a rate of several orders of magnitude higher than existing best commercial desalination technology, using reverse osmosis (RO) membranes. Another advantage of porous graphene membranes over RO is its lower energy requirements due to lower operating pressures. Hence, it is possible to build smaller and more modular desalination plants in the future due to smaller graphene membrane area requirements.

For a more detailed description of graphene applications, readers are recommended to read the recent review by Novoselov et al. [7](a).

1.6 Motivation of the thesis

Among the various interesting physical properties of graphene nano-flakes and graphene like materials (e.g., h-BN and fluorographene), the present work concern the spectral and electronic properties of the graphene nano-flakes and thermo-mechanical properties of boron nitride and fluorographene. One of the main challenges to utilize graphene-based devices is its zero band gap, therefore GNFs are important due to their potential for a size controllable energy band gap, bottom-up fabrication of molecular devices, spintronics and quantum dot technology [103]. According to the well-known Mermin-Wagner theorem [18], the stability of any two dimensional crystal is only possible in the presence of ripples. Understanding the behavior of the ripples is important because they affect the electronic transport properties, i.e., in GE the ripples are believed to be one of the dominant scattering sources which limits the electron mobility [104, 105]. The goal of this thesis is to explore *the spectral and electronic properties of GNFs, and the thermal rippling behavior of free standing monolayers of various functionalised graphene and graphene-like materials (e.g., h-BN).*

1.7 Organization of the thesis

The thesis is organized as follows:

Chapter 2 presents a brief introduction of the computational methodology which are relevant for the calculations in this thesis. In particular molecular dynamics simulations and density functional theory are discussed.

In **Chapter 3**, the eigenmodes and the vibrational density of states of the ground configuration of graphene clusters are calculated using classical molecular dynamics simulation. The compressional and shear properties are obtained from the divergence and rotation of the velocity field. For symmetric and defective clusters with pentagon arrangement on the edge, the highest frequency modes are shear modes. The specific heat of the clusters is also calculated within the harmonic approximation and the convergence to the result for bulk graphene is investigated.

In **chapter 4**, density-functional tight-binding and classical molecular dynamics simulations are used to investigate the structural deformations and melting of planar carbon nano-clusters. The melting point was obtained by using the bond energy, the Lindemann

criteria, and the specific heat. We found that hydrogen-passivated graphene nano-flakes have a larger melting temperature than non-passivated graphene nano-flakes.

In **chapter 5**, we studied the melting process of partially fluorinated graphene. The obtained melting phase diagram for fully fluorinated graphene (FFG) and partial fluorinated graphene (PFG) contribute to elucidate the effect of the concentration of F-atoms on the experimental observed reversal of the fluorination process.

In **chapter 6**, using atomistic simulations we investigate the thermodynamical properties of a single atomic layer of hexagonal boron nitride (h-BN). The thermal induced ripples, heat capacity, and thermal lattice expansion of large scale h-BN sheets are determined and compared to those found for graphene (GE) for temperatures up to 900 K.

In **chapter 7**, large scale atomistic simulations using the reactive force field approach (ReaxFF) are implemented to investigate the thermomechanical properties of fluorinated graphene (FG). Molecular dynamics (MD) simulations are used to investigate the thermal rippling behavior, mechanical properties of FG and are compared to graphene (GE), graphane (GA) and a sheet of BN.

In **chapter 8**, the electronic properties of graphene nano-flakes (GNFs) with H- and F- edge passivation is investigated by using density functional theory. Our study shows clearly the effect of geometry, size, termination and bilayer on the electronic properties of small GNFs. This study reveals important features of graphene nano-flakes which can be detected using Raman spectroscopy.

Finally I conclude by highlighting the remarkable results of the thesis in **chapter 9**. Every chapter is relatively independent of the others, and can be read separately.

CHAPTER 2

Atomistic simulation

In the past, theoretical models were used to calculate rather simple systems, e.g. electronic and phonon band structure in perfect infinite crystals. But, they usually fail to describe many body phenomenon, e.g. physics and chemistry of defects and surfaces, an accurate treatment of temperature effect including anharmonicities and phase transitions. Due to the increase in computational power over the last decade, more sophisticated and accurate assumptions can be made and hence more realistic systems can be investigated. Therefore computer simulation becomes an extremely powerful tool not only to understand and interpret the experiments at the microscopic level, but also to study the region which are not accessible experimentally, e.g. harsh conditions such as under extremely high pressure and temperature, or at atomistic size and time-scale that cannot be measured directly.

Atomistic modeling techniques use modern computing power to see what happens at the atomic scale in solids, liquids and molecules. Hydrogen diffusion in metals, current-induced dynamics in molecular electronics, defects (crack tips, dislocations, etc.), micro/nano-scale materials and structures (e.g. CNTs, GNFs), atomic-scale friction and many other nano-scale phenomenon can be modeled with atomic scale accuracy. Quantum mechanical simulations are considered to be highly accurate but due to massive computational cost they are limited to a few hundreds of atoms. Besides quantum mechanical simulation techniques, atomistic modeling can also be done with effective interactions between atoms, called interatomic potentials. Empirical interatomic potentials (e.g. Lennard-Jones, Morse) and semi-empirical potential (e.g. bond order potentials by Tersoff and Brenner which are derived from quantum-mechanical arguments) do not treat the quantum na-

ture of electrons explicitly hence allowing enormously faster calculations than quantum-mechanical methods. Therefore these interatomic potentials allow to simulate systems with millions of atoms.

In the present thesis, two classes of computational methods have been employed: classical molecular-dynamics (MD) and first-principles density functional theory (DFT) calculations. A brief review of these methods is presented which will be useful to understand and interpret the results of the following chapters.

2.1 Molecular dynamics

Molecular-Dynamics (MD) simulation [106] is a powerful tool for computing the equilibrium and transport properties of a classical many body system. The advantage of MD over Monte Carlo (MC) is that MD probe not only the configuration space like MC, but also the phase space which give additional information about the dynamics of the system (e.g. transport coefficient, time-dependent responses to perturbations). MD is usually used to predict properties of defect mechanisms, fracture, surface, friction, clusters, mechanical and transport in solids, phase equilibria and phase transitions among many others possible applications.

I will discuss the most important features of molecular dynamics simulations in more detail:

2.1.1 Initialization

In the beginning of MD simulation, the initial positions and velocities of all particles in the system are assigned. A good initial guess of positions and velocities helps to get fast convergence and reliable results. From the theorem of equipartition of energy, for the average kinetic energy per degree of freedom, we have the following relation

$$\langle \frac{1}{2} m \nu_\alpha^2 \rangle = \frac{1}{2} \kappa_B T. \tag{2.1}$$

The instantaneous temperature at time t can be given as

$$T(t) = \sum_{i=1}^{N} \frac{m_i \nu_i^2(t)}{\kappa_B N_f}, \tag{2.2}$$

where N_f is the number of degrees of freedom.

2.1.2 Force calculation

This is the most time consuming part in the molecular dynamics simulations. Forces are derived as the gradient of the potential energy $U(\mathbf{r}_{ij})$ with respect to the atomic displacements:

$$\mathbf{F}_{ij} = -\frac{\partial U(\mathbf{r}_{ij})}{\partial \mathbf{r}_{ij}}, \tag{2.3}$$

where $\mathbf{r}_{ij}$ is the distance between atoms i and j and $\mathbf{F}_{ij}$ is the force acting on particle i by particle j.

2.1.3 The Integrator

Now one can generate the atomic trajectories of a set of interacting N atoms by numerical integration of Newton's equation of motion with certain initial and boundary conditions:

$$m_i \frac{d^2\mathbf{r}_i}{dt^2} = \sum_{j=1(\neq i)}^{N} \mathbf{F}_{ij}, \qquad for \;\; i = 1, 2, 3, ..., N \tag{2.4}$$

where m_i and $\mathbf{r}_i$ are the mass and position vector for each particle i, and t is the time. An integrator should be accurate (approximate the true trajectory), stable (conserve energy) and robust (should not be sensitive to the time step scale). Here, we discuss the very simple and most used velocity Verlet integrator [107]. For a small time step Δt, Taylor expansion of the coordinate of a particle is given by

$$r(t + \Delta t) = r(t) + \nu(t)\Delta t + \frac{f(t)}{2m}(\Delta t^2) + \dddot{r}\frac{\Delta t^3}{3!} + \mathcal{O}(\Delta t^4). \tag{2.5}$$

similarly by performing $\Delta t \longrightarrow$ -Δt

$$r(t - \Delta t) = r(t) - \nu(t)\Delta t + \frac{f(t)}{2m}(\Delta t^2) - \dddot{r}\frac{\Delta t^3}{3!} + \mathcal{O}(\Delta t^4). \tag{2.6}$$

After summing the above equations, we get

$$r(t + \Delta t) + r(t - \Delta t) = 2r(t) + \frac{f(t)}{m}(\Delta t^2) + \mathcal{O}(\Delta t^4), \tag{2.7}$$

$$r(t + \Delta t) \approx 2r(t) - r(t - \Delta t) + \frac{f(t)}{m}(\Delta t^2) + \mathcal{O}(\Delta t^4). \tag{2.8}$$

In this way, the new positions are calculated with an error of order Δt^4 where Δt is the time step. We can derive the velocity also from above Eqs. (2.5) and (2.6) using the central difference scheme:

$$r(t + \Delta t) - r(t - \Delta t) = 2\nu(t)\Delta t + \mathcal{O}(\Delta t^3), \tag{2.9}$$

or

$$\nu(t) = \frac{r(t + \Delta t) - r(t - \Delta t)}{2\Delta t} + \mathcal{O}(\Delta t^2). \tag{2.10}$$

The velocities are used to calculate the kinetic energy and therefore, instantaneous temperature. In each time step, the current temperature and potential energy are calculated.

2.1.4 Ensembles

According to statistical physics, physical quantities are represented by an average over configurations, distributed according to a certain statistical ensemble. For long MD simulation times, we expect the phase space to be fully sampled ("system at equilibrium") in our systems

$$\langle A \rangle = \lim_{t\to\infty} \frac{1}{t} \int_{t_0}^{t_0+t} A(\tau) d\tau. \tag{2.11}$$

At equilibrium this average cannot depend on the initial time t_0. Since position and momenta are obtained, the time average represents both static properties such as thermodynamics, and dynamic properties such as transport coefficients.

The conventional MD simulation over which the N particles and the volume V and the total energy E are constant are equivalent to ensemble averages in the microcanonical (NVE) ensemble. Unfortunately, most experiments are carried out at a specific temperature. Therefore, NVT (isochoric-isothermal) or NPT (isothermal-isobaric) simulations using a thermostat are required. In the problems addressed in this thesis, the MD simulations were performed in the NPT ensemble. For temperature and pressure control in the simulations, the Nosé-Hoover thermostat and barostat were employed. The goal of the thermostat is to ensure that the average temperature and pressure of the system is the desired one.

The isothermal ensemble: Using statistical mechanics, a desired temperature can be imposed on a system by bringing it into thermal contact with a large heat bath. Here, three most widely used thermostat will be discussed.

1. Andersen Thermostat: In this thermostat, the system reaches the desired temperature by having random collisions of molecules associated with a heat bath. The strength of the coupling to the heat bath is determined by the frequency ω of stochastic collisions.

If the successive collisions are uncorrelated, the distribution of time intervals [t, t+Δt] between two successive stochastic collision $P(t,\omega)$ is given by the Poisson form

$$P(t,\omega) = \omega\ exp[-\omega t]. \tag{2.12}$$

The probability that a particle undergoes a collision with the heat bath in a time step Δt is $\omega\Delta t$. This selected particle attains a new velocity according to the Maxwell-Boltzmann distribution corresponding to the desired temperature. The rest of the particles in the system have no effect of this collision. Usually, in the limit of an infinitely long trajectory average, the Andersen thermostat generates the correct canonical ensemble probabilities. It yields good results for static (time-independent) properties (e.g. the distribution of kinetic and potential energies, pressure). But due to its stochastic collisions, the Andersen method generates unphysical dynamics, hence dynamical properties (e.g. diffusion coefficient) gives erroneous values.

2. Berendsen Thermostat: The velocity-rescaling method does not allow temperature fluctuations which are present in the canonical ensemble. To overcome this, the Berendsen thermostat [108] is introduced where the system is weakly coupled to a heat bath with coupling constant τ. The velocities are rescaled $\nu' = \lambda\nu$ globally where λ is the scaling factor:

$$\nu' = \lambda\nu, \tag{2.13}$$

$$\lambda^2 = 1 + \frac{\Delta t}{\tau}(\frac{T_0}{T}). \tag{2.14}$$

Where T_0 is the desired temperature, T is the instantaneous temperature, τ is the coupling time constant which determines the time scale at which the desired temperature is reached. The Berendsen thermostat does not capture the correct energy fluctuations.

3. Nosé-Hoover Thermostat: The Nosé approach was based on an extended Lagrangian, i.e. Lagrangian that contains additional artificial coordinates and velocities. The idea is to consider the heat bath as an integral part of the system by the addition of an artificial variable s, associated with a mass Q>0 as well as a velocity (ds/dt). The magnitude of Q determines the coupling between the reservoir and the real system that influences the temperature fluctuations. Although any finite (positive) mass is sufficient to guarantee in principle the generation of a canonical ensemble. Small Q (tight coupling) leads to high frequency oscillations of energy coupled with s and frequency collisions with the real system. On the other hand, too large value of Q (loose coupling) may cause a poor temperature control (Nosé-Hoover thermostat with Q$\rightarrow\infty$ is MD that generates a microcanonical ensemble). The kinetic energy of s is (1/2)Q$(ds/dt)^2$, and potential energy -$N_f k_b T_0 ln$s is chosen to ensure that the algorithm produces a canonical ensemble. Accompanying the fluctuations of s, heat transfer occur between the system and a heat bath,

which regulate the system temperature [109]. For the Nosé-Hoover thermostat in which there are no external forces and the center of mass remains fixed, a canonical distribution will be generated.

The isothermal-isobaric ensemble: In constant pressure MD simulation, the volume is taken as a dynamical variable which changes during the simulation in such a way that the (average) internal pressure is the same as the external pressure, which is described by the pressure virial theorem:

$$\langle P^{(int)} \rangle = P^{(ext)}, \tag{2.15}$$

where $P^{(ext)}$ is the external pressure and $\langle P^{(int)} \rangle$ the internal pressure. The instantaneous pressure has the following form [110]:

$$P^{(int)} = \frac{Nk_BT}{V} + \frac{1}{Vd} \sum_{i<j} \mathbf{r}_{ij}\mathbf{F}_{ij}, \tag{2.16}$$

where d is the dimension of the system, $\mathbf{r}_{ij}$ is the distance between particle i and j, and $\mathbf{F}_{ij}$ is the force between two particles.

1. Berendsen barostat: From Eq. (2.16), it is clear that a change in pressure can be realised by rescaling the distance $\mathbf{r}_{ij}$. Scaling of the particle coordinates ($\mathbf{r}_i$) and unit cell l can be done by using the Berendsen barostat [108] as:

$$\mathbf{r}_i' = \left[1 - \frac{\Delta t}{\tau_p}(P_0 - P^{(int)})\right]^{1/3} \mathbf{r}_i = \mu \mathbf{r}_i \tag{2.17}$$

$$l' = \mu l, \tag{2.18}$$

where τ_p is the damping factor for the barostat and P_0 is the desired pressure.

2. Nosé-Hoover chain barostat: The equation of motion has the following basis form for the d-dimensional system (N_f=dN, total number of degrees of freedom):

$$\dot{V} = \frac{dVp_\epsilon}{W}, \tag{2.19}$$

$$\dot{p}_\epsilon = dV(P^{(int)} - P^{(ext)}) + \frac{d}{N_f} \sum_{i=1}^{N} \frac{\mathbf{P}_i^2}{m_i} - \frac{p_\xi}{Q} p_\epsilon, \tag{2.20}$$

here, V is the volume, p_ϵ is the barostat momentum, p_ξ is the thermostat momentum, W is the mass associated with the fluctuation of the volume. These equations which are called MTK equations [111] are added to the equation of motion to produce the correct NPT phase space distribution.

2.1.5 Bond-order potential

A proper interatomic potential function which is capable of describing accurately the interactions in the material system is of crucial importance. Classical empirical force fields can be used in large-scale atomistic simulations with low computational cost. Nonreactive empirical potentials used e.g. for drug design and polymer research, are generally reliable only near equilibrium with fixed reactivity and charges. Recently, a new approach named as bond-order potentials emerged that depend on the local chemical environment in reactive simulations. In contrast to classical empirical potential, bond-order potentials capture bond formation and breaking, saturated and unsaturated bonds, dangling and radical bonds, as well as single, double or triple bonds [112].

The interatomic potentials can be divided into two formats: a separated format and an integrated format. The first format consists of two-body and three-body (and higher) energy terms separately such as the Finnis-Sinclair, embedded-atom method (EAM), modified EAM (MEAM), and Stillinger-Weber (SW) potentials. In the integrated format, the potential energy has integrated many-body effect and two-body interaction via a bond order term such as Tersoff and reactive empirical bond order (REBO) potentials.

Although the bond order approach with charge-free and fixed-charged (Tersoff, REBO) has demonstrated successfully to model many systems, but the lack of a dynamic charge scheme to readjust the atomic charge according to its environment prevent it to model complex systems accurately. The self-consistent charge equilibrium approach is developed on the basis of the principle of electronegativity equalization to automatically and consistently determine atomic charge to match local explicit electrostatic effects such that as those present in ionic or heterogenous systems. ReaxFF (reactive force field) and charge-optimized many-body (COMB) are two variable charge potentials which can simulate a variety of elements and multifunctional systems [113].

The potential energy function: There are many problems in physics, chemistry and material science (e.g. thermal and mechanical properties of materials, phonon dispersions and interactions, surface reconstruction and diffusion paths and barriers) which require the knowledge of the total energy of a system as a function of the atomic coordinates. Potential energy modeling plays a fundamental important role in atomistic simulations as it provides the ability to lead to results which can be compared with experiments. A good potential energy model should be able to balance both the radial forces in the system which resist a change in the bond length from the equilibrium value and the angular forces in the system which resist in the shape of the bond angle at the unstrained equilibrium state.
A classical potential takes the form

$$V = \sum_i V_1(r_i) + \sum_{i,j} V_2(r_i, r_j) + \sum_{i,j,k} V_3(r_i, r_j, r_k) + \cdots \tag{2.21}$$

Where, V is the total potential energy of the system, V_1 represents a single particle potential which corresponds to an external potential, V_2 is a pair-potential (or two body potential) and only depends upon the distance between the atoms i and j. V_3 is the three-body interaction in the system and may contain angular dependent terms. Three-body and higher order potentials are grouped into a category called many-body potentials.

It is also a common practice to put a cut-off function for a potential energy to avoid massive computation due to long-range forces beyond 1^{st} nearest neighbor atoms. Hence $V(r_{ij}) \rightarrow 0$ for $r_{ij} > r_c$ where r_c is the cut-off radius. To prevent a discontinuity in the second derivatives of this cut-off function at $r_{ij} = r_c$, which gives unphysical behavior, a trigonometric smoothing function is usually introduced in the interval $r_c < r_{ij} < (r_c + \Delta r)$ which makes the potential and the force continuous.

The Tersoff Potential: An empirical interatomic potential energy function was introduced by J. Tersoff in 1986 [114] for silicon. The main idea was the bond order (i.e., the strength of each bond) which depends upon the local environment [115]. Usually an atom with many neighbors forms weaker bonds than an atom with few neighbors. Due to the crucial role of bond order and its dependence upon local geometry, it seems attractive to include an environment dependent bond order explicitly into the potential. The interatomic potential can be written in the form

$$V_{ij} = f_c(r_{ij})[a_{ij} f_R(r_{ij}) + b_{ij} f_A(r_{ij})] \tag{2.22}$$

here V_{ij} is the bond energy, the indices i and j run over the atoms of the system and r_{ij} is the distance from atom i to atom j.

The function f_R and f_A represent repulsive and attractive pair potentials, respectively.

$$\begin{aligned} f_R(r) &= A\, exp(-\lambda_1 r), \\ f_A(r) &= -B\, exp(-\lambda_2 r). \end{aligned} \tag{2.23}$$

The extra term f_c is a smooth cutoff function, to limit the range of the potential, since for many applications short-ranged functions permit a tremendous reduction in computational effort.

$$f_c(r) = \begin{cases} 1, & r < R - D \\ [\frac{1}{2} - \frac{1}{2} sin(\frac{\pi}{2}(r - R)/D], & R - D < r < R + D \\ 0, & r > R + D \end{cases} \tag{2.24}$$

which is continuous with a continuous derivative for all r, and goes smoothly from 1 to 0 in a small range around R. R is chosen to include only the nearest-neighbors. The function

b_{ij} is a measure of the bond order. The terms which act to limit the range of interaction to the first neighbors are included in b_{ij}.

$$\begin{aligned} b_{ij} &= (1+\beta^n \zeta_{ij}^n)^{-1/2n}, \\ \zeta_{ij} &= \sum_{k\neq i,j} f_c(r_{ik}) g(\theta_{ijk}) exp[\lambda_3^3 (r_{ij}-r_{ik})^3], \\ g(\theta) &= 1 + c^2/d^2 - c^2/[d^2 + (h - cos\theta)^2], \end{aligned} \tag{2.25}$$

where θ_{ijk} is the bond angle between bonds ij and ik.

The a_{ij} has the form

$$\begin{aligned} a_{ij} &= (1+\alpha^n \eta_{ij}^n)^{-1/2n}, \\ \eta_{ij} &= \sum_{k\neq i,j} f_c(r_{ik}) exp[\lambda_3^3 (r_{ij}-r_{ik})^3], \end{aligned} \tag{2.26}$$

with α taken sufficiently small that $a_{ij} \simeq 1$ unless η_{ij} is exponentially large, which will only occur for atoms that are located outside the first-neighbors. The optimised Tersoff parameters for h-BN used in this thesis can be found in Appendix E.

The Brenner Potential: The Brenner second generation reactive empirical bond order (REBOII) potential for solid carbon and hydrocarbon molecules that is developed by Brenner [116] is used in this thesis in order to describe graphene nano-flakes. This potential is based on the empirical bond-order formalism and allows for covalent bond binding and breaking with associated changes in atomic hybridization. Consequently, such a classical potential allows to model complex chemistry in large many-atom systems. This potential contains improved analytic functions and an extended database over the original REBO potential developed by Brenner [117], which was based on the concept of the bond-order function introduced by Tersoff and includes many-body effects into an effectively two-body (pair) potential [118].

The REBOII potential has the functional form

$$E_b = \sum_i \sum_{j(>i)} [V^R(r_{ij}) - b_{ij} V^A(r_{ij})]. \tag{2.27}$$

Here E_b is the binding energy in electron volt (eV) unit, the functions $V^R(r_{ij})$ and $V^A(r_{ij})$ are pair-additive repulsive and an attractive term, respectively, where r_{ij} is the distance between atoms i and j given by

$$V^R(r) = f^c(r)(1 + Q/r) A e^{-\alpha r}, \tag{2.28}$$

$$V^A(r) = f^c(r) \sum_{n=1,3} B_n e^{-\beta_n r}. \tag{2.29}$$

The subscript n refers to the type of bonds (e.g. single, double or triple). The screened Coulomb function Q is used for the repulsive pair interaction which goes to infinity as interatomic distances approach zero. The cut-off function $f^c(r)$ is taken from the switching cutoff scheme which also ensures that the interactions include only the first neighbor shell.

$$f_{ij}^c(r) = \begin{cases} 1, & r < D_{ij}^{min} \\ \big[1 + cos\big(\dfrac{\pi(r - D_{ij}^{min})}{(D_{ij}^{max} - D_{ij}^{min})}\big)\big]/2, & D_{ij}^{min} < r < D_{ij}^{max} \\ 0, & r > D_{ij}^{max} \end{cases} \tag{2.30}$$

where $D_{ij}^{max} - D_{ij}^{min}$ defines the distance over which the function goes from one to zero and $A, Q, \alpha, B_n, \beta_n, (1 \leq n \leq 3)$ are parameters for the carbon-carbon pair terms. Although this expression is a simple sum over bond energies, it is not a pair potential since the b_{ij}, which is called bond-order factor, is in essence a many-body term. For example, in the Brenner potential the b_{ij} depends on the bond and torsional angles, the bond lengths, and the atomic coordination in the vicinity of the bond. The many-body nature of b_{ij} makes the bond energy depend on the local environment of the bond. This feature allows the Brenner potential to predict correct geometries and energies for many different carbon structures and correct hybridization. The empirical bond order used in this work can be written as a sum of terms:

$$\overline{b_{ij}} = \frac{1}{2}[b_{ij}^{\sigma-\pi} + b_{ji}^{\sigma-\pi}] + b_{ij}^{\pi}. \tag{2.31}$$

The function b_{ij}^{π} can be further written as a sum of two terms:

$$b_{ij}^{\pi} = \Pi_{ij}^{RC} + b_{ij}^{DH}. \tag{2.32}$$

Where the first term Π_{ij}^{RC} depends on radical character of a bond between atoms i and j while the second term b_{ij}^{DH} depends on the dihedral angle for carbon-carbon double bonds. The first term in Eq. (2.31) is given as

$$b_{ij}^{\sigma-\pi} = \big[1 + \sum_{k(\neq i,j)} f_{ik}^c(r_{ik}) G_C(cos(\theta_{ijk})) e^{\lambda_{ijk}} + P_{ij}(N_i^C, N_i^H)\big]^{-1/2}. \tag{2.33}$$

Here, the function P exhibit a bicubic spline and quantities N_i^C and N_i^H represent the number of carbon and hydrogen atoms, respectively, that are neighbors of atom i. N_i^C and N_i^H are defined by the sums

$$N_i^C = \sum_{k(\neq i,j)}^{carbon\ atoms} f_{ik}^c(r_{ik}).$$

$$N_i^H = \sum_{l(\neq i,j)}^{hydrogen\ atoms} f_{il}^c(r_{il}).$$

The values of λ and the function P are zero for the solid-state form of carbon. The angular function $G_C(cos(\theta_{ijk}))$ modulates the contribution of each nearest neighbor and is determined by the cosine of the angle of the bonds between atoms $i-j-k$.

The term π_{ij}^{RC} in Eq. (2.32) shows the influence of radical energetics (e.g. vacancy formation energies in diamond) and π-bond conjugation on the bond energies. This function can be written as

$$\pi_{ij}^{RC} = F_{ij}(N_i^t, N_j^t, N_{ij}^{conj}) \tag{2.34}$$

where F is a tricubic spline. π_{ij}^{RC} depends on the total number of neighbors of bonded atoms i and j. N_i^t, the coordination of atom i is given by

$$N_i^t = N_i^C + N_i^H. \tag{2.35}$$

N_{ij}^{conj} depends on local conjugation is given by the function

$$N_{ij}^{conj} = 1 + \big[\sum_{k(\neq i,j)}^{carbon} f_{ik}^c(r_{ik})F(X_{ik})\big]^2 + \big[\sum_{l(\neq i,j)}^{carbon} f_{jl}^c(r_{jl})F(X_{jl})\big]^2. \tag{2.36}$$

where

$$F(x_{ik}) = \begin{cases} 1, & x_{ik} < 2 \\ \big[1 + cos(2\pi(x_{ik}-2))\big]/2, & 2 < x_{ik} < 3 \\ 0, & x_{ik} > 3 \end{cases} \tag{2.37}$$

and

$$x_{ij} = N_k^t - f_{ik}^c(r_{ik}). \tag{2.38}$$

Here, if the pair of bonded carbon atoms i and j have four or more neighbors, the value of N_{ij}^{conj} will be one and the bond between these atoms is not the part of a conjugated system. For the coordination numbers smaller than four, N_{ij}^{conj} becomes larger than one and the bond will be considered as a conjugated system.

The term b_{ij}^{DH} is given by

$$b_{ij}^{DH} = T_{ij}(N_i^t, N_j^t, N_{ij}^{conj})\big[\sum_{k(\neq i,j)}\sum_{l(\neq i,j)}(1 - cos^2(\Theta_{ijkl}))f_{ik}^c(r_{ik})f_{jl}^c(r_{jl})\big]. \tag{2.39}$$

where

$$\Theta_{ijkl} = e_{jik}e_{ijl}. \tag{2.40}$$

Here, the function $T_{ij}(N_i^t, N_j^t, N_{ij}^{conj})$ is a tricubic spline. e_{jik} is the unit vector in the direction of the cross product $\mathbf{R_{ji}} \times \mathbf{R_{ik}}$, where $\mathbf{R}$ is the vector connecting the subscripted atoms. Forces for rotation about dihedral angles for carbon-carbon double bonds are included in analytic bond order using these equations. T_{ij} is taken zero for a planar system, and one for angles of 90°. The function T_{CC} determines the barrier for rotation about carbon double bonds and it's contribution to the bond order is zero for bonds that are not double bonds.

The values for all the parameters used in our calculation for the Brenner potential can be found in Ref. [116] and Appendix E.

The ReaxFF (reactive force field) Potential: ReaxFF was developed by Adri van Duin, William A. Goddard III, and co-workers for molecular dynamics simulations of large scale reactive chemical systems (order of hundreds of thousands of particles) at the California Institute of Technology [119]. ReaxFF, a reactive force field uses the concept of bond order to model the interaction within the system. With bond order dependence we mean a dynamic description of each atomic and molecular interaction that does not depend on the predefined reactive sites as defined in empirical potentials. A detailed parameterization of the atomic, bonding, angle and torsion properties of each particle and interaction are fitted against quantum and experimental data. ReaxFF also has Coulomb and van der Waals potentials to describe nonbond interactions between all atoms. ReaxFF describes the stability and geometry of non-conjugated, conjugated, and radical-containing compounds and, additionally, the dissociation and formation of chemical bonds. The reactive force field divides the system energy up into various partial energy contributions:

$$E_{system} = E_{self} + E_{Coulomb} + E_{vdW} + E_{bond} + E_{angle} + E_{torsion} + E_{conjugation} + \\ + E_{H-bond} + E_{lone-pair} + E_{over} + E_{under} + E_{others} \quad (2.41)$$

The self-energy term, E_{self}, captures the difference in energy of the various charge states of an atom, whereas the Coulomb term, $E_{Coulomb}$, captures the electrostatic interactions. ReaxFF also includes an energy term to handle non-bonded interactions through the van der Waals energy, E_{vdW}. Complex physics and chemistry are captured in the bond-order terms contained within E_{bond}. The bond-order terms are corrected for overcoordination to allow for the long-range bond order necessary for accurate reaction barriers. ReaxFF also explicitly includes energy contributions related to valence and torsion angle distortion (E_{angle} and $E_{torsion}$); energy contribution related to three-body and four-body conjugation ($E_{conjugation}$); a weak hydrogen bond term (E_{H-bond}) to properly describe X-H-X non-bonded interactions in polar molecules; energy terms related to the number of valence electrons around an atom ($E_{lone-pair}$, E_{over} and E_{under}); several energy terms (E_{others}) to correct for allene-type, terminal triple-bond, and C_2 species. All the energy

contributions in ReaxFF, excluding the van der Waals and Coulomb terms, are bond-order dependent and disappear upon bond dissociation. These many-body potential terms allows one to describe a wide range of chemical and material systems, from strictly covalent system such as hydrocarbon to either completely ionic or partially ionic systems such as silica.

The bond order BO'_{ij} between a pair of atoms can be calculated directly from the instantaneous interatomic distances r_{ij}. For example, the bond order for C-C interaction consists of three exponential terms: (1) the single (σ) bond (p_{bo1} and p_{bo2}) which is unity below $\sim$ 1.5 Å but negligible above $\sim$ 2.5 Å; (2) the double (pi) bond (p_{bo3} and p_{bo4}) which is unity below $\sim$ 1.2 Å and negligible above $\sim$ 1.75 Å; and (3) the triple (double pi) bond (p_{bo5} and p_{bo6}) which is unity below $\sim$ 1.0 Å and negligible above $\sim$ 1.4 Å

$$BO'_{ij} = BO^{\sigma}_{ij} + BO^{\pi}_{ij} + BO^{\pi\pi}_{ij} = exp\left[p_{bo1}.\left(\frac{r_{ij}}{r^{\sigma}_{0}}\right)^{p_{bo2}}\right] + exp\left[p_{bo3}.\left(\frac{r_{ij}}{r^{\pi}_{0}}\right)^{p_{bo4}}\right] + exp\left[p_{bo5}.\left(\frac{r_{ij}}{r^{\pi\pi}_{0}}\right)^{p_{bo6}}\right], \tag{2.42}$$

where p is the bonding term and r_0 the equilibrium bond length of each type of bond are parameterized in such a manner that bond strengths and distances agree with quantum mechanically predicted values at distance r_{ij}. In ReaxFF, bonding interactions start at a much larger distance than other empirical methods. Therefore, it can accurately model the long range, partially bonded configurations of transition states.

Due to the long range interaction, each carbon has a weak bond order with its second nearest neighbour, hydrogen atoms. This type of bonding produces unrealistic results and is corrected by neglecting long range order if the carbon atom has a bond order of 4 or more. Conversely, if the carbon atom has less than 4 bonds, long range weak interaction should be included.

In non-reactive force fields, angle and torsion interactions among atoms are rigid, which is usually described with simple harmonic potentials regardless of how strong or weak the bond is. However, in ReaxFF, these angle and torsion interactions are bond order dependent, meaning that as an atom breaks a bond and leaves a molecule, the force exerted on it due to angle torsion with respect to the rest of the molecule weakens smoothly along with the bond order.

For nonbonded interactions, a distance-corrected Morse potential is employed to calculate the van der Waals interactions (Eq. (2.43)). Whereas all atom pairs on the system are subject to the nonbonded interaction calculation regardless of connectivity, a shielded interaction helps to avoid excessively high repulsions at short distances between atoms

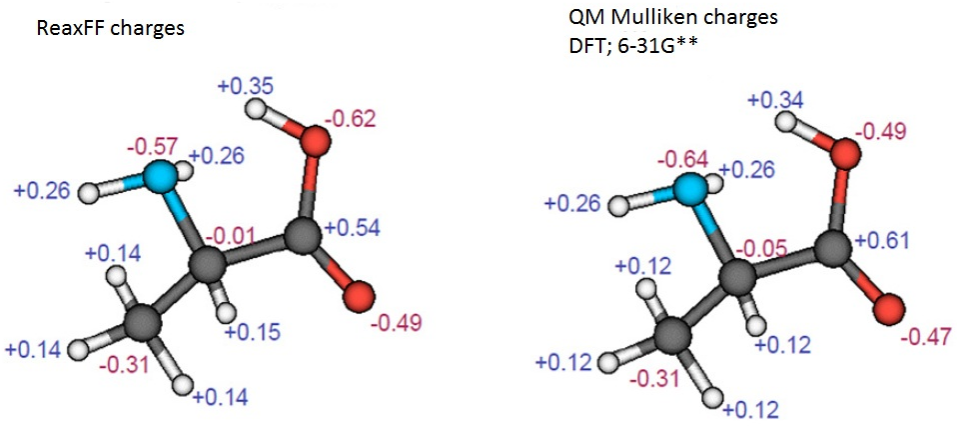

Figure 2.1: Comparison of the ReaxFF calculated charges versus quantum mechanical value of the same molecule. The ReaxFF closely reproduces the Mullikan charges on each atom and models the polarizability of the molecule. (Taken from ref. [120].)

sharing a bond and a valence angle:

$$E^{vdW} = Tap.D_{ij}.exp[\alpha_{ij}.(1 - \frac{f_{13}(r_{ij})}{r_{vdW}})] - 2.exp[\frac{1}{2}.\alpha_{ij}.(1 - \frac{f_{13}(r_{ij})}{r_{vdW}})], \tag{2.43}$$

$$f_{13}(r_{ij}) = [r_{ij}^{pvdW1} + (\frac{1}{\gamma_\omega})^{pvdW1}]^{\frac{1}{pvdW1}}, \tag{2.44}$$

where D_{ij} is the van der Waals dissociation energy, r_{vdW} is the van der Waals radius, and γ_ω is a shielding parameter. A distance-dependent seventh-order polynomial taper function, Tap(r), is used as a smooth cutoff boundary.

The ReaxFF is also used to calculate the polarization of charge within molecules (Eq. (2.45)) which is achieved by electronegativity and hardness parameters based on the Electronegativity Equalization Method (EEM) [121] and charge equilibration (QEq) [122] methods. The calculation of the polarization is given by

$$\frac{\partial E}{\partial q_i} = \chi_i^* + 2\eta_i^* q_i + Tap.C \sum_{j \neq i}^{N} \frac{q_j}{[r_{ij}^3 + (1/\gamma_{ij})^3]^{1/3}}, \tag{2.45}$$

where χ_i^* and η_i^* are the effective electronegativity and the chemical hardness of atom i that are parameterized against quantum mechanical charge distributions. To take into account

the shielding between overlapping electron clouds at short distances, a shielding parameter for each atom pairs, γ_{ij}, is included. q_i and q_j are the charges of the two atoms, and C is the conversion factor. The electrostatic energy is minimized with the equilibrium charge distribution under the total charge constraints. Charges are updated at every step, which is the most computationally part of the ReaxFF energy calculations. The optimised ReaxFF parameters for the C-F system used in this thesis can be found in Appendix E.

2.2 Density functional theory

Density-functional theory (DFT) is one of the most popular and successful quantum mechanical approaches to investigate the electronic structure (in principal only the ground state) of many-body systems, in particular atoms, molecules, and the condensed phases. I will use DFT calculations in the study of the electronic properties of graphene nano-flakes in this thesis.

2.2.1 The Schrödinger equation

Most of the properties of interest here can be deduced from static, i.e. time-independent, non-relativistic Schrödinger equation

$$\hat{H}\Psi_i(\mathbf{r}_1, ..., \mathbf{r}_N, \mathbf{R}_1, ..., \mathbf{R}_M) = E_i\Psi_i(\mathbf{r}_1, ..., \mathbf{r}_N, \mathbf{R}_1, ..., \mathbf{R}_M) \tag{2.46}$$

where the coordinates $\mathbf{r}_i$ represent both the position coordinates, and the spin coordinates of the N electrons and the coordinates $\mathbf{R}_i$ are the position coordinates of the M atomic nuclei in the system. $\hat{H}$ is the Hamilton operator for a molecular system consisting of M nuclei and N electrons in the absence of magnetic and electric fields. $\hat{H}$ is a differential operator representing the total energy:

$$\begin{aligned}\hat{H} &= -\frac{\hbar^2}{2m_e}\sum_{i=1}^{N}\nabla_i^2 - \sum_{A=1}^{M}\frac{\hbar^2}{2M_A}\nabla_A^2 - \sum_{i=1}^{N}\sum_{A=1}^{M}\frac{Z_A e^2}{|\mathbf{r}_i - \mathbf{R}_A|} \\ &\quad + \frac{1}{2}\sum_{i\neq j}^{N}\frac{e^2}{|\mathbf{r}_i - \mathbf{r}_j|} + \frac{1}{2}\sum_{A\neq B}^{M}\frac{Z_A Z_B e^2}{|\mathbf{R}_A - \mathbf{R}_B|},\end{aligned} \tag{2.47}$$

where m_e is the mass of the electron and M_A and Z_A are respectively the mass and the charge (atomic number) of the nuclei. The first and the second term of Eq. (2.47) correspond to the kinetic energies of the electrons and nuclei, while the others represent the

electron-nucleus, electron-electron, and nucleus-nucleus Coulomb interaction terms, respectively. It is impossible to solve this equation exactly except for the very simple hydrogen atom. Therefore, a number of approximations are introduced to this equation so that approximate solutions are feasible.

2.2.2 The Born-Oppenheimer or adiabatic approximation

The Schrödinger equation can be further simplified using the famous *Born-Oppenheimer* approximation by considering the large difference in mass between electrons and nuclei. Even the proton weighs approximately 1800 times more than an electron and for the carbon atom the mass ratio is already 22000. Therefore kinetic energy of the nuclei which is inversely proportional to the nuclear mass M_A, is relatively small and can be neglected. If the nuclei are fixed in space then their kinetic energy is zero and the nucleus-nucleus repulsion term becomes merely a constant. Therefore, the electronic Hamiltonian can be written as

$$\begin{aligned} \hat{H}_{ele} &= -\frac{\hbar^2}{2m_e}\sum_{i=1}^{N}\nabla_i^2 - \sum_{i=1}^{N}\sum_{A=1}^{M}\frac{Z_A e^2}{|\mathbf{r}_i - \mathbf{R}_A|} + \frac{1}{2}\sum_{i\neq j}^{N}\frac{e^2}{|\mathbf{r}_i - \mathbf{r}_j|} \\ &= \hat{T} + \hat{V}_{Ne} + \hat{V}_{ee}. \end{aligned} \tag{2.48}$$

The solution of the Schrödinger equation $\hat{H}_{ele}$ is the electronic wave function Ψ_{ele} and the electronic energy E_{ele}. The total energy E_{tot} is the sum of E_{ele} and the constant nuclear repulsion term,

$$E_{nuc} = \frac{1}{2}\sum_{A\neq B}^{M}\frac{Z_A Z_B e^2}{|\mathbf{R}_A - \mathbf{R}_B|}, i.e., \tag{2.49}$$

$$\hat{H}_{ele}\Psi_{ele} = E_{ele}\Psi_{ele} \tag{2.50}$$

and

$$E_{tot} = E_{ele} + E_{nuc} \tag{2.51}$$

The attractive potential exerted on the electrons due to the nuclei V_{Ne} is often termed as external potential, even though the external potential is not necessary limited to the nuclear field but also may include external magnetic or electric fields.

2.2.3 The force theorem

Suppose that it would be feasible to find the exact ground state wavefunction, $\Psi_0(\mathbf{x}_1, ..., \mathbf{x}_N)$, for any given set of nuclear coordinates $\mathbf{R}_A$. Is it possible in this case to find that particular set of nuclear coordinates that minimizes the total energy? After all, it does not seem possible to check all sets of coordinates and then pick the one with the lowest energy. However, if we can calculate the forces on the nuclei we can move them according to classical mechanics until all forces on them vanish, i.e.

$$\mathbf{F}_A = -\frac{\partial E_{tot}}{\partial \mathbf{R}_A} = 0 \qquad for \quad A = 1, ..., M. \tag{2.52}$$

For the calculation of these forces we can apply the force theorem stated by Hellmann [123] and Feynman [124]: an evaluation of the forces from Eqs. (2.48) and (2.51) gives

$$-\frac{\partial E_{tot}}{\partial \mathbf{R}_A} = -\langle \frac{\partial \psi_0}{\partial \mathbf{R}_A} | \hat{H}_{ele} | \psi_0 \rangle - \langle \psi_0 | \frac{\partial \hat{H}_{ele}}{\partial \mathbf{R}_A} | \psi_0 \rangle - \langle \psi_0 | \hat{H}_{ele} | \frac{\partial \psi_0}{\partial \mathbf{R}_A} \rangle - \frac{\partial E_{nuc}}{\partial \mathbf{R}_A} \tag{2.53}$$

The first and the third term on the right vanish because of the variation principle. So we get

$$\begin{aligned} \mathbf{F}_A &= -\langle \psi_0 | \frac{\partial \hat{H}_{ele}}{\partial \mathbf{R}_A} | \psi_0 \rangle - \frac{\partial E_{nuc}}{\mathbf{R}_A} \\ &= -\langle \frac{\partial \hat{T}}{\partial \mathbf{R}_A} \rangle - \langle \frac{\partial \hat{V}_{ee}}{\partial \mathbf{R}_A} \rangle - \langle \frac{\partial \hat{V}_{ext}}{\partial \mathbf{R}_A} \rangle - \frac{\partial E_{nuc}}{\partial \mathbf{R}_A} \\ &= -\langle \frac{\partial \hat{V}_{ext}}{\partial \mathbf{R}_A} \rangle - \frac{\partial E_{nuc}}{\partial \mathbf{R}_A} \\ &= -\int d\mathbf{r} \rho_0(\mathbf{r}) \frac{\partial V_{ext}(\mathbf{r})}{\partial \mathbf{R}_A} - \frac{\partial E_{nuc}}{\partial \mathbf{R}_A}, \end{aligned} \tag{2.54}$$

with the ground state electron density, $\rho_0(\mathbf{r})$,defined as

$$\rho_0(\mathbf{r}) = N \int |\psi(\mathbf{r}_1, ..., \mathbf{r}_N)|^2 d\mathbf{r}_1 d\mathbf{r}_2 ... d\mathbf{r}_N. \tag{2.55}$$

So the forces on the nuclei only depend on the ground state density and the positions of the other nuclei and can be calculated if the wavefunction (or electron density) is known.

2.2.4 The Hartree approximation

The simplest way to solve the many-electron equation is to rewrite Eq. (2.50) as a one-particle equation for an electron moving in an average potential from all the electrons, as proposed by Hartree. The wave function then becomes

$$\psi(\mathbf{r}_1, \mathbf{r}_2, ..., \mathbf{r}_N) = \phi(\mathbf{r}_1)\phi(\mathbf{r}_2) \cdots \phi(\mathbf{r}_N). \tag{2.56}$$

The $\phi_i(\mathbf{r}_i)$ are n independent electron wave functions. A fundamental result in quantum mechanics states that if E_0 is the ground state energy solution of the Schrödinger equation, for any wavefunction φ:

$$\frac{\langle\varphi|\hat{H}|\varphi\rangle}{\langle\varphi|\varphi\rangle} \geq E_0. \tag{2.57}$$

This is called the variational principle. This principle can be used with the Hamiltonian in Eq. (2.47) and the constraint that the wave function should have the Hartree form (presented in Eq. (2.56) to prove that the solution to the Schrödinger equation in the Hartree approximation is obtained by solving the *Hartree equation*

$$\begin{aligned}[-\frac{\hbar^2}{2m_e}\sum_{i=1}^{N}\nabla_i^2 - \sum_{i=1}^{N}\sum_{A=1}^{M}\frac{Z_A e^2}{|\mathbf{r}_i - \mathbf{R}_A|} + \\ \sum_{j\neq i}^{N}\int \phi_j^*(\mathbf{r}_j)\frac{e^2}{|\mathbf{r}_i - \mathbf{r}_j|}\phi_j(\mathbf{r}_j)]\phi_i(\mathbf{r}_i) &= \epsilon_i\phi_i^*(\mathbf{r}_i).\end{aligned} \tag{2.58}$$

In the Hartree approximation, each electron i is treated independently but in an effective potential determined by an integration over the wave functions of the other electrons. Thus, the Hartree approximation is a mean-field approximation replacing the complicated many-body problem by n simpler problems in a mean-field potential. Hartree also proposed a self-consistent way to solve this equation since for the i^{th} wave function, the effective potential depends on all the other wave functions. Self-consistency is a procedure in which the wave function for step k are found through solving Eq. (2.58) with the effective potential determined by the wave function in step $k-1$. The procedure is repeated until all the wave functions are converged.

2.2.5 The Hartree-Fock approximation

Electrons being fermions, the exact many-particle wavefunction needs to be antisymmetric for exchange of electrons:

$$\psi(\mathbf{r}_1, \mathbf{r}_2, ..., \mathbf{r}_j, ..., \mathbf{r}_k, ...\mathbf{r}_N) = -\psi(\mathbf{r}_1, \mathbf{r}_2, ..., \mathbf{r}_k, ..., \mathbf{r}_j, ...\mathbf{r}_N). \tag{2.59}$$

This constraint can be added to the independent electron Hartree approach by using a Slater determinant as wavefunction instead of Eq. (2.56):

$$\psi(\mathbf{r}_1, \mathbf{r}_2, ..., \mathbf{r}_N) = \frac{1}{\sqrt{N!}} \begin{vmatrix} \phi_1(\mathbf{r}_1) & \phi_2(\mathbf{r}_1) & \cdots & \phi_N(\mathbf{r}_1) \\ \phi_1(\mathbf{r}_2) & \phi_2(\mathbf{r}_2) & \cdots & \phi_N(\mathbf{r}_2) \\ \cdot & \cdot & \cdot & \\ \cdot & \cdot & \cdot & \\ \cdot & \cdot & \cdot & \\ \phi_1(\mathbf{r}_N) & \phi_2(\mathbf{r}_N) & \cdots & \phi_N(\mathbf{r}_N) \end{vmatrix}. \tag{2.60}$$

Using the variational principle with this Slater determinant, it can be proven that the best solution is obtained by solving the Hartree-Fock equation:

$$[-\frac{\hbar^2}{2m_e}\sum_{i=1}^{N}\nabla_i^2 - \sum_{i=1}^{N}\sum_{A=1}^{M}\frac{Z_A e^2}{|\mathbf{r}_i - \mathbf{R}_A|} + \sum_{j\neq i}^{N}\int \phi_j^*(\mathbf{r}_j)\frac{e^2}{|\mathbf{r}_i - \mathbf{r}_j|}\phi_j(\mathbf{r}_j)]\phi_i(\mathbf{r}_i)$$
$$-\sum_{j\neq i}^{N}[\int \phi_j^*(\mathbf{r}_j)\frac{e^2}{|\mathbf{r}_i - \mathbf{r}_j|}\phi_i(\mathbf{r}_j)]\phi_j(\mathbf{r}_i) = \epsilon_i\phi_i^*(\mathbf{r}_i) \tag{2.61}$$

The effect of the new constraint is to add a term, called the exchange potential, to the Hartree Eq. (2.58).

2.2.6 The correlation energy

The Hartree-Fock approach assuming independent electrons in an effective potential is an approximation to the true many-body problem. The energy missing is defined as the correlation energy ($E_{corr.}$=E_{exact}-E_{HF}). Many methods exist to introduce this correlation energy very accurately for instance Møller-Plesset (MP) perturbation theory, configuration interaction (CI), or coupled cluster (CC) methods or quantum Monte-Carlo methods. However, these methods are computationally very expensive and only the smallest systems can currently be computed. On the other hand, Density Functional Theory (DFT) offers a good compromise between the qualitative description of electronic structure and the computational effort required to produce the result. Thus DFT is one of the most popular and successful quantum mechanical approaches to describe matter. It is nowadays routinely applied for calculating, e.g., the binding energy of molecules in chemistry and the electronic band structure of solids in physics. In this thesis we apply DFT to solve the electronic Hamiltonian for H- and F-passivated clusters. There are many excellent reviews and books available [125–128] to which the reader may be referred for more details. In the following subsections we will discuss the basic theorems of DFT and the approximations that are used in practical calculations.

2.2.7 The Hohenberg-Kohn theorems

Modern theory of DFT is based on the two Hohenberg-Kohn (HK) theorems [129, 130]: the first theorem states that the wavefunction, which has a central position in standard quantum theory, can be replaced by the electron ground state density without any loss of information and the second theorem is more or less the equivalent of the variation principle in standard quantum mechanics.

2.2.8 The first Hohenberg-Kohn theorem

The first Hohenberg-Kohn theorem can be stated as follows: *The external potential, $\hat{V}_{ext}(\mathbf{r})$, of any system of interacting particles is uniquely determined (up to a constant) by the particle density, $\rho_0(\mathbf{r})$, of the ground state.*

So the Hamiltonian in Eq. (2.48), which is completely specified by this external potential, is also uniquely determined by the ground state electron density. The rigorous proof of the first theorem can be found from standard DFT book [127].

The fact that the ground state particle density specifies the Hamiltonian Eq. (2.48) of the system, allows us to consider all properties of the system as functionals of the ground state density. In particular the ground state energy of the system with Hamiltonian Eq. (2.48) can be written as

$$\begin{aligned} E_{HK}[\rho_0] &= T[\rho_0] + V_{ee}[\rho_0] + V_{ext}[\rho_0] \\ &\equiv F_{HK}[\rho_0] + \int \rho_0(\mathbf{r}) V_{ext}(\mathbf{r}) d\mathbf{r}, \end{aligned} \tag{2.62}$$

where $F_{HK}[\rho_0] = T[\rho_0] + V_{ee}[\rho_0]$ is a universal functional of the density completely independent of the system. If it were known exactly we would have solved the Schrödinger equation, not approximately, but exactly. The explicit form of this functional is unknown. From the electron-electron interaction term, we can extract at least the classical Coulomb part $J[\rho]$.

$$E_{ee}[\rho] = J[\rho] + E_{ncl}[\rho], \tag{2.63}$$

where, $E_{ncl}[\rho]$ is the non-classical contribution to the electron-electron interaction containing all the effects of the self-interaction correction, exchange and Coulomb correlation. Finding explicit expressions for $T[\rho]$ and $E_{ncl}[\rho]$ represent the major challenge in DFT.

2.2.9 The second Hohenberg-Kohn theorem

From first Hohenberg-Kohn theorem, it is clear that the ground state density is in principle sufficient to obtain all properties of interest. But, how can we be sure that a certain density is really the ground state density that we are looking for? The second theorem based on the variational principle is helpful in this matter.
The second Hohenberg-Kohn theorem can be stated as follows: *F_{HK}, the functional that delivers the ground state energy of the system, delivers the lowest energy if and only if the input density is the true ground state density, ρ_0.*

This is of course nothing else than the variational principle which in the present context can be expressed as

$$E_0 \leq E[\rho] = T[\rho] + E_{Ne}[\rho] + E_{ee}[\rho]. \tag{2.64}$$

In other words this means that for any trial density $\rho_0(\mathbf{r})$ - which satisfies

$$E[\rho_0] = T[\rho_0] + E_{Ne}[\rho_0] + E_{ee}[\rho_0]. \tag{2.65}$$

with the necessary boundary conditions such as $\rho_0(\mathbf{r}) \geq 0$, $\int \rho_0(\mathbf{r})d\mathbf{r} = N$, and which is associated with some external potential V_{ext} - the energy obtained from the functional given by Eq. (2.65) represents an upper bound to the true ground state energy E_0. E_0 results if and only if the exact ground state density is inserted into Eq. (2.62). It should also be noted that using the Hohenberg- Kohn formulation of DFT implies that we are working at T = 0 K.

2.2.10 The Kohn-Sham approach

Kohn and Sham introduced the concept of a non-interacting reference system built from a set of orbitals (i.e., one electron functions) such that the major part of the kinetic energy can be computed to good accuracy. The remainder is merged with the non-classical contribution to the electron-electron repulsion- which are also unknown, but usually fairly small. By this method, as much information as possible is computed exactly, leaving only a small part of the total energy to be determined by an approximate functional.

We only know how to express the kinetic energy as a functional of the wavefunction, i.e. $T[\Psi] = \langle\Psi| - 1/2 \sum_i \nabla_i^2 |\Psi\rangle$. The problem is that the same density can be reproduced by a variety of wavefunctions and these can actually have any kinetic energy. This can be demonstrated by regular plane waves, $e^{i\vec{k}.\vec{r}}$, which all correspond to the same density

but their kinetic energy is proportional to k^2. The actual ground state wavefunction is uniquely specified as the one corresponding to the lowest (total) energy but it should be clear now that it is not easy to get this directly from the density. Therefore Kohn and Sham proposed to make use of an auxiliary system for which it is possible to find the wavefunctions. It was shown in the Hartree-Fock approach that it is possible to construct a non-interacting hamiltonian which has Slater-determinants as exact solutions for the many-body wavefunction. The idea of Kohn and Sham was to construct a similar non-interacting reference system, i.e. a system of which the wavefunction can be found, so that its density equals the density of the real system. In other words, they assumed a reference system described by a hamiltonian with an effective local potential $V_s(\mathbf{r})$,

$$\hat{H}_s = -\frac{1}{2}\sum_i^N \nabla_i^2 + \sum_i^N V_s(\mathbf{r_i}), \tag{2.66}$$

of which the solution is a Slater-determinant $\Psi_s = |\phi_1\phi_2...\phi_N|$ so that

$$\rho_S(\mathbf{r}) = \sum_i^N |\phi_i|^2 = \rho_0(\mathbf{r}). \tag{2.67}$$

Kohn and Sham suggested to use the expression of the Hartree-Fock kinetic energy to obtain the exact kinetic energy of the non-interacting reference system with the same density as the real, interacting one

$$T_S = -\frac{1}{2}\sum_i^N \langle\phi_i|\nabla_i^2|\phi_i\rangle. \tag{2.68}$$

Of course, the non-interacting kinetic energy is not equal to the true kinetic energy of the interacting system, even if the system shares the same density, i.e., $T_S \neq T$. Kohn and Sham accounted for that by introducing the following separation of the functional F$[\rho]$

$$F[\rho(\mathbf{r})] = T_S[\rho(\mathbf{r})] + J[\rho(\mathbf{r})] + E_{XC}[\rho(\mathbf{r})] \tag{2.69}$$

where J is the classical Coulomb interaction term and E_{XC}, the so-called exchange-correlation energy is defined through previous equation as

$$E_{XC}[\rho] \equiv (T[\rho] - T_S[\rho]) + (E_{ee}[\rho] - J[\rho]) = T_C[\rho] + E_{ncl}[\rho] \tag{2.70}$$

The residual part of the true kinetic energy, T_C, which is not covered by T_S, is simply added to the non-classical electrostatic contributions. In other words, the exchange-correlation

energy E_{XC} is the functional which contains everything that is unknown, a kind of junk-yard where everything is stowed away which we do not know how to handle exactly.

Now, how can we define V_S such that it really provides us with a Slater determinant which is characterized by exactly the same density as our real system? To solve this problem, we write down the expression for the energy of our interacting real system

$$\begin{aligned} E[\rho(\mathbf{r})] &= T_S[\rho] + J[\rho] + E_{XC}[\rho] + E_{Ne}[\rho] \\ &= T_S[\rho] + \frac{1}{2}\int\int \frac{\rho(\mathbf{r}_1)\rho(\mathbf{r}_2)}{r_{12}} d\mathbf{r}_1 d\mathbf{r}_2 + E_{XC}[\rho] + \int V_{Ne}\rho(\mathbf{r}) d\mathbf{r}. \end{aligned} \quad (2.71)$$

The only term for which no explicit form can be given, i.e., the big unknown, is of course E_{XC}. We now apply the variational principle and ask: what condition must the orbitals ϕ_i fulfill in order to minimize this energy expression under the usual constraint of $\langle\phi_i|\phi_i\rangle = \delta_{ij}$? The resulting equations are:

$$\begin{aligned} (-\frac{1}{2}\nabla^2 + [\int \frac{\rho(\mathbf{r}_2)}{r_{12}} d\mathbf{r}_2 + V_{XC}(\mathbf{r}_1) - \sum_A^M \frac{Z_A}{r_{1A}}])\phi_i &= (-\frac{1}{2}\nabla^2 + V_{eff}(\mathbf{r}_1))\phi_i \\ &= \varepsilon_i\phi_i, \end{aligned} \quad (2.72)$$

if we compare this with the one-particle equation from the non-interacting reference system, we see immediately that the expression in square bracket, i.e. V_{eff}, is identical to V_S

$$V_{eff}(\mathbf{r}_1) \equiv V_S(\mathbf{r}_1) = \int \frac{\rho(\mathbf{r}_2)}{r_{12}} d\mathbf{r}_2 + V_{XC}(\mathbf{r}_1) - \sum_A^M \frac{Z_A}{r_{1A}}. \quad (2.73)$$

Thus, once we know the various contributions in Eq. (2.73) we have a grip on the potential V_S which we need to insert into the one-particle equation, which in turn determine the orbitals and hence the ground state density and the ground state energy by employing the energy expression (2.71). It should be noted that V_{eff} already depend on the density (and thus on the orbitals) through the Coulomb term as shown in Eq. (2.71). Therefore, just like the Hartree-Fock equations, the Kohn-Sham one-electron equations also have to be solved iteratively.

The term V_{XC} is simply defined as the functional derivative of E_{XC} with respect to ρ, i.e.,

$$V_{XC} = \frac{\delta E_{XC}}{\delta\rho}. \quad (2.74)$$

It is very important to realize that if the exact form of E_{XC} and V_{XC} were known (which is unfortunately not the case), the Kohn-Sham strategy would lead to the exact energy,

i.e. the correct eigenvalue of the Hamilton operator $\hat{H}$ of the Schrödinger equation. Thus, unlike the Hartree-Fock model, where the approximation is introduced right from the start (the wave function is assumed to be a single Slater determinant, which therefore can never deliver a true solution) the Kohn-Sham approach is in principle exact. The approximation only enters when we have to decide on an explicit form of the unknown functional for the exchange-correlation energy E_{XC} and the corresponding potential V_{XC}.

2.2.11 The exchange correlation functional

Several approximations have been devised to get an explicit form for the functional E_{XC}. The most widely used approximations in solid state physics are the local density approximation (LDA) and the generalized gradient approximation (GGA). The idea behind the local density approximation is to assume that the E_{XC} can be written in the following form

$$E_{XC}^{LDA}[\rho] = \int \rho(\mathbf{r})\epsilon_{xc}(\rho(\mathbf{r}))d\mathbf{r} \tag{2.75}$$

where $\epsilon_{xc}(\rho(\mathbf{r}))$ is a function that gives the exchange-correlation energy per particle of an electron gas of a uniform density $\rho(\mathbf{r})$. The exchange part of this uniform electron gas can be found exactly whereas very accurate data, based on quantum Monte-Carlo simulations, is available for the correlation part [131]. At first sight, it would seem that LDA is not very accurate since the density of any real system is far from homogeneous, but in practice it seems to work surprisingly well. LDA can be regarded as the zeroth order approximation of the exchange-correlation functional. When gradient corrections are added to this approximation,

$$E_{XC}^{GGA}[\rho] = \int \epsilon_{xc}(\rho(\mathbf{r}), |\nabla\rho(\mathbf{r})|, ...)d\mathbf{r} \tag{2.76}$$

we get the so-called generalized gradient approximations (GGA). There are a lot of different exchange-correlation functionals of the GGA type which are based on both ab-initio and empirical data. In general, one can say that GGA improves on LDA when it comes to calculating bond lengths and energies, but for some systems where GGA fails, LDA leads to correct results because of some hazardous error cancellations.

As we know HF methods overestimate whereas LDA and GGA underestimate the band-gap. To produce the correct band gap, hybrid functionals are developed which are combinations of both HF and LDA (GGA).

CHAPTER 3

Vibrational properties of nanographene

The eigenmodes and the vibrational density of states of the ground state configuration of graphene clusters are calculated using atomistic simulations. The modified Brenner potential is used to describe the carbon-carbon interaction and carbon-hydrogen interaction in case of H-passivated edges. For a given configuration of the C-atoms the eigenvectors and eigenfrequencies of the normal modes are obtained after diagonalisation of the dynamical matrix whose elements are the second derivative of the potential energy. The compressional and shear properties are obtained from the divergence and rotation of the velocity field. For symmetric and defective clusters with pentagon arrangement on the edge, the highest frequency modes are shear modes. The specific heat of the clusters is also calculated within the harmonic approximation and the convergence to the result for bulk graphene is investigated.

3.1 Introduction

During the past few years considerable attention has been paid to the study of the spectral properties such as the energy spectrum, the eigenmodes (i.e. phonon spectrum), and the phonon density of states of carbon allotropes such as graphene [132–135], carbon

The results of this chapter were published as
Sandeep Kumar Singh and F. M. Peeters, Nanoscale Systems: Mathematical Modeling, Theory and Applications **2**, 10 (2013).

nanotubes [136, 137], fullerenes [133, 138, 139], graphene flakes [140] and carbon clusters [141, 142].

Raman spectroscopy is a widely used tool to study the vibrational modes of carbon based materials [6, 143, 144]. Because the normal modes of molecules are unique, they have their own set of Raman frequencies. Similarly for graphene clusters their phonon modes will give us information on e.g. their structural and dynamical properties.

Lattice dynamics calculations of a single graphene sheet were done by Rao et al. [145] based on C-C force constants [146, 147] which were obtained from a fit to the two dimensional, experimental phonon dispersion. Good agreement with Raman spectra of single wall carbon nanotubes was found. Tommasini et al. [148] presented a semiempirical approach for modeling the off-resonance Raman scattering of molecular models of confined graphene and compared with the results from density functional theory calculations. Pimenta et al. [149] reviewed the defect-induced Raman spectra of graphitic materials and presented Raman results on nanographites and graphenes. Ryabenko et al. [150] analyzed the spectral properties of single-wall carbon nanotubes encapsulating fullerenes and found that fullerene alters the average diameter of the electron cloud around the single wall carbon nanotube. Michel et al. [151] presented a unified theory of the phonon dispersion and elastic properties of graphene, graphite and graphene multilayer systems. They started from a fifth-nearest-neighbor force-constant model derived from the full in-plane phonon dispersions of graphite [152], and extended this model with interplanar interactions, and found that the graphite eigenfrequency $\omega_{B_{2g_1}} \approx 127$ cm^{-1} is reached within a few percent for N=10 layers which agrees with similar results obtained for the electron spectrum [153]. The structural, dynamical and thermodynamical properties of carbon allotropes were computed by Mounet et al. [154] using a combination of density-functional theory total-energy calculations and density-functional perturbation theory lattice dynamics in the generalized gradient approximation. Very good agreement was found for the structural properties and the phonon dispersion.

High-level ab initio calculations were carried out to reexamine the relative stability of bowl, cage, and ring isomers of C_{20} and C_{20}^{-} by An et al. [155] The total electronic energies of the three isomers showed a different energy ordering which depends on the used hybrid functional.

Finite size planar structures which are close to the ground state, and in particular nanographene-like structures were studied by Kosimov et al. [156] using energy minimization with the conjugate gradient (CG) method. The lowest energy, i.e. the ground state [156, 157] configurations were determined for up to N=55 carbon atoms as shown in Figs 3.1, 3.2. In Fig. 3.1 we depict the minimum energy configurations for carbon clusters which are carbon lines up to 5 atoms (Fig. 3.1(a)), carbon rings for up to 18 atoms (Fig. 3.1(b)), graphene nano-flakes up to 55 atoms (Fig. 3.1(c)) and hydrogen passivated

graphene nano-flakes (Fig. 3.2). Notice that by passivating the dangling bonds by hydrogens in graphene flakes some structural deformations are possible. In Fig. 3.2 the minimum energy configurations for hydrogen passivated graphene nano-flakes (which were obtained by passivating the structures in Fig. 3.1) are shown. It is interesting to note that most of these minimum configuration structures have zig-zag edges which is due to the higher stability of these kind of edges as compared to arm-chair edges [158].

In this chapter we investigate the normal modes for the ground state configuration of flat carbon clusters, also called nanographene as function of the number of C atoms in the cluster. The normal modes for linear (N $\leq$ 5) and ring ($6 \leq N \leq 18$) clusters which are exactly one and two dimensional, respectively are discussed. The phonon spectrum of two dimensional nanographene (19$\leq$ N $\leq$ 55) and trigonal-shaped nanodisk [159, 160] as well as the effect of hydrogenation of the edge carbon atoms on the phonon spectrum are investigated.

3.2 Simulation Method

The Brenner second generation reactive empirical bond order (REBO) potential function between carbon and hydrogen atoms is used in the present work. A brief discussion of this potential is presented in chapter 2.

Using molecular dynamic (MD) simulations with the Berendsen after corrector thermostat, we obtain the equilibrium configuration of stable quasi-planer clusters. We found that about 10^4-5×10^5 MD steps are needed to obtain an accuracy of 10^{-5}-10^{-6} eV in the energy per particle. We used free boundary conditions in our simulation.

Here, we calculate the dynamical matrix numerically using the finite-displacement method. We displace particle j in the direction β by a small amount $\pm u$, and evaluate the forces on every particle in the system $F^{\pm}_{\alpha,i}$ (we took typically u=0.003 Å). Then, we compute numerically the derivative using the central-difference formula

$$\frac{dF_{\alpha,i}}{du_{\beta,j}} = \lim_{u\to 0} \frac{F^{+}_{\alpha,i} - F^{-}_{\alpha,i}}{2u_{\beta,j}} = \frac{d^2 E_b}{du_{\alpha,i} du_{\beta,j}}. \tag{3.1}$$

Diagonalization of the dynamical matrix yields the eigenvalues and the eigenvectors from which we can calculate the vibrational modes. The eigenfrequencies are the square root of the eigenvalues. The stability of the configuration can be verified because all eigenvalues have to be real.

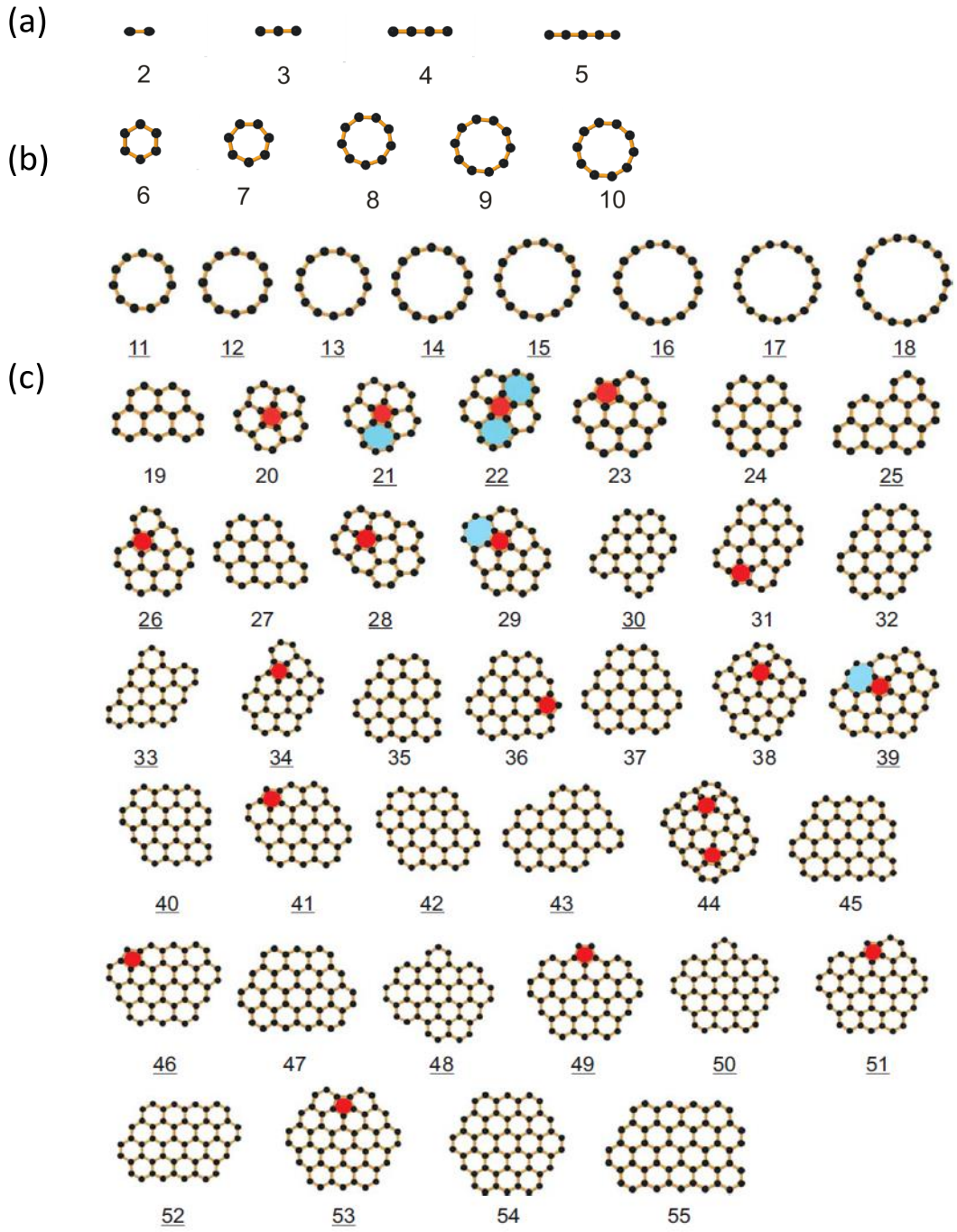

Figure 3.1: The investigated configurations for carbon lines (a) carbon rings (b) and graphene nano-flakes (c). Pentagons (heptagons) are colored red (blue).

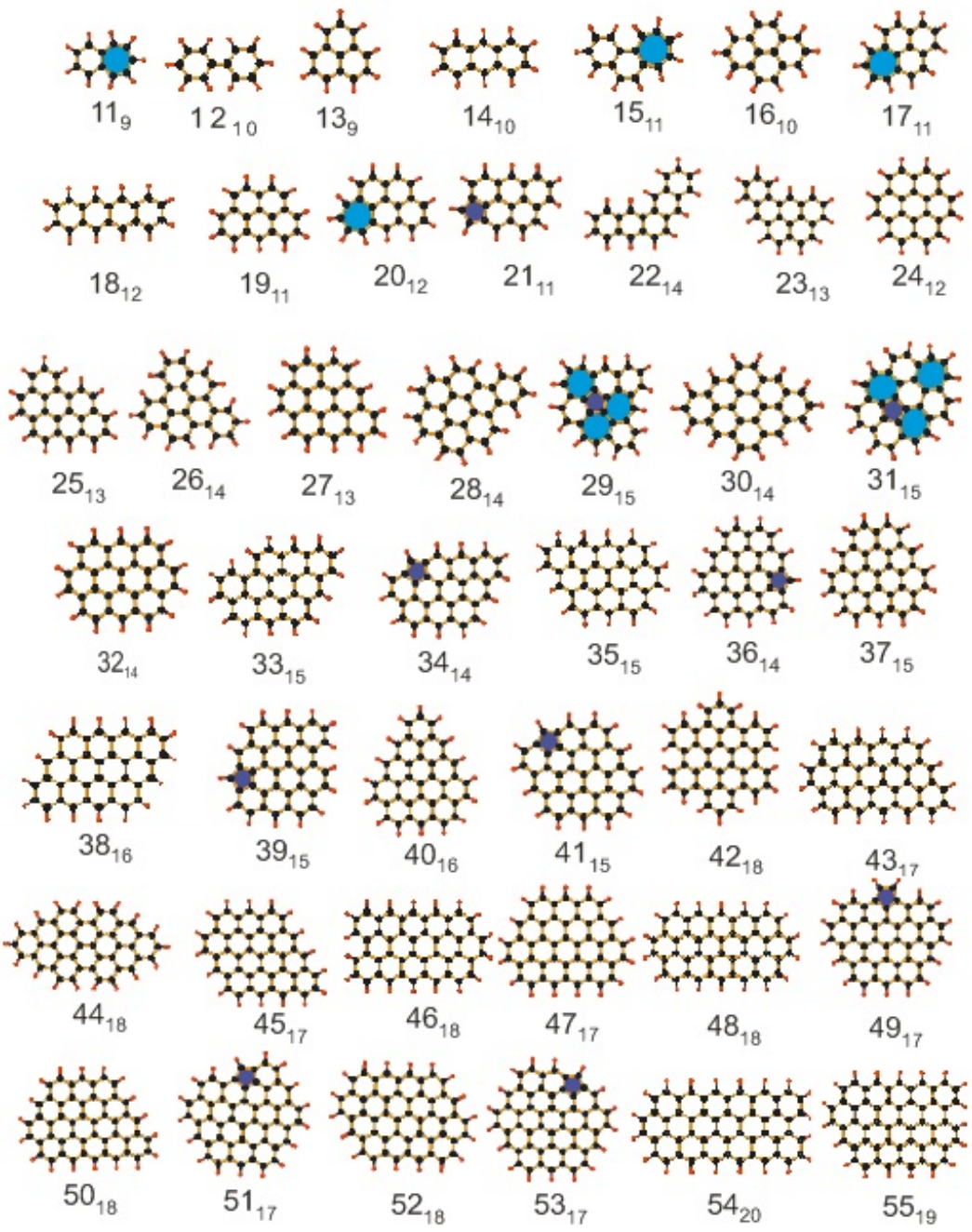

Figure 3.2: By H-passivating the structures in Fig. 3.1 most of them transit to new structures.

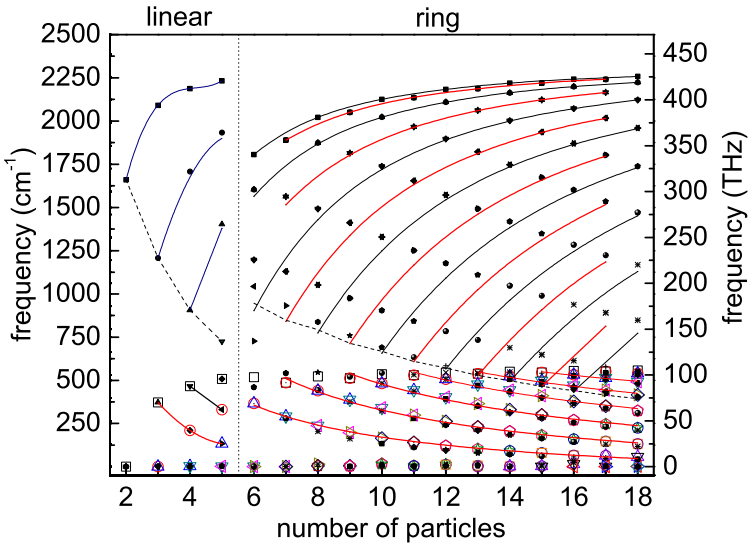

Figure 3.3: Spectrum of normal modes as a function of the number of particles in the cluster for linear N ≤ 5 and ring $6 \leq N \leq 18$ clusters. The solid curves are the analytical results from a simple chain (N ≤ 5) and ring ($6 \leq N \leq 18$) model. The dashed curve indicates the breathing mode. The symbols are the numerical results from the present simulation where the solid (hollow) symbols are the frequencies with corresponding eigenvectors which are in plane (out of plane). The frequencies that decrease with the number of particles are fitted to a $1/N$ dependence (solid curves).

3.3 Linear and ring clusters

The energy of the normal modes corresponding to the ground-state configuration for linear and ring clusters is shown in Fig. 3.3 as function of the number of C atoms in the clusters. The number of normal modes for N-particles moving in 3-dimensions is 3N. Some of these modes will be degenerate. There are 5 modes with $\omega = 0$ which correspond to 3 uniform translations and 2 independent rotations of the whole cluster, due to the translational and rotational invariance of the cluster.

When clusters are exactly one dimensional, the phonon modes correspond to oscillations along the chain or orthogonal to it. The normal modes of such a chain of N particles connected by springs with spring constant κ and mass m can be calculated analytically [161] and is given by $\omega = f \times \frac{sin(\phi_n/2)}{sin\phi_N}$ where $f = 2\sqrt{\frac{\kappa}{m}}$, and $\phi_n = (n-1)\pi/N$

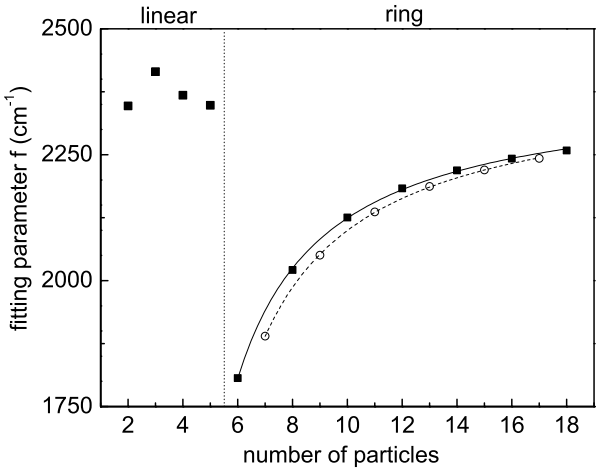

Figure 3.4: Fitting parameter f of linear chain (N $\leq$ 5) and ring ($6 \leq N \leq 18$) model of particles connected by identical springs as a function of the number of particles. For $N \geq 6$ the results are fitted by a simple analytical expression for even (full curve) and odd (dashed curve) clusters.

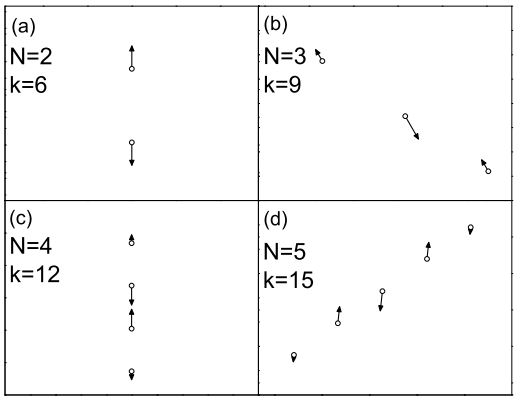

Figure 3.5: Eigenvectors of the highest frequency modes for the clusters with N=2,3,4 and 5 particles for different mode number with frequency (a) $\omega_6 = 1660$ cm^{-1}, (b) $\omega_9 = 2092$ cm^{-1}, (c) $\omega_{12} = 2188$ cm^{-1} and (d) $\omega_{15} = 2233$ cm^{-1}.

$(n = 1, 2, \cdots, N)$. For each value of N, we determined f by taking the maximum frequency obtained from our model equal to our numerically found result. The obtained frequencies of our linear spring chain model (solid curves in Fig. 3.3) agree remarkably well with our numerical results. For $N \leq 5$, the obtained spring constant is plotted in Fig. 3.4 and is almost constant (less than 4% variation). As shown in Ref. [157] all the C-C bonds in the chain are not identical and therefore all the spring constants between the C-atoms are expected not to be identical, which is the reason why our simple model does not give perfect agreement with our numerical data.

Notice that the low frequency eigenmodes are not described by this simple model. Some of them correspond to out-of-plane motion. For cluster N=2 with mode k=6 (k counts the eigenvalues in increasing order) and for N=4 with mode k=12, the particles move in opposite direction to each other along the chain as depicted in Fig. 3.5. While the cluster N=3 with mode k=9 and the cluster N=5 with k=15 have alternating particles moving in opposite direction which makes an angle with the chain direction (see Fig. 3.5).

The breathing mode for the linear chain is shown by the dotted line in Fig. 3.3. For N=2 the excitation corresponding to the breathing mode is shown in Fig. 3.5(a). But for N=3, this mode is similar for N=2 but where the direction of oscillation makes an angle with the chain direction and the middle particle does not move due to conservation of momentum. Similarly, for N=5 we found that the breathing mode is similar to the one for N=4 except that the deflection makes an angle with the chain direction and the middle particle is at rest (see Figs. 3.6(a, b)). For mode k=6 and 7 with N=3,4,5 particles, the particles on the boundaries of the clusters move in the same direction while the remaining particles move in the opposite direction with different amplitudes to conserve total angular momentum (see Fig. 3.6(c)) for both in-plane and out-of-plane direction. The corresponding frequency of these modes can be reasonably well fitted by $\frac{a}{N}$+b (solid curve in left panel of Fig. 3.3) where the fitting parameters are (a,b)= (1809 (± 103), -234 (± 27)) cm^{-1}. And for mode k=8 and 9 with N=4, 5 particles, adjacent particles move in opposite direction with different amplitudes where the central particle is at rest in the case of N=5 particles (see Fig. 3.6(d)) for both in plane and out of plane direction and they can be fitted by the same function with (a,b)= (1783 (± 103), 0.0) cm^{-1}.

The ground state configuration for C_N (N=6-18) consists of particles arranged in a ring. For clusters that are exactly two dimensional, as is the case of these ring structures, the phonon modes correspond to motion in the plane or vertical to the plane. There is no coupling between the in-plane and the out-of-plane motion. We can construct a simple model of equidistant particles arranged in a ring, where neighbor particles are connected by a spring. This model can be viewed as the linear chain model with periodic boundaries. For fixed radius of the ring this results in the following eigenfrequencies [162] $\omega = f \times sin(k/2)$, where $k = 2\pi n/N$, $(n = 1, 2, \cdots, N)$. As before we determined f such

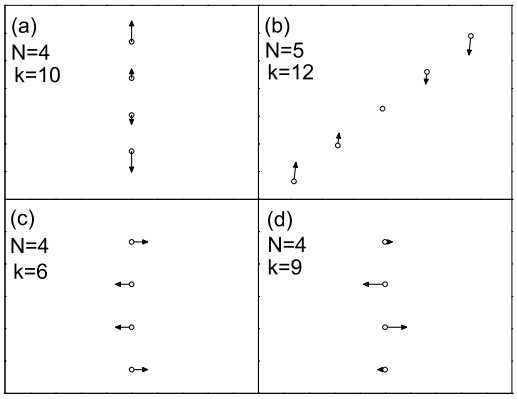

Figure 3.6: Eigenvectors for the clusters with N=4 and 5 particles for different mode number with frequency (a) $\omega_{10} = 905$ cm^{-1}, (b) $\omega_{12} = 725$ cm^{-1}, (c) $\omega_6 = 150$ cm^{-1} and (d) $\omega_9 = 466$ cm^{-1}.

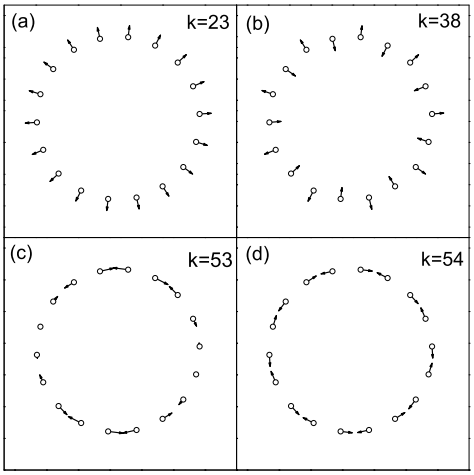

Figure 3.7: Eigenvectors for a cluster with N=18 particles for different mode number with frequency (a) $\omega_{23} = 398$ cm^{-1}, (b) $\omega_{38} = 550$ cm^{-1}, (c) $\omega_{53} = 2224$ cm^{-1} and (d) $\omega_{54} = 2259$ cm^{-1}.

that the maximum frequency obtained from the model equals the numerical result. This fitted value is shown in Fig. 3.4 which can be described approximately by the function $f(N) = a \times \frac{(1+bN)}{(1+cN)}$, where: a=3200 cm^{-1} and i) for even N clusters b = -0.295 ($\pm$ 0.001), and c = -0.395 ($\pm$ 0.002); and ii) for odd N clusters b = -0.276 ($\pm$ 0.001), and c = -0.369 ($\pm$ 0.001). Several of the numerical frequencies are reasonably well described by this simple model. Notice that the eigenfrequencies exhibit a clear discontinuous behavior when a cluster changes from a linear into a ring configuration. As an example we show in Fig. 3.7 some of the interesting eigenmodes of a cluster with N=18 particles which are arranged in a circle and is therefore pure two dimensional. The mode k=23 is the breathing mode while mode k=38 corresponds to radial out of phase radial oscillation of nearest neighbor particles. The modes k=53, and 54 correspond to pure angular oscillations of the particles.

It is interesting to note that for an even number of particles, there is a nearly common frequency (i.e. N=8 (545 cm^{-1}), N=10 (543 cm^{-1}), N=12 (546 cm^{-1}), N=14 (547 cm^{-1}), N=16 (549 cm^{-1}), N=18 (550 cm^{-1})) which is almost independent of N (see Fig. 3.3). This mode corresponds to out of phase oscillations of nearest-neighbor atoms (see Fig. 3.7(b) the k=38 mode for N=18 and Fig. 3.8(a) the k=24 mode for N=12). But for odd ring clusters i.e. N=13, the corresponding normal mode corresponds to nearest-neighbor atoms oscillating out of phase with different amplitudes except for the two neighbor atoms that oscillate in phase (see Fig. 3.8(b) k=23 (471 cm^{-1})) which results in a lower frequency by about 20 % as compared to the corresponding even N ring clusters.

A breathing mode exists for all the ring clusters as shown in Fig. 3.8. The frequencies for N=8, 12, 13, 16, and 18 are 837 cm^{-1}, 585 cm^{-1}, 543 cm^{-1}, 447 cm^{-1}, and 398.25 cm^{-1}, respectively, and have a clear dependence on N. The simple spring model [163] predicts that this breathing mode has the frequency ω=$(\pi \times f)/N$ which remarkably agrees with our numerical results.

The eigenmodes corresponding to ω_{max} have similar vibrational modes for even number of particles. We plotted the normal modes of ω_{max} of cyclic structures for N=12 ($\omega_{36} = 2183\ cm^{-1}$) as shown in Fig. 3.8(e) and they correspond to dipole-type of oscillations between nearest neighbor particles while for odd number of ring structures i.e. N=13 ($\omega_{39} = 2187$ cm^{-1} in Fig. 3.8(f)), similar dipole-type of oscillations between nearest neighbor particles are found but with decreasing magnitude towards opposite sides.

Now we investigate the eigenmodes for out-of-plane vibrations for ring clusters. For N=10 and mode k=10, the normal mode corresponds to a bending mode while for mode k=16, the normal mode corresponds to a sinusoidal type of motion. The higher modes k=17 and k=19 have nearest-neighbor atoms oscillating in opposite direction perpendicular to the ring-plane with different wavelength along the ring as seen in Fig. 3.9. For even

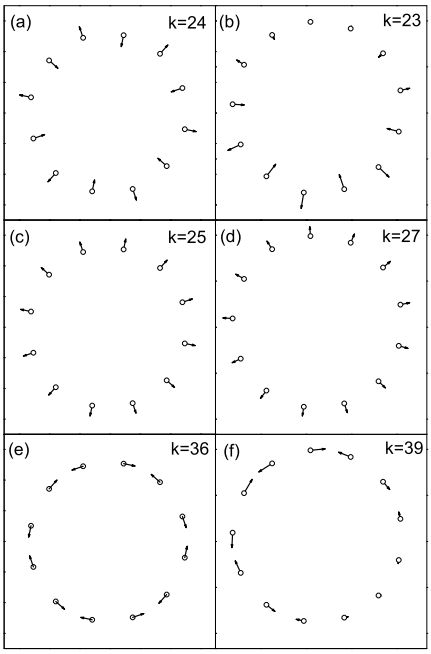

Figure 3.8: Normal modes for the out-of-phase (top panels), breathing (middle panels) and ω_{max} (bottom panels) for the clusters N=12 (left panel) and N=13 (right panel).

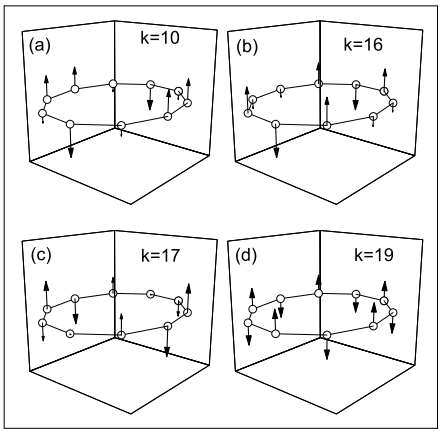

Figure 3.9: Eigenvectors for out-of-plane motion for a cluster with N=10 particles for different mode number with frequency (a) $\omega_{10} = 165$ cm^{-1}, (b) $\omega_{16} = 482$ cm^{-1}, (c) $\omega_{17} = 482$ cm^{-1} and (d) $\omega_{19} = 536$ cm^{-1}.

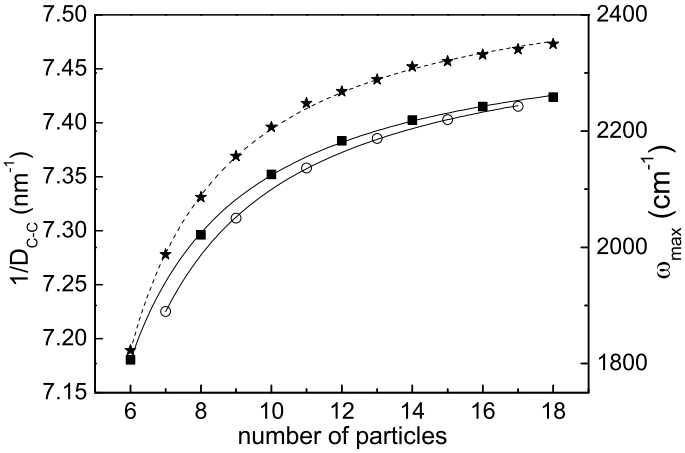

Figure 3.10: $1/D_{C-C}$ (dashed curve) and ω_{max} (solid curve for even and odd N) as a function of the number of particles.

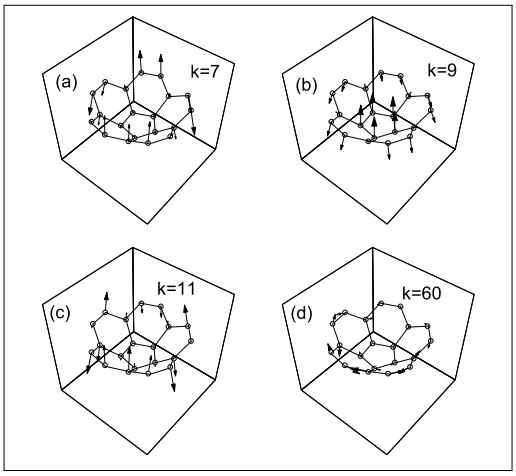

Figure 3.11: Eigenvectors for a cluster with N=20 particles for different mode number with frequency (a) $\omega_7 = 124$ cm^{-1}, (b) $\omega_9 = 161$ cm^{-1}, (c) $\omega_{11} = 233$ cm^{-1} and (d) $\omega_{60} = 1772$ cm^{-1}.

ring structures the highest mode for out-of-plane vibration is similar to the one shown in Fig. 3.9(d). The out-of-plane vibration can be reasonably well fitted by $\frac{a}{N}+b$ (solid curves in Fig. 1 for ω<550 cm^{-1}) where the fitting parameters a and b are listed in Table 3.1. The eigenmodes belonging to each solid curve correspond to the same type of mode.

From Fig. 3.3, it is interesting to note that the maximum frequency in the excitation spectrum for ring clusters, on the average, slowly increases with N. This can be explained by calculating the phonon spectrum of an infinite system. In Fig. 3.10 we show that the minimal interparticle distance decreases slowly with the number of C-atoms in the cluster. As a consequence, the maximum value of the wave vector $k \approx \pi/l_0$ (l_0 is the mean distance between the particles) and also the corresponding frequency will increase weakly with cluster size. The inverse of the inter-carbon distance could be fitted to (dashed curve in Fig. 3.10)

$$\frac{1}{D_{C-C}} = \frac{1}{D_0}\frac{1+aN}{1+bN} \tag{3.2}$$

with the fitting parameters: $\frac{1}{D_0}$=7.9 nm^{-1}, a = -0.316 ($\pm$ 0.002), and b = -0.331 ($\pm$ 0.002). We are able to fit a curve through the maximum frequency of these ring clusters using

Table 3.1: Fitting parameters for the eigenfrequencies of out-of-plane motion shown by the solid curves in Fig.1 for ω<550 cm^{-1}: $\omega = \frac{a}{N} + b$.

a cm^{-1}	b cm^{-1}
2782 ($\pm$48)	-107 ($\pm$5)
4258 ($\pm$120)	-97 ($\pm$11)
5405 ($\pm$251)	-62 ($\pm$20)
5686 ($\pm$59)	25 ($\pm$5)
5814 ($\pm$499)	102 ($\pm$33)
4942 ($\pm$589)	220 ($\pm$36)

(solid curves in Fig. 3.10)

$$\omega = \omega_0 \frac{1 + aN}{1 + bN}, \tag{3.3}$$

where ω_0=3200 cm^{-1}, and: i) for even N clusters a = -0.295 ($\pm$ 0.001), and b = -0.395 ($\pm$ 0.002); and ii) for odd N clusters a = -0.276 ($\pm$ 0.001), and b = -0.369 ($\pm$ 0.001).

3.4 Nanographene ($N > 18$)

The clusters with $N > 18$ have an inner structure and their configurations have been investigated in detail in Ref. [156]. Their ground state configuration can be classified in three groups: 1) nanographene clusters consisting of only hexagons, 2) clusters with pentagon on the boundary, and 3) bowl shaped configurations that have typically pentagons in the inner part of the cluster. For the latter one $< z^2 > \neq 0$, where z is the position coordinate of the cluster along the out-of-plane direction and they are found for N=20, 28, 38 and 44 which are buckled-like structures. In these clusters one pentagon is surrounded by five hexagons. The normal mode oscillations in-plane and out-of-plane are now coupled, i.e. the normal mode oscillations are 3-dimensional and some of the interesting ones are shown in Fig. 3.11 for N=20 and mode k=7, 9, 11 and 60. For mode k=7, the opposite atoms on the boundary of the cluster vibrate in the same direction whereas for k=9, the normal mode corresponds to a bending mode of the cluster. But, for the higher mode k=11, the corner atoms show mixed type of oscillations while for large value of k, the normal modes correspond to in-plane oscillations of the C-atoms.

The normal mode frequencies for $N \geq 19$ are plotted in Fig. 3.12. For N=22 and 39, a heptagon is on the boundary surrounded with pentagon and hexagon. In such a case local modes are found where only particles close to the defects (pentagon and heptagon)

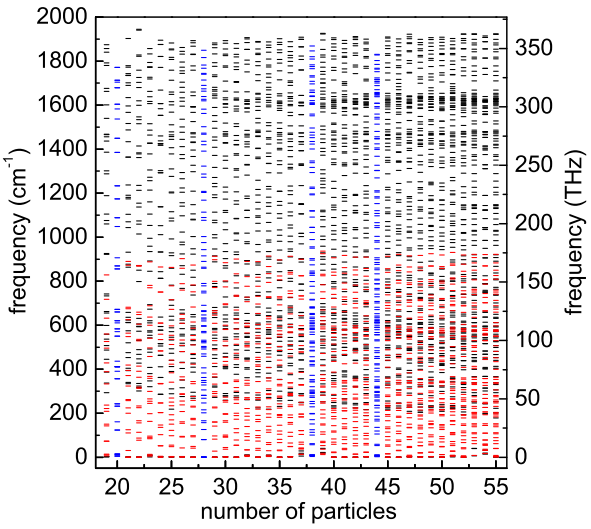

Figure 3.12: Normal mode spectrum as a function of the number of C atoms for $19 \leq N \leq 55$. The modes with eigenvectors in-plane are shown in black, those with out-of-plane eigenvectors in red and mixed type eigenvectors in blue.

oscillate. If there is one pentagon on the boundary i.e. N=49, and 51, the local modes with larger amplitudes are on the opposite side of the clusters while for N=53 where a pentagon is surrounded by four hexagons, the local modes with larger amplitudes are found only near the defect. For clusters which are symmetric and without defect i.e. N=54, we found that the local modes are situated on the boundary as shown in Fig. 3.13.

A special subgroup of clusters consists of hexagonal and trigonal shaped nanographene. The clusters with size N=24 and N=54 are planar graphene structures which are hexagonal shaped with zigzag edges. These clusters have a close-packed structure, which consist purely of hexagons. Let us consider the cluster with N=54 (see Fig. 3.14), the mode k=34 corresponds to the breathing mode. Mode k=58 exhibits circular motion of atoms arranged in hexagons near the 6 corners of the hexagonal disk. The next mode k=59 is similar but now hexagons are displaced by an angle of 30° and are centered in the middle of the sides of the hexagonal disk. Notice that for k=58 the 6 rotational oscillations are in the same direction while for k=59 they alternate, i.e. vortex/anti-vortex like arrangements. For higher modes k=139, only the inner particles participate in the normal mode oscillations. For k=148, a dipole type of oscillations is found of nearest neighbor C-atoms arranged in a shell around the middle between the center and the perimeter. For higher frequency only the outer particles oscillate while the inner particles exhibit only very small displacements as shown in Fig. 3.14.

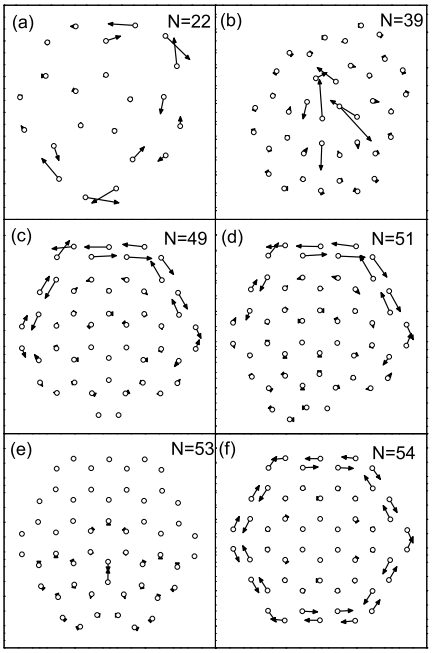

Figure 3.13: Eigenvectors for highest mode number for clusters with N=22, 39, 49,51, 53, 54 particles with frequency (a) $\omega_{66} = 1944$ cm^{-1}, (b) $\omega_{117} = 1926$ cm^{-1}, (c) $\omega_{147} = 1907$ cm^{-1}, (d) $\omega_{153} = 1903$ cm^{-1}, (e) $\omega_{159} = 1952$ cm^{-1} and (f) $\omega_{162} = 1914$ cm^{-1}.

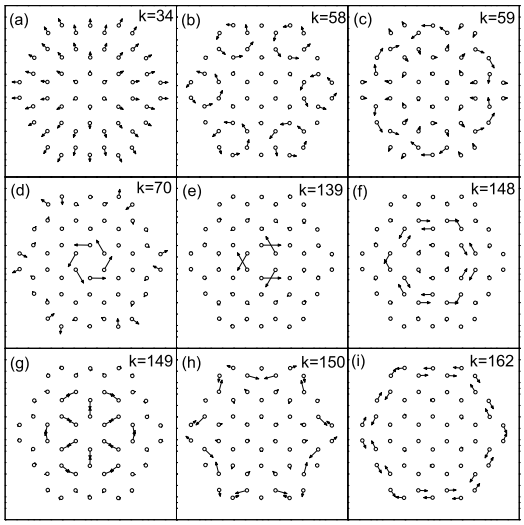

Figure 3.14: Eigenvectors for a cluster with N=54 particles for different mode number with frequency (a) $\omega_{34} = 313$ cm^{-1}, (b) $\omega_{58} = 531$ cm^{-1}, (c) $\omega_{59} = 534$ cm^{-1}, (d) $\omega_{70} = 593$ cm^{-1}, (e) $\omega_{139} = 1589$ cm^{-1}, (f) $\omega_{148} = 1624$ cm^{-1}, (g) $\omega_{149} = 1628$ cm^{-1}, (h) $\omega_{150} = 1638$ cm^{-1} and (i) $\omega_{162} = 1914$ cm^{-1}.

From Fig. 3.12 we notice that there is a region along the frequency axis with a higher density of normal modes. Examples of the displacements of such modes are shown in Fig. 3.15 for N=54. Mode k=27 corresponds to the excitation of a vortex/antivortex pair. Mode k=33 consists of rotational oscillations around the hexagonal corners of the nanodisk, while for k=35 these rotational motions are centered around the middle of the hexagonal sides. Notice that mode k=45 consists of a central large vortex motion surrounded by 6 anti-vortex type of motions situated closer to the edge of the nanodisk.

The nanodisk cluster with N=46 carbon atoms has a metastable configuration consisting of closed zigzag edges and a trigonal-shaped structure [156]. As shown in Fig. 3.16 the mode k=18 consists of an asymmetric vortex/antivortex pair while mode k=29 is a clear breathing mode. The modes k=24 and k=32 show three rotations situated close to the three corners of the trigonal nanodisk, but notice that the rotation direction and the position of the center of the rotation is not always the same for both modes .

We plotted the average distance between the C-C atoms as a function of the number of particles N. The average radius increases linearly with the chain length for (N=3-5) which could be fitted to $D_{C-C} = D_0 + a \times N$ where $D_0 = 0.13$ nm and a=0.00055 ($\pm$

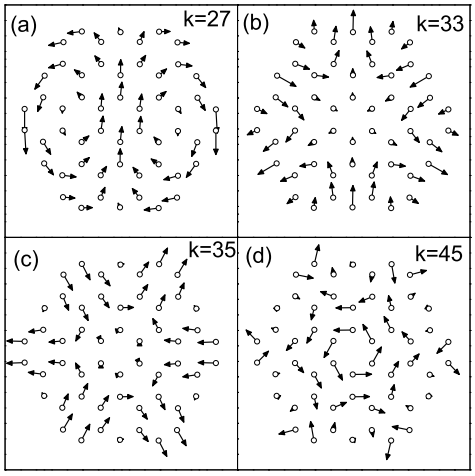

Figure 3.15: Eigenvectors for the cluster with N=54 particles for four different values of the mode number k with frequency (a) $\omega_{27} = 244$ cm^{-1}, (b) $\omega_{33} = 302$ cm^{-1}, (c) $\omega_{35} = 314$ cm^{-1} and (d) $\omega_{45} = 408$ cm^{-1}.

0.00009) nm (see solid curve in Fig. 3.17). For ring clusters it decreases exponentially as $D_{C-C} = D_0 + a \times exp(b \times N)$ (see solid curve in Fig. 3.17) where the parameter $D_0 = 0.134$ nm, $a = 0.039(\pm 0.001)$ nm and $b = -0.337(\pm 0.007)$ as the number of particles increases. For $N > 18$ the average C-C distance fluctuates as function of N around the average value 0.141 nm which compares with 0.142 nm for the C-C distance in bulk graphene. The clusters with pentagon and Stone-Wales defects inside the clusters show larger average C-C distance than the pure hexagonal structures while the clusters with pentagons on the boundary (i.e. N=26, 31, 34, 36, 41, 46, 51 and 53) show the highest average distance as shown in Fig. 3.17.

For completeness we also plotted (in Fig. 3.18) the energy spectrum of the normal modes for ground-state H-passivated C_N (N=11-55) clusters [156]. Notice that different from Fig. 3.12 (i.e. non H-passivated graphene) there is a region with enhanced density of modes, i.e. around 2900 cm^{-1}. The corresponding modes are connected to oscillations of the C-H atoms. This is illustrated in Fig. 3.19 for H-passivated nanographene clusters with N=53 and 54. In the optical region which is a region along the frequency axis with higher density of normal modes, for N=53 with k=172 the corresponding local normal modes with larger amplitudes are on the opposite side of the defect while for N=54 with k=187, only the inner C-atoms oscillate with larger amplitude (Figs. 3.19 (a, b)). The highest frequency mode of the N=53 and 54 clusters (Figs. 3.19 (c, d)) is a local mode near the

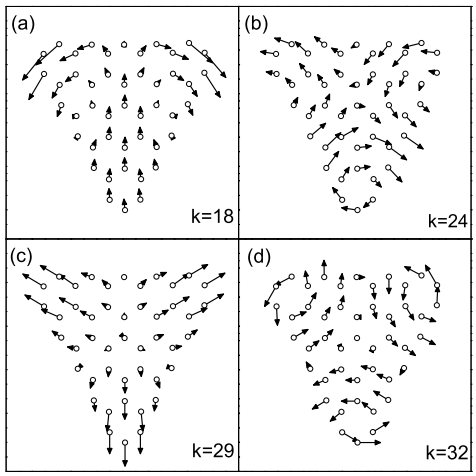

Figure 3.16: Eigenvectors for a cluster with N=46 particles for different mode number with frequency (a) $\omega_{18} = 185$ cm^{-1}, (b) $\omega_{24} = 244$ cm^{-1}, (c) $\omega_{29} = 288$ cm^{-1} and (d) $\omega_{32} = 322$ cm^{-1}.

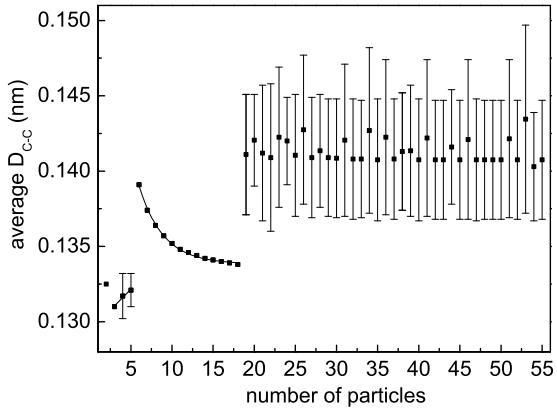

Figure 3.17: The average distance between C-C atoms as a function of the number of particles in the graphene cluster. The error bars indicate the range of C-C distances within each cluster.

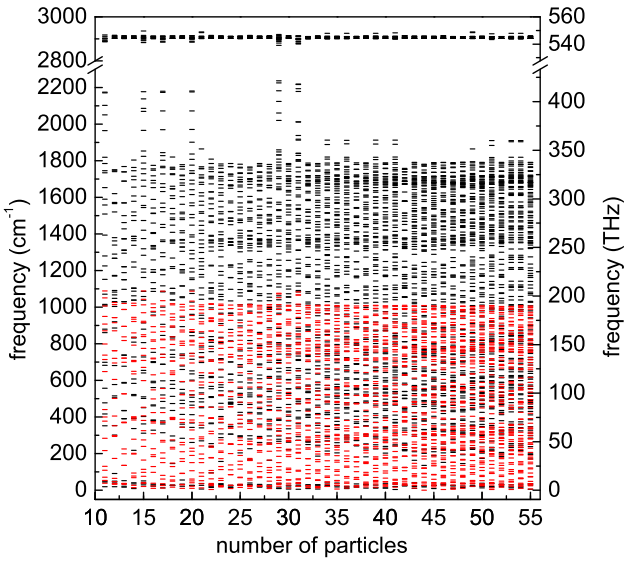

Figure 3.18: Normal mode spectrum as a function of the number of C particles for $11 \leq N \leq 55$ H-passivated clusters. The modes with eigenvectors in plane are shown in black, those having out-of plane eigenvectors in red.

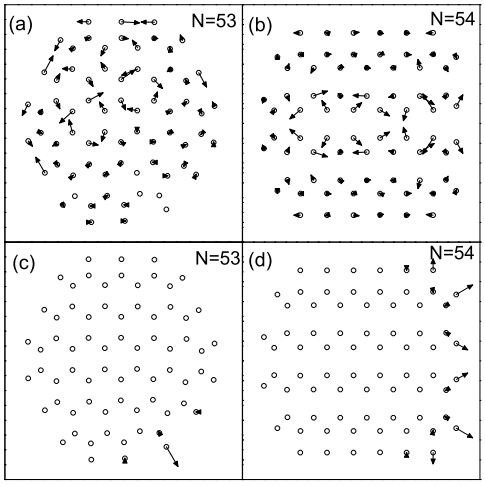

Figure 3.19: Eigenvectors for a cluster with N=53, and 54 with H-passivation for k=172 for N=53 and k=187 for N=54, and for ω_{max} corresponding to frequency (a) $\omega_{172} = 1693$ cm^{-1}, (b) $\omega_{187} = 1698$ cm^{-1}, (c) $\omega_{210} = 2925$ cm^{-1} and (d) $\omega_{222} = 2915$ cm^{-1}.

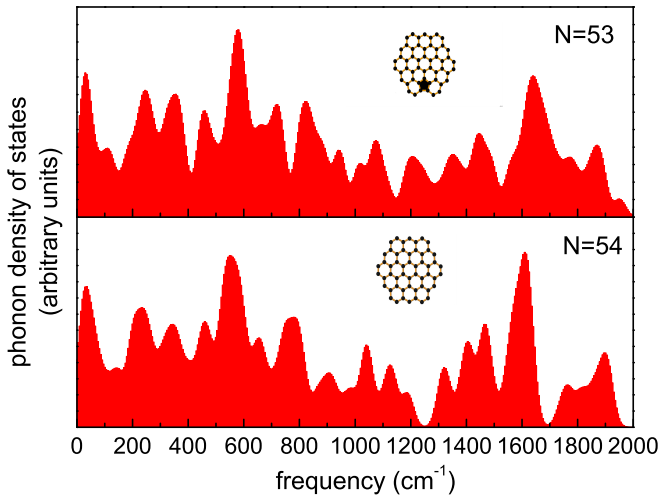

Figure 3.20: The phonon density of states for clusters with N= 53 and 54 carbon atoms.

local defect where mainly outer C-H atoms of the armchair C-atoms oscillate.

3.5 Phonon density of states

In order to compare the normal modes with those of graphene we calculate the phonon density of states (PDOS). Furthermore, we calculated the PDOS of exactly trigonal and hexagonal two dimensional and defective clusters and analyze what is the effect of defects on the density of states. Because of the discreteness of the normal modes frequency spectrum we introduced a Gaussian broadening

$$\rho(\omega) = \sum_{i=1}^{3N} exp(-(\omega - \omega_i)^2/\delta\omega^2), \tag{3.4}$$

where the summation is over all normal modes, ω_i is the normal mode frequency of the i^{th} mode, broadening is chosen $\delta\omega = 30$ cm^{-1} and N is the total number of atoms in the cluster. We notice that the introduction of a pentagon in the N=53 cluster as compared to the perfect hexagon lattice in N=54 introduces more high frequency modes as shown in Fig. 3.20 which are due to modes localized around the defect.

Fig. 3.21 shows the phonon density of states (PDOS) of armchair hexagonal and zigzag trigonal clusters. Notice that several of the peaks in the PDOS of the hexagonal clusters

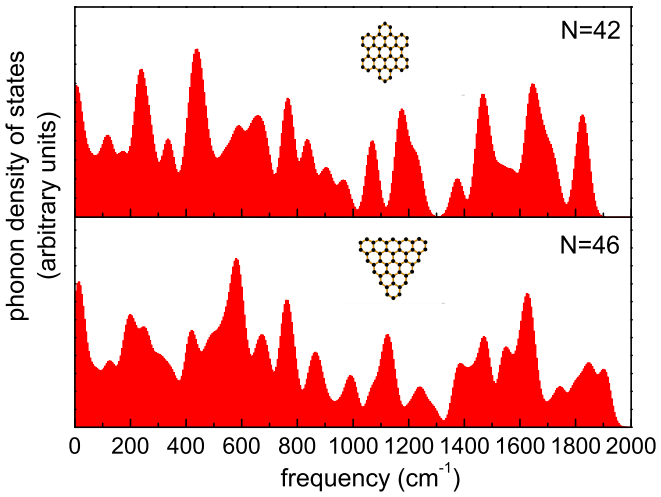

Figure 3.21: The phonon density of states for clusters with N=42 (hexagonal with armchair) and 46 (trigonal) carbon atoms.

are split into two peaks in the PDOS of the trigonal shaped cluster. This is a consequence of the reduced rotational symmetry of the trigonal cluster.

We compare in Fig. 3.22 the phonon density of states of clusters N=55 and 1600 with those for graphene [164] which shows nicely the convergence of the phonon spectrum of nanographene to bulk graphene. For N=1600 we almost recover the theoretical results of graphene [164]. Notice that for small clusters there is a pronounced PDOS for $\omega = 0$ which is due to the relative importance of the $\omega = 0$ translational and rotational motion.

The effect of H-passivation of the edge atoms of the cluster is shown in Fig. 3.23 for N=53 and 55. The C-H bonds introduce high frequency modes in the N=53 and N=55 clusters as compared to the non H-passivated N=53 and N=55 clusters. The H-passivated clusters exhibit pronounced peaks around 1700 and 2900 cm^{-1} which correspond to the optical region and the C-H atom frequency region, respectively. We also notice that the introduction of a pentagon in the N=53 cluster as compared to the perfect hexagon lattice for N=55 introduces more high frequency modes as shown in Fig. 3.23 similar to the case for non H-passivated clusters (see Fig. 3.20) which are due to modes localized around the defect.

The modes can have a shear-like or a compression-like character. The compressional and shear properties can be extracted from the divergence and rotation of the velocity field. Here, we will associate a single number for the shear-like and compression-like character

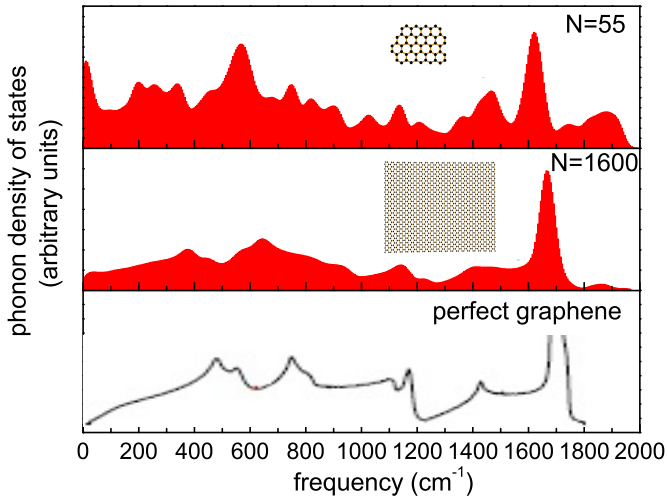

Figure 3.22: The phonon density of states for clusters with N=55, 1600 and perfect graphene (bottom panel is taken from Ref. [164]).

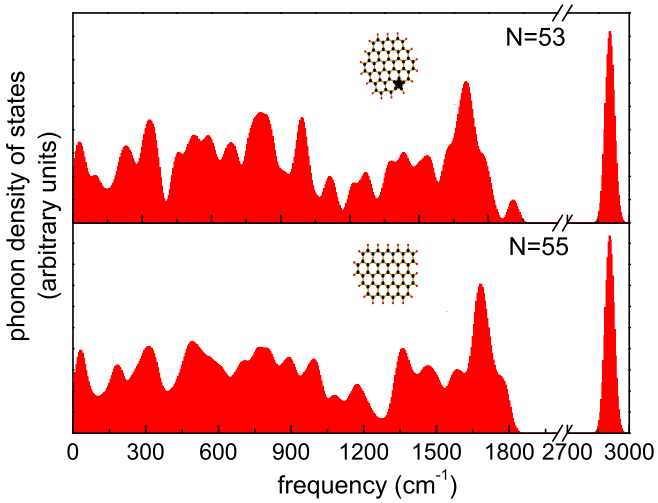

Figure 3.23: The phonon density of states for H-passivated clusters with N=53 and 55.

of the different modes by calculating the squared average of the divergence $\vec{\nabla}.\vec{v}$ and the vorticity $(\vec{\nabla} \times \vec{v})_z$ of the velocity field, following the approach of Ref. [165].

The z component of the rotation $\Psi_r(k) = \vec{e}_z.rot\Psi(k)$ and the divergence $\Psi_d(k) = div\Psi(k)$ of the field of the eigenvectors of mode k are

$$\Psi_d(k) = \frac{1}{N}\sum_{i=1}^{N}\Psi_{d,i}^2(k), \tag{3.5}$$

$$\Psi_r(k) = \frac{1}{N}\sum_{i=1}^{N}\Psi_{r,i}^2(k), \tag{3.6}$$

where the values of $\Psi_{d,i}(k)$ and $\Psi_{r,i}(k)$ for the i^{th} particle are, respectively, given by

$$\Psi_{d,i}(k) = \frac{1}{J}\sum_{j=1}^{J}(\vec{r_i} - \vec{r_j}).[\vec{A_i}(k) - \vec{A_j}(k)]/|\vec{r_i} - \vec{r_j}|^2, \tag{3.7}$$

$$\Psi_{r,i}(k) = \frac{1}{J}\sum_{j=1}^{J}(\vec{r_i} - \vec{r_j}) \times [\vec{A_i}(k) - \vec{A_j}(k)]/|\vec{r_i} - \vec{r_j}|^2. \tag{3.8}$$

Here, j and J denote the index and the number of neighboring particles of particle i, respectively. $\vec{r_j}$ is the positional coordinate of a neighboring particle and $\vec{A_i}(k)$ is the eigenvector of particle i for mode k. Note also that we calculate the squared average over all the particles because the simple spatial average is of course zero.

We plot $\Psi_d(k)$ and $\Psi_r(k)$ as a function of the mode number k for cluster N=39 which contains a 5-7 defect, cluster N=49 with pentagon defect on the boundary, the pure symmetric hexagonal cluster with N=54 and for a large cluster having N=398 particles. In general, the lower eigenfrequency spectrum corresponds to rotational type of excitations which are vortex-antivortex like excitations for large clusters (see Fig. 3.15). Vortex excitation is only expected for sufficiently large clusters, because the velocity of dissipation of the vortex energy is inversely proportional to R^2, where R is the radius, which increases with increasing cluster size. In the second half of the spectrum the divergence $\Psi_d(k)$, which corresponds to compression-like modes, is appreciably different from zero and we have mixed modes that have both a shear-like and a compression-like component. For symmetric clusters and defective clusters with pentagon on the boundary, the highest modes consist of only shear-like modes (see Figs. 3.13(c, d, f)). For cluster N=39 with a 5-7 defect, compression-like modes appear for the highest frequency modes (see Fig. 3.13(b)).

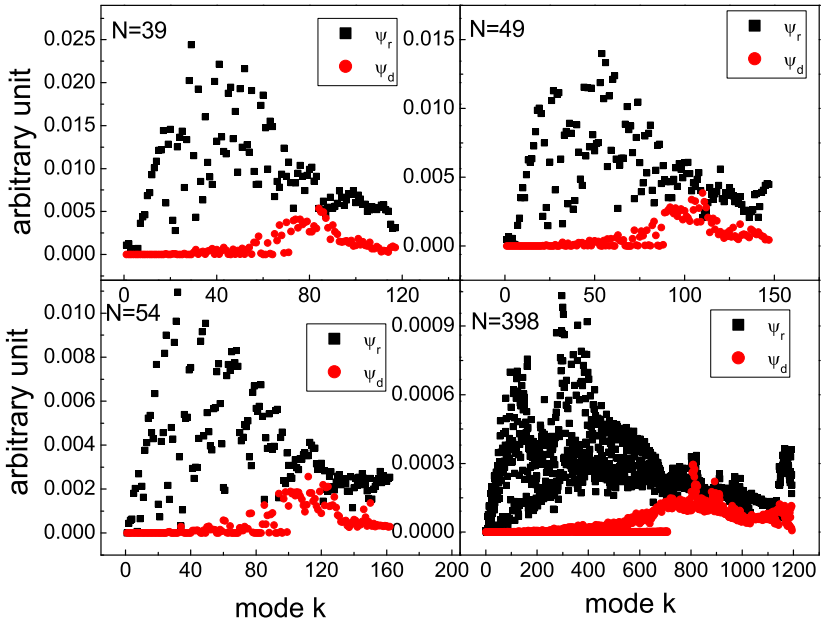

Figure 3.24: Distribution of the rotation Ψ_r and the divergence Ψ_d as function of the mode number k for N=39, 49, 54 and 398 particles.

3.6 Specific heat

The heat content of a system is directly related to the specific heat whose lattice contribution is determined by the phonons i.e. the eigenmodes of the system, while electronic contribution to it can be neglected even at a few Kelvins [166]. The specific heat C_P per unit mass, at temperature T is within the harmonic approximation [167] given by the following expression:

$$C_P = \frac{k_B}{MN} \sum_{k=1}^{3N} \left(\frac{\hbar\omega_k}{2k_B T} \right)^2 csch^2 \left(\frac{\hbar\omega_k}{2k_B T} \right), \tag{3.9}$$

where the summation is over all normal modes, k_B is the Boltzmann constant, M is the mass of each carbon atom and N is the total number of atoms in the cluster. From Eq. (3.9), the specific heat depends sensitively on the characteristics of the phonon spectrum and on its vibrational density of states.

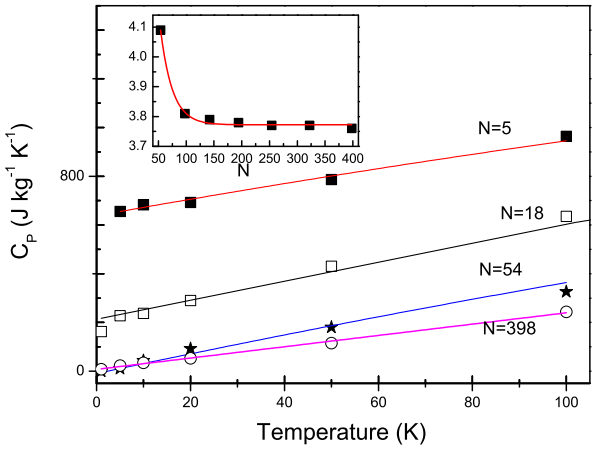

Figure 3.25: Phonon contribution to the constant pressure heat capacity of clusters with N=5, 18, 54 and 398 at low temperature. The curves are linear fits to the numerical results. In the inset we show the N-dependence of the slope of the low temperature linear T-dependence of the specific heat.

The numerical results for N=5, 18, 54 and 398 are shown in Fig. 3.25. It may be noted that at low temperature, cluster sizes with N=5, 18, 54 and 398 have a specific heat C_P which exhibits a clear linear dependence in T. The slope of the low temperature C_P behavior is shown in the inset of Fig. 3.25 as a function of N which can be fitted to: a + b $\times$ exp(c $\times$ N) (solid curve) where a=3.77 J kg^{-1} K^{-1}, b=3.87 (± 1.23) J kg^{-1} K^{-1} and c=-0.05 (± 0.01) K^{-1}.

The high temperature behavior is shown in Fig. 3.26. For large temperatures all results approach the value 2078 J kg^{-1} K^{-1} which is in good agreement with the bulk graphene value given in Refs. [132, 154].

We fitted the numerical results using the formula

$$C_P = a + b \times exp(c \times T), \tag{3.10}$$

where a=2078.0 J kg^{-1} K^{-1} and b and c are fitting parameters. After fitting the curve, we obtained the parameters listed in Table 3.2. Notice that $|b|$ increases with N while $|c|$ decreases.

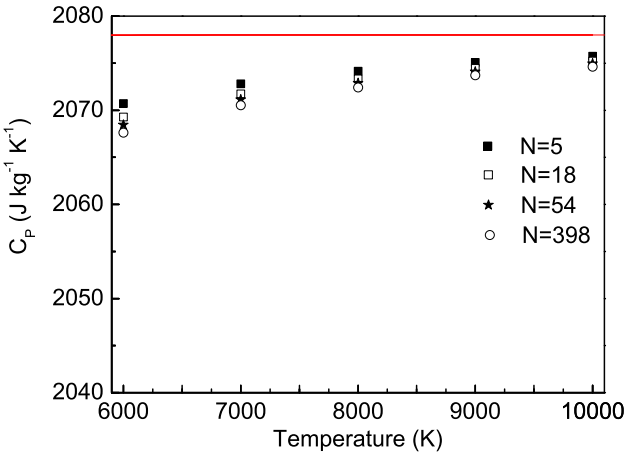

Figure 3.26: Phonon contribution to the constant pressure heat capacity of clusters with N=5, 18, 54 and 398 at high temperature. The numerical results approach the fitted value 2078 $Jkg^{-1}K^{-1}$.

Table 3.2: Fitting parameters for the specific heat (Eq. (16))

N	b (J kg^{-1} K^{-1})	c (K^{-1})
5	-1502 ($\pm$38)	-0.00237 ($\pm$0.00021)
18	-1865 ($\pm$21)	-0.00236 ($\pm$0.00010)
54	-2087 ($\pm$10)	-0.00195 ($\pm$0.00003)
398	-2109 ($\pm$14)	-0.00178 ($\pm$0.00004)

3.7 Summary

Atomistic simulations were performed using the Brenner second-generation reactive bond order (REBO) interatomic potential function in order to study the vibrational properties of nanographene. In the present work we investigated the frequency of the normal modes as a function of the number of particles for nanographene C_N ($2 \leq N \leq 55$) and H-passivated carbon clusters ($11 \leq N \leq 55$). We also presented a simple model for the eigenfrequencies for linear chain and ring structures and obtained analytical results that are in good agreement with our numerical results. The phonon density of states of different clusters are compared with theoretical results for graphene and found to be in good agreement for the acoustic and optical phonon density in the case of large clusters. Using the eigenfrequencies of the normal modes we calculated the specific heat within the harmonic approximation for different size carbon clusters and found that in the high temperature limit they approach the bulk value as given in Refs. [154].

CHAPTER 4

Melting of graphene clusters

Density-functional tight-binding and classical molecular dynamics simulations are used to investigate the structural deformations and melting of planar carbon nano-clusters C_N with N=2-55. The minimum energy configurations for different clusters are used as starting configuration for the study of the temperature effects on the bond breaking/rotation in carbon lines (N<6), carbon rings (5<N<19) and graphene nano-flakes. The larger the rings (graphene nano-flake) the higher the transition temperature (melting point) with ring-to-line (perfect-to-defective) transition structures. The melting point was obtained by using the bond energy, the Lindemann criteria, and the specific heat. We found that hydrogen-passivated graphene nano-flakes (C_NH_M) have a larger melting temperature with a much smaller dependence on its size. The edges in the graphene nano-flakes exhibit several different meta-stable configurations (isomers) during heating before melting occurs.

4.1 Introduction

The study of the melting of crystals is one of the important subjects in the field of phase transitions. Melting phenomena occurs at the surface of bulk materials [168] and needs a microscopic theory for a deep understanding. Nano-scale molecular clusters due to their

The results of this chapter were published as
Sandeep Kumar Singh, M. Neek-Amal, and F. M. Peeters, Phys. Rev. B **87**, 134103 (2013).

size-dependent properties show melting processes different from those of bulk materials and infinite size two-dimensional materials. The melting of nano-clusters has received considerable attention recently and it was found that nano-clusters melt typically below their corresponding bulk melting temperature [169–171]. This is due to the higher chemical reactivity of nano-clusters which is the consequence of the increased accessible surface and the presence of more free dangling bonds.

The microscopic behavior of nano-clusters at finite temperature can be understood theoretically using a variety of molecular dynamics (MD) methods [172–177] and can be determined directly by experiment [178–180]. In most of the simulations the microscopic structure is characterized in terms of bond-lengths and their average fluctuations over many cycles of the MD simulation [181–183].

Since the discovery of two dimensional materials, i.e. graphene [2, 6] and hexagonal boron nitride sheet [184] the melting of these new materials have attracted many researches [185]. The new 2D crystalline materials respond to an increasing temperature by loosing their lattice symmetry, e.g. Zakharchenko et al. [185] studied the high temperature behavior of graphene using atomistic simulations. The melting temperature of graphene was estimated to be about 4900 K. Before melting first Stone-Wales defects appear because of their smallest energy barrier. When increasing temperature further eventually spaghetti-type of carbon chains are formed that spread in 3D. A similar melting process can be found for carbon nanotubes using a much smaller critical Lindemann parameter [186]. The melting temperature of perfect single-wall carbon nanotubes (SWNTs) was estimated to be around 4800 K [186]. In graphene nano-ribbons different types of edges (i.e. zig-zag, armchair) affect the melting process differently, e.g. Lee et al. [187] found that at 2800 K edge reconstruction occurs in a zig-zag ribbon.

In our previous chapter we found that the minimum energy configuration for flat carbon clusters up to N=5 atoms consists of a line of carbons [157] (linear chain) which is in agreement with ab-initio [188] calculations. Carbon planar rings were found for $5<N<19$ and graphene nano-flakes are minimum energy configurations for larger N [156]. Here we investigate the effect of temperature on those minimum energy configurations and find the melting temperature of such small flat carbon clusters, as function of the size of the clusters.

A systematic study of the size dependence of the melting temperature is still lacking as well as the effect of H-passivation of the edge atoms on the melting process. We present such a study and identify the different fundamental steps in the melting process. We found that graphene nano-flakes have a lower transition temperature as compared to bulk graphene and graphene nanoribbons. We also found that H-passivated clusters exhibit higher melting temperature than non H-passivated clusters. In all cases, once clusters are defected they can be in different meta-stable structures (none-planar isomers). We

will compare our results with those found for graphene and graphene nano-ribbons. The Lindemann index increases with respect to temperature in all cases while its slope versus temperature increases (decreases) linearly for the ring structures (graphene nano-flakes). Furthermore, using ab-initio molecular dynamics simulation we analyse the energy change due to defect formation.

4.2 Simulation Method and Model

4.2.1 Minimum energy configurations

The second-generation of Brenner reactive empirical bond order (REBO) potential [116] function between carbon atoms is used in the present chapter. All the parameters for the Brenner potential can be found in Ref. [116] and are therefore not listed here.

In the present chapter we study the temperature effects on the structural transition and melting properties of these minimum energy configurations. Using molecular dynamic simulations, we obtain the new configuration of the above mentioned clusters at a given temperature T. This temperature is maintained during the whole simulation by the Langevin thermostat [189]. The MD time step was taken to be 0.5 fs. Different properties of the cluster were measured during the MD simulation of 10^6 MD steps (500 ps) at fixed temperature.

4.2.2 Density-functional tight-binding molecular dynamics

In order to have an independent test of the results obtained from the bond order potential for the melting of graphene nano-flakes, we also performed independent calculations using the DFTB/MD (density-functional based tight-binding molecular dynamics) approach which is a QM/MD technique based on a tight binding method using an approximate density-functional formalism [190–192]. DFTB passed several benchmark tests with first principle density functional theory (DFT) [190, 193, 194] for carbon structures. Alberto et al. [194] showed that DFTB accurately reproduced the structures and energies for a range of point defects such as vacancies and Stone-Wales defects in graphene. Migration barriers for vacancies and Stone-Wales defect formation barriers are also accurately reproduced. Kuc et al [158] studied the stability of graphene nano-flakes using DFTB and by comparing their results with DFT, good agreement was found between the two methods. Although this method is two orders of magnitude faster than DFT but for the purpose of this work where we will study about 90 different configurations it will be computationally expensive. Therefore, we will use DFTB for a few N-values in order to show the accuracy

of our classical MD simulation by considering one of the line carbons, two of the rings, five of graphene nano-flakes and six of H-passivated systems.

4.2.3 Lindemann criterion and specific heat

The root-mean-square relative bond length variance (Lindemann criterion) in addition to the caloric curve gives a reasonable computational method for determining the melting point of nano-clusters. It is sensitive to any change in the bond lengths at the microscopic scale. The Lindemann criterion [195, 196] is often used in molecular dynamics and Monte Carlo simulations in order to estimate the melting temperature in three dimensional bulk systems [197, 198], two dimensional materials [185] and nano-clusters [199]. We used the distance-fluctuation of the Lindemann index (δ) in order to identify the melting temperature of our nano-clusters. For a system of N atoms, the local Lindemann index for the i^{th} atom in the system is defined as [200, 201]

$$\delta_i = \frac{1}{N-1} \sum_{j(\neq i)} \frac{\sqrt{\langle r_{ij}^2 \rangle_T - \langle r_{ij} \rangle_T^2}}{\langle r_{ij} \rangle_T} \tag{4.1}$$

and the system-average Lindemann index is then given by

$$\delta = \frac{1}{N} \sum_i \delta_i \tag{4.2}$$

where r_{ij} is the distance between the i^{th} and j^{th} atoms, N is the number of atoms and $\langle \cdots \rangle_T$ denotes the thermal average at temperature T. The Lindemann index [202] depends on the specific system and its size which varies in the range 0.03-0.15, e.g. it was recently [200] applied to nanoparticles and homopolymers and found to be in the range of 0.03-0.05, for Ni nanoclusters it was found to be around 0.08 [199] and for carbon nanotubes about 0.03 [186].

For sufficiently low temperature there is no structural transition and the atoms exhibit thermal fluctuation around the $T = 0$ equilibrium position. The oscillation amplitude increases linearly with temperature due to Hooke's regime for the atomic vibrations leading to a linear increase of the Lindemann index with T. At higher temperature, the anharmonic vibrations (non-linear effects) become important and the Lindemann index exhibits a non-linear dependence on T. The particle oscillation amplitude increases faster than linear with T, but the system does not melt yet, since the arrangement of atoms have still some ordered structure, i.e. solid-liquid coexistence state. For small nano-clusters the latter is related to not well defined small three dimensional structures. In general, melting occurs when

the Lindemann index increases very sharply with T over a small T-range. In this study we will assume that the melting point is around the sharp jump in δ, i.e. when the system becomes almost a random coil. We will show that the Lindemann index adequately indicates the structural deformation (melting-like transition) of carbon nano-clusters. The obtained linear regime in δ is smoother than some of the previous studies [199] for small nano-clusters. Therefore, we will not only use the critical value of δ to determine the melting point but we will also pay particular attention to the temperature dependence of the Lindemann index when identifying the melting temperature.

In addition to the Lindmann index, the total energy (caloric curve) and specific heat variation versus T are two common quantities which can be used to determine the phase transition. We calculated the specific heat C_P using the equation [203]

$$C_P(T) = \frac{\langle E_{total}^2 \rangle_T - \langle E_{total} \rangle_T^2}{k_B T^2}, \tag{4.3}$$

where $E_{total} = \sum_i \frac{1}{2} m_i v_i^2 + E_P$. The average potential energy of the system was calculated as a function of temperature. In the crystalline state the total energy of the system increases almost linearly with temperature, and then after the critical temperature is reached, it increases more steeply which is a signature of melting. We will show that for graphene nano-flake with 54 carbon atoms (C_{54} and $C_{54}H_{20}$) energy and heat capacity calculations are found to be consistent with the results for the melting temperature that we obtained from the analysis of the Lindemann index.

4.3 Results and Discussion

4.3.1 Energy

The temperature dependence of the total energy of graphene nano-flakes (C_{54} and $C_{54}H_{20}$) are depicted in Fig. 4.1 using the Brenner potential. For C_{54} the energy increases linearly at low temperatures and starts to deviate from the linear behavior around T=2300 K due to the reconstruction of the zigzag edges and the formation of pentagon-heptagon (5-7) defects. It indicates that the first nucleation of melting starts around 2300 K and modifies the edges. As temperature increases, the formation of pentagon, heptagon, 5-7 defects or 5-8-5 are possible and eventually large ring structures results in a dramatic increase of the energy. Above T= 3400 K, there is a sharp increase in the energy showing a completely molten structure.

For $C_{54}H_{20}$, passivation removes the dangling orbitals of the C atoms at the edge, lowering the reactivity, and increasing the stability of the cluster. It was found that unlike

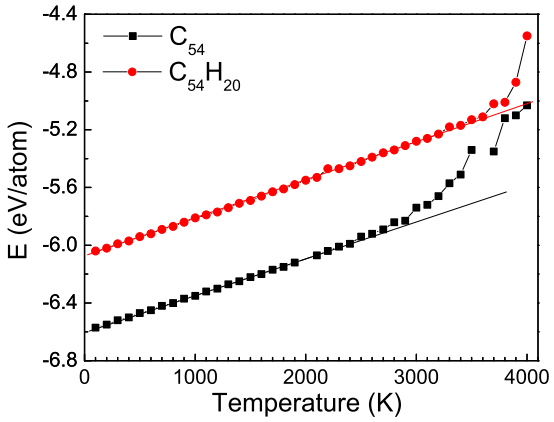

Figure 4.1: The temperature dependence of the total energy of the graphene nanoflake C_{54} and the H-passivated $C_{54}H_{20}$ using the REBO potential.

previous case (without H-passivated clusters), the H-passivated clusters keep their initial atomic arrangement up to higher temperature and therefore no noticeable change in the geometry was found for temperatures up to T=3200 K for $C_{54}H_{20}$. The binding energy of the H-passivated clusters are larger than for non-passivated clusters. As temperature increases further to T=3500 K, some hydrogen atoms start to dissociate and finally the clusters convert into hydrocarbon chains around T=4000 K showing larger melting temperature than the corresponding non-passivated cluster which has a melting temperature of 3400 K (see Fig. 4.1).

4.3.2 Lindemann index

Fig. 4.2 displays the variation of the Lindemann index with temperature for (a) C_{54} and (b) $C_{54}H_{20}$. The corresponding structures during heating for a few typical temperatures are shown in the insets. The slope of the function $\delta(T)$ (i.e. $\alpha = \frac{d\delta}{dT}$) is plotted in Fig. 4.3 for all studied structures of Figs. 3.1 and 3.2. The value of α (before reaching the melting point) increases monotonically for the carbon lines (Fig. 3.1(a)) and carbon rings (Fig. 3.1(b)). This is an indication of keeping the initial configuration while non-linear effects indicate defect formation, e.g. 5-7 defects in C_{54}. The increase of α is fitted in Fig. 4.3 by the red line for $N \leq 18$ which is given by the function $\alpha(N) = a + b \times N$, where: a=1.005 $(\pm 0.032) \times 10^{-5} K^{-1}$ and b=0.070 $(\pm 0.004) \times 10^{-5} K^{-1}$. Note that increasing temperature forces the system to be out-of-planed, e.g. the rings at finite

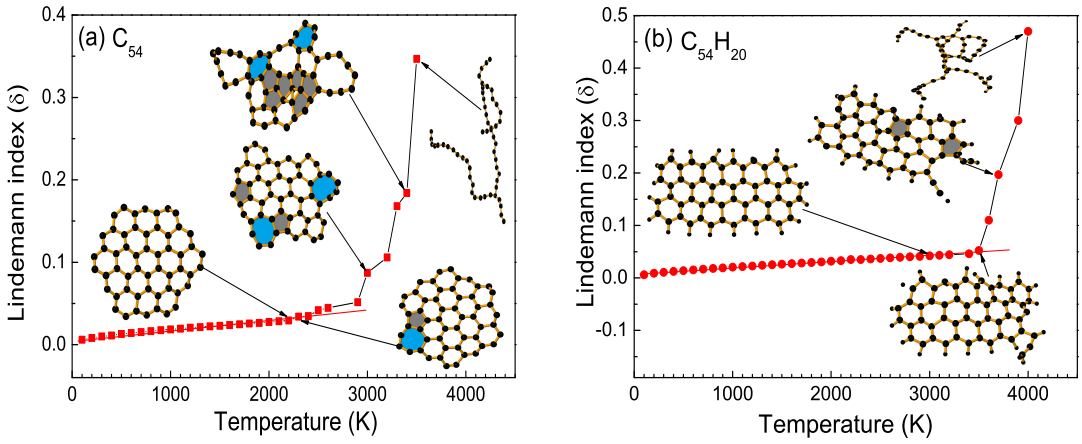

Figure 4.2: The temperature dependence of the Lindemann index for the cluster (a) without H-passivated C_{54} and (b) with H-passivated $C_{54}H_{20}$. The insets show typical C (a) and C-H (b) atoms configurations where the solid areas indicate topological defects.

temperature are not circles and become deformed ellipsoids in 3D.

For N $\geq$ 19, there is a sudden decrease in α of size $\Delta\alpha = 1.11 \times 10^{-5}K^{-1}$ due to the strong sp^2 bonds within the graphene like clusters (instead of simple covalent bonds in the carbon lines and rings) and a decreasing number of dangling bonds. The average behavior is fitted by the red line $\alpha(N) = a + b \times N$, where: a= 1.63($\pm$0.06) $\times$ $10^{-5}K^{-1}$ and b=-0.012 ($\pm$0.001) $\times$ $10^{-5}K^{-1}$. For bowl like clusters (N=20, 28, 38, 44), due to the presence of topological defective pentagon inside the cluster, the α value is larger as compared to their neighbor clusters. Therefore the important message is that dangling bonds and any kind of defects enhance anharmonic effects.

In order to investigate the effect of large size samples we also calculated α for a few large graphene nano-flakes and found that α decreases with N (see inset in Fig. 4.3). The maximum considered size of graphene nano-flakes had 4000 atoms. For large N, one expects saturation of α, thus a line with negative slope which we fitted for 19 $\leq$ N $\leq$ 55 should not be applicable. Therefore, we used the fit $\alpha(N) = \alpha(\infty)+a/(1+b\times N)$, where: $\alpha(\infty) = 0.134 \times 10^{-5}K^{-1}$, a=1.213 ($\pm$0.005) $\times$ $10^{-5}K^{-1}$ and b=48.7 ($\pm$4.9) $\times$ 10^{-4} on large clusters. These results clearly indicate that δ for small graphene nano-flakes is considerably larger than for larger flakes and graphene. Although the Lindemann index was defined initially in the thermodynamical limit (bulk material) we show that it is also a good parameter to investigate the effect of temperature and melting of nano size systems.

For completeness, we calculated α for H-passivated graphene nano-flakes for 11$\leq$ N $\leq$ 55 number of C-atoms and found that α, on average, decreases with N (see Fig. 4.3(b)).

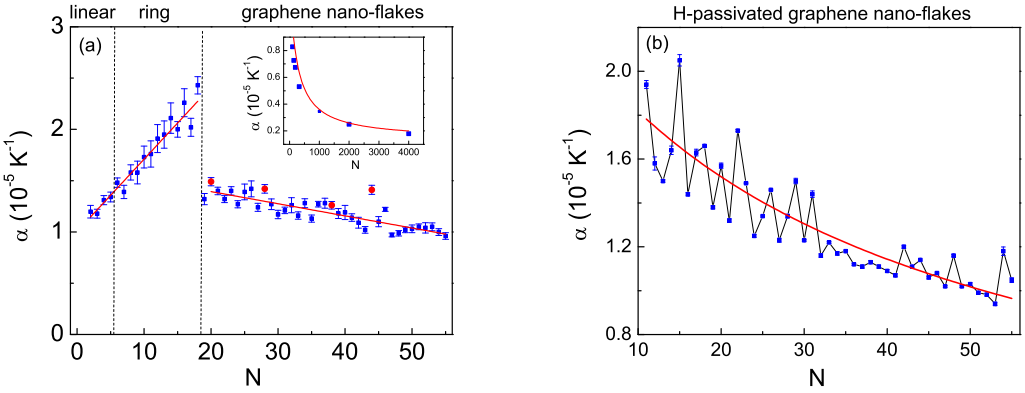

Figure 4.3: The low temperature rate of the Lindmann index versus the number of atoms in (a) graphene nano-flakes and (b) H-passivated graphene nano-flakes. The red solid lines are linear fits to the average behavior of α. The bowl-like clusters are shown by red solid circles (a). In the inset, the same quantity versus the number of atoms in graphene nano-flakes for N up to 4000 (a).

The average behavior is fitted by the red line $\alpha(N) = a/(1 + b \times N)$, where: a=2.262 $(\pm 0.115) \times 10^{-5} K^{-1}$ and b=0.024 $(\pm 0.003) \times 10^{-5}$. The rapid decrease in the latter fit (Fig. 4.3(b)) is an indication of the role of H-passivation in making the graphene nano-flakes more stable against temperature for larger N.

4.3.3 Specific heat

The calculated specific heat curve for C_{54} is shown in Fig 4.4. A clear peak is observed in the specific heat with a maximum around 3400 K which we identify as the melting temperature, and which is close to the results from the analysis using the Lindemann index. The specific heat curve is also shown for $C_{54}H_{20}$ (see red symbols in Fig. 4.4) and displays a peak around T=4000 K which is identified as the melting temperature, showing good agreement with the result of the previous caloric curve (see Fig. 4.1). A discontinuity or a sharp peak in the heat capacity is a clear indication of a phase transition. However, here this is not exactly a solid-to-liquid like transition, but rather a nano-flake to random-coil transition.

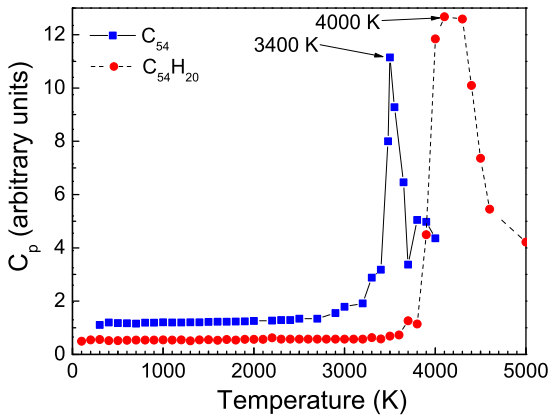

Figure 4.4: The temperature dependence of the specific heat for C_{54} and $C_{54}H_{20}$.

Table 4.1: Melting temperature for large clusters

N	$T_m(K)$
98	3800
142	4000
194	4100
322	4200
1000	4400
graphene	5500

4.3.4 Melting-temperature

The melting temperature for all studied clusters $C_N(2 \leq N \leq 55)$ is shown in Fig. 4.5(a). For small linear structures except for the carbon dimer the melting temperature increases with the number of atoms (linear chains have bond breaking).

In order to check if for large N we approach the melting temperature of bulk graphene, we also calculated the melting temperature of three large graphene nano-flakes and graphene (by performing a simulation having 4000 atoms with periodic boundary condition with NPT ensemble) and presented the results in Table 4.1. From Table 4.1 it is clear that large flakes approach slowly the melting temperature of graphene, i.e. 5500 K. As a comparison the melting temperature reported in Ref. [185] by using the LCBOPII potential was 4900 K and in Ref. [204] using REBO was 5200 K.

We fitted the melting temperature for graphene like clusters (red curve in Fig. 4.5(a)) by the function $T_m(N) = T_m^{bulk} - (a/(b+N))$ where $a = 417(\pm 47) \times 10^3 K$, $b =$

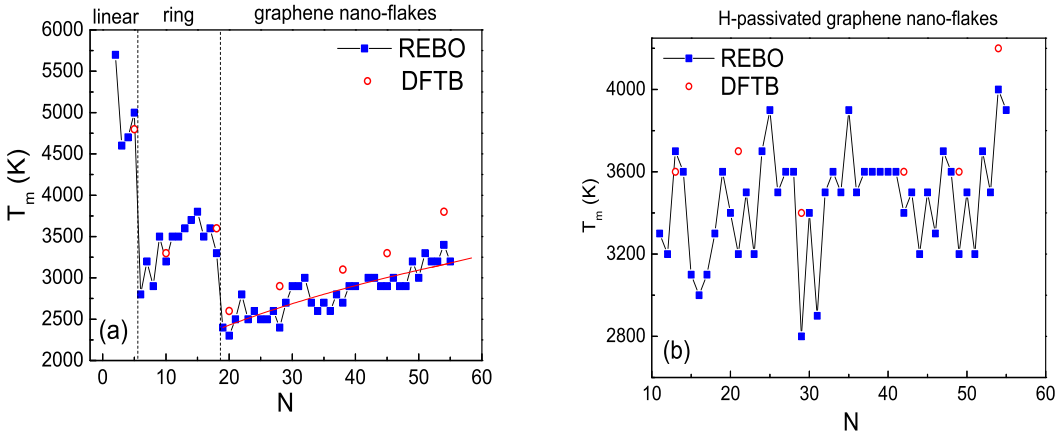

Figure 4.5: The melting temperature versus the number of atoms using Brenner (square symbols) and DFTB (open circles) for (a) nano-graphene and (b) hydrogenated nano-graphene. The error bar is 50 K.

$119.34(\pm 17.71)$ and $T_m^{bulk} = 5500K$ for graphene was taken from our simulation. We included the results of Table 4.1 in this fit. We also calculated the melting temperature using DFTB for the clusters with N=5, 10, 18, 20, 28, 38, 45, and 54 (C_{54}) which are represented by the open red circles in Fig. 4.5(a). They are found to slightly overestimate the melting temperature but exhibit clearly the same N-dependent trend.

For completeness, we also calculated the melting temperature of H-passivated clusters for N=11-55 C-atoms (Fig. 4.5(b)). The melting temperature fluctuates around T=3500 K (note that on average T_m increases slowly with N with large fluctuations imposed on it) for most of the clusters with minima for N=29 and N=31 C-atoms due to the large number of defects in their structures. The clusters which have pentagon defects on the boundary usually have lower melting temperature than the others. Here, the melting temperature for the clusters N=13, 21, 29, 42, 49 and 54 were also calculated using DFTB (open red circles in Fig. 4.5(b)). In most cases the DFTB results are close to the Brenner potential results indicating that the Brenner bond order potential is a useful specialized potential for thermal effects in hydrocarbons.

4.4 Topology of Defects

In this section we consider the topology of some of the defects which are created during the melting process of C_{54} using DFTB calculations. We found that these defects have

a pronounced effect on the melting behavior of the system whose mechanism is different from both graphene and graphene nanoribbons. At low temperature the probability of defect creation is small and the flakes remains perfect which for this low temperature range is similar to graphene [185] and graphene nanoribbon [205]. Increasing temperature (above about 2300 K) the energy increases and the system can overpass certain potential barriers and we found that during the molecular dynamics simulation the system transits from one metastable state to another, see Figs. 4.6(a-b). We show five snap shots of C_{54} at different temperature in Fig. 4.6. The transition temperature at which the edge reconstruction occurs, i.e. T$\sim$ 2400 K is lower than those found for defect formation in graphene, i.e. 3800 K and edge reconstruction in graphene nano-ribbons [187], i.e. 2800 K. As seen in Fig. 4.6(b) the first defected structure has one heptagon and one pentagon at the edge with different bond lengths. The energy difference between non-defected (Fig. 4.6(a)) and defected (Fig. 4.6(b)) one is about 0.28 eV/atom which is due to the 900 K difference in the temperature between these two structures. In Fig. 4.6 the next defected configuration due to a 1200 K increase in temperature is shown which has more heptagon and pentagon defects (colored parts). By increasing temperature further we found some transition in the defected parts and even an edge reconstruction from heptagon to hexagon and vise versa until the appearance of a tail-like part in the cluster, Fig. 4.6(e). The melting temperature for C_{54} as shown in Fig. 4.5(a) (open circle symbol) is around 3900 K. This melting temperature is lower than those found for graphene. The larger the graphene nano-flake the higher the melting temperature. For small graphene nano-flakes the larger number of dangling bonds results in a lower melting temperature and larger boundary effects. The energy diagram for five snap shots is depicted in Fig. 4.6(f). The presented energy is the difference between the total energy of the system at given temperature and the zero temperature total energy for C_{54}.

In Figs. 4.7(a-d) we show the temperature effect on $C_{54}H_{20}$. In Fig. 4.7(e) the corresponding energy diagram is shown. Hydrogens become released at T=3900 K. Notice that DFTB calculations for the shown configurations in Figs. 4.7(a-d) were performed separately, i.e. we do not increase temperature of sample Fig. 4.7(a) in order to obtain Fig. 4.7(b), but instead we performed four different calculations for these four snap shots. Thus we do not expect that we have sequential configurations.

4.5 Conclusion

Using molecular dynamics simulation and the Lindemann index for melting supplemented with results for the total energy and the specific heat, we investigated the melting of carbon nano clusters. The melting temperature of small carbon flakes is lower than those for

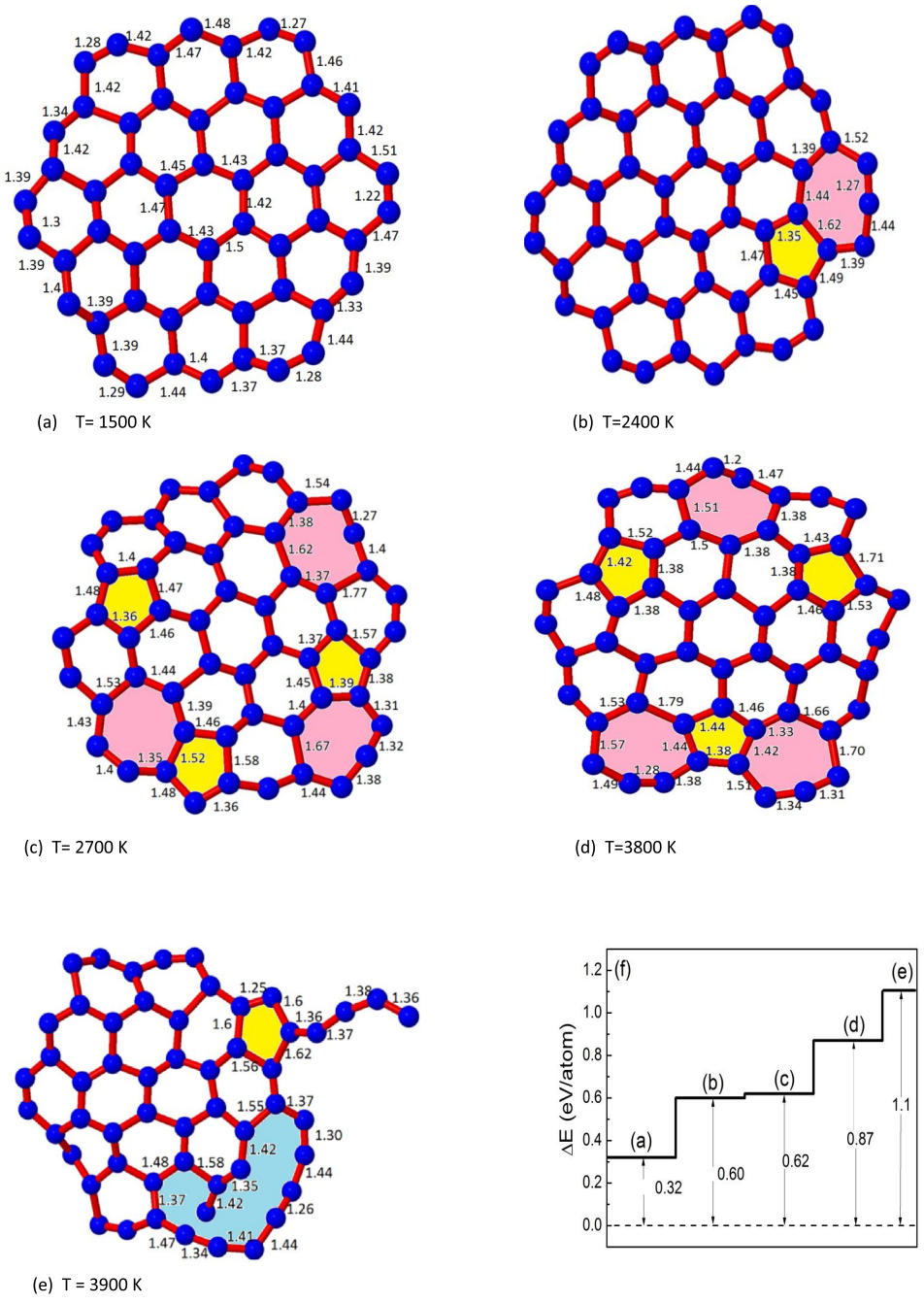

Figure 4.6: Five different snap shots of the cluster C_{54} at different temperature (a-e). Bond lengths are indicated in the figure and the colored areas indicate defect structures. (f) The corresponding energy diagram for the five snap shots.

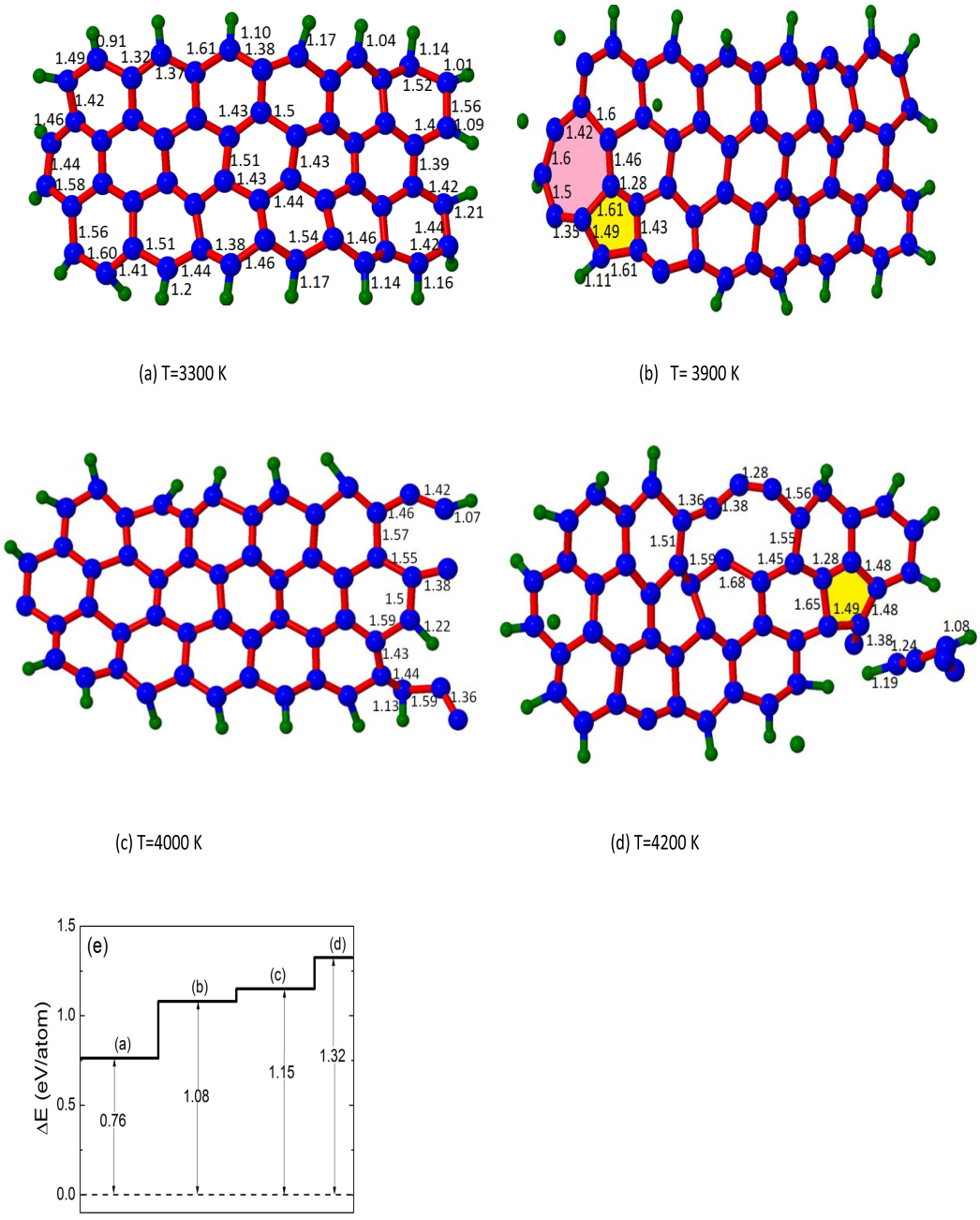

Figure 4.7: Four different snap shots of the cluster $C_{54}H_{20}$ at different temperature (a-d). Bond lengths are indicated in the figure and the colored areas indicate defect structures. (e) The corresponding energy diagram for the four snap shots.

graphene and graphene nano-ribbons. The Lindemann index is sensitive to temperature and is a good quantity for determining when structural deformations of the clusters start to occur. The melting temperature of small flakes on average increases versus the number of atoms in carbon nano clusters. All clusters investigated show premelting behavior with different premelting intervals. For certain N-values defects are already present inside the cluster which lowers the melting temperature. H-passivated clusters have a higher melting temperature than the non H-passivated clusters with the same number of C-atoms. The melting temperature for H-passivated clusters is larger than for non-passivated clusters. Our simulation results also help to understand the formation of defects (due to the increase of temperature) in the graphene nano-flake which can then be applied to understand the growth and thermal treatment of nanographene. We supplemented our analysis by DFTB calculations which confirm the N-dependence of the melting temperature.

CHAPTER 5

Melting of partially fluorinated graphene

The melting process of partially fluorinated graphene is investigated by molecular dynamics simulations with ReaxFF potentials for the inter-atomic interactions. Although for temperatures below 1000 K, fully fluorinated graphene (FFG) is thermo-mechanically more stable than graphene (GE), we found that it transits to random coils at $T_m \approx 2800$ K which is almost twice lower than the melting temperature of graphene, i.e. 5300 K. During the melting transition each C-atom inside the single chains remains bonded to an F-atom. For partially fluorinated graphene (PFG), three distinct regimes of melting are identified: i) up to $\sim 30\%$ of fluorination, ripples causes detachment of individual F-atoms around 2000 K, ii) for 40-60% of fluorination, large defects are formed beyond ≈ 1500 K (F-atoms break the original local bonds and attach to the edges of these rings), and iii) for fluorination larger than 60% F-atoms remain bonded to graphene until melting. We construct a melting phase diagram which helps to understand the effect of the concentration of F-atoms on the experimental reversibility of the fluorination process.

The results of this chapter were published as
Sandeep Kumar Singh, S. Costamagna, M. Neek-Amal, and F. M. Peeters, J. Phys. Chem. C **118**, 4460 (2014).

5.1 Introduction

Several distinct atomic arrangements of adatoms (fluor, hydrogen, chlorine, etc) have been proposed for tuning the electronic properties of graphene (GE) [57, 58, 86]. The main advantage of using fluor is that C-F bonds are energetically more stable than e.g. C-H ones [59, 206] since F-atoms posses larger binding and desorption energies to C than H-atoms [57]. Furthermore, fluorination is easier to control via temperature and reactant gases leading to reproducibly precise C/F stoichiometries [207–209]. In the presence of F adatoms C-bonds in graphene transit from sp^2 to sp^3 hybridization, which turn the conjugated, graphitic C-C bonds into single C-C bonds. The lattice structure results in an angstrom scale out-of-plane buckled shaped membrane known as chair configuration [206] that influences the high temperature stability of FG. Owing to the properties mentioned above, a complete understanding of the thermal behavior of the FG sheet is hence very important.

Previous studies have shown that, different from graphene, fully fluorinated and also hydrogenated [210, 211] graphene, are more rigid for temperatures up to 1000 K. It is then reasonable to ask what is the situation beyond 1000 K up to the melting temperature. Raman spectroscopy experiments reveal that the fluorination time and the N_C/N_F ratio (where N_C and N_F are the number of carbon and fluor atoms, respectively) in the samples are two important key factors in the preparation of FG [57, 58]. It was found that the process can be reversed for low coverage and during the fluorination process large membrane holes could appear due to losses of C atoms at room temperature [212, 213]. Despite this macroscopic information, the microscopical features and temperature stability is still not well understood. In this letter, by using the art of molecular dynamics simulations employing our recently proposed ReaxFF force field for FG and the Lindemann-criterion analysis we investigate several microscopical features of the melting process on FG with different F coverage. We analyze the importance of the N_C/N_F ratio and the modifications induced by vacancy defects.

5.2 Simulation Method

The melting of FG is studied by molecular dynamics (MD) simulations using reactive force fields (ReaxFF [119, 214, 215]) present in the large-scale atomic/molecular massively parallel simulator (LAMMPS) code [216]. It was shown that this potential describe correctly the thermal properties of FG [211]. A description of the new set of parameters appropriate for structures with C-F bonds can be found in our previous study [211]. We considered square shaped computational unit cells having N_C =1008 C-atoms in the graphene sheet with partial fluorination up to fully fluorinated graphene (FFG). The simulations were per-

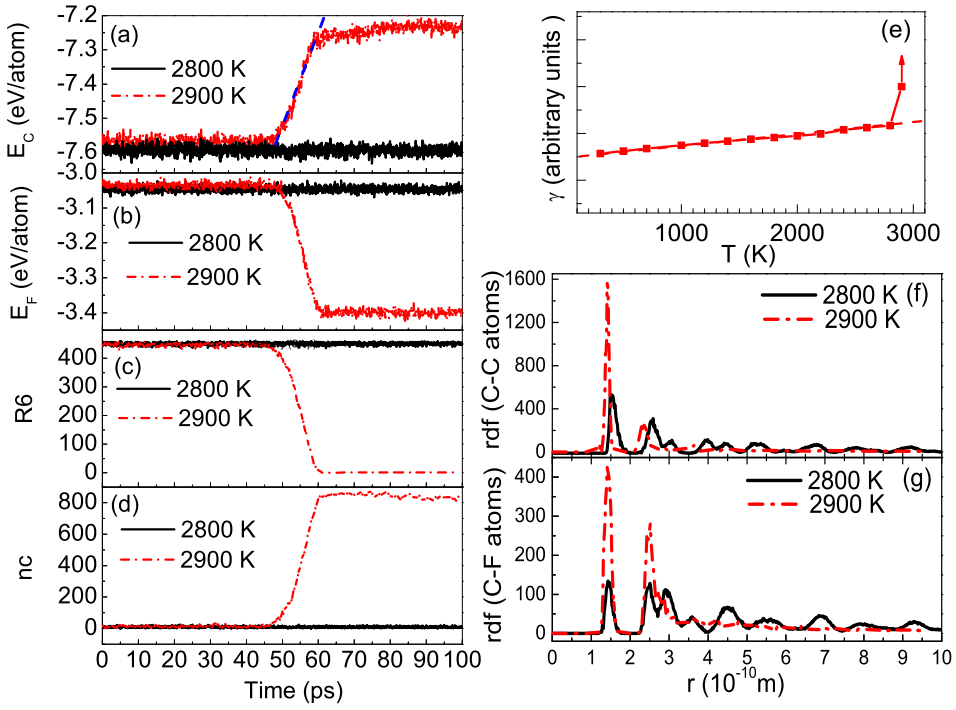

Figure 5.1: Fully fluorinated graphene. (a) E_C, (b) E_F, (c) number of six-membered rings R6, and (d) chains (nc) with more than three connected twofold-coordinated atoms, as a function of time for T=2800 K (below melting) and at T=2900 K where melting occurs. (e) Modified Lindemann parameter γ versus temperature. (f) C-C and (g) C-F radial distribution function.

formed in the NPT (P=0) ensemble with periodic boundary conditions. Temperature was maintained by the Nosé-Hoover thermostat [217] and the MD time-step was taken to be 0.1 fs. The partial covered samples (PFG) were designed by adding randomly F atoms equally distributed on both sides of an initially flat graphene lattice [211]. The dependence of the averaged lattice parameter with increasing F concentration was found to be in agreement with recent results [218].

To account for the melting transition we analyzed the variation of the total potential energy E_T per atom with temperature identifying partial contributions from C-atoms (E_C) and F-atoms (E_F). The Lindemann criterion was used to characterize the ordered state by considering the modified parameter γ_n, used previously for 2D systems [219, 220]. The

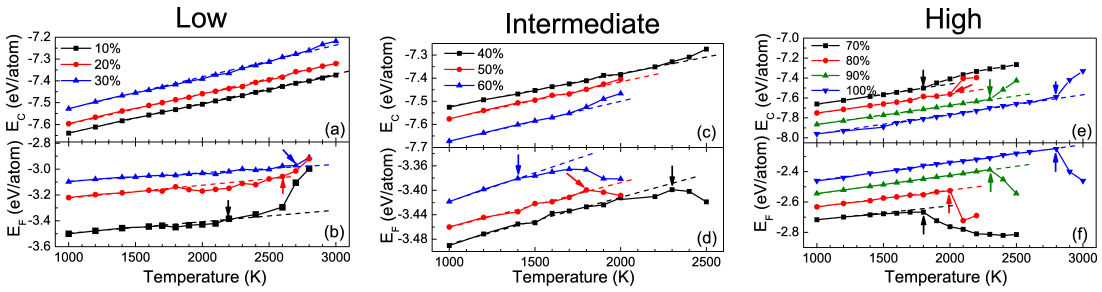

Figure 5.2: Dependence of E_C (upper panels) and E_F (lower panels) versus temperature for the three regimes of melting indicated. Curves were shifted for a better comparison ((i) for E_C: 30, 40 and 60% fluorination, curves are shifted by 0.05, 0.45 and -0.5 eV/atom, respectively. (ii) for E_F: for 20, 30, 70, 80, 90, and 100% fluorination, curves are shifted by 0.3, 0.4, 0.65, 0.7, 0.75, and 0.8 eV/atom, respectively). Notice that E_F increases in (b) while it decreases in (d) and (f) which is an indication of the evaporation of fluor in “low" concentration regime and ring/defect formation and their saturation by F in “intermediate" and “high" concentration regimes".

parameter γ_n is defined as

$$\gamma_n = \frac{1}{a^2}\langle|\mathbf{r}_i - \frac{1}{n}\sum_j \mathbf{r}_j|^2\rangle, \tag{5.1}$$

where $a = 1/\sqrt{\pi\rho_0}$, ρ_0 is the 2D particle density at T = 0 K, $\mathbf{r}_i$ is the position of the ith atom and the sum over j runs over the n atoms closest to i. Here we took $n = 3$ by including only nearest neighbour atoms.

5.3 Results

We first analyze the case of FFG. Figures 5.1(a,b) show the variation of potential energy per atom of carbon and fluor atoms, i.e. E_C and E_F respectively, with time at 2800 K and 2900 K. The sharp increase (decrease) in E_C, which is about 4.5% (E_F about 10%), is a signature of melting at 2900 K. During melting, (10 ps) the number of six-membered rings (R6) of the crystalline phase is reduced (Fig. 5.1(c)) and chains composed by single C-atoms bonded to F-atoms are formed (Fig. 5.1(d)). The melting temperature $T_m = 2800$ K is further confirmed by the Lindemann parameter γ (Fig. 5.1(e)). Due to the strong covalent nearest-neighbor C-C interaction γ increases linearly up to close the melting temperature where it diverges.

After melting the C-atoms in the single chains remain bonded to the F-atoms, i.e. a spaghetti of 3D-polymers constructed from C-F monomers (a snap shot of the molten FFG

will be shown in Fig. 5.4(c)). For large simulation time the molten structure is composed of C-chains which form an entangled three-dimension network which looks more like a polymer gel than a simple liquid [221]. The larger reduction in E_F suggests that F atoms prefer to be bonded to carbon atoms of rings/chains rather than the carbons of GE. This indicates that presumably during fluorination in experiments F atoms first prefer to be bonded to defective regions, where the environment is more similar to a C-chain. The radial distribution function (rdf) indicates that the C-C distance in chains is shorter and after melting (double bonds appear) only one significant peak remains (see Fig. 5.1(f)). However the C-F rdf in Fig. 5.1(g) shows that after melting there are two significant peaks which correspond to the appearance of -C-F_2 and -C-F bonds. In the case of PFG, conjugated C-C double bonds in the non-fluorinated parts coexist at low temperatures with covalent C-F bonds in corrugated fluorocarbon regions [222, 223]. However the mechanism at higher temperature is more complicated. We found three different melting regimes depending on the fluor percentage for PFG:

5.3.1 Low fluorination (10-30%)

In Figs. 5.2 (a,b) we display E_C and E_F against temperature. The main feature here is evaporation of F-atoms and the formation of large rings, e.g. R10, R14. While E_C increases linearly against temperature due to a smooth expansion of the C-C inter-atomic distance (small deviations are due to the formation of large rings), because of C-F bond breaking, E_F instead behaves non-linear (and get higher energies: F atoms are in gas phase, see Fig. 5.4(a)) with T (indicated by the arrows). Detachment starts around 2000 K and continues until almost all the F-atoms are removed from the membrane [224]. With further increment in temperature, Lindemann criterion indicates that melting occurs at 5100 K, 4500 K and 3500 K for 10, 20 and 30% fluorination, respectively and F-atoms are less likely to be bonded to the GE. Thus, the linear increase in E_C, Fig. 5.2(a), shows that the PFGs with $N_F/N_C \leq 30\%$ around 3000 K are pristine graphene (with a few number of rings).

5.3.2 Intermediate fluorination (40-60%)

In this regime at about $T \approx 1500$ K, E_C shows small deviations from linear behavior due to the formation of large defective rings (Fig. 5.2(c)). In contrast to the case of low N_F/N_C ratio, E_F shown in Fig. 5.2(d), becomes more negative since F-atoms instead of being detached from the sheet, now break the original local bonds and are transferred to the edges of the rings (a snapshot of this configuration is shown in Fig. 5.4(b)). Then, at melting temperature clusters of C-F are formed near the defects and they detach from the

sheet. The microscopic configurations consist of a mixture of 2D and 3D phases.

5.3.3 High fluorination (70-90%)

Finally, in the high-fluorination regime with increasing temperature large ripples develop but F atoms remain bonded to graphene until melting occurs. Now, E_C receives positive contributions due to the breaking of C-C bonds at melting (Fig. 5.2(e)) and since the C-F bond becomes stronger E_F is reduced (Fig. 5.2(f)). The microscopical features of melting in this case posses similar characteristics as FFG. Notice that arrows in Fig. 5.2 are not pointing necessarily to the melting transitions, instead they indicate mostly evaporation (b) and defect formation thresholds (d,f). The reduction in the E_F indicates the appearance of polymers constructed from C-F monomers. The average melting temperatures T_m were estimated from the behavior of the Lindemann parameter. Starting from 60%, when we increase further the F-content T_m is seen to pass a minimum around 70% and then increases due to the suppression of long wave-length ripples [211].

We depict the energy variation during melting for a typical case 90% in Figs. 5.3(a,b). Here, the number of hexagons approach zero and many single chains are formed as shown in Figs. 5.3(c,d). From the slope of E_C versus time we obtain the rate at which the hexagonal shape of the sample becomes lost as $\delta = dE_C/dt$ (e.g. dashed blue curve in Fig. 5.3(a)). Values of δ are shown in Fig. 5.3(e) together with T_m. The main result is that the larger the ratio N_F/N_C, the higher the melting temperature and the faster that melting takes place.

5.4 Effect of vacancies in the melting of FFG

It is important to study the effect of the presence of atomic vacancies in FFG on the melting temperature. We performed several additional simulations for FFG with p number of vacancies which were randomly distributed over FFG, i.e. $N_C \to N_C - p$ and $N_F \to N_F - p$. The presence of atomic defects in the GF sheet makes it less stiff [225] and consequently results in a lowering of the melting temperature, see Fig. 5.3(f). The melting temperature is fitted by the red line T_m(N)=a+bN, where a=(2780$\pm$75) K and b=(-60$\pm$6) K. These results clearly indicate that T_m decreases sharply as the number of defects in the FFG increases.

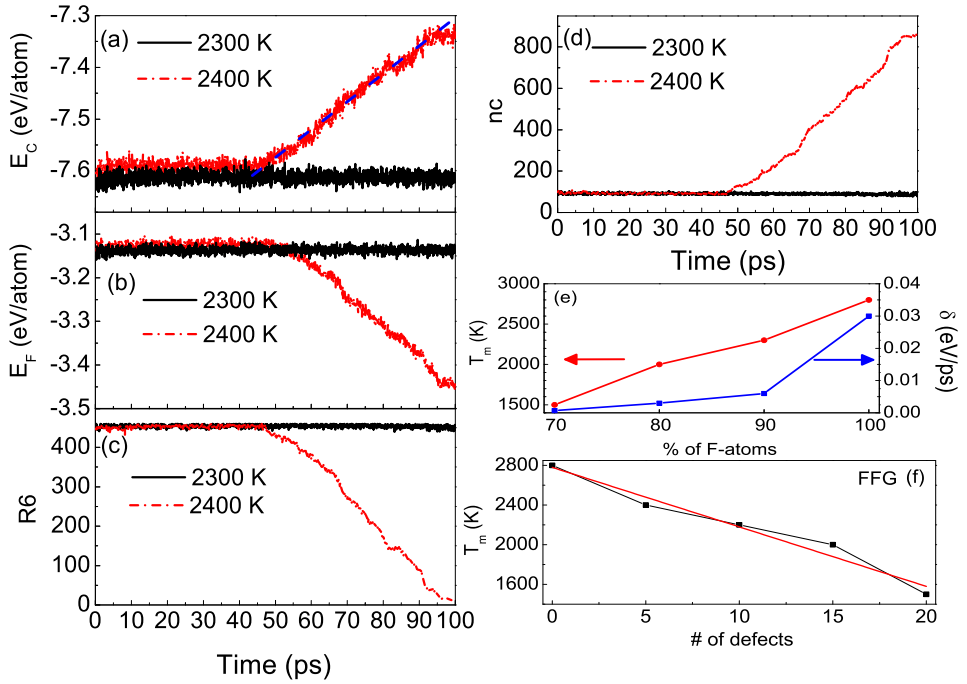

Figure 5.3: Partially fluorinated graphene 90%. (a) Total energy of C-atoms, (b) total energy of F-atoms, (c) number of six-membered rings R6, (d) number of chains (nc) with more than three connected twofold-coordinated atoms, as a function of time at T=2300 K (below melting) and at T=2400 K where melting occurs, (e) δ and T_m versus percentage of F atoms, and (f) variation of the melting temperature T_m against the number of defects in fully fluorinated graphene.

5.5 Discussion

FFG is an insulator with a large gap while graphene shows metallic properties, thus one naturally expects the transition from GE to FFG by increasing the ratio N_F/N_C. This gives the appropriate melting trend for a typical metal to an insulator. However, the melting of GE and FFG is different because of their 2D-nature. The existence of flexural phonons makes GE and FFG also different from typical 3D crystals [59] and the bending rigidity is a temperature dependence parameter [226, 227]. Although at low temperature FFG is thermo-mechanically more stable than GE, by increasing temperature, due to the excitation of the vibrational C-F mode, in FFG the entropy term increases faster with T which is being responsible for the observed lower melting temperature.

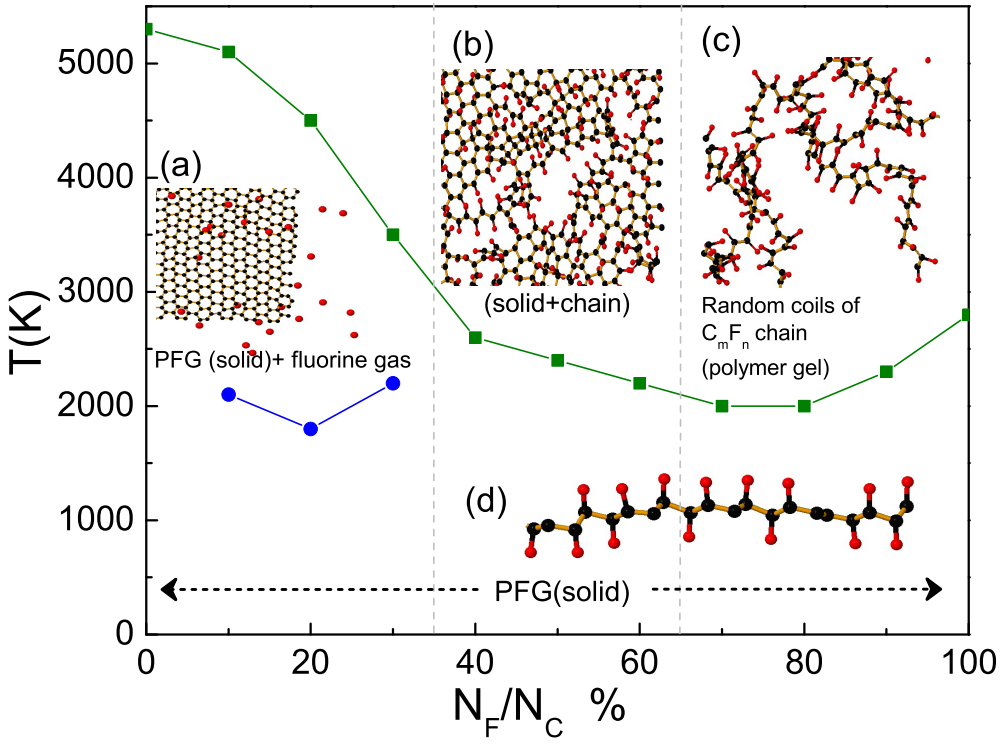

Figure 5.4: Melting phase diagram for fluorinated graphene. Circular symbols refer to the evaporation of F atoms (blue circles). The insets show the top view of the simulated FG before (a) and after melting (b,c). The inset (d) is a side view of the simulated PFG with $N_F/N_C = 80\%$.

In PFG the distribution of masses through the system is non-uniform, hence the vibrational frequencies are not well defined and are position dependent. This randomness in the system produces very large out-of-plane fluctuations even at low temperature. This broadening in the frequency range brings the system closer to the transition point.

Moreover, for a low ratio N_F/N_C when we heat the system F-atoms are evaporated in order to reduce the total energy. Then, the system behaves like pristine graphene and evaporated F atoms have no chance to be re-bonded to the system. For intermediate ratio N_F/N_C, the concentration of F atoms in some random domains make the system unstable due to the growth in the mean square value of the height fluctuations $\langle h^2 \rangle$ resulting in the formation of ring-defects with increasing temperature and the melting of this new defected FG is more complex. Finally, for high fluorination we deduce that the melting temperature is proportional to the number of randomly distributed defects and the coverage percentage, e.g. decreasing the coverage percentage from 100% to 90% (80%) decreases the melting

temperature with about 16% (30%).

It is worthwhile to compare our results qualitatively with recents experiments [57, 58]. Raman spectra of graphene after exposure to atomic F shows dramatic changes induced by fluorination: the D peak emerges at early times of fluorination and the 2D peak is suppressed which indicates that F atoms are bonded to C atoms and the formation of atomic defects. The process of fluorination has been shown to be reversible only when the exposure time is relatively short (< 20 hours) and the concentration of F atoms is presumably low. FFG is obtained only for longer exposure time, beyond 30 hours, where the evaporation of F atoms and the restoring to pristine graphene is impossible. In our simulations, we found that for low coverage percentage (less than 40%) increasing the temperature causes evaporation of F atoms and almost pristine graphene can be recovered in agreement with experiment. However, percentage beyond 40% are related to long time fluorination (> 20 hours) where the process was reported to be irreversible. The presence of vacancies decrease dramatically the melting temperature, thus PFG of experimental samples with a few vacancies can be heated up to temperatures much lower (∼500-700 K) to restore to not-perfect pristine graphene [57].

5.6 Summary

The phase diagram displayed in Fig. 5.4 summarizes our results: green squares refers to the transition temperature and blue circles indicate the starting point of evaporation of F-atoms. Two insets (b) and (c) show top views of the system after the transition points, inset (a) shows top view of a snap shot of a system which lost fluor and inset (d) shows a side view of a typical PFG at low temperature. The PFG above the blue symbols for $N_F/N_C < 40\%$ looses fluor and become pristine graphene with some defects and above the green line it transits to the liquid phase, however for N_F/N_C ∼40-60% above the green line and below (∼5000 K) PFG do not loose F and very slowly transits to the liquid phase so that below 5000 K the liquid and the solid phases are coexisting. For larger N_F/N_C ∼60-100% above the green curve PFGs rapidly transits to the liquid phase with 3D dimension. The minimum melting temperature is found to be around 70% fluorination. The vertical dashed lines separate three different regions for different percentage of F atoms. Our findings are therefore consistent with the experimental reversibility of the fluorination process in single layer graphene.

CHAPTER 6

Thermomechanical properties of a single hexagonal boron nitride sheet

Using atomistic simulations we investigate the thermodynamical properties of a single atomic layer of hexagonal boron nitride (h-BN). The thermal induced ripples, heat capacity, and thermal lattice expansion of large scale h-BN sheets are determined and compared to those found for graphene (GE) for temperatures up to 900 K. By analyzing the mean square height fluctuations $\langle h^2 \rangle$ and the height-height correlation function $H(q)$ we found that the h-BN sheet is a less stiff material as compared to graphene. The bending rigidity of h-BN: i) is about 16% smaller than the one of GE at room temperature (300 K), and ii) increases with temperature as in GE. The difference in stiffness between h-BN and GE results in unequal responses to external uniaxial and shear stress and different buckling transitions. In contrast to a GE sheet, the buckling transition of a h-BN sheet depends strongly on the direction of the applied compression. The molar heat capacity, thermal expansion coefficient and the Grüneisen parameter are estimated to be 25.2 $J\,mol^{-1}\,K^{-1}$, $7.2\times10^{-6}K^{-1}$ and 0.89, respectively.

The results of this chapter were published as
Sandeep Kumar Singh, M. Neek-Amal, S. Costamagna, and F. M. Peeters, Phys. Rev. B **87**, 184106 (2013).

6.1 Introduction

A single layer of hexagonal boron-nitride (h-BN) is a wide gap insulator that is very promising for opto-electronic technologies [228,229], tunnel devices and field-effect transistors [230–232]. According to the well known Mermin-Wagner theorem [18], the stability of any two dimensional crystal is only possible in the presence of atomic corrugations which distort the perfect honey-comb lattice and allow the atoms to explore the out-of-plane direction. Experimental observations have found ripples in suspended sheets of GE [233,234] and atomistic simulations suggest that the strong bonds between the carbon atoms determine the features of these ripples [20]. Understanding the behavior of the ripples is important for many reasons [210]. They affect the electronic transport properties, e.g., in GE the ripples are believed to be one of the dominant scattering sources which limits the electron mobility [104,105].

h-BN ribbons doped by carbon has recently been proposed [232,235]. In addition, BN based nanostructures are potential materials for thermal management applications [236–241] because of their high thermal conductivity. Therefore, the knowledge of the shape and the temperature dependence of the intrinsic ripples is fundamental to devise novel nano-devices based on this material.

Both GE and h-BN sheets have a honeycomb lattice structure, however the different electronic properties and phonon band structure [47,50,242] results in unequal morphologies and corrugations. Transmission electron microscopy is widely used to resolve the individual atoms in suspended h-BN sheets [184] where ripples inherently exist. First-principle calculations have been performed using small unit cells, periodically replicated, which are unable to model long wavelength corrugations which require thousands of atoms [49] while the mechanical properties of a h-BN sheet can be estimated by using DFT [243]. Conversely, atomistic simulations using molecular dynamics simulations (MD) enable to study thermo-mechanical properties directly on large scale samples. The modified Tersoff potential [118] (TP) (parameterized originally for carbon and silicon) with various set of parameters have shown to predict reasonable values for the thermo-mechanical properties of the h-BN sheet. In the pioneer work by Albe *et al* re-parameterized TP was used to study the impact of energetic boron and nitrogen atoms on a cubic-BN target [244]. Some other groups have also parameterized TP using various experimental data, e.g. Sekkal *et al* [245] treated h-BN as a one-component system, using the same potential parameters for both boron (B) and nitrogen (N) (neglecting the B-N interaction) to investigate the structural properties. Matsunaga *et al* [246] proposed the TP of B in order to simulate cubic boron carbonitrides which are compatible with the parameters of nitrogen fitted by Kroll [247], and recently, Liao *et al* [248] and Sevik *et al* [249] reported TP parameters that were used to study the mechanical properties and the thermal

conductivity of a h-BN sheet, respectively.

In this study, we investigate the thermal rippling behavior of free standing monolayer h-BN by using state of the art molecular dynamics (MD) simulations. We adopted the TP potential re-parametrized by Sevik *et al* which has been shown to represent the experimental structure and the phonon dispersion of the two-dimensional h-BN sheet. We found that h-BN is more corrugated and a less stiff material as compared to GE. The height-height correlations can be explained by the theory for continuum membranes [250]. In addition, we report results of both uniaxial and shear stress of a h-BN sheet and compare it with those found for GE. The buckling transition for compressed h-BN occurs earlier than for GE and the induced pattern of ripples when subjected to either uniaxial or shear stress shows significant differences.

6.2 Methods

Classical atomistic molecular dynamics (MD) simulation is employed to simulate large scale samples of h-BN and GE at temperatures varying from 10 K up to 900 K. We used a modified Tersoff potential (which is an ordinary defined potential in the LAMMPS package [216, 251]) according to the parameters proposed by Sevik *et al* for the h-BN sheet. All the parameters and a detailed description of the potential energy is given in Ref. [249]. To simulate GE we have used the AIREBO potential [252] which is suitable for simulating hydrocarbons. We employed NPT ensemble simulations with P=0 using the Nosé-Hoover thermostat which enables us to allow the size of the system to equilibrate (i.e. the size of the system is not fixed). All the reported values have been computed averaging over $300 - 400$ snapshots taken over uncorrelated samples.

We start with a square shaped h-BN sheet with periodic boundary conditions and initial dimensions 322 Å $\times$321 Å (315 Å $\times$315 Å for GE) in the x and y direction, respectively, which correspond to a total number of N=37888 atoms, and which are sufficiently large in order to capture the long-wavelength regime. Periodic boundary conditions were adopted in both directions.

To analyze the thermal ripples we computed the diffraction pattern which is typically studied in experiments to detect the size and shape of the corrugations [233]. We obtained also the mean square value of the out-of plane displacements $\langle h^2 \rangle$ of the atoms and, by following previous works [227, 253], the height-height correlation function $\langle H(q) \rangle$ which was determined by considering an average of the height between the first neighbors of each atom. The latter was shown to follow a q^{-4} behavior that is expected from the theory of continuum two-dimensional membranes at large values of q in the harmonic approximation (see below). To analyze the differences between the strain induced corrugations

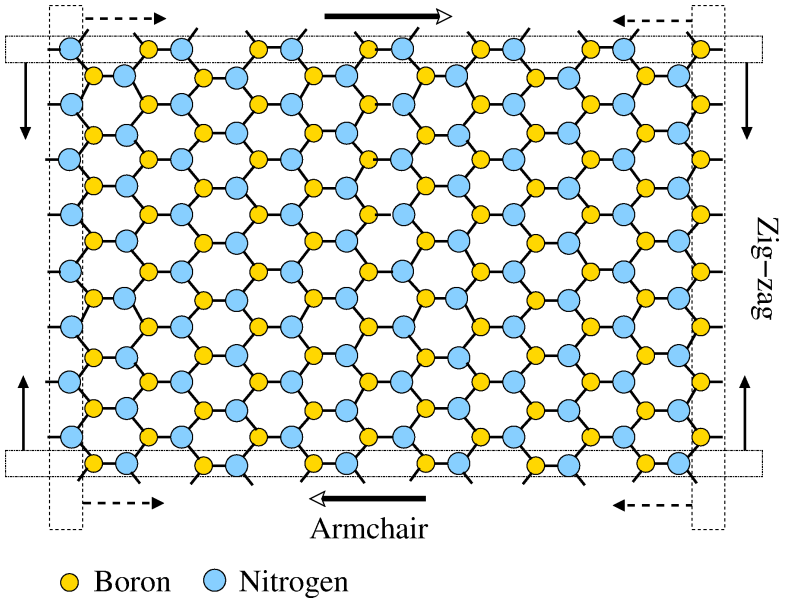

Figure 6.1: Schematic view of the single h-BN sheet. Smaller-yellow (bigger-blue) circles refer to the B (N) atoms. The rectangles indicate the atoms that are fixed during compression. Dashed (straight) lines correspond to arm-chair (zig-zag) uniaxial compression in the direction given by the arrows. Open arrows indicate the shear stress applied in the armchair direction.

in the h-BN and the GE sheets we applied uniaxial and shear stress on both systems as is schematically shown in Fig. 6.1. In order to apply strain we set the force on the two ends equal to zero and move the end atoms with an infinitesimal compression step ($\delta x = 0.01$) in the desired direction. After each compression step we wait for 2 ps to allow the system to relax and to ensure that the system is in thermal equilibrium [254]. Uniaxial compressive stress is applied along the zig-zag or armchair direction separately, and the shear stress is applied on the armchair edges with the opposite velocity for the top and bottom edges. The details of the used method of applying the boundary stress can be found in our previous studies [254–256]

The TP function [118] used in the LAMMPS package [216, 251] can be expressed as

$$E = \sum_i E_i = \frac{1}{2} \sum_{(i \neq j)} \phi(r_{ij}), \tag{6.1}$$

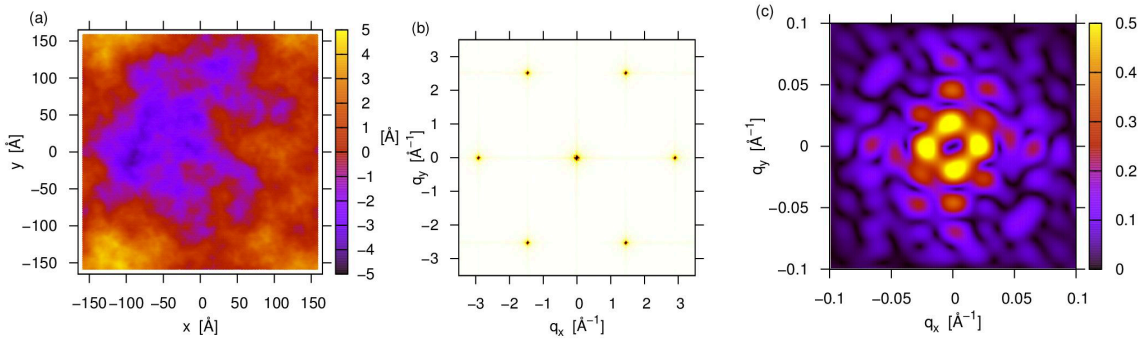

Figure 6.2: (a) Contour plot of the heights for an arbitrary snapshot taken during the MD simulation at 300 K. (b) Corresponding simulated diffraction pattern for the sample shown in (a). (c) Zoom view of (b) around $\mathbf{q}$=(0,0).

with

$$\phi(r_{ij}) = \sum_i \sum_{j(>i)} f_c(r_{ij})[f_R(r_{ij}) + b_{ij} f_A(r_{ij})], \tag{6.2}$$

where f_c, f_R and f_A are cutoff functions, the repulsive pair term, and the attractive pair term, respectively. r_{ij} and b_{ij} are respectively the distance from atom i to atom j and the bond order function. The use of TP disregard contributions coming from charge redistribution which may occur in an ionic crystal. The inclusion of this effect in h-BN modifies the phonon spectrum significantly only for energies corresponding to the optical modes [257, 258]. The large scale thermal ripples addressed here are governed mainly by the transversal acoustic mode (TA), which accounts for out-of-plane fluctuations, and it couples with the in-plane modes which renormalizes the long wave-length behavior, e.g. the bending rigidity κ can be calculated directly from the TA mode [259]. Therefore, the charge redistribution is expected not to affect the thermal fluctuations analyzed here and the use of the TP is justified [260].

6.3 Results and Discussion

6.3.1 Thermal excited ripples

In Fig. 6.2(a) we show a height contour plot of the atoms of the h-BN sheet for an arbitrary snapshot taken during the MD simulation at 300 K. The corresponding modeled diffraction pattern is shown in Fig. 6.2(b). This pattern is very similar to the one obtained for the GE sheet [233] with the main difference in the distance between the Bragg points due to the

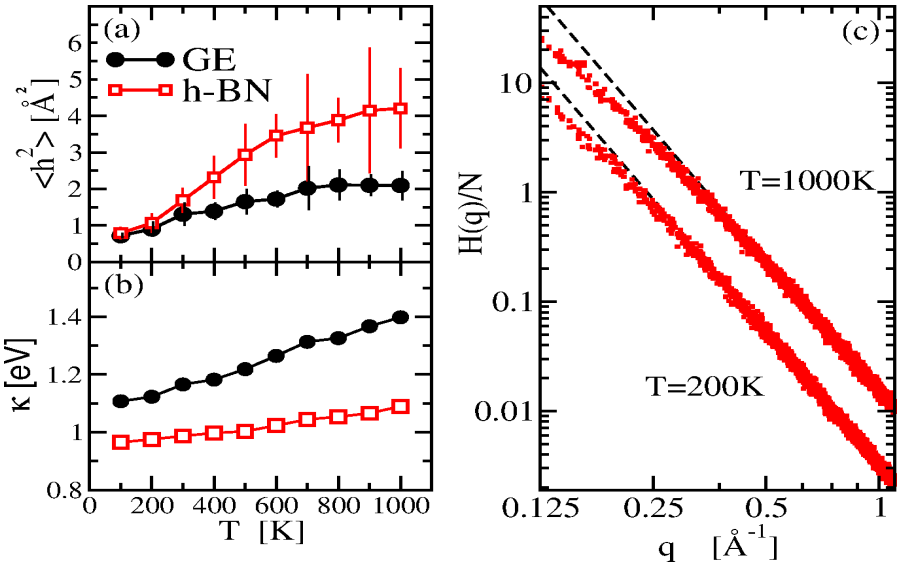

Figure 6.3: Variation of (a) $< h^2 >$ and (b) the bending rigidity versus temperature for both h-BN (open squares) and GE (solid circles). (c) Height-height correlation function $H(q)$ of h-BN at two different temperatures as is indicated. The dashed lines are the harmonic q^{-4} law.

unequal lattice constant of h-BN and GE. From the zoom plot around **q**=(0,0) (Fig. 6.2(c)) one observes the local structure of the central Bragg point for these intrinsic thermal ripples of h-BN. Notice that the lack of the presence of the **q**=(0,0) component is a consequence of the absence of a perfectly flat h-BN sheet.

The signatures of the thermal induced ripples can also be seen in the mean square value of the out-of-plane fluctuations $\langle h^2 \rangle$. In Fig. 6.3(a) we show $\langle h^2 \rangle$ as function of temperature. In comparison with GE (included also in this figure for comparative purposes) we observe that $\langle h^2 \rangle$ is always larger for the h-BN sheet. The weaker (stronger) the atomic B-N (C-C) bonds, the larger (smaller) the corrugations in h-BN (GE). Notice that the B-N bond is not pure covalent and it has an ionic character which is due to the different electronegativity between the two elements, i.e. the electrons are localized closer to the N atoms rather than the B atoms. Although this partially ionic structure of the h-BN layer increases the interlayer interaction resulting in a larger hardness of 3D bulk h-BN relative to graphite, it makes the single layer of BN less stiff than graphene. Moreover, the stacking

of h-BN sheets in bulk h-BN is AAA stacking which is different for the ABC stacking in graphite [184].

6.3.2 Bending rigidity κ

Accordingly to the two-dimensional theory of continuum membranes the height-height correlation function, in the harmonic approximation, where the out-of-plane and in-plane modes are decoupled, is expected to behave as

$$H(q) = \langle |h(q)|^2 \rangle = \frac{N k_B T}{\kappa S_0 q^4}, \tag{6.3}$$

where κ is the bending rigidity of the membrane, N is the number of atoms of the sample, S_0 the surface area per atom and k_B is the Boltzmann constant. In the large wavelength limit, i.e. for $q \rightarrow 0$, the height fluctuations are suppressed by anharmonic couplings between bending and stretching modes giving rise to a renormalized q-dependent bending rigidity and hence Eq. (6.3) is no longer valid [227, 253, 261]. In Fig. 6.3(b) we show κ for h-BN calculated from the harmonic part of $H(q)$ between q=0.5Å^{-1} and q=1 Å^{-1}. In agreement with the larger values of $\langle h^2 \rangle$, we observe that the h-BN membrane posses a smaller κ as compared to GE and in the whole temperature range it is about $16\ \%$ smaller at room temperature (300 K). Note that κ for both h-BN and GE increase with temperature. In Fig. 6.3(c) we show $H(q)$ at 200 K and 1000 K were the harmonic behavior can be clearly observed (fitted with a dashed line) and, as expected, with increasing temperature $H(q)$ is shifted to larger q. This figure also reveals that the ripples are not characterized by an unique wave-length and instead follows the behavior expected from continuum membrane theory.

Before ending this section it is worthwhile to investigate an alternative method to estimate the bending rigidity (flexural rigidity). A common method for calculating the bending rigidity of BN-sheet is by performing simulations of BN-nanotubes as a function of its radius (R) of the curved tubes and then extrapolating the results to R$\rightarrow \infty$. Hence, one can calculate the elastic energy of the nanotube as a function of the inverse square of the radius, $E = \frac{1}{2}\kappa R^{-2}$. This method was used in Ref. [25] and in our previous work [256] to calculate the zero temperature bending rigidity of GE and h-BN which were found to be 1.46 eV and 1.29 eV, respectively. The result obtained with the Tersoff potential using Eq. (6.3) is less than the result of Ref. [243]. The bending rigidity of GE is larger than h-BN with about 0.15 eV in agreement with Ref. [243]. In order to have an independent check we estimated the bending rigidity of a BN sheet by performing several ground state simulations for (n,n) BN-nanotubes with n=5,.., 20 using the Tersoff potential. Figure 6.4 shows the variation of the strain energy per atom as function of the inverse square radius

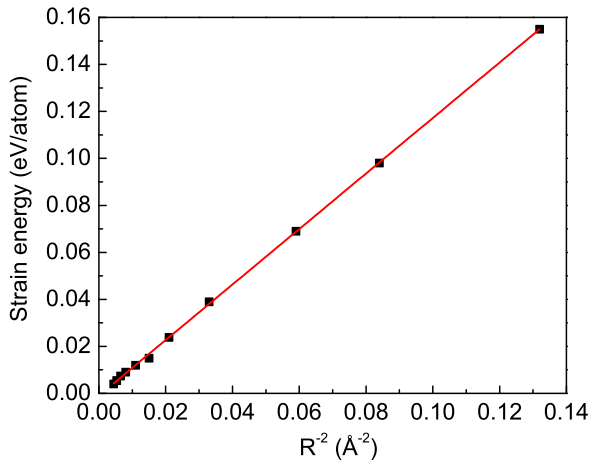

Figure 6.4: Variation of strain energy versus inverse square of BN-nanotube radius using Tersoff potential.

of the tube. Fitting a line to the data and dividing by the area of half of unit cell atom results in $\kappa = 0.86$ eV. The result of Tersoff potential agrees well with our estimation for κ using Eq. (3) (Ref. [25]). Thus we can conclude that result based on the Tersoff potential underestimate the bending rigidity as compared to the result from DFT.

6.3.3 Heat capacity, thermal expansion and Grüneisen parameter

The variation of the total energy per atom with temperature ($\geq 10K$) is shown in Fig. 6.5(a). The total energy varies linearly with temperature and gives the corresponding lattice contribution to the molar heat capacity at constant pressure (the average size of the system after relaxation is taken constant) which for the h-BN sheet results into

$$C_P = \frac{dE_T}{dT} = 25.2(3)\, J\, mol^{-1} K^{-1}, \tag{6.4}$$

which is comparable to the one for a GE sheet, i.e. 24.5(9) $J\, mol^{-1} K^{-1}$ and close to the well known classical molar heat capacity, i.e., $C = 3\Re \simeq 24.94\ J\, mol^{-1} K^{-1}$, i.e., the Dulong-Petit value, where $\Re$ is the universal gas constant. Notice that the heat capacity is a temperature dependent parameter that will decrease for temperature below the

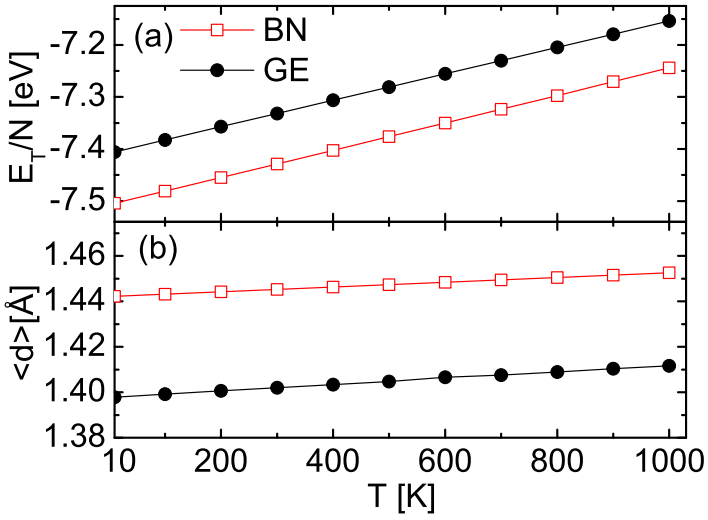

Figure 6.5: Variation of (a) the total energy per atom and (b) the averaged bond length versus temperature for h-BN and GE (The error bar is less than 10^{-4} eV/atom for the total energy).

Debye temperature. However, the classical MD simulation gives the correct high temperature asymptotic limit i.e., the Dulong-Petit value, but fails in the low and intermediate temperature range.

In Fig. 6.5(b) we show the variation of the averaged B-N bond length with temperature. The linear behavior enables us to calculate the linear thermal expansion of the lattice parameter of a h-BN sheet as

$$\gamma_{BN} = \frac{1}{a}\frac{da}{dT} = 7.2(1) \times 10^{-6} K^{-1} \tag{6.5}$$

where a=1.442 Å is the zero temperature lattice parameter. The obtained γ is 33% larger than the one measured for cubic BN, i.e. $4.8\times10^{-6}K^{-1}$ [262] and is comparable to the one found for GE, i.e. $\gamma_{GE} = 10.0(7) \times 10^{-6}\, K^{-1}$. The latter (i.e. γ_{GE}) is in good agreement with our previous studies [254, 255].

From the obtained values of γ and C we can compute the Grüneisen parameter

$$\alpha_{BN} = \frac{\gamma B}{C\rho} = 0.89, \tag{6.6}$$

where B is the two dimensional bulk modulus and ρ is the mass density. Using B_{h-BN}=3 eVÅ^{-2} (B_{GE} = 12.7 eVÅ^{-2} [263]), $\rho_{h-BN} = 24.82/S_{h-BN} = 3.81 \times 10^{-4}$g m^{-2} ($\rho_{GE}$ =

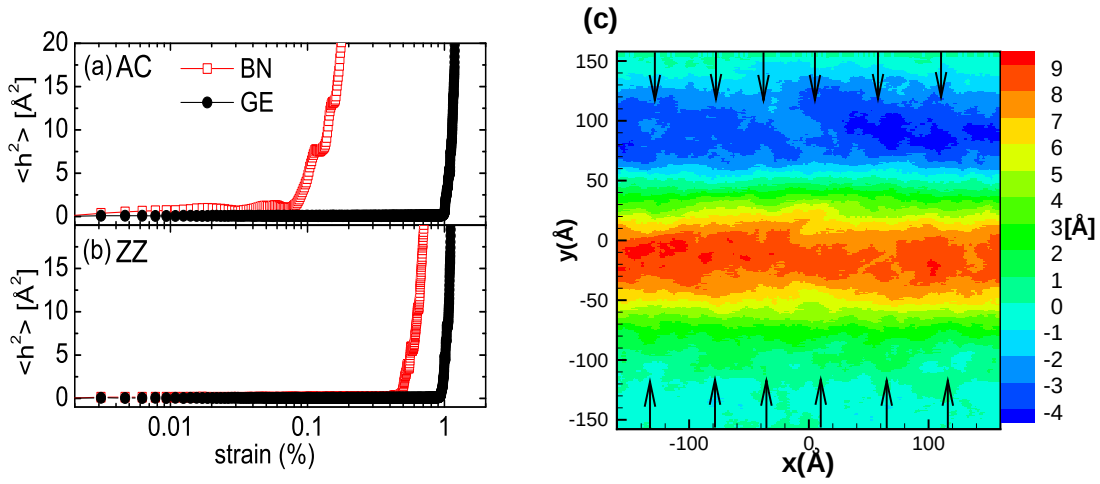

Figure 6.6: Variation of $< h^2 >$ versus external uniaxial strain in the (a) armchair and (b) zig-zag direction. Contour plot of the heights of compressed h-BN sheet samples subjected to a compressive strain for fixed $< h^2 >= 20$ Å^2 for compression in (c) zig-zag direction of the h-BN sheet. Arrows indicate the stress direction.

7.6×10^{-4}g m^{-2}) for h-BN (GE), we obtain $\alpha_{BN} = 0.89$ (α_{GE}=1.2). Note that the estimated value of α_{GE} is better than the one found in Ref. [264], i.e. -0.2, and is closer to the experimental result, i.e. 2.0 [265].

6.3.4 Buckling transition

The different stiffness between the h-BN and GE sheets results in different buckling transitions. To study this, we compressed the systems uniaxially where we considered both zig-zag and armchair directions. This was done by fixing one row of atoms in each edge during the compression steps as is indicated schematically in Fig. 6.1. The compression rate was taken $\mu = 0.5m/s$ which is similar to the one used in our previous study [255], and small enough to guarantee that the system is in equilibrium during the whole compression process [266]. The simulations were carried out at room temperature. Figure 6.6(a) shows the variation of $< h^2 >$ versus strain, i.e. $\epsilon = \mu t/l$ where t is the time (after starting the compression) and l is the initial box length in the direction of the compression. The buckling transition for the h-BN sheet kept at room temperature is found to be 0.6 (0.1) which is smaller than the one for GE, i.e. 1.0 (1.2), for uniaxial compression along the zig-zag (armchair) direction. Hence, when the compression is applied in the zig-zag di-

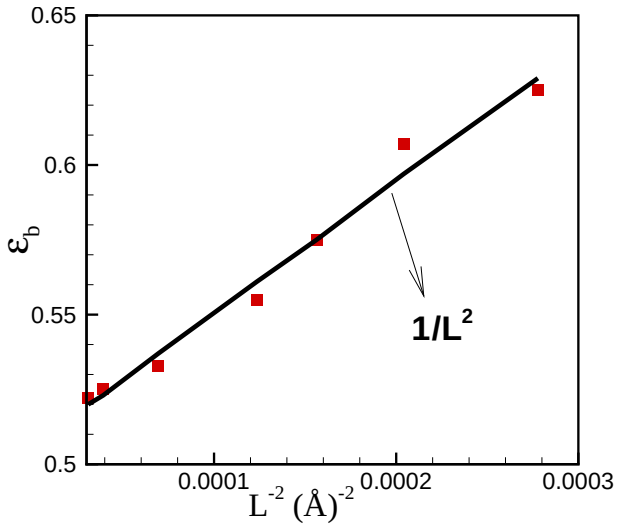

Figure 6.7: Variation of buckling strain with the longitudinal length of the BN sheet which is compressed along the zig-zag direction.

rection, the h-BN sheet resists much more against the external uniaxial stress as compared to the case the stress is applied along the armchair direction. The smaller critical strain at which the buckling transition in the armchair direction of the h-BN sheet takes place indicates its more sensitive nature to external uniaxial stress [267]. Although the same argument holds for GE, the difference between the two directions is much smaller. Notice that DFT calculations result in a deviation in bending rigidity (flexural rigidity) between ZZ BN-nanotube and AC BN-nanotube (ZZ becomes larger than AC) for radius smaller than $\simeq 3$ [25] while for larger radius they are the same.

A contour plot of the buckled h-BN sheet with $\langle h^2 \rangle$=20 Å^2 and compressed in the zig-zag direction is shown in Fig. 6.6(c). The obtained buckling transition for GE, i.e. 0.8%, agrees very well with our previous studies [254] and is in the range of the experimental measured buckling transition for suspended GE, i.e. 0.5%-0.7% [268, 269].

It is also interesting to compare the buckling strain with those predicted by the theory of loaded beam. Euler theory for a two end-loaded beam having length L predicts that $\epsilon_b \propto L^{-2}$ [255, 270]. The first demonstration by MD of Euler buckling in nanostructures goes back to the pioneer work by Yakobson *et al* [271]. We performed several simulations in order to find the length dependence of the buckling strain for BN sheets which are e.g. compressed along the zig-zag direction. Figure 6.7 shows the variation of ϵ_b with the longitudinal length (L) of the zig-zag BN sheet. The solid line is a fit to L^{-2} and the symbols are the results of our MD simulations which are qualitatively in agreement with

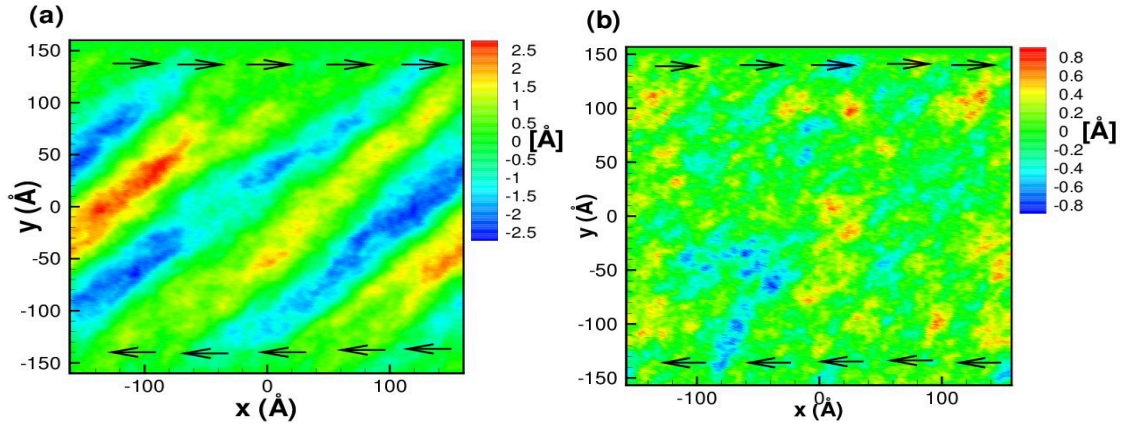

Figure 6.8: Effect of a shear stress of about 1.5 $\%$ on the out-of-plane deformation of (a) the h-BN sheet and (b) the graphene sheet. Arrows indicate the stress direction on the armchair edges. Note the larger values of the heights in h-BN.

the theory of loaded beam.

Finally, we report the results for h-BN and GE sheets under shear stress. Here we applied the stress only in the armchair direction as is described schematically in Fig. 6.1. We found that, due to the larger stiffness, to reach the same value of $\langle h^2 \rangle$ a larger shear stress has to be applied in GE as compared to h-BN. In Figs. 6.8(a,b) one can observe significant differences between the corrugated configurations of h-BN and GE sheets. These samples were subjected to a shear stress of $\epsilon = 1.5\%$. While h-BN is highly sensitive to shear stress and deforms easily, GE can resist larger stress values due to its larger rigidity.

6.4 Conclusions

The thermal properties of a boron nitride sheet were studied using large scale atomistic simulations. We showed that the scaling properties of a h-BN sheet follows closely the results of membrane theory and hence the thermal excited ripples are not characterized by any particular wave-length. Using the harmonic part of the height-height correlation function we found an increasing bending rigidity with temperature which is smaller than the one of graphene. We found that the buckling transition for h-BN depends on the applied compression direction and is much smaller than the one of graphene. The obtained molar heat capacity agrees very well with the well-known Dulong-Petit number, 25.2 $J\ mol^{-1}K^{-1}$ and the thermal expansion coefficient was found to be positive and

equal to 7.2 $\times 10^{-6} K^{-1}$. The Grüneisen parameter 0.89 is found to be smaller than the one for graphene, i.e. 1.2. We showed that the different stiffness between the GE and h-BN sheets leads to different patterns of deformations in the presence of either uniaxial or shear stress.

CHAPTER 7

Thermal properties of fluorinated graphene

Large scale atomistic simulations using the reactive force field approach (ReaxFF) are implemented to investigate the thermomechanical properties of fluorinated graphene (FG). A new set of parameters for the reactive force field potential (ReaxFF) optimized to reproduce key quantum mechanical properties of relevant carbon-fluor cluster systems are presented. Molecular dynamics (MD) simulations are used to investigate the thermal rippling behavior of FG and its mechanical properties and compare them with graphene (GE), graphane (GA) and a sheet of BN. The mean square value of the height fluctuations $\langle h^2 \rangle$ and the height-height correlation function $H(q)$ for different system sizes and temperatures show that FG is an un-rippled system in contrast to the thermal rippling behavior of graphene (GE). The effective Young's modulus of a flake of fluorinated graphene is obtained to be 273 N/m and 250 N/m for a flake of FG under uniaxial strain along arm-chair and zig-zag direction, respectively.

7.1 Introduction

The fascinating properties of single layer graphene (GE) have triggered a broad interest in the solid state physics community [1, 6, 272–274]. Despite its high electron mobility [2],

The results of this chapter were published as
Sandeep Kumar Singh, S. Goverapet Srinivasan, M. Neek-Amal, S. Costamagna, Adri C. T. van Duin, and F. M. Peeters, Phys. Rev. B **87**, 104114 (2013).

the zero band gap defies its employment in nano transistors where it is desirable to have a large on-off ratio between conducting and non-conducting states. A band gap can be induced by the addition of adatoms, which changes locally the hybridization of the carbon (C) atoms, but also modifies the electron mean free-path affecting the electron transport properties. Hydrogen (H) and fluor (F) are two well tested candidates [57, 58, 86, 208] that leads to a large band gap opening. Graphane (GA, hydrogenated graphene) and fluorographene (FG) have been studied both experimentally and theoretically [59, 64, 209, 213] to engineer the band gap.

When H or F atoms are attached to the C atoms of GE, the bonds transit from an sp^2 to an sp^3 hybridization, which turns the conjugated graphitic C-C bonds into single C-C bonds. In the fully covered cases both GA and FG are insulating materials [57, 86] and the structure changes locally the planar shape of GE into an angstrom scale out-of-plane buckled shaped membrane [275] known as *chair configuration* [206, 276].

From its potential applications in nanotechnology, FG is a more favourable material than GA since the C-F bonds are energetically more stable than the C-H bonds [59, 206, 275, 277]. Fluorographene has a very large temperature-dependent resistance and when the fluor content is increased it induces large changes in the electron transport [278]. As in GE, it is expected that temperature also affects strongly the lattice structure and the mechanical properties of FG.

According to the Mermin-Wagner theorem, [18], thermal excited ripples in two dimensional like materials (GE, bilayer GE, GA and FG) has to play an important role in the stability of the membrane. While in GE and bilayer GE the corrugations are well described within the theory of two dimensional continuous membranes [233, 234, 279], for GA instead, we recently found that the angstrom scale buckling of the carbon layer of GA prevents the formation of intrinsic long wavelength thermal ripples for temperatures up to at least 900 K [210].

Since the C atom has a higher (lower) electronegativity than H (F), it will take (give) away charge from the H (F) atom and consequently transforms the resulting C-H and C-F covalent bonds into sp^3 bonds. Therefore, it is expected that similar rippling effects as in GA will occur in FG although the C-F bonds are somewhat stronger than the C-H bonds. The latter is due to the larger amount of charge that is shifted from C to F as compared to the one from H to C [59]. However in order to simulate large scale FG samples an appropriate force field is needed which describes the true chemical bond in C-F. Indeed, the absent of such a suitable interatomic potential for C-F restricted most of the recent studies to ab-initio calculations of their electronic properties using a small computational unit cell.

ReaxFF potential serves to describe both bond and non-bond interactions in solids. Recently, such potentials were parameterized and were well tested for different kind of struc-

Table 7.1: Comparison of equilibrium geometrical parameters between ReaxFF and DFT.

	DFT	ReaxFF
F_2 bond length	1.43Å	1.4012Å
C-F bond length in H_3C-CF_2-CH_3	1.3841Å	1.4057Å
C-F bond length in H_3C-$CF(CH_3)$-CH_3	1.3841Å	1.4158Å
Non-bonding C-F distance in CF_2 dimer	2.00 Å	2.4471Å
F-C-F angle in H_3C-CF_2-CH_3	105.65^o	107.2197^o
C-C-F angle in H_3C-$CF(CH_3)$-CH_3	106.2^o	109.9625^o

tures, e.g. hydrocarbons [119], carbon allotropes [280], etc. In this chapter we present a new set of parameters for ReaxFF, appropriate for structures with C-F bonds. Using molecular dynamics (MD) simulations over large scale samples we study the thermal corrugations of FG and compare the results with those found for GA, GE and BN. We show that fully covered FG follows the same trend as GA and does not develop long-wavelength ripples or significant corrugation. The bending rigidity κ of FG is found to be larger than the one of GE, GA and BN. Furthermore, κ turns out to be temperature independent. Our results indicate that long-wavelength ripples are instead present in partial covered FG samples with a larger amplitude as compared to GA.

7.2 ReaxFF potential for Fluorographene

ReaxFF [119] is a general bond-order dependent potential. A brief discussion of this potential is presented in chapter 2.

The reactive force field for C/F containing systems was developed by parameterizing the potential against DFT data obtained at the B3LYP/6-31g** level of theory (which is implemented in Schrodinger [281] which is an electronic structure packages) for various quantities such as fluorine and carbon atom charges in $H_3C{-}CF_2{-}CH_3$, C−F and C−C bond lengths in $H_3C{-}CF_2{-}CH_3$ and $H_3C{-}CF(CH_3){-}CH_3$, F−F bond length in the F_2 molecule, potential energy curve for C-F bond dissociation in $H_3C{-}CF_2{-}CH_3$, F-C-F angle bending in $H_3C{-}CF_2{-}CH_3$, C-C-F angle bending in $H_3C{-}CF_2{-}CH_3$ and F-C-C-F dihedral twisting in $F_2C{=}CF_2$ along with various chemical reactions involving fluoroalkanes and fluoroalkenes. The results of the force field training are presented in Figs. 7.1(a)-(d) and in Table 7.1. Fig. 7.2 depicts the geometrical quantities relevant to Figs. 7.1(a)-(d). It can be seen from Table 7.1 that ReaxFF reproduces closely the DFT based equilibrium ge-

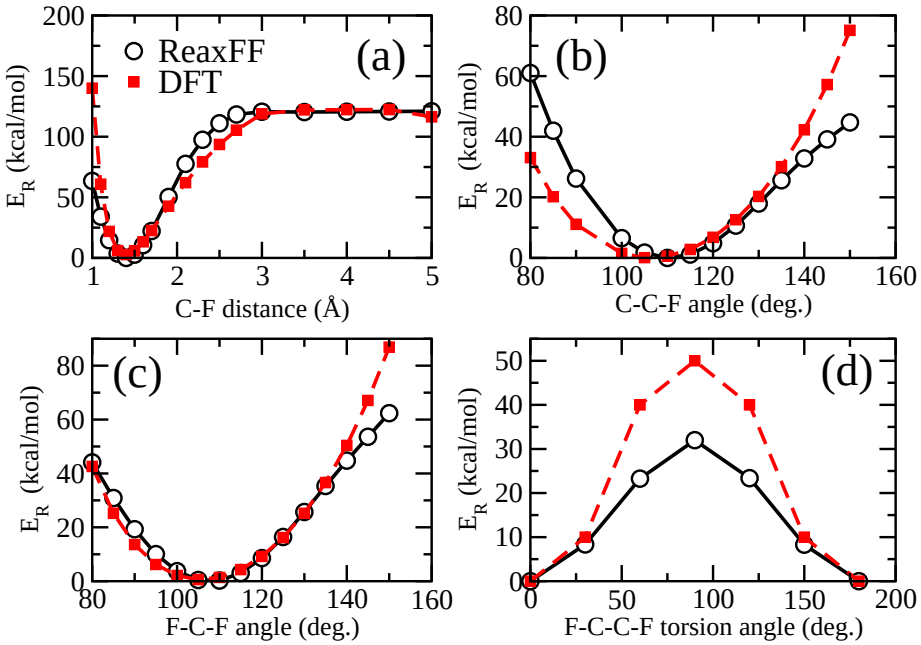

Figure 7.1: Comparison between DFT (solid squares) and ReaxFF (open circles) results for: (a) C-F bond dissociation in H_3C-CF_2-CH_3 (b) C-C-F angle bending in H_3C-$CF(CH_3)$-CH_3, (c) F-C-F angle bending in H_3C-CF_2-CH_3 ,and (d) F-C-C-F dihedral twisting in F_2C=CF_2.

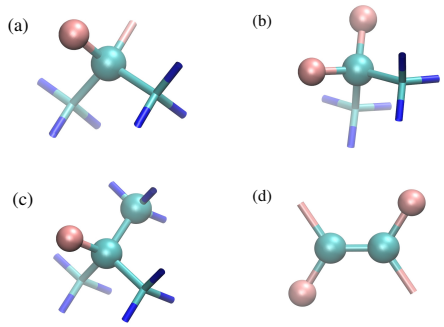

Figure 7.2: The molecules used for parameterizing the ReaxFF force field in this study. (a) C-F bond in H_3C-CF_2-CH_3 (b) F-C-F angle in H_3C-CF_2-CH_3 (c) C-C-F angle in H_3C-$CF(CH_3)$-CH_3, and (d) F-C-C-F dihedral angle in F_2C=CF_2. The atoms constituting the geometric parameters are represented by balls while the rest of the atoms are represented by sticks. F atoms are colored brown, C atoms are colored green and H atoms are colored blue.

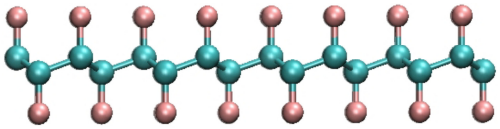

Figure 7.3: Side view of the buckled structure, known as chair configuration, of fully fluorinated graphene. The averaged bond-angle, and C-C and C-F distances, are respectively 109.5°, d_{C-C} =1.58 and d_{C-F} =1.41 at room temperature.

ometries for various compounds. ReaxFF predicts F_2 dissociation energy of 36.6 kcal/mol, in very good agreement with the DFT value of 37 kcal/mol. Fig. 7.1(a) shows that ReaxFF based potential energy curve for the C-F bond dissociation in $H_3C{-}CF_2{-}CH_3$ closely follows the DFT based potential energy curve. ReaxFF is able to predict very precisely the equilibrium C-F bond length (see Table 7.1) and the C-F bond dissociation energy. Similarly the force field can closely reproduce the DFT based potential energy curve and the equilibrium geometry (see Table 7.1) for C-C-F angle bending and the C-F-C angle bending as shown in Figs. 7.1(b)-(c). Figure 7.1(d) shows the variation of the potential energy upon F-C-C-F dihedral angle twisting. Though ReaxFF predicts the correct trend, the torsional rotation barrier in ReaxFF is around 18 kcal/mol lower than that predicted by DFT. Overall, the ReaxFF force field for C/F systems can closely reproduce the DFT based energies and geometries for a number of molecules and reactions. This force field

will now be employed in large scale fully reactive molecular dynamics simulation of C/F containing systems.

In the next section we study the thermal structural fluctuations and mechanical properties of a single layer of FG using large scale atomistic simulations employing the presented ReaxFF parameters. These parameters were implemented in the large-scale atomic/molecular massively parallel simulator package LAMMPS [216, 251].

7.3 Results

7.3.1 Thermal rippling behavior of FG

In order to study the rippling behavior of FG we considered a square shaped computational unit cell of FG with both armchair and zigzag edges in the x and y directions. Partial fluor contents of 10%, 50%, 70%, 90% and the fully covered 100% case (with a total number of $N = 17280$ atoms) were studied. In our simulation we employed the NPT ensemble with P=0 using the Nosé-Hoover thermostat and varied the temperature from 10 K to 900 K. Figure 7.3 shows the obtained buckled shape of fully fluorinated sample after relaxation which is in agreement with recent DFT results [59].

One would expect that the thermal excited ripples in FG can be described by membrane theory for a 2D continuous membrane [250]. This theory, described in a series of related works [20, 210, 227, 282], is supposed to be universal and independent of the atomic scale details of the membrane. The main predictions of this theory are as follows. Let h be the out-of plane displacement of a given atom of a sheet, then the Fourier transform of the height-height correlation function is in the harmonic approximation given by

$$H(q) = \langle |h(q)|^2 \rangle = \frac{N k_B T}{\kappa S_0 q^4} \ , \tag{7.1}$$

where q is the wave-vector, N is the number of atoms, S_0 is the surface area per atom, κ is the bending rigidity of the membrane, and k_B is the Boltzmann constant.

In the large wavelength limit, anharmonic couplings between bending and stretching modes are important resulting in a renormalization of the q-dependent behavior

$$H(q) = \frac{N k_B T}{\kappa S_0 q^{4-\eta}} \tag{7.2}$$

where η is an universal scaling exponent which is about ≈ 0.85 [253, 261, 283].

In order to compare our results for FG with other two dimensional materials, we used a modified Tersoff potential (which is an ordinary defined potential in the LAMMPS package [216]) according to the parameters proposed by Sevik *et al* for the h-BN sheet [[249]].

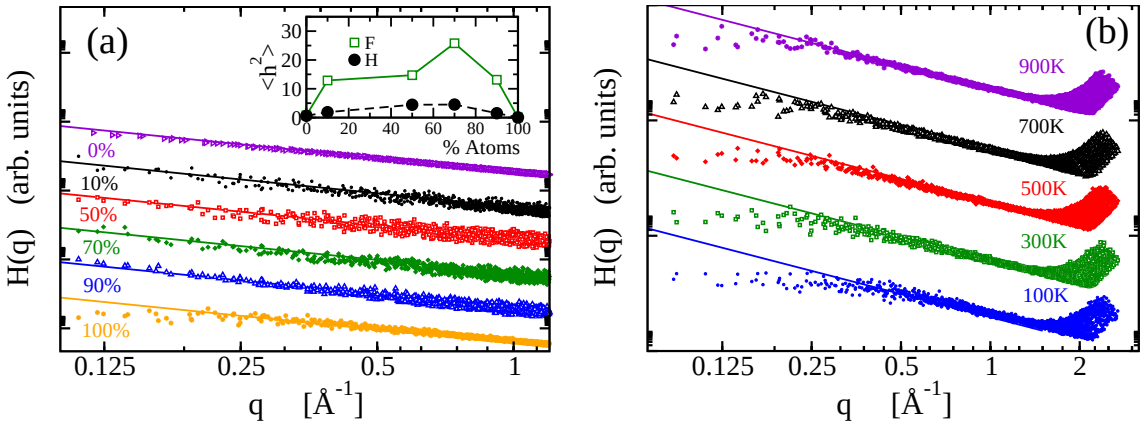

Figure 7.4: (a) Log-log plot of $H(q)$ for different coverage of F atoms at T=300 K. The solid lines show the harmonic q^{-4} behavior valid in the limit of large q values. Note the strong deviation, starting roughly at $q^* \approx 0.2^{-1}$ in the limit of long wave-lengths, for the case of fully fluorinated graphene. The variation of $\langle h^2 \rangle$ is shown in the inset. (b) $H(q)$ for fully fluorinated FG at different temperatures.

To simulate GE and GA we have used the AIREBO potential [252] which is suitable for simulating hydrocarbons.

Recently, we found that in GA, $H(q)$ acquires a strong renormalization for small wave-vectors q and the layer remains almost flat even for temperatures as high as 900 K [210]. Here we will analyze the thermal rippling behavior of FG and compare it with GA. A comparison with GE and BN single layers which behave as 2D membranes [20, 226] will also be presented. $H(q)$ for FG was calculated following the steps described in our previous work [210].

Starting from a pure GE sheet, the variation of the height-height correlation function $H(q)$ at room temperature for different partial fluor contents is shown in Fig. 7.4 (a). The curves were shifted for a better comparison. We found that while for 10 to 90% coverage, $H(q)$ follows Eq. (7.2) up to small $q-$values which is similar to the case of GE [227]. But, for fully FG at $q^* \approx 0.2$ Å^{-1}, $H(q)$ deviates from the harmonic law (solid line) and approaches roughly a constant value similar to was previously found for GA [210]. In the inset of Fig. 7.4(a) we show the square average of the out-of-plane fluctuations $\langle h^2 \rangle$ at 300 K. Notice that the out of plane fluctuations for partially covered samples are considerably larger for FG than for GA. The temperature dependence of $H(q)$ for fully fluorinated graphene is shown in Fig. 7.4(b). Irrespective of temperature, the short wave-length limit of $H(q)$ tends always approximately to a constant value. The characteristic q-value where $H(q)$ deviates from the harmonic approximation result decreases with increasing temper-

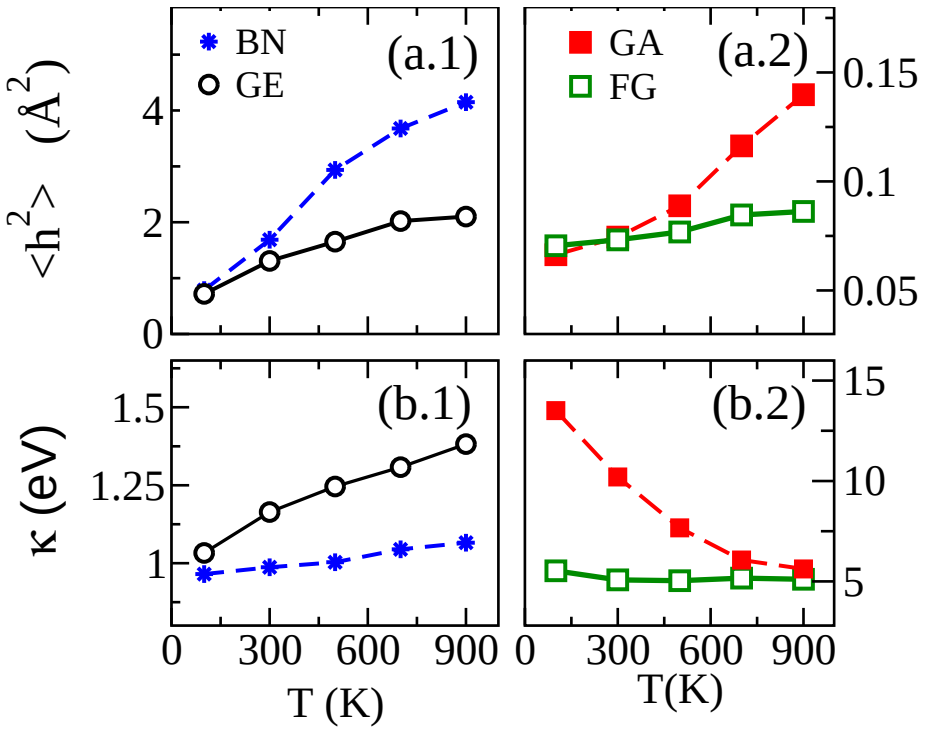

Figure 7.5: Variation of (a) $\langle h^2 \rangle$, and (b) κ against temperature for FG (open squares), GA (filled squared), GE (open circles), and BN (stars).

ature.

The renormalization of $H(q)$ for long wavelengths indicates the suppression of large out-of-plane height fluctuations. In Fig. 7.5(a) we compare the behavior of $\langle h^2 \rangle$ against temperature for GE, BN (panel (a.1)), FG and GA (panel (a.2)). Notice that $\langle h^2 \rangle$ increases from 0.7 Å^2 up to 4 Å^2 in BN and from 0.7 Å^2 up to 2 Å^2 in GE when temperature is varied from $10\ K$ up to 900 K. Due to the absence of long wave-length ripples, $\langle h^2 \rangle$ remains approximately constant for GA and FG, and the variations are smaller than those for BN and GE, over the same temperature range. The temperature dependence of the bending rigidity κ, computed from the harmonic part of H(q) is shown in Fig. 7.5(b). Note that the larger magnitude for GA and FG is a consequence of the smaller corrugations present in these materials. We also find the opposite temperature dependence for BN and GE when compared with GA and FG. In this sense GE and BN behave anomalously. The corresponding bending rigidity and $\langle h^2 \rangle$ at room temperature for GE, GA and FG are listed in Table 7.2.

Density functional calculations for band structure of FG (and GA) [284] shows that

Table 7.2: Comparison of AIREBO and ReaxFF for the bending rigidity and $\langle h^2 \rangle$ for GE, GA and FG at 300 K.

	AIREBO		ReaxFF	
	$\kappa(eV)$	$\langle h^2 \rangle (\text{Å}^2)$	$\kappa(eV)$	$\langle h^2 \rangle (\text{Å}^2)$
GE	1.165	1.307	1.16	0.627
GA	10.19	0.070	7.26	0.074
GF	–	–	5.07	0.073

the acoustic out-of-plane modes (ZA) in FG (and GA) are different from that of GE. The most important difference from GE is the decoupled optical and acoustic bands in FG and GA close to the Γ point. The light H atom contributes to the highest phonon frequencies which is not the case for F atoms. It is also seen that the ZA modes close to the Γ point for FG (and GA) are not well fitted by a quadratic function in contrast to the GE case. This is clear indication of anharmonicity. In summary, the atomistic details of the structure of FG is more complicated and therefore more details of this structure should be included in any continuum theory.

Before ending this section, note that as we discussed in our previous work [210], the scaling with the system size present in GE is no longer valid for FG and GA ($\langle h^2 \rangle$ in FG and GA is almost constant irrespective to the system size). The lower wavelengths (q) adopted for the calculation of $H(q)$ are equal to $q_{x-min} = \dfrac{2\pi}{l_x}$ and $q_{y-min} = \dfrac{2\pi}{l_y}$ and represent the 'computational' cut-offs of possible large wavelength ripples where l_x and l_y are the dimension of the system. Notice that deviation from the harmonic behavior takes place at larger value of q and hence this effect can not be a finite size effect and is instead an intrinsic phenomenon of the material.

7.3.2 Effective Young's modulus

In order to study the mechanical stiffness we consider a FG flake with dimension $l_x \times l_y = 15 \times 15\,\text{nm}^2$. Before the stretching process, the sample is equilibrated for 5 ps (i.e. 50,000 time steps). Stretching direction is always along x and the uniaxial strain is applied within the NPT ensemble [285] where the pressure is slowly increased, i.e. 2 GPas/ps. For the lateral edges in the y direction (taken as the arm-chair directions), we used both free (FBC) and periodic boundary conditions (PBC). We kept temperature fixed at T=10 K.

The total strain energy per atom of the strained flake can be written as a function of the

imposed strain (ϵ)

$$E_T(l_y, \epsilon) = E_0 + \frac{S_0}{l_y}\gamma(\epsilon) + \frac{S_0}{2}Y\epsilon^2 \tag{7.3}$$

where E_0 is the energy of the infinite planar undeformed flake, $\gamma(\epsilon)$ is the excess edge energy, and Y is Young's modulus (Y) of the flake.

For nano-ribbons with no lateral edges we have $\gamma = 0$ (assuming that the longitudinal edges which are fixed make no contribution). This is due to the fact that free edges increase the energy due to buckling and bond-order changes [286]. Recently Lu *et al* used the Brenner potential [116] in molecular dynamics simulations and studied the excess edge energy of graphene nano-ribbons as a function of width and chirality [286]. Our systems are different from those of Ref. [286]. In contrast to Ref. [286] we are not interested in effects due to the edge energy effect and the size dependence. We effectively rewrite Eq. (7.3) in the following which qualitatively gives a good description of the mechanical stiffness of all the examined 2D materials. Nevertheless our results are in qualitative agreement with those reported by Lu *et al.*, i.e. increasing of total energy for the FBC case as compared to a nano-ribbon. Assuming a quadratic relation for $\gamma(\epsilon) = \frac{l_y}{2}\epsilon^2$ valid for small ϵ, the simplest method to estimate Young's modulus is by fitting the quadratic function to the total energy (per area):

$$E_T = E_0 + \frac{1}{2}Y_{eff}\epsilon^2, \tag{7.4}$$

where Y_{eff} is the effective Young's modulus of the system. Using aforementioned fitting process we found Y_{eff} respectively for a flake with arm-chair and zig-zag FG, to be 273 N/m and 250 N/m. Notice that the experimental result is 100 N/m for not perfect FG [57] while the DFT result is 250 N/m [277]. The latter disagreement between theory and experiment may be explained due to the fact that in experimental samples the fluor-to-carbon ratio is larger than unity, i.e. 1.1 [57], because of the presence of defects. Such defects become active regions which can adsorb the free F (and even H) atoms. Therefore, in the defected parts more F atoms will be found which is responsible for a F/C ratio larger than one.

In order to understand the effect of the different boundary conditions, we depict in Fig. 7.6 the variation of E_T per atom with ϵ for flakes with both FBC (dashed lines) and PBC, i.e. nano-ribbon (solid lines). It is seen that for flakes with FBC the free edges result in an increase of the energy. The inset shows the difference between two curves, i.e. $\Delta E_T = E_{FBC} - E_{PBC}$ which is positive. Because the free boundaries have many dangling bonds which are not saturated by F atoms it results in extra energy. This can also occur in other systems, e.g. graphene [205]. Notice that for the studied low temperature here, i.e. T=10 K we do not expect that bond reconstruction at the edges is important.

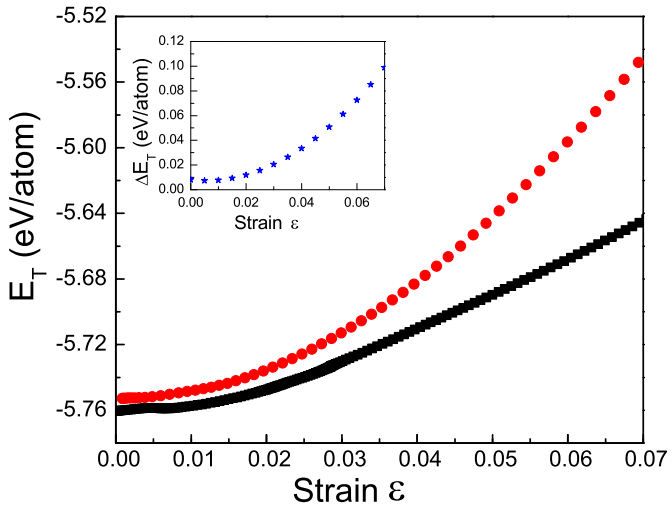

Figure 7.6: (a) Variation of total energy against uniaxial strain for FG subjected to free boundary condition (FBC) and periodic boundary condition (PBC) for the lateral edges, i.e. the dashed and solid curves respectively. The inset shows the difference between the two energy curves.

Notice that even by saturating all the bonds by F, still the change in the bond order term in ReaxFF (due to different chemical environment of the boundary atoms) results in higher energy as compared to PBC.

Furthermore, both FBC and PBC results exhibit a quadratic behavior which is an indication of the harmonic regime for the applied uniaxial strain. As is clear from the inset of Fig. 7.6, the difference between the two curves is increasing with applied strain. This is due to the deviation from equilibrium for the C-F bonds, C-C-F (F-C-F) bond angles, and the dihedral angles (F-C-C-F torsion angle) of the free edge atoms. The larger the strain (and the larger the length of ribbon), the larger the deviation from equilibrium for the bonds and the angles. In the PBC case there is no such edge effect but nevertheless because of the fixing of the two longitudinal ends (the edges which are under uniaxial stress) the energy variation of the PBC system should be different from that of an infinite FG which is periodic in both directions while it is under tension from the arm-chair direction. The fixed longitudinal ends do not have any effect in our results because both FBC and PBC have the same contributions.

7.4 Conclusions

We provided a new set of parameters for the ReaxFF potential for the C-F covalent bond and tested it on various molecules. Subsequently, molecular dynamics simulations were used to investigate the thermal rippling behavior and the mechanical response of fluorographene (FG) under uniaxial stress. The obtained results are compared with those for graphene (GE), graphane (GA) and hexagonal boron nitride sheet (h-BN). We found that fluorographene remains a flat sheet similar to graphane even at high temperature, i.e. up to 900 K. The bending rigidity of FG is found to be independent of temperature and its Young's modulus is in good agreement with experiment.

CHAPTER 8

Electronic properties of graphene nano-flakes

The electronic properties of graphene nano-flakes (GNFs) with different edge passivation is investigated by using density functional theory. Passivation with F and H atoms are considered: C_{N_c} X_{N_x} (X=F or H). We studied GNFs with $10 < N_c < 56$ and limit ourselves to the lowest energy configurations. We found that: i) the energy difference Δ between the highest occupied molecular orbital (HOMO) and the lowest unoccupied molecular orbital (LUMO) decreases with N_c up to N_c=35 and is almost constant beyond it, ii) topological defects (pentagon and heptagon) break the symmetry of the GNFs and enhance the electric polarization, iii) the mutual interaction of bilayer GNFs can be understood by dipole-dipole interaction which were found sensitive to the relative orientation of the GNFs, iv) the permanent dipoles depend on the edge terminated atom, while the energy gap is independent of it, and v) the presence of heptagon and pentagon defects in the GNFs results in the largest difference between the energy of the spin-up and spin-down electrons which is larger for the H-passivated GNFs as compared to F-passivated GNFs. Our study shows clearly the effect of geometry, size, termination and bilayer on the electronic properties of small GNFs.This study reveals important features of graphene nano-flakes which can be detected using Raman spectroscopy.

The results of this chapter were published as
Sandeep Kumar Singh, M. Neek-Amal, and F. M. Peeters, J. Chem. Phys. **140**, 074304 (2014).

8.1 Introduction

Graphene nano flakes (GNFs) and graphene nano ribbons (GNRs) are promising graphene based materials with a size controllable energy band gap, which may be useful for different technological applications [2, 30]. In particular, these graphene nano-flakes are important due to their potential for bottom-up fabrication of molecular devices, spintronics and quantum dot technology [103]. Bottom-up and top-down approaches are two alternatives for the production of GNFs. In the first approach, large aromatic hydrocarbons are produced using a large variety of chemical reactions between small molecular units [26, 287]. The top-down method starts with a large piece of graphene sheet and cuts the GNFs out of it. Single graphene sheets can be obtained by a variety of methods, e.g. micromechanical cleavable of a graphite single crystal [1], starting from graphite oxide [288] or by chemically unzipping of carbon nanotubes [28].

Tight-binding (TB) approximation based on the π orbitals of carbon, the free massless particle Dirac's equation and ab-initio calculations are three common theoretical methods for studying the electronic and magnetic properties of GNFs and GNRs. Similar to TB calculations [289] or solutions of the Dirac equation, [290] ab-initio calculations also show that the GNRs have a non-zero direct band gap [291]. Already several studies have appeared on the electronic and magnetic properties of small GNRs using various methods [103, 292–297]. However much less extensive and systematic studies are available on various properties of the GNFs, e.g. the size, edge termination and polarization are still poorly understood. Using tight-binding calculation and Hartree-Fock theory the energy gap dependence of triangular and hexagonal GNFs on size, shape and edge were studied by Güçlü et al. [298]. It was found that triangular GNFs with zigzag edges exhibit optical transitions in wide spectral ranges, i.e. from teraHertz up to the UV. Because of the small size of the GNFs, they can be considered as a zero-dimensional form of graphene which exhibit very different properties from GNRs and bulk graphene. They are promising for a variety of applications, e.g. electronic and magnetic devices with various molecular sizes and shapes. Graphene nano flakes (graphene quantum dots) can be useful for light absorption relevant for photovoltaics due to their edge structure and wide spectrum. GNFs are found to possess unique electronic, magnetic, and optical properties due to their tunable band gap, e.g., they can be used in solar cells and light-emitting diode LED technology [299]. They have different corners, mixed zig-zag and arm-chair edges which provide additional degrees of engineering freedom. The small size of GNFs leads to discrete energy levels similar to atomic levels in single atoms. The saturation with different atoms or molecular groups on the zigzag edges of rectangular GNFs leads to a spin-polarized ground state with a non zero total magnetic moment, a spin density, and an electronic energy gap that strongly depends on the atomic group used to passivate the dan-

gling bonds [300]. First-principles calculations were also used to investigate the magnetic properties of GNFs with triangular shape and fractal structure [34, 35, 301] (see Ref. [37] for a review).

Only a few studies on the electronic and magnetic properties of GNFs have been published, however most of those studies are limited to triangular or hexagonal shapes of graphene nano flakes with pure zig-zag or arm-chair edges without considering edge passivation, stability [158], polarization effects and melting phenomenon [221]. Here we report on various GNFs with different shapes that are the most energetically favorable configurations for given number of carbon atoms in the flake, as found in our previous work [157]. Such nano flakes were found to have lower melting temperature than graphene [221]. There are few works on bilayer GNFs, e.g. Güçlü et al. [302] studied graphene bilayer triangular quantum dots and found that it exhibits a shell of degenerate states at the Fermi level. Moreover applying a vertical electric field on bilayer GNF can turn off or reduce the total spin to a single localized spin. In the present study we focus on the electronic properties and permanent polarization of those GNFs with two different edge passivation. We show that the electric dipole moments strongly depend on the symmetry of the GNFs and the type of edge passivation. Our findings for GNFs with n-fold symmetry can be extended to larger flakes without loss of generality, they are always un-polarized independent of the type of edge terminated atoms. We also found that the stability of bilayer GNFs depends on the mutual orientation of the permanent dipole moments.

8.2 The Computational Method

In order to find the electronic dipole moments of the nano flakes we performed DFT calculations on GNFs. We employed density functional theory as implemented in GAUSSIAN (G09) [303] which is an electronic-structure package that uses a basis set of Gaussian type of orbitals. For the exchange-correlation (XC) functional, the hybrid B3LYP [304] is adopted in G09, which was shown to give a good representation of the electronic structure in C-based nanoscale systems [305]. Using the polarized basis set 6-311G** in G09, we expect that our calculation is capable to provide a reliable description of the electronic properties of the different systems. Notice that for the H-passivated (F-passivated) GNFs if the total number of electrons or equivalently N_H e.g. $C_{21}X_{11}$ ($N_F = 11$) is an odd number the total spin is non zero and therefore in that case we performed spin polarized calculations.

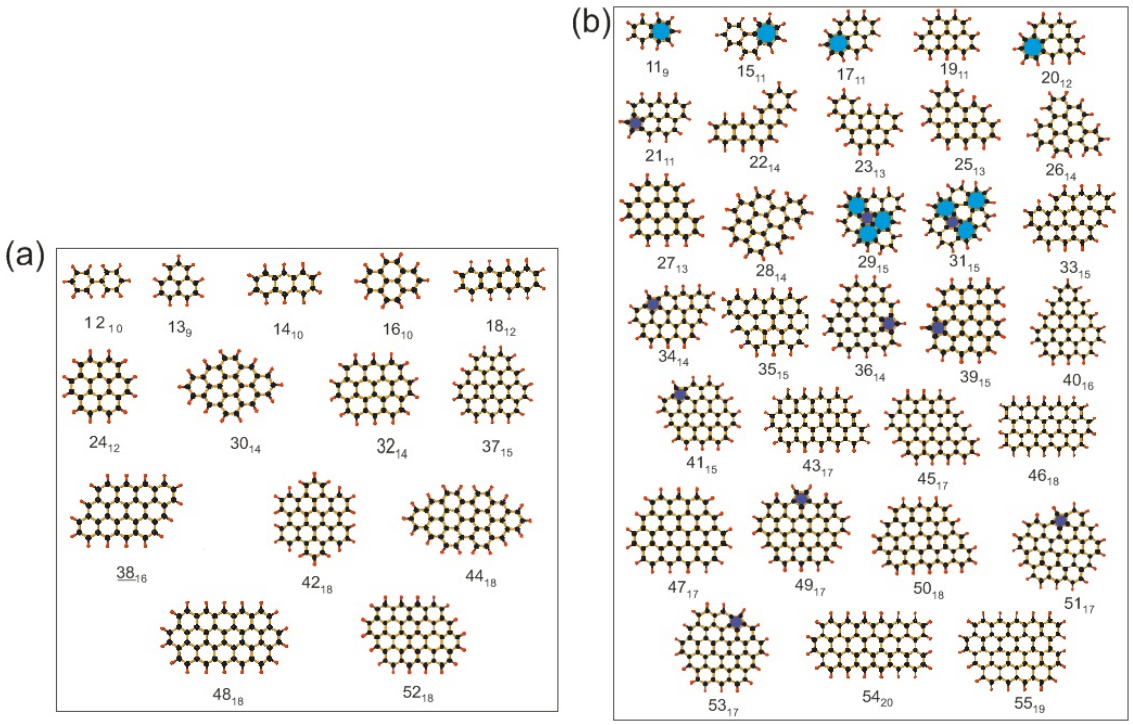

Figure 8.1: The minimum energy configurations of the studied GNFs. The black balls indicate C atoms and the red balls can be H or F atoms which saturate the edges. (a) The GNFs with n-fold symmetries (the underlined GNFs have 2-fold symmetry). (b) GNFs without n-fold symmetry. The pentagons have indigo color and the heptagons are in blue. The subindex in each GNFs refers to the number of H or F atoms and the main number equals the number of C-atoms in the flakes. The shaded polygons are not hexagons.

8.3 Symmetry effect

In the case of H-passivation (F-passivation), the passivated C atoms absorb (gives) part of the electron of the H (to F) atom making the H (F) atom positively (negatively) charged. This makes the GNFs polarized with a permanent polarization where the net dipole moment is determined from a summation over all local dipoles at the edges. Therefore, the net dipole moment will depend on the geometry of the system which we will study in this section. The electronic and magnetic properties of GNFs originate from this un-balance in charge distribution at the edges.

In Fig. 8.1 we depict the minimum energy configurations which are saturated by hydrogen or fluorine atoms. These configurations were obtained using the conjugate gradient

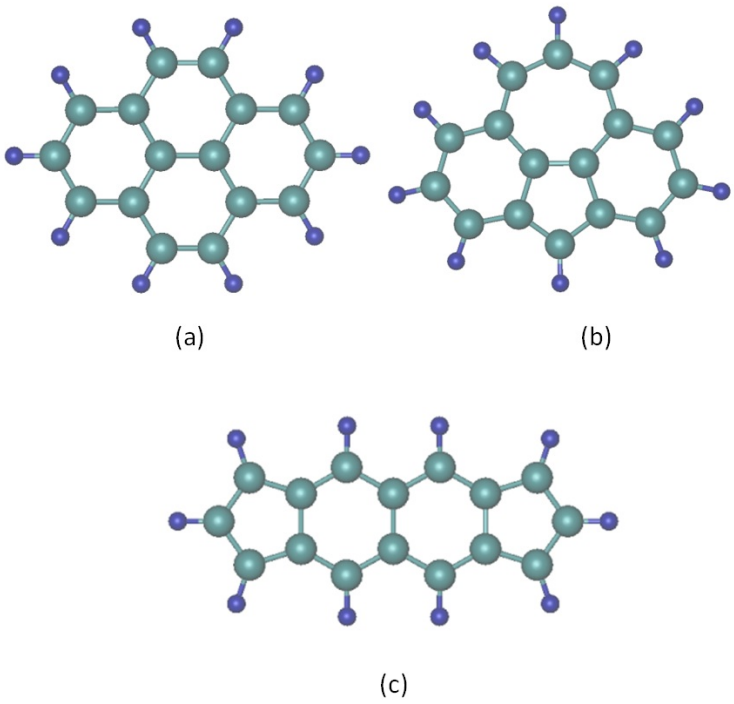

Figure 8.2: Three minimum energy isomers of $C_{16}X_{10}$ whose energy are given in Table I.

Table 8.1: Binding energy for the three isomers of $C_{16}X_{10}$ that are depicted in Fig. 8.2.

	Binding energy (eV)
$C_{16}H_{10}$(a)	-170.49
$C_{16}H_{10}$(b)	-168.10
$C_{16}H_{10}$(c)	-167.78
$C_{16}F_{10}$(a)	-171.81
$C_{16}F_{10}$(b)	-169.47
$C_{16}F_{10}$(c)	-169.62

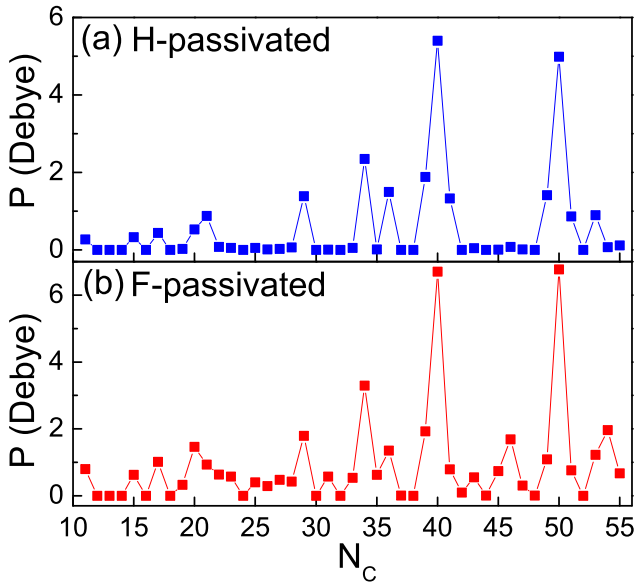

Figure 8.3: The absolute value of the dipole moment versus the number of carbon atoms for the H-passivated (a) and the F-passivated (b) GNFs. The largest dipoles are for GNFs with $N_c = 40$ and $N_c = 50$ in both cases.

minimization method as outlined in our previous work [157] and revisited in the current study by DFT optimization. In order to check the minimum energy configuration we performed extra calculations for three typical isomers with N_C=16 (see Fig. 8.2). The corresponding binding energy are listed in Table 8.1. The lowest energy configuration is the 16_{10} structure in Fig. 8.1. The defective H- and F-passivated small clusters are slightly buckled after relaxation. We categorized the studied GNFs into two different groups: i) fourteen GNFs with n-fold symmetry, e.g. $C_{12}H_{10}$ with $n = 2$, $C_{13}H_9$ with $n = 3$ and so on, which are shown in Fig. 8.1(a); and ii) the systems with pentagon and heptagon defects (shaded) and those without n-fold symmetry, e.g. $C_{11}H_9$ which are shown in Fig. 8.1(b). The latter systems may have mirror symmetry. Here we limit our study to those C_{N_c} X_{N_x} structures that have minimum energy. The first aforementioned group has always zero dipole moment while the second group has non-zero total dipole moment and in some cases are even a giant polar molecule. Notice that larger flakes with n-fold symmetry (the first group) should also have zero total dipole moment.

In the first group (Fig. 8.1(a)), e.g. in the 2-fold symmetry cases a rotation of 180° around the z-axis transforms $\mathbf{r}_i \rightarrow -\mathbf{r}_i$ and consequently $\overrightarrow{P}_T$=0. In the second group there is no n-fold symmetry where different edges have different orientation of local dipole

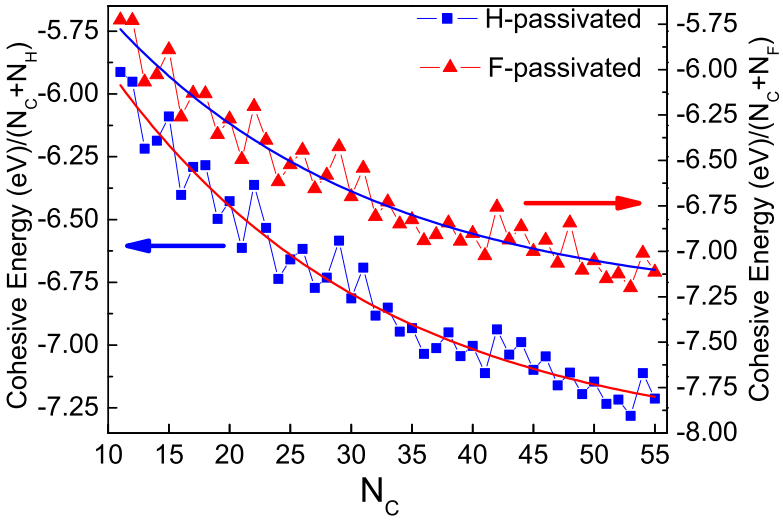

Figure 8.4: The cohesive energy versus the number of carbon atoms in H-passivated and F-passivated GNFs. The solid lines are the best fits using to Eq.(8.1).

moments which do not cancel each other hence resulting in a non-zero net dipole moment. More defects that are randomly distributed increase the dipole moment strength.

In Fig. 8.3 we show the absolute value of the total dipole moment versus N_c for all studied GNFs. In Fig. 8.3(a) the H-passivated system and in Fig. 8.3(b) the F-passivated system are shown. We see that in both cases the above mentioned symmetry issues are obeyed. The net dipole of GNFs with F-passivation are larger than those for H-passivation which is due to the larger electronegativity of F. It is interesting to note that the two systems with mirror symmetry, i.e. $C_{40}H_{16}$ and $C_{45}H_{17}$ have respectively the largest - 6.35 Debye - and the smallest - 0.015 Debye - dipole moment. The corresponding dipole moment for $C_{40}F_{16}$ and $C_{45}F_{17}$ are 7.69 Debye and 0.61 Debye, respectively. The system $C_{50}X_{18}$ without particular symmetry has the second largest dipole moment. The ratio between the dipole moments of $C_{40}F_{16}$ and $C_{40}H_{16}$ is 1.21.

It is surprising that a simple linear summation over all local dipole moments in e.g. $C_{40}X_{16}$, apparently leads to a zero dipole moment if one assumes equal $\overrightarrow{p}_{C-X}$ for all saturated bonds, while this cluster has the largest dipole moment. The reason for such effect is that the local dipole moments $\overrightarrow{p}_{C-X}$ are not in the same direction due to the non-uniform distribution of the C-X second neighbors, i.e. most of the C atoms in the bottom of $C_{40}X_{16}$ (see Fig. 8.1(b)) are connected to the inner C atoms but at the top of the system there is no inner C atom to give more electron charge to the corresponding C-X bonds.

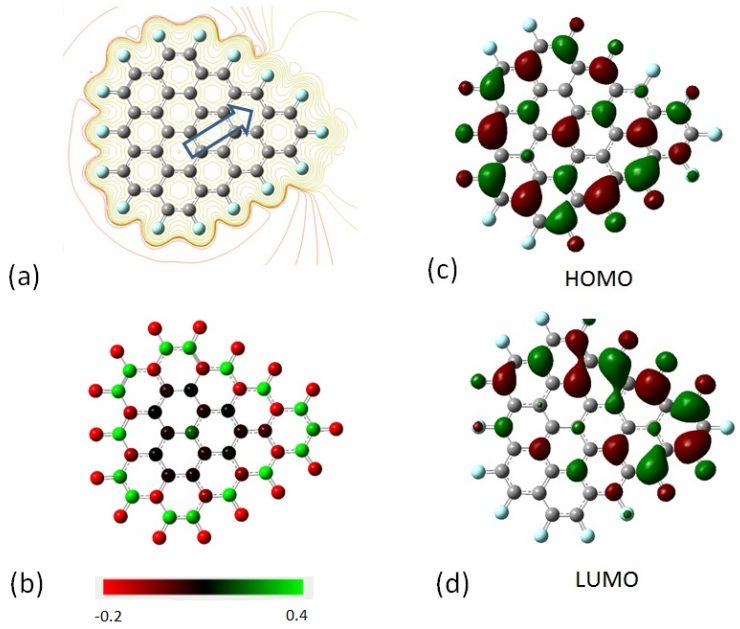

Figure 8.5: (a) Electrostatic potential contours around F-passivated GNFs - $C_{40}F_{16}$- which has the largest dipole moment indicated by the arrow, (b) Corresponding charge distribution, (c) HOMO and (d) LUMO orbitals. The red and green colors stand for the positive and negative signs of the molecular orbital wave function, respectively.

8.4 Energy difference between HOMO and LUMO

We study small carbon flakes that are saturated by H or F which have discrete energy levels and are filled by electrons. In the case of spin polarized calculations there is an extra energy level. In Fig. 8.4 we plot the cohesive energy versus N_c for all studied GNFs. It is seen that the energy per atom decreases with N_c in both H-passivated and F-passivated GNFs. Increasing the number of C atoms in GNFs increases the number of C-C bonds more rapidly than the C-X bonds at the edges. Since the total cohesive energy is a function of C-C and C-X binding energy we expect that the total cohesive energy rapidly approaches the bulk cohesive energy (e_0). On average we found that the energy decreases according to

$$E/(N_c + N_X) = e_0 + be^{-\lambda N_c} \tag{8.1}$$

where e_0=-7.4 eV, b=-2.37 eV and λ=0.045 for H-passivated and e_0=-7.3 eV, b=-2.53 eV and λ=-0.046 for F-passivated GNFs which are shown by the solid curve in Fig. 8.4. Because the C-F binding energy is larger than C-H in F saturated GNFs the curve for

F-passivated is above the one of H-passivated. For larger N_X/N_C ratio the total cohesive energy is far from the bulk energy which is due to the so called, i.e. edge effect. Adding a C atom to a typical GNF decreases the energy if the new formed GNF becomes more stable which is mostly the case for those GNFs without pentagon and heptagon defects. If the next GNF has pentagon or heptagon defects the energy is larger, see e.g. N_c=11,15,17,20,29,31. We emphasize that most of the studied GNFs are planar-like structures. Moreover the systems with a larger ratio $\frac{N_c - N_x}{N_x}$ have lower energy which corresponds to higher stability due to the lower number of edge atoms. It is seen that $\Delta E = E_{N_{c+2}} - E_{N_c} = constant$ for some N_c (e.g. between N_c =42 and N_c =53) where $\Delta N_H = 0$ in H-passivated GNFs. This is promising for quantum dot design: fixing the number of edge H-atoms and increasing the number of C atoms decreases the energy of the system with constant increments. The latter effect is similar to the regular jumps observed in the electrochemical potential in quantum dots. First we compare the energy of two typical GNFs (with only hexagons, e.g. $C_{37}X_{15}$ and with also pentagon and heptagon, e.g. $C_{39}X_{15}$) with the same flakes without X-atoms at the edges (bare flakes). Results show that in both cases independent of the type of X atom edge passivation the total energy is reduced, i.e. E($C_{37}F_{15}$)-E(C_{37})=-1.9948 eV, E($C_{37}H_{15}$)-E(C_{37})=-1.9380 eV, E($C_{39}F_{15}$)-E(C_{39})=-1.9298 eV, and E($C_{39}H_{15}$)-E(C_{39})=-1.8724 eV. The energy decreases much more in $C_{37}X_{15}$ than for $C_{39}X_{15}$. Therefore the GNFs with regular hexagon edges becomes more stable when they are saturated by X atoms with respect to the GNF which contain heptagons and pentagons. This is in agreement with those reported for triangular GNFs flakes in Ref. [301].

In Fig. 8.5 we show for $C_{40}F_{16}$ (a) the electrostatic contour, (b) charge distribution, (c) the corresponding HOMO and (d) LUMO. The arrow in (a) indicates the giant permanent dipole in $C_{40}F_{16}$. There is a clear relation between the electrostatic potential and the charge distribution. The LUMO is localized on the parts with transferred charges to the HOMO region. The less symmetry in any GNFs leads to the non-horizontal direction of the dipole moment. The dipole moment is directed to the region with the LUMO orbitals.

In all n-fold symmetric GNFs the net dipole is zero while one can define local dipoles which eventually cancel each other. Note that using a different functional for the exchange correlation in our DFT calculation may change the energy gap slightly, however the energy gap for H-passivated and F-passivated GNFs are close to each other. This is in agreement with the results of Ref. [300].

In Fig. 8.6 we show the electrostatic contour lines around $C_{41}F_{15}$ (a) which has non-zero total spin. The corresponding spin-up and spin-down HOMO and LUMO are shown in (b). There is a clear difference in the orientation between orbitals of spin-up and spin-down which results in a different energy gap between spin-up and spin-down electrons.

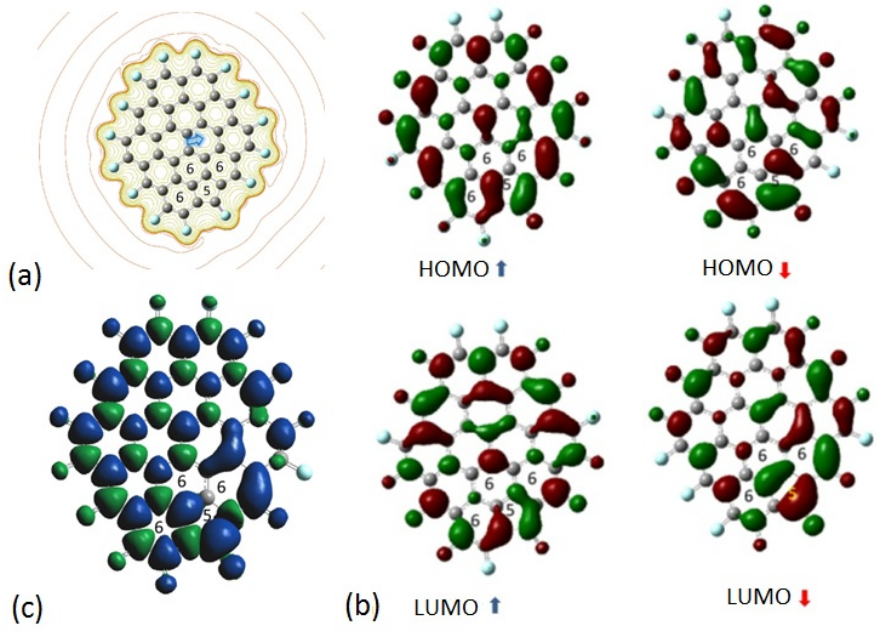

Figure 8.6: Electrostatic potential contours around $C_{41}F_{15}$ with non zero total spin. The dipole moment is indicated by the arrow. (b) The corresponding spin-up and spin-down HOMO and LUMO orbitals. The red and green colors stand for the positive and negative signs of the molecular orbital wave function, respectively. (c) Isosurfaces of spin density for $C_{41}F_{15}$. Blue and green isosurfaces are 0.0004 e/Å^3 and -0.0004 e/Å^3, respectively.

The spin-up electrons have larger energy gap as compared to spin-down. Notice that we do not show the HOMO and LUMO for all studied GNFs which can be made available upon request. As a typical case, the isosurface of the spin density for $C_{41}F_{15}$ is shown in Fig. 8.6(c). Although the frontier orbital are mostly nonuniformly distributed at the edges, the isosurface of the spin density are uniform except on the heptagon's atoms, i.e. only the α spin has a considerable value different from zero. In general for a graphene nanoflakes with zigzag edges, the spin magnetizations of A and B sublattices are aligned antiparallel, i.e. antiferromagnet spin ordering [34, 35] which is not similar to our studied GNFs. This alternative is broken by the defect in a way that depend on the out-of-plane distortion [306].

In Fig. 8.7 we show the HOMO-LUMO energy gap Δ versus N_c which on average decreases linearly up to $N_c \sim 35$. The larger the electrostatic potential difference between

the ends of GNFs, the lower the energy gap. The electrostatic potential due to the local charge transfer between C and X decreases the energy of the LUMO level and increases the energy of the HOMO level thus reducing the energy gap. We fit a linear line to the results for both H-passivated and F-passivated systems. This curve is shown in Fig. 8.7. For large GNFs ($N_c > 35$) the energy gap is almost constant. It is well known that the energy gap of graphene is zero. Tight binding calculations predict that in hexagonal (triangular) GNFs having more than 10^3 (10^6) C atoms the energy gap approaches zero [298]. In finite size GNFs the energy gap strongly depends on the geometry of the system and the type of edges, e.g. zigzag versus armchair. We found in previous work that the energy gap decreases like a/N where a=4.9 eV [307]. On the other hand experiments on GNFs revealed that the energy gap decreases like 1/L where L is the lateral dimension of GNF [6, 308]. Here our studied GNFs typically have no particular edge structure and we found that the energy gaps decrease up to about 2 eV.

Although the polarization of GNFs can be understood from the possible symmetries of GNFs, however the difference between the energy of the HOMO and the LUMO (Δ) can not be explained simply as due to an increase of the dipole moment, i.e. the energy gap is a scaler physical quantity and one does not expect that all systems with $\overrightarrow{P}_T$=0 have zero energy gap. In other words there is no straightforward relation between the symmetry and the energy gap in GNFs. The energy gap is affecten by the non-uniform distribution of the electrostatic potential which is a function of the non-uniform charge distribution over the GNFs. Nevertheless as seen from Figs. 8.3 and 8.7 the GNFs with the largest dipole moment have the lowest energy gap hence the polar GNFs in this study have a lower energy gap which originate from the un-balanced charge distribution. This effect strongly depends on the geometry and can not be generalized to every isomer with the same number of C atoms.

8.5 Density of states and spin polarized results

In Fig. 8.8 we show the density of states (DOS) for those systems with the largest dipole moment, i.e. $C_{40}X_{16}$ and $C_{50}X_{18}$(zero energy gap Δ). We set the Fermi energy at zero by defining $E_F = (E_{HOMO} + E_{LUMO})/2$. Although the energy gap is almost zero in GNFs with $N_c = 40, 50$ but there is a significant gap between the HOMO, $HOMO_2$ and LUMO and $LUMO_2$ which results in larger ionization energy for the electrons in $HOMO_2$, where index 2 refers to the closest occupied state to HOMO with larger energy than HOMO. Furthermore the occupied states in F-passivated GNFs have larger DOS as compared to H-passivated GNFs which is attributed to the larger charge transfer to the system by F atoms than H atoms.

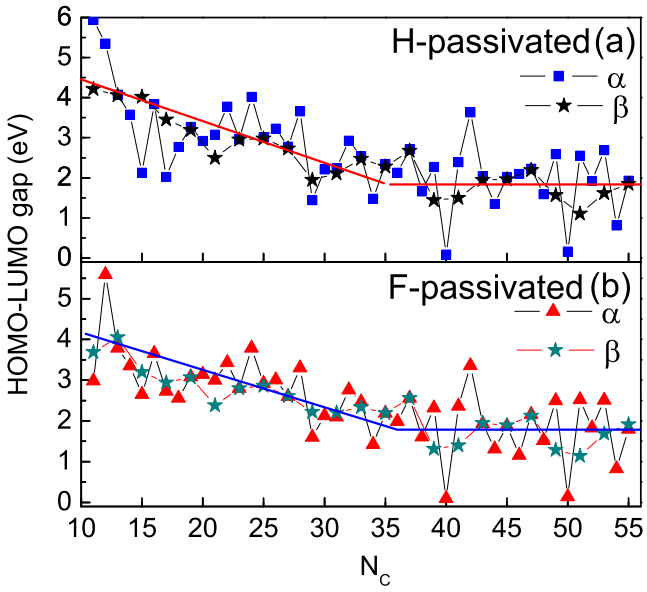

Figure 8.7: HOMO−LUMO gap versus the number of carbon atoms in H-passivated (a) and F-passivated GNFs(b). The gap approaches zero and is close to zero beyond $N_c = 35$. α and β stand for the HOMO−LUMO gap for spin up and spin down, respectively. The solid lines show the overall change in the gaps.

It is also interesting to investigate the DOS of systems with non-zero total spin. In Fig. 8.9 the DOS of α (spin-up: top panels with black color) and β (spin-down: bottom panels with red color) spins are shown for three typical systems, i.e. $C_{51}X_{17}$, $C_{41}X_{15}$ and $C_{35}X_{15}$. The spin-up and spin-down DOS are almost symmetrical except around the gap region. There is a clear difference between Figs. 8.9(a) and 8.9(b) (and also (c)) while the number of X atoms are the same, $N_x = 15$. In order to find the Fermi energy we sorted all the energy levels for spin-up and spin-down and we found the middle point of the new HOMO and LUMO. We found that the energy gaps between the spin-up and spin-down electrons are different. In Fig. 8.10 we show the absolute value of the difference between the energy gap of α spin and β spin, i.e. $\Delta_\alpha - \Delta_\beta$. It is surprising that the presence of pentagons in GNFs with non-zero total spin maximize $\Delta_\alpha - \Delta_\beta$. The largest difference is for $N_c = 15$ and $N_c = 51$ which have one heptagon and one pentagon, respectively. The symbols '5', '6' and '7' in Figs. 8.10(a,b) indicate the presence of pentagon, only hexagons and heptagon in the corresponding GNFs. Notice that the H-passivated GNFs have a larger difference between the energy gap of spin-up and spin-down electrons however the overall

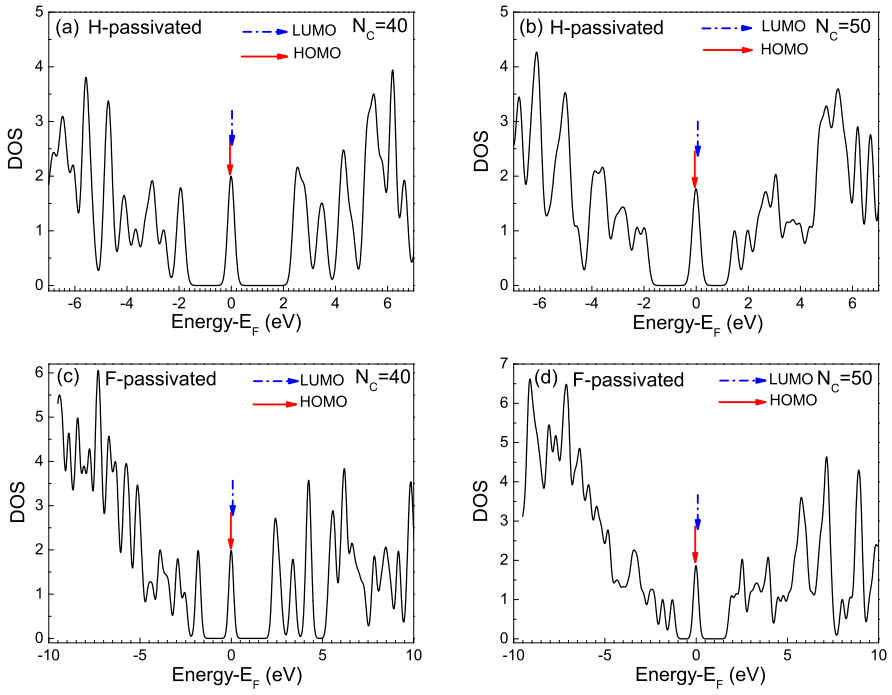

Figure 8.8: Density of states for H-passivated (a,b) and F-passivated (c,d) graphene nano flakes; the energy gap in (a,b,c,d) is almost zero while they have maximum dipole moment among the studied GNFs. The vertical arrows refer to the position of the HOMO (red) and LUMO (blue). The Fermi energy was set at zero.

pattern in Fig. 8.10 is the same. Using these results one can predict that for large GNRs with a few pentagons and/or heptagons half-metallicity can be found.

The GNRs exhibit half-metallicity in the presence of electric field [103]. It was found that the half-metalicity in GNRs originates from the fact that the applied electric field induces an energy level shift of opposite sign for the spatially separated spin ordered edge states.

8.6 Bilayer GNFs ($C_{40}H_{16}$ and $C_{40}F_{16}$)

Bilayer GNFs, which to the best of our knowledge, have not been investigated from first principles. We select GNFs which have the largest dipoles. In order to study the bilayer GNFs we performed three typical DFT calculations for two bilayer GNFs $C_{40}H_{16}$ and three

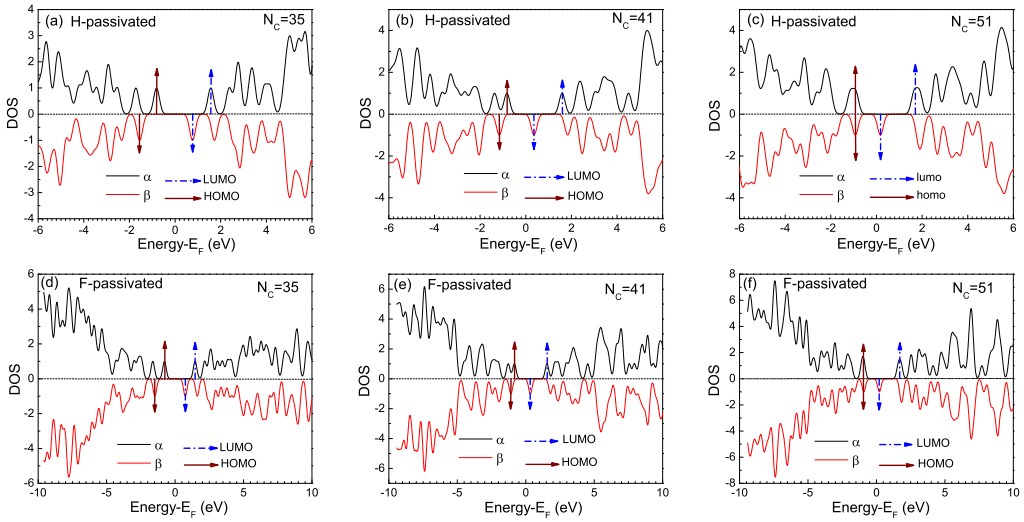

Figure 8.9: Density of states for H-passivated (a,b,c) and F-passivated (d,e,f) graphene nano flakes with non-zero total spin; the energy gap in (b,c,e,f) are different for spin-up (denoted by α) and spin-down (denoted by β) electrons with a shift in Fermi energy with respect to each other. In (a,d) the energy gap for spin-up and spin-down are almost the same with a shift in Fermi energy with respect to each other. The Fermi energy occurs at zero.

other DFT calculations $C_{40}F_{16}$ which have different mutual orientation which is characterized by rotation angle with respect to each other θ, i.e. parallel with $\theta = 0^\circ$, (Fig. 8.11(a)), parallel with $\theta = 180^\circ$ (Fig. 8.11(e)) and parallel with $\theta = 90^\circ$ (Fig. 8.11(i)). For the case $\theta = 0^\circ, 180^\circ$ GNFs in adjacent layers are arranged head-to-head (and tail-to-tail) and head-to-tail arrangement, respectively.

i) $\theta = 0^\circ$: In Figs. 8.11(a)(b) we show a side and top view, respectively, of the optimized structure for two bilayer $C_{40}H_{16}$ with $\theta = 0^\circ$ which after optimization are found to be bent with positive curvature. GNFs of $C_{40}H_{16}$ in the adjacent layers are directed head-to-head and tail-to-tail. The closest and longest distance between two adjacent layers (not including the hydrogen atoms) are found to be 3.27 and 4.83 Å, respectively, which are closer and longer than the distance between graphite layers, i.e. 3.35 Å . The optimized structure indicates charge repulsion in the ends (tails) in bilayer GNFs. Because $C_{40}H_{16}$ is a giant polar molecule, we can understand the repulsion of two bilayer molecules as the dipole-dipole interaction, i.e. $U = \vec{P}_1.\vec{P}_2/R^3$ where R is the perpendicular distance between two dipoles. If the sheets do not bent we expect that $\theta = 180^\circ$ has lower energy

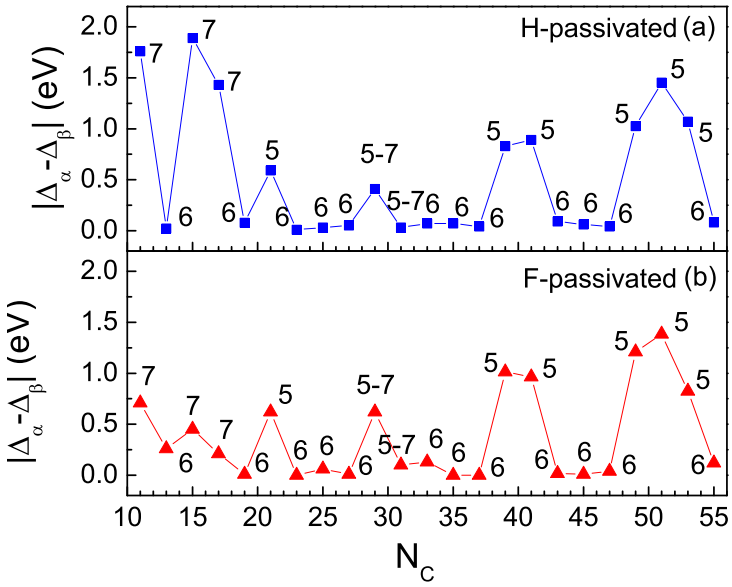

Figure 8.10: The energy gap between spin up and spin down for H-passivated (a) and F-passivated (b) graphene nanoflakes. The numbers refer whether there are pentagon (5), hexagon (6) or heptagon (7) in the corresponding GNF.

than $\theta = 0°$, however bending reduces the energy and makes both energies close to each other. In Table 8.2 we listed all results for bilayer $C_{40}H_{16}$ and $C_{40}F_{16}$.

The HOMO-LUMO and DOS for $\theta = 0°$ are illustrated in Figs. 8.11(c,d) and Fig. 8.12(a), respectively. There is a clear mixing of orbitals between two HOMOs in adjacent GNFs (see Fig. 8.11(c)). This is different from the stacking of graphite where the layers are parallel and there is no electron-sharing between two layers and the interaction is mostly a weak van der Waals interaction. This mixing effect reduces the energy, otherwise we expect that the $\theta = 0°$ case has higher energy than $\theta = 180°$. The HOMO-LUMO gap 0.99 eV appears in bilayer GNFs which was found to be almost zero for a single GNF $C_{40}H_{16}$, see Fig. 8.7. Now there is a small gap between the HOMO, $HOMO_2$ and LUMO and $LUMO_2$ in contrast to single GNF $C_{40}H_{16}$.

ii) $\theta = 180°$: For this case the head of the top GNF is directed towards the tail of the bottom GNF. The optimized structure leads to a relative rotation, i.e. the optimized structure does not satisfy the condition $\theta = 180°$. Here curvature is negative and the closest distance between different layers (not including hydrogen atoms) thus appears in the vicinity of these head-tail, and the distance of the head1-tail2 and tail1-head2 between two

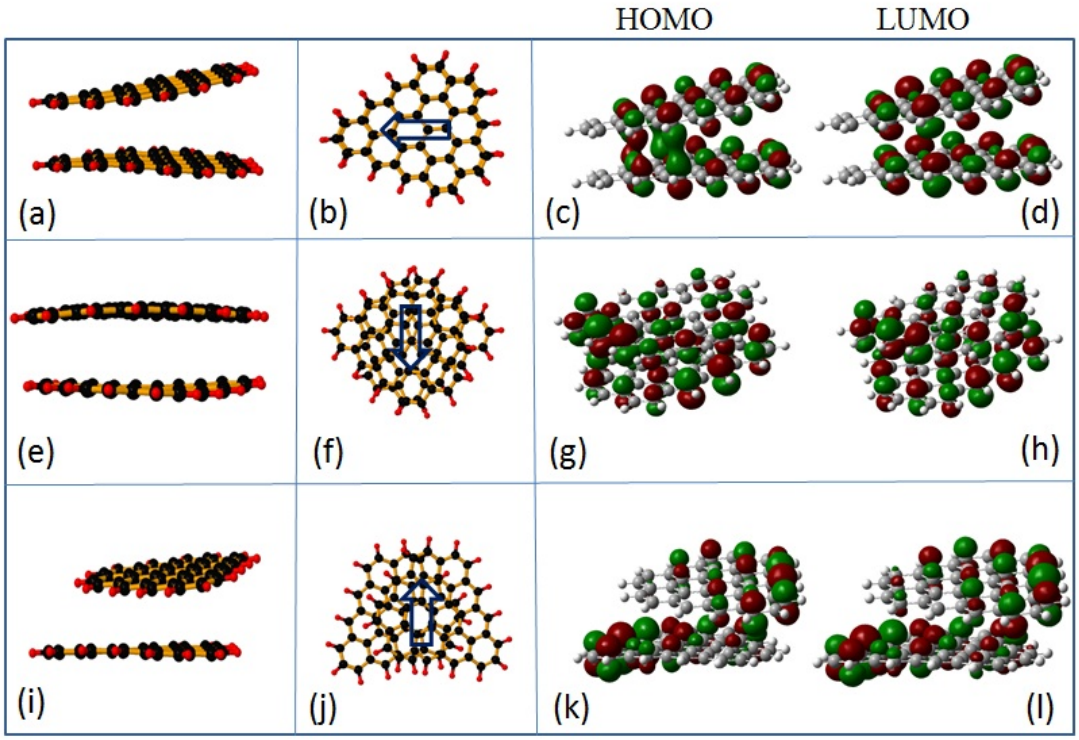

Figure 8.11: Bilayer GNFs $C_{40}H_{16}$: parallel with $\theta = 0^{\circ}$(a) side view (b) top view (c) HOMO (d) LUMO; parallel with $\theta = 180^{\circ}$ (e) side view (f) top view (g) HOMO (h) LUMO; parallel with $\theta = 90^{\circ}$ (i) side view (j) top view (k) HOMO (l) LUMO. The arrows in Figs.(b,f,j) indicate the direction of polarization.

layers are 3.46 and 4.02 Å, respectively. Therefore the distances are larger than in graphite stacking and we expect a weak interaction between the two GNFs. By careful examination of bilayer GNFs, we do not found that the interatomic distance in different molecules is closer than this value. The HOMO-LUMO and DOS are shown in Figs. 8.11(g,h) and Fig. 8.12(b), respectively. There is no mixing in the frontier orbital. The energy is slightly higher than in the case with $\theta = 0^{\circ}$. Note that if the GNFs does not bent the mutual interaction energy of $\theta = 180^{\circ}$ could be lower than $\theta = 0^{\circ}$. The energy gap is found to be 0.82 eV which is less than for the $\theta = 0^{\circ}$ case. This is due to the fact that the bilayer GNFs with $\theta = 180^{\circ}$ has a larger net dipole and a different orientation as compared to the previous case.

iii) $\theta = 90^{\circ}$: The tail of the top GNF is directed towards the head and away from the

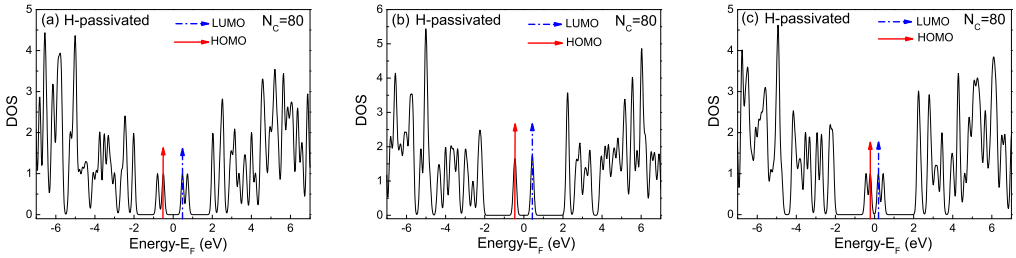

Figure 8.12: Density of states for H-passivated bilayer GNFs (a) parallel with $\theta = 0^\circ$ (b) parallel with $\theta = 180^\circ$ (c) parallel with $\theta = 90^\circ$. An energy gap appears in contrast to almost zero gap in single GNF $C_{40}H_{16}$. The vertical arrows refer to the position of the HOMO (red) and LUMO (blue).

tail of the bottom GNF. After optimization the mutual angle is not $\theta = 90^\circ$ and there is an additional mutual rotation. The closest and longest distances between different layers (not including hydrogen atoms) thus appear in the vicinity of these head-tail and tail-tail, are 3.35 and 4.89 Å, respectively, which are equal and longer than the graphite stacking distance, respectively. The HOMO-LUMO and DOS are shown in Figs. 8.11(k,l) and Figs. 8.12(c), respectively. There is no mixed frontier orbitals and the energy is larger than those for $\theta = 0^\circ$ and $\theta = 180^\circ$. The net dipole is much larger than those of $\theta = 0^\circ$ and $\theta = 180^\circ$ resulting to a lower energy gap, i.e. 0.41 eV. Note that for two GNFs consisting of two $C_{40}F_{16}$ our calculation was not fully optimized, hence $\theta = 180^\circ$ is not likely the preferential bilayer structure for this GNFs.

Based on the above results, we may reasonably regard that for a large-polar GNFs such as $C_{40}H_{16}$, the polarity of GNFs determines the mutual orientation of the GNFs arrangement in the crystal structure. Additionally, it is interesting to note that while a single $C_{40}H_{16}$ is planer, however it bends when it interact with other GNFs which is due to its finite size (the edges interact). The resulting bilayer structures depend on the type of stacking and there is a tilting of the flakes.

8.7 Raman Spectroscopy

Raman spectroscopy [309] is a non-destructive and quick characterization technique which gives structural and electronic information. For graphene nano-flakes, the most intense peaks are G and D, appearing around 1585 cm^{-1} and 1350 cm^{-1}, respectively. The G peak corresponds to the C-C bond stretching, i.e. the first order Raman-allowed E_{2g} phonon at the Brillouin zone center. The D peak requires a defect to be activated. Density functional

Table 8.2: Net dipole moment, energy gap and cohesive energy for bilayer GNFs with different mutual orientation

	P(Debye)	Gap (eV)	$\frac{Energy}{N_C + N_{H,F}}$(eV/atom)
$\theta = 0^\circ$			
$C_{40}H_{16}$	0.006	0.99	-7.012
$C_{40}F_{16}$	0.781	0.90	-6.905
$\theta = 180^\circ$			
$C_{40}H_{16}$	0.059	0.82	-7.010
$C_{40}F_{16}$	-	-	-
$\theta = 90^\circ$			
$C_{40}H_{16}$	0.999	0.41	-7.008
$C_{40}F_{16}$	1.977	0.38	-6.904

calculations using the hybrid functional B3LYP with polarized basis set 6-311g** have been carried out in order to obtain the Raman spectrum (we used standard method for scaling of the frequencies which has been adopted in GAUSSIAN09 software).

Raman spectra are calculated for some typical H- and F- passivated nano-flakes (as shown in Fig. 8.1) and bilayer GNFs. We notice that the introduction of a pentagon in the $C_{41}H_{15}$ nano-flake introduces more high frequency modes beyond the G-peak as compared to non-defective nano-flake (e.g. $C_{50}H_{18}$ as shown in Fig. 8.14 (b)), which is due to the fact that modes localize around the defect (as shown in Fig. 8.13). Introduction of a pentagon in the $C_{41}F_{15}$ also introduces more high frequency modes similar to H-pasivated clusters. Furthermore, a prominent feature at 1260 cm^{-1} characteristic of covalent C-F bond stretching [310] has been observed. D peak can be found in all GNFs due to the finite crystalline size where the edges of the nano-flakes can be seen as defects. The ratio of the intensities of D and G peak increases as the nano-flake size decreases due to the relative increase of the number of edge atoms and the less ordered crystalline structure in smaller GNFs (see Fig. 8.14(a)). For highly symmetric nano-flakes, e.g. $C_{24}H_{12}$ only G- and D-peaks are dominant. A localized mode is found to appear at $\approx$3100 cm^{-1} in H-passivated GNFs, which is the typical vibrational mode of the C-H bond [311].

For a parallel bilayer GNFs, broad G- and D- bands appear (Fig. 8.14(d)). We also found that the intensity of the Raman spectra in GNFs are different than those experimentally reported for graphene [309]. Firstly, because of the edge effects which causes non-uniform distribution of C-C bonds over the GNFs and secondly because of the large ratio between the number of defects and the total number of carbon atoms in each particular GNF. These enhance the intensity of D peak with respect to G peak while they are not

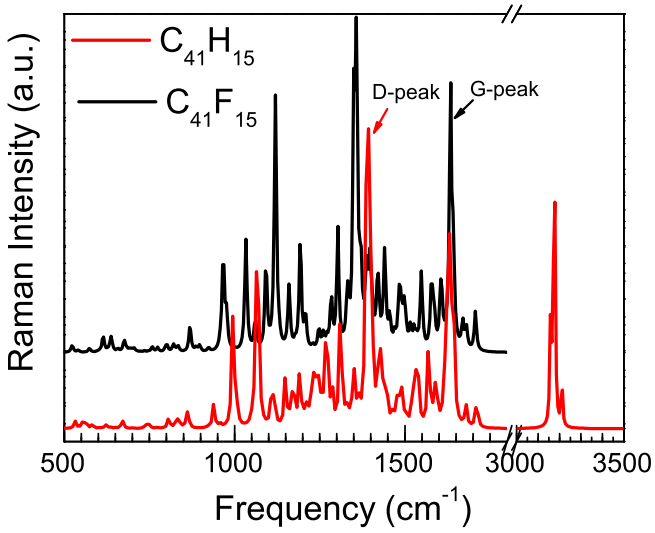

Figure 8.13: Raman spectrum of $C_{41}H_{15}$ and $C_{41}F_{15}$ nano-flakes.

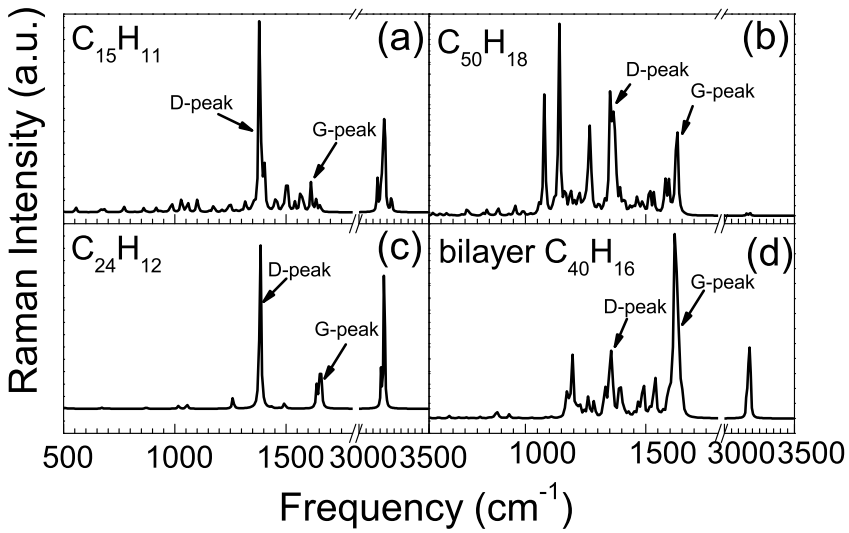

Figure 8.14: Raman spectrum of H-passivated nano-flakes: (a) $C_{15}H_{11}$, (b) $C_{50}H_{18}$, (c) $C_{24}H_{12}$, and (d) bilayer $C_{40}H_{16}$.

shifted with respect to graphene.

8.8 Conclusion

Using extensive ab-initio calculations we studied the electronic properties of GNFs with several different number of carbon atoms and two different atoms for edge termination. The n-fold symmetry causes no net dipole in GNFs. Breaking the n-fold symmetry by heptagon and pentagon defects and reducing the symmetries to mirror symmetry enhances the polarization. We found that the larger the dipole moment the lower the energy gap for both type of saturated atoms. The cohesive energy of GNFs reduces with increasing carbon atoms for constant number of passived atoms. On average the energy gap decreases rapidly. The electrostatic potential around GNFs control both the polarization and the energy gap of the GNFs. Our spin polarized calculations show that the difference between the energy gap of up and down spin is maximized mostly for GNFs with pentagon (and heptagon) defects. The H-passivated GNFs have a larger difference between the spin-up and spin-down energy gap as compared to F-passivated GNFs. The bilayer GNFs reveal a clear dipole-dipole interaction which is a consequence of the mutual orientation between the permanent dipoles in the system. The bilayer GNFs are not necessarily planar structures and may have a curved structure.

CHAPTER 9

Summary and future prospects

9.1 Concluding remarks of the thesis

Exceptional properties of 2D materials are at the forefront of current research thanks to the recently discovered graphene and other 2D materials (e.g., h-BN, fluorographene, MoS_2, silicene, etc.). In the present thesis, I theoretically investigated the spectral and electronic properties of graphene nano-flakes and thermo-mechanical properties of monolayers of hexagonal boron-nitride (h-BN) and fluorographene (FG). In my PhD thesis, I employed classical molecular dynamics using bond-order potentials and density functional theory approaches.

In chapter 3, atomistic simulations were performed using the Brenner second-generation reactive bond order (REBOII) interatomic potential function in order to study the vibrational properties of nanographene. The frequency of the normal modes as a function of the number of particles for nanographene C_N ($2 \leq N \leq 55$) and H-passivated carbon clusters ($11 \leq N \leq 55$) were investigated. The phonon density of states of different clusters were compared with theoretical results for graphene and found to be in good agreement for the acoustic and optical phonon density of large clusters. Using the eigenfrequencies of the normal modes we calculated the specific heat within the harmonic approximation for different size carbon clusters and found that in the high temperature limit they approach the bulk value.

In chapter 4, we investigated the melting of nanographene that were reported in chapter 3, using molecular dynamics simulation and the Lindemann index. The melting tem-

perature of small flakes is lower than those for graphene and graphene nano-ribbons. The Lindemann index is sensitive to temperature and was found to be a good quantity in order to determine when structural deformations of the clusters start to occur. The melting temperature of small flakes on average increases versus the number of atoms in carbon nanoflakes. All nanoflakes investigated show premelting behavior with different premelting intervals. The melting temperature of defective nanoflakes are found to be lower than defect free neighboring nanoflakes. H-passivated clusters have a higher melting temperature than the non H-passivated clusters with the same number of C-atoms. Our simulation results also help to understand the formation of defects (due to the increase of temperature) in the graphene nano-flake which can then be applied to understand the growth and thermal treatment of nanographene. DFTB calculations also confirm the N-dependence of the melting temperature.

In chapter 5, atomistic simulations were carried out using the ReaxFF interatomic potential in order to study the melting of partial fluorinated graphene (PFG) and fully fluorinated graphene (FFG). The PFGs for $N_F/N_C < 40\%$ start to loose fluor atoms around 2000 K and become pristine graphene with defects at higher temperature. However, for PFGs with N_F/N_C ∼40-60%, large defects are formed beyond ≈ 1500 K (F atoms break the original local bonds and attach to the edges of these rings) and very slowly transits to the liquid phase as temperature increases so that below 5000 K the liquid and the solid phases are coexisting. For larger N_F/N_C ∼60-100%, F-atoms remain bonded to graphene until melting and PFGs and FFG rapidly transits to the 3D spaghetti like carbon chains. The melting temperature for FFG was calculated to be 2800 K. The minimum melting temperature is found to be around 70% fluorination. Our findings are therefore consistent with the experimental reversibility of the fluorination process in single layer graphene.

In chapter 6, the thermal properties of a boron nitride sheet were studied using large scale atomistic simulations. We showed that the scaling properties of a h-BN sheet follows closely the results of membrane theory and hence the thermal excited ripples are not characterized by any particular wave-length. Using the harmonic part of the height-height correlation function we found an increasing bending rigidity with temperature which is smaller than the one of graphene. We found that the buckling transition for h-BN depends on the applied compression direction and is much smaller than the one of graphene. The obtained molar heat capacity agrees very well with the well-known Dulong-Petit number, 25.2 $J\ mol^{-1}K^{-1}$ and the thermal expansion coefficient was found to be positive and equal to 7.2 $\times 10^{-6}K^{-1}$. The Grüneisen parameter 0.89 is found to be smaller than the one for graphene, i.e. 1.2. We showed that the different stiffness between the GE and h-BN sheets leads to different patterns of deformations in the presence of either uniaxial or shear stress.

In chapter 7, we provided a new set of parameters for the ReaxFF potential for the

C-F covalent bond and tested it on various molecules. Subsequently, molecular dynamics simulations were used to investigate the thermal rippling behavior and the mechanical response of fluorographene (FG) under uniaxial stress. The obtained results are compared with those for graphene (GE), graphane (GA) and hexagonal boron nitride (h-BN). We found that fluorographene remains a flat sheet similar to graphane even at high temperature, i.e. up to 900 K. The bending rigidity of FG is found to be independent of temperature and its Young's modulus is in good agreement with experiment.

In chapter 8, using extensive ab-initio calculations we studied the electronic properties of graphene nano-flakes (GNFs) that were reported in chapter 3 for two different atoms of edge termination. The n-fold symmetry causes no net dipole in GNFs. Breaking the n-fold symmetry by heptagon and pentagon defects and reducing the symmetries to mirror symmetry enhances the polarization. We found that the larger the dipole moment the lower the energy gap for both type of saturated atoms. On average the energy gap decreases rapidly up to $N_c = 35$ and is almost constant beyond it. The electrostatic potential around the GNFs control both the polarization and the energy gap of the GNFs. Our spin polarized calculations show that the difference between the energy gap of up and down spin is maximized mostly for GNFs with pentagon (and heptagon) defects. The H-passivated GNFs have a larger difference between the spin-up and spin-down energy gap as compared to F-passivated GNFs. The bilayer GNFs reveal a clear dipole-dipole interaction which is a consequence of the mutual orientation between the permanent dipoles in the system. The bilayer GNFs are not necessarily planar and may have a curved structure.

9.2 Future prospects

In chapter 6 and 7, I investigated the thermo-mechanical properties of 2D graphene-like material, e.g. h-BN and FG. Of particular interest will be the investigation of thermal rippling of different 2D materials e.g. silicene, silicane, MoS_2, hydrogenated BN, their corresponding bilayer van der Waals structures (e.g. bilayer MoS_2) and hybrid van der Waals structures (e.g. graphene on h-BN). For graphene on h-BN it is known that it results in a strong enhancement of the mobility as compared to the usual graphene on a SiO_2 surface. It will be interesting to investigate whether or not the h-BN substrate changes fundamentally the thermal rippling properties of graphene.

In the other parts of the thesis, I studied the spectral and electronic properties of graphene nanoflakes. Chemical, electronic, and magnetic properties of clusters were found to vary noticeable with size and composition due to both chemical interactions and quantum confinements. Therefore, cluster-assembled materials with highly tunable magnetic

and electronic properties can be useful for a great variety of potential technologies. It is also demonstrated recently that cluster-assembled materials can retain the characteristics of the original building block [312]. It will be interesting to investigate clusters of 2D materials (e.g., h-BN, silicene, etc.), their corresponding bilayer counterpart and to learn how size and shape of those clusters influence their mechanical properties.

CHAPTER 10

Overzicht en toekomst perspectieven

10.1 Overzicht van de thesis

Dankzij de uitzonderlijke eigenschappen van grafeen en andere 2D materialen (zoals h-BN, fluorografeen, MoS_2, ...), zijn overal ter wereld onderzoeksgroepen deze materialen aan het bestuderen. In deze thesis onderzoek ik de spectrale en elektronische eigenschappen van grafeen nanovlokken en de thermo mechanische eigenschappen van enkele lagen hexagonaal boron-nitride (h-BN) en fluorografeen (FG). In mijn doctoraat heb ik klassieke moleculaire dynamica gebruikt met 'bond-order' potentialen en dichtheidsfunctionaal theorie.

In hoofdstuk 3 worden atomistische simulaties besproken die gebruik maken van de Brenner tweede generatie "bond order" (REBOII) interatomaire potentiaal functie om de vibrationele eigenschappen van nanografeen te bestuderen. We onderzochten de frequentie van de normaal modi als functie van het aantal deeltjes voor nanografeen C_N ($2 \leq N \leq 55$) en 'H-passivated' koolstof clusters ($11 \leq N \leq 55$). De fonon toestandsdichtheid van verschillende clusters werd vergeleken met de theoretische resultaten voor grafeen. We vonden dat deze goed overeenkwamen voor de akoestische en optische fononen in grote clusters. Gebruik makend van de eigenfrequenties van de normaal modi berekenden we de specifieke warmte binnen de harmonische benadering voor koolstof clusters met verschillende groottes. We vonden dat in de hoge temperatuurslimiet deze de bulk waarde benaderden.

In hoofdstuk 4 bestudeerden we het smelten van nanografeen dat geobserveerd werd in hoofdstuk 3. Hierbij maakten we gebruik van moleculaire dynamica simulaties en de Lindemann index. De smelttemperatuur van kleine vlokken is lager dan deze van grafeen of grafeen nanostroken. De Lindemann index is temperatuursafhankelijk en het bleek een goede grootheid te zijn om te bepalen of er structurele veranderingen van de clusters optraden. De smelttemperatuur van kleine vlokken stijgt, gemiddeld gezien, als functie van het aantal atomen in de koolstof nanovlokken. Alle onderzochte nanovlokken vertonen een karakteristiek gedrag alvorens te gaan smelten. De smelttemperatuur van nanovlokken met defecten is lager dan deze van defectloze naburige nanovlokken. 'H-passivated' clusters hebben een hogere smelttemperatuur dan gewone clusters met hetzelfde aantal koolstofatomen. Onze simulaties helpen ook om de vorming van defecten (als gevolg van stijgende temperatuur) in grafeen nanovlokken te begrijpen. Dit kan gebruikt worden om de groei en de thermische behandeling van nanografeen te begrijpen. DFTB berekening bevestigen ook de N-afhankelijkheid van de smelttemperatuur.

In hoofdstuk 5 bespreken we atomistische simulaties die gebruik maken van de ReaxFF interatomaire potentiaal om het smelten van gedeeltelijk gefluoriceerd grafeen (PFG) en volledig gefluoriceerd grafeen (FGF) te bestuderen. De PFG's voor $N_F/N_C < 40\%$ beginnen fluor atomen te verliezen rond 2000 K en worden dan pristine grafeen met defecten op hogere temperaturen. Bij PFG's met N_F/N_C $\sim$40-60$\%$ worden er echter grote defecten gevormd rond $\approx$ 1500 K (F atomen breken de originele lokale bindingen en zetten zich vast aan de rand van deze ringen). Zeer traag gaan ze over naar de vloeistof fase als de temperatuur stijgt zodat onder 5000 K de vloeistof en de vaste stof fases coëxistent zijn. Voor grotere N_F/N_C $\sim$60-100$\%$, blijven de F-atomen gebonden aan grafeen tot de vlokken smelten. PFG's en FFG's veranderen snel in 3D spaghetti-achtige koolstofketens. De smelttemperatuur voor FFG is berekend op 2800K. De minimum smelttemperatuur wordt verkregen bij een fluorbezetting van 70$\%$. Onze bevindingen zijn daarom consistent met de experimentele reversibiliteit van fluorinatie in monolaag grafeen.

In hoofdstuk 6 zijn de thermische eigenschappen van een boor nitride vel bestudeerd gebruikmakend van atomistische simulaties op grote schaal. We toonden aan dat de schalingseigenschappen van een h-BN vel zeer goed overeenkomen met deze verkregen uit membraan theorie en dus dat de thermisch geëxciteerde golven niet gekarakteriseerd worden door een bepaalde golflengte. Gebruik makend van het harmonisch deel van de hoogte-hoogte correlatie functie vonden we dat de stijfte van het materiaal stijgt met de temperatuur, maar minder dan bij grafeen. We vonden dat de overgang naar een geknikt systeem bij h-BN afhangt van de richting waarin compressiekrachten werken en dat deze veel kleiner is dan bij grafeen. De gevonden molaire warmtecapiciteit stemt zeer goed

overeen met het bekende Dulong-Petit getal, 25.2 $J\,mol^{-1}K^{-1}$ en de thermische expansie coëfficiënt blijkt positief te zijn en gelijk aan 7.2 $\times 10^{-6}K^{-1}$. De Grüneisen parameter 0.89 blijkt kleiner te zijn dan deze van grafeen, namelijk 1.2. We toonden aan dat het verschil in stijfheid tussen GE en h-BN leidt tot verschillende manieren van vervormingen in de nabijheid van ofwel uniaxiale- of schuifspanning.

In hoofdstuk 7 voerden we een nieuwe set parameters in voor de C-F covalente binding in de ReaxFF potentiaal en testte ze op verscheidene moleculen. Vervolgens werden er moleculaire simulaties gebruikt om het gedrag van thermische rimpels en de mechanische respons van fluorografeen FG onder uniaxiale spanning te bestuderen. De resultaten werden dan vergeleken met deze voor grafeen (GE), grafaan (GA) en hexagonaal boor nitride (h-BN). We vonden dat fluorografeen een vlak vel blijft, gelijkaardig met grafaan, tot hoge temperaturen, i.e. tot 900K. De stijfheid van FG blijkt onafhankelijk te zijn van temperatuur en de gevonden Young's modulus komt goed overeen met het experiment.

In hoofdstuk 8 hebben we gebruik gemaakt van uitvoerige ab-initio berekeningen om de elektronische eigenschappen van de grafeen nanovlokken (GFN's) die in hoofdstuk 3 voorkwamen voor twee verschillende randconfiguraties te bestuderen. De n-voudige symmetrie verzaakt geen netto dipool in GNF's. Het breken van deze n-voudige symmetrie door heptagon en pentagon defecten en het reduceren van de symmetrie tot spiegel symmetrie versterkt de polarizatie. We vonden dat hoe groter het dipool moment is, hoe lager de energie kloof voor beide types van gesatureerde atomen. Gemiddeld verkleinde de energiekloof snel tot $N_c = 35$ maar werd erna zo goed als constant. De elektrostatische potentiaal rond de GNF's beïnvloeden zowel de polarisatie als de enerigekloof van de GNF's. Onze spin gepolariseerde berekeningen tonen dat het verschil tussen de energiekloven van spin op en -neer elektronen maximaal is voor GNFs met voornamelijk pentagon (en heptagon) defecten. De H-passivated GNF's hebben een groter verschil tussen de spin-op en spin-neer energiekloof in vergelijking met F-passivated GNF's. De bilaag GNF's tonen een duidelijke dipool-dipool interactie, dewelke het gevolg is van wederzijdse oriëntatie van de permanente dipolen in het systeem. De bilaag FNF's zijn niet noodzakelijk vlak en kunnen gebogen structuur bezitten.

10.2 Toekomst perspectieven

In hoofdstuk 6 en 7 onderzocht ik de thermo-mechanische eigenschappen van 2D grafeenachtige materialen, e.g. h-BN en FG. Het zou zeer interessant zijn om thermische rimpels te onderzoeken bij andere 2D materialen zoals silicene, silicane, MoS_2, H-BN en hun cor-

responderende van der Waals structuren (zoals bilaag MoS_2) en hybride van der Waals structure (zoals grafeen op h-BN). Voor grafeen op h-BN weet men dat het resulteert in een sterke stijging van de mobiliteit in vergelijking met het normale grafeen op een SiO_2 oppervlak. Het is interessant om na te gaan of het h-BN substraat de thermische rimpels van grafeen substantieel beïnvloedt.

In andere delen van de thesis onderzocht ik de spectrale en elektronische eigenschappen van grafeen nanovlokken. Chemische, elektronische en magnetische eigenschappen van clusters bleken sterk te variëren met de grootte en de samenstelling als gevolg van zowel chemische interacties al kwantum opsluiting. Hierdoor hebben materialen die gebaseerd zijn op clusters hoge aanpasbare magnetische en elektrische eigenschappen die gebruikt kunnen worden voor een zeer breed gamma van mogelijke technologieën. Recent werd ook aangetoond dat materialen die gebaseerd zijn op clusters de karakteristieken van de originele bouwstenen kunnen bewaren [312]. Het is interessant om na te gaan hoe bij clusters van 2D materialen (zoals h-BN, silicene, ...) en hun bijbehorende bilagen de grootte en vorm hun mechanische eigenschappen beïnvloedt.

APPENDIX A

LAMMPS

LAMMPS (Large-scale Atomic/Molecular Massively Parallel Simulator) is a molecular dynamics program from Sandia National Laboratories [216, 251]. LAMMPS makes use of MPI for parallel communication and is a free, open-source software, distributed under the terms of the GNU General Public License, which means anybody can use or modify the code. LAMMPS can model atomic, polymeric, biological, metallic, granular, and coarse-grained systems using a variety of force fields and boundary conditions. LAMMPS can model systems from a few particles up to million or billions.

LAMMPS integrates Newton's equations of motion for collections of atoms, molecules, or macroscopic particles that interact via short- or long-range forces with a variety of initial and/or boundary conditions. For computational efficiency LAMMPS uses nearest-neighbor lists to track nearby particles. The lists are optimised for systems with particles that are repulsive at short distances, so that the local density of particles never becomes too large. On parallel machines, LAMMPS uses spatial-decomposition techniques to partition the simulation domain into small 3D sub-domains, one of which is assigned to each processor. Processors communicate and store "ghost" atom information for atoms that border their sub-domain. LAMMPS is most efficient (in a parallel sense) for systems whose particles fill a 3D rectangular box with roughly uniform density.

A.1 LAMMPS features

In this section, we highlights some LAMMPS features with specific commands which give more details.

A.1.1 General features

- Runs on a single processor or in parallel
- Distributed-memory message-passing parallelism (MPI)
- Spatial-decomposition of simulation domain for parallelism
- Open-source distribution
- Highly portable C++
- Easy to extend with new features and functionality
- Runs from an input script

A.1.2 Particle and model types

- Atoms
- Granular materials
- Coarse-grained mesoscale models
- Organic molecules
- Rigid collections of particles

A.1.3 Force fields

- **Pairwise potentials:** Lennard-Jones, Morse, Yukawa
- **Many body potentials:** Tersoff, REBO, AIREBO, ReaxFF, COMB, Stillnger-Weber, EAM, MEAM

A.1.4 Ensembles, constrains, and boundary conditions

- 2D or 3D systems
- Constant NVE, NVT, NPT integrators
- Thermostatting option for groups of atoms
- Pressure control via Nose/Hoover or Berendsen barostatting in 1 to 3 dimensions
- Variety of additional boundary conditions and constrains

A.1.5 Integrators

- Velocity-Verlet integrator
- Brownian dynamics
- Rigid body integration
- Energy minimization via conjugate gradient or steepest descent relaxation

A.1.6 Output

- Log file of thermodynamic info
- Text dump files of atom coordinates, velocities, other per-atom quantities
- User-defined system-wide (log file) or per-atom (dump file) calculations
- Spatial and time averaging of per-atom quantities

A.1.7 Specialized features

- *Stochastic rotation dynamics (SRD)*
- *Atom-to-continuum coupling* with finite elements
- *Direct Simulation Monte Carlo* for low-density fluids
- *Targeted* and *steered* molecular dynamics
- *Two temperature electron model*
- *Peridynamics mesoscale modeling*

A.2 LAMMPS non-features

Many tools which are needed to pre- and post- process the data are not included in LAMMPS for several reasons:

- To make LAMMPS simple
- They may be not parallel operations
- There exits already many well robust codes

Specially, LAMMPS does not build molecular system and visualize MD simulations. Usually, most of the users use other codes or write their own codes for these tasks. For high-quality visualisation, visual molecular dynamics (VMD) package is recommended.

APPENDIX B

DFTB+

Density functional theory (DFT) methods are the standard theoretical techniques for electronic structure calculations. But due to demanding computational calculations and unable to handle long range forces (e.g. van der Waals) correctly, charge transfer excitations, isomerization reactions, its applications are restricted to small systems and small time scale. Large biosystems, adsorption process, nanostructures, molecular dynamics studies on nanosecond time scales, clusters and molecules with thousands of atoms, computer aided drug and materials design, self-assembling systems, nanoreactors and supramolecular chemistry are some of the fields beyond the capability of ab-initio or DFT methods.

Density-functional tight-binding (DFTB) is an approximate method based on DFT which does not require large amounts of empirical parameters as other semi-empirical methods (e.g., AM1 (Austin Model 1), PM3) require. The parameters are obtained from DFT calculations. The wave function in DFTB are Kohn-Sham-like orbitals, so any property can be inherited from DFT. DFT extensions such as relativistic effects and London dispersion can be easily added to DFTB. It has many various potential applications such as calculation of hyperfine coupling constants, magnetic properties, vibrational spectra of solids and molecule, nuclear magnetic shielding tensors, geometries, and dynamical properties. Optical properties can also be calculated using time-dependent DFTB. DFTB is also closely connected to the tight-binding methods. The self-consistent charge extension of DFTB (SCC-DFTB) improves the accuracy of the method.

The non-self-consistent DFTB methods are suitable for homonuclear covalent systems or highly ionic systems. But where chemical bonds are sensitive to more charge bal-

ance between atoms, i.e. heteronuclear molecules and polar semiconductors and the cases where long-range Coulomb interactions have a significant role, self-consistent charge correction DFTB (SCC-DFTB) improves the results.

London interactions, also called dispersion force (attractive force between nonpolar molecules, due to their mutual polarizability) are weak in nature. It affects many fundamental processes in chemistry, physics and biology such as the formation of molecular crystals, the structure of biological molecules such as proteins and DNA, absorption processes, π-π stacking interactions. DFTB and SCC-DFTB don't calculate the dispersion relation because they treat only short-range atomic potentials. Therefore, dispersion energy is calculated separately using empirical potential and then added to the DFTB total energy. Some brief reviews on DFTB are recommended [313, 314].

B.0.1 Strength

- Complements quantum chemical semi-empirical methods
- Transparent derivation, inclusion of electron correlation on the DFT-GGA level
- Parametrization process based on a few molecules per pair of atom type predict molecular geometries quite reliably

B.0.2 Weakness

- Improvement in heat of formation (basis for most of the semi-empirical methods for parametrization) and parametrization of more elements across the periodic table needed

DFTB+ is a standalone fast and efficient DFTB implementation [315]. It is developed at the Bremen Center for Computational Material Science (Prof. Frauenheim). The main features of DFTB+ are:

- SCC (self-consistent charge correction) and Non-SCC calculations
  - Cluster/molecular systems
  - Periodic systems (arbitrary K-point sampling, band structure calculations, etc.)
- Geometry and lattice optimisation
- Geometry optimisation with constraints (in xyz-coordinates)
- Molecular dynamics (NVE, NPH, NVT, and NPT ensembles)

- Numerical vibrational mode calculations
- Finite temperature calculations
- Dispersion corrections (van der Waals interactions)
- Spin polarised calculations
- Ability to treat f-electrons
- LDA+U/pSIC extensions
- L.S coupling
- 3rd order correction and other DFTB3 features
- OpenMP parallelisation

APPENDIX C

GAUSSIAN09

Gaussian is a widely used computational chemistry package originally developed in 1970 by John Pople [316]. Gaussian contains a wide range of ab initio functionality, such as Hartree-Fock (HF), Møller-Plesset perturbation theory (MP2, MP3, MP4, MP5), configuration interaction (CI), coupled cluster (CC), quadratic configuration interaction (QCI), and quantum chemistry composite methods (G1,G2,G3,W1). Semiempirical methods available include Austin Model 1 (AM1), Parameterized Model number 3 (PM3). Molecular mechanics methods include "Assisted Model Building with Energy Refinement" (Amber) and Universal force field (UFF). Gaussian also supports large number of DFT methods. B3LYP is the most popular hybrid method because it uses corrections for both gradient and exchange correlation. GaussView is the famous graphic interface to create Gaussian files and viewing results.

C.1 Basis Sets

A basis set is a set of functions that describes the shape of atomic orbitals (AOs). The molecular orbitals (MOs) are computed using the linear combination of AOs (LCAO). Both Slater Type Orbitals (STOs) and Gaussian Type Orbitals (GTOs) are used to describe AOs. STOs describe the shape of AOs more closely than GTOs, but GTOs are much easier to compute. Therefore, it is common practise to compute several GTOs and combine them to describe an orbital than to compute one STOs. This is why the combination of GTOs are commonly used to describe STOs, which in turn, describe AOs.

C.1.1 Split valence

Split valence basis sets (also called Pople basis sets) allow to specify the number of GTO's to use for core and valence electron separately. There are double Zeta (2 functions per AO) or triple Zeta. The notation is as follow: K-LMG, where

- K=number of sp-type inner shell GTOs
- L=number of inner valence s- and p- type GTOs
- M=number of outer valence s- and p- type GTOs
- G=indicates that GTOs are used

examples:

- 3-21G: 3 GTOs for inner shell, 2 GTOs for inner valence, 1 GTO for outer valence
- 6-311G: 6 GTOs for core orbital, 3 GTOs for inner valence, 2 different GTOs for outer valence (triple zeta)

C.1.2 Polarized

Pople basis sets can be modified by letting the AOs distort from their original shape (get polarized under the influence of the surroundings).

- (d) or * type: d-type functions added on to atoms other than hydrogen and f-type functions added on to transition metals
- (d,p) or ** type: p-type functions added on to hydrogens, d-type functions added on to all other atoms, f-type functions added on to transition metals

example: 6-31G(d) or 6-31G**

C.1.3 Diffuse

Pople basis sets can be improved by letting the electron move far away from the nucleus, creating diffuse orbitals (useful with anions, excited states and molecules with lone pairs). Diffuse functions can be added as + or ++ in front of G.

- +: diffuse functions added on to atoms other than hydrogen
- ++: diffuse functions added on to all atoms

example: 6-31+G(d) or 6-31++G(d)

C.1.4 Correlation-consistent

Pople basis sets are optimised at a Hartree-Fock level but create doubt that this optimization might not be best for correlated computation. Thom Dunning created a set of basis sets optimised using correlated (CISD) wavefunctions. They are denoted as cc-pVXZ, where:

- cc= indicates that it is a correlation-consistent basis
- pV= indicates that it is a polarized valence basis
- XZ= indicates the zeta number (X=D for double, T for triple, Q for quadruple)
- The prefix aug-can be used to add diffuse functions

example: cc-pVDZ or aug-cc-pVTZ

C.2 Types of calculation

Gaussian can perform many calculations on a given molecule at the same time. Few operations are addressed below:

C.2.1 Geometry optimization

Keyword: Opt
Geometry optimization is the procedure to find the minimum energy of the molecule. This process is computationally demanding so better to save the optimized structure for further study rather than optimizing again. Stable = Opt or vibrational analysis (with no imaginary frequency) can be performed to test the stability of the system.

C.2.2 Frequencies

Keyword: Freq
Scaling: The frequencies generated must be scaled according to the theoretical method and basis set used.
Stability: If all the frequencies are real then the system is stable.
Anharmonic frequencies: By default, Gaussian09 compute frequencies based on harmonic oscillator approximation. For more accurate results, anharmonic corrections can be included using "Anharmonic" keyword.
Raman: Raman intensities can be calculated using "raman" keyword.

Note: Same combination of theoretical model and basis set should be for both the Opt and Freq calculations.

C.2.3 Molecular orbitals and population analysis

Keyword: Pop=X; X=None, Reg, Full, NBO,...
Population analysis: Population analysis is a mathematical way of partitioning a wave function or electron density into charges on the nuclei, bond orders, and other related information. These are probably most widely used results that are not experimentally observable.

- X=None; no orbital information displayed
- X=REG; HOMO-5 up to LUMO+5 orbital information displayed
- X=FULL; all orbitals information displayed
- X=NBO; Mulliken analysis is replaced by Natural Bond-Order analysis
- X=ESP; This method uses electrostatic potential to compute charges on nuclei. ESP is usually the best to describe charge interactions with other species

APPENDIX D

Theory of 2-dimensional crystalline membrane

The structural and thermal properties of membranes are of fundamental importance and are relevant for technological applications. Phenomenological theories based on elasticity display nontrivial scaling behavior of physical properties, like in- and out-of-plane atomic displacements. In 3D systems, this type of behavior takes place only close to the critical points, whereas in 2D systems this behavior happens at any finite temperature. Graphene, a truly 2D membrane presents a model system for which an atomistic description becomes possible using accurate inter-atomic potentials.

The experimental observation of ripples and bending fluctuations in freely suspended graphene, which can be one of the dominant scattering mechanisms limiting the electron mobility, initiated new theoretical approach in order to look into its structural properties. The structural state influences the mechanical properties that are important for numerous potential applications of graphene. Phenomenological theories assume that the membrane thickness is negligible in comparison to the lateral dimensions while using atomistic simulations, one can also distinguish between single, bi- and many layers. The aim of this appendix is to understand the physics of 2D membrane from phenomenological theories and compare them with atomistic approaches.

Phenomenological Theory of Crystalline Membranes: Lattice dynamics theories are based on the harmonic approximation assuming atomic displacements from equilibrium to be much smaller than the interatomic distance d. For 3D systems, harmonic approximation holds up to the melting temperature while in 2D system, this assumption fails. Therefore, Landau and Peierls (in 1930s) and later Mermin-Wagner, suggested that

2D crystals cannot exist.

Lattice dynamics of graphene: Assume that the atomic displacements $\vec{u}$ satisfy the condition (harmonic approximation)

$$\left\langle \vec{u}_{n,j}^2 \right\rangle << d^2. \tag{D.1}$$

Since graphene has two atoms per unit cell. Therefore, there are six phonon branches (3 acoustic and 3 optical) which contain four in-plane and two out-of-plane modes . In case of finite temperature (in the harmonic approximation), the mean-square atomic displacement is

$$\left\langle u_{nj}^{\alpha} u_{nj}^{\beta} \right\rangle = \sum_{\lambda} \frac{\hbar}{2N_0 M_j \omega_\lambda} (e_{\lambda j}^{\alpha})(e_{\lambda j}^{\beta}) coth\left(\frac{\hbar\omega_\lambda}{2T}\right), \tag{D.2}$$

where $\lambda = (\vec{q}, \zeta)$ are phonon labels, $\vec{e}$ is the polarization vector and N_0 is the number of elementary cells.

For in-plane deformations at any finite temperature, the sum in Eq. (D.2) is logarithmically divergent due to the contribution of the acoustic branches with $\omega \propto q$ for $q \to 0$. This divergence is cut at the minimal wavevector $q_{min} \sim L^{-1}$ (L is the sample size), thus

$$\left\langle x_{nj}^2 \right\rangle = \left\langle y_{nj}^2 \right\rangle \approx \frac{T}{2\pi M c_s^2} ln\left\langle \frac{L}{d} \right\rangle, \tag{D.3}$$

where c_s is the average sound velocity. For $\alpha = z$, the out-of-plane acoustic phonons divergence more strongly than in-plane phonons (from Eq.(D.2))

$$\left\langle h_{nj}^2 \right\rangle \propto \frac{T}{E_{at}} \sum_{q} \frac{1}{q^4} \propto \frac{T}{E_{at}} L^2, \tag{D.4}$$

where E_{at} is of the order of the cohesive energy. Landau and Peierls concluded from these results that 2D crystals cannot exits. But in a true sense, this shows only the in-applicability of the harmonic approximation, due to the violation of Eq. (D.1).

The Statistical Mechanics of Crystalline Membranes. In the limit of $q \to 0$, acoustic modes can be described within elasticity theory. Therefore, the deformation energy can be read as

$$H = \frac{1}{2} \int d^2x \left(\kappa(\nabla^2 h)^2 + 2\mu u_{\alpha\beta}^2 + \lambda u_{\alpha\alpha}^2\right), \tag{D.5}$$

where h is out-of-plane deformation, and the deformation tensor $u_{\alpha\beta}$ is

$$u_{\alpha\beta} = \frac{1}{2}\left(\frac{\partial u_\beta}{\partial x_\alpha} + \frac{\partial u_\alpha}{\partial x_\beta} + \frac{\partial h_\beta}{\partial x_\alpha}\frac{\partial h_\alpha}{\partial x_\beta}\right), \tag{D.6}$$

κ is the bending rigidity and μ and λ are Lamé coefficients. In the deformation tensor, the nonlinear terms $\frac{\partial h_\beta}{\partial x_\alpha}$ are included while $\frac{\partial u_\gamma}{\partial x_\alpha}$ is excluded since out-of-plane fluctuations are stronger than in-plane ones. Neglecting all nonlinear terms in the deformation tensor, H is split into two independent Hamiltonians in $\vec{q}$ representation

$$H_0 = \frac{\kappa}{2}\sum_{\vec{q}} q^4 |h_{\vec{q}}|^2 + \frac{1}{2}\sum_{\vec{q}} \left[\mu q^2 |\vec{u}_{\vec{q}}|^2 + (\lambda+\mu)(\vec{q}.\vec{u}_{\vec{q}})^2\right], \tag{D.7}$$

where the subscript 0 indicates the harmonic approximation and $h_{\vec{q}}$ and $\vec{u}_{\vec{q}}$ are Fourier components of h($\vec{r}$) and $\vec{u}(\vec{r})$, respectively.

The correlation functions in the harmonic approximation are

$$G_0(\vec{q}) = \left\langle |h_{\vec{q}}|^2 \right\rangle_0 = \frac{T}{\kappa q^4}, \tag{D.8}$$

$$D_0^{\alpha\beta}(\vec{q}) = \left\langle u^*_{\alpha\vec{q}} u_{\beta\vec{q}} \right\rangle_0 = \frac{q_\alpha q_\beta}{q^2}\frac{T}{(\lambda+2\mu)q^2} + \left[\delta_{\alpha\beta} - \frac{q_\alpha q_\beta}{q^2}\right]\frac{1}{\mu q^4}, \tag{D.9}$$

where $<>_0$ means averaging with the Hamiltonian H_0.

For a surface z=h(x,y) the components of the normal are

$$n_x = -\frac{\partial h}{\partial x}\frac{1}{\sqrt{1+|\nabla h|^2}}, \tag{D.10}$$

$$n_y = -\frac{\partial h}{\partial y}\frac{1}{\sqrt{1+|\nabla h|^2}}, \tag{D.11}$$

$$n_z = \frac{1}{\sqrt{1+|\nabla h|^2}}, \tag{D.12}$$

where ∇h is a 2D gradient. If $|\nabla h| << 1$, the normal-normal correlation function is related to $< |h_{\vec{q}}|^2 >$ by

$$\left\langle \vec{n}_{\vec{q}} \vec{n}_{\vec{-q}} \right\rangle = q^2 \left\langle |h_{\vec{q}}|^2 \right\rangle. \tag{D.13}$$

On substituting Eq.(D.8) into Eq.(D.13), we find

$$\left\langle \vec{n}_{\vec{q}} \vec{n}_{\vec{-q}} \right\rangle_0 = \frac{T}{\kappa q^2}. \tag{D.14}$$

A membrane is globally flat if the correlation function

$$\langle \vec{n}_0 \vec{n}_{\vec{R}} \rangle = \sum_{\vec{q}} \left\langle |\vec{n}_{\vec{q}}|^2 \right\rangle exp\left(i\vec{q}\vec{R}\right) \tag{D.15}$$

tends to a constant as R$\rightarrow \infty$ (normals at large distances have, on average, the same direction). Instead, substituting Eq.(D.14) into Eq.(D.15) leads to a logarithmic divergence. Moreover, the mean square in-plane and out-of-plane displacements calculated from Eqs.(D.8) and (D.9) are divergent as L$\rightarrow \infty$ as already shown by using lattice dynamics calculations in previous section. Therefore it is concluded that the statistical mechanics of 2D systems cannot be based on the harmonic approximation. This situation can be changed by considering the coupling between $\vec{u}$ and h (the nonlinear terms) in the deformation tensor (Eq. (D.6)).
The problem of interacting fluctuations where the low-q contribution is dominant occurs at a critical point in a 3D system whereas for a 2D system, such critical situation occurs at any finite temperature.

The correlation function $G(\vec{q}) = \left\langle |h_{\vec{q}}|^2 \right\rangle$ satisfies the Dyson equation

$$G^{-1}(\vec{q}) = G_0^{-1}(\vec{q}) + \Sigma(\vec{q}), \tag{D.16}$$

where self-energy $\Sigma(\vec{q})$ can be calculated using perturbation theory. The renormalized bending rigidity $\kappa_R(q)$ can be introduced by

$$G(\vec{q}) = \frac{T}{\kappa_R(q) q^4}. \tag{D.17}$$

The first-order anharmonic correction to κ is

$$\delta\kappa \equiv \kappa_R(q) - \kappa = \frac{3TY}{8\pi\kappa q^2}, \tag{D.18}$$

where Y=$[4\mu(\lambda+\mu)/\lambda+2\mu]$ is the 2D Young modulus. At

$$q = q^* = \sqrt{\frac{3TY}{8\pi\kappa^2}} \tag{D.19}$$

the correction $\delta\kappa = \kappa$, and the coupling between in-plane and out-of-plane distortions cannot be considered in the context of perturbation.

In the presence of strongly interacting long-wavelength fluctuations, scaling considerations are useful. Let us assume the behaviour of the renormalized bending rigidity $\kappa_R(q)$ at small q is determined by some exponent η, $\kappa_R(q) \propto q^{-\eta}$, hence

$$G(q) = \frac{A}{q^{4-\eta} q_0^{\eta}}, \left\langle |\vec{n}_{\vec{q}}|^2 \right\rangle = \frac{A}{q^{2-\eta} q_0^{\eta}} \tag{D.20}$$

where the parameter $q_0 = (Y/\kappa)^{1/2}$ of the order of d^{-1} is introduced to make A dimensionless. One can assume also a renormalization of the effective Lamé coefficients $\lambda_R(q)$, $\mu_R(q) \propto q^{\eta_u}$ which means

$$\left\langle u^*_{\alpha\vec{q}} u_{\beta\vec{q}} \right\rangle \propto \frac{1}{q^{2+\eta_u}}. \tag{D.21}$$

Finally, we assume that anharmonicities changes Eq. (D.4) into

$$< h^2 > \propto L^{2\zeta}. \tag{D.22}$$

The values η, η_u and ζ are similar to the critical exponent in the theory of critical phenomena and are not independent

$$\zeta = 1 - \eta/2, \eta_u = 2 - 2\eta. \tag{D.23}$$

The exponent η_u is positive if $0<\eta<1$. This means that the interaction between out-of-plane and in-plane phonons makes the former one harder and the latter one softer. The so-called Self-Consistent-Screening-Approximation gives $\eta \approx 0.82$ [**?**, 317], whereas a more accurate renormalization group approach yields $\eta \approx 0.85$ [318]. Now, there is no divergence in the correlation function from the region of small q (see Eq.(D.20)).

For a complete description of membrane theory, readers are highly recommended to read chapter 9 of Ref. [319].

APPENDIX E

Optimised potential parameters

E.1 REBOII potential parameters for Hydrocarbons:

Table E.1: Parameters for the carbon-carbon pair terms (taken from Ref. [116]). These parameters are valid for all atoms interacting within the first neighbor range in REBOII potential as discussed in Chapter 2.

Parameter	Value
B_1 (eV)	12388.79197798
B_2 (eV)	17.56740646509
B_3 (eV)	30.71493208065
β_1 (Å^{-1})	4.7204523127
β_2 (Å^{-1})	1.4332132499
β_3 (Å^{-1})	1.3826912506
Q (Å)	0.3134602960833
A (eV)	10953.544162170
α (Å^{-1})	4.7465390606595
D_{min}	1.7
D_{max}	2.0

Table E.2: Parameters for the pure hydrogen bond order potential (taken from Ref. [116]).

Parameter	Value
B_1 (eV)	29.632593
B_2 (eV)	0
B_3 (eV)	0
β_1 (Å^{-1})	1.71589217
Q (Å)	0.370471487045
A (eV)	32.817355747
α (Å^{-1})	3.536298648
D_{min}	1.1
D_{max}	1.7

Table E.3: Parameters for the carbon-hydrogen pair terms (taken from Ref. [116]).

Parameter	Value
B_1 (eV)	32.3551866587
B_2 (eV)	0
B_3 (eV)	0
β_1 (Å^{-1})	1.43445805925
Q (Å)	0.340775728
A (eV)	149.94098723
α (Å^{-1})	4.10254983
D_{min}	1.3
D_{max}	1.8

E.2 Optimized Tersoff potential parameters for hexagonal boron nitride:

Table E.4: Tersoff optimized interatomic potential parameters for hexagonal boron nitride structures (taken from Ref. [249]). These parameters are valid for all atoms interacting within the first neighbor range in Tersoff potential as discussed in Chapter 2.

Parameter	Value
A (eV)	1380
B (eV)	340.0
λ_1 (Å^{-1})	3.568
λ_2 (Å^{-1})	2.199
λ_3 (Å^{-1})	0.000
n	0.72751
c	25000
β (10^{-7})	1.25724
d	4.3484
h	-0.89000
R (Å)	1.950
D (Å)	0.050

E.3 ReaxFF potential parameters for fluorographene:

Table E.5: General parameter values used in the ReaxFF force field for C-F molecules.

Atom	Mass (a.m.u.)	Val	Val(e)	Val(boc)
C	12.0000	4.0000	4.0000	4.0000
F	18.9984	1.0000	4.0000	4.0000

Table E.6: Parameter values used in the bond order term of the ReaxFF force field for C-F molecules.

Bond	p_{bo1}	p_{bo2}	p_{bo3}	p_{bo4}	p_{bo5}	p_{bo6}
CC	6.7452	1.0000	9.0638	1.0000	-0.4710	0.5108
CF	5.4719	1.0000	15.0000	1.0000	-0.5000	1.0460
FF	7.3516	1.0000	15.0000	1.0000	-0.3500	0.8427

Table E.7: Parameter values used in the valence angle term of the ReaxFF force field for C-F molecules.

Angle	p_{val1}	p_{val2}	p_{val4}	p_{val7}	Θ
CCC	38.5829	0.7209	1.0670	0.1409	72.7917
CCF	35.8484	6.6125	3.0000	0.9453	74.0446
FCF	49.0744	5.9913	2.3020	0.7835	77.8443
CFC	19.9962	3.2299	1.1537	2.1012	0.0000
CFF	25.0000	1.0000	1.0400	1.0000	0.0000

Table E.8: Parameter values used in the torsion angle term of the ReaxFF force field for C-F molecules.

Atom	V_1 (Kcal/mol)	V_2 (Kcal/mol)	V_3 (Kcal/mol)	p_{tor1}	p_{cot1}
CCCC	-0.5000	53.0886	-0.1335	-6.2875	-1.9524
0CC0	0.0000	50.0000	0.3000	-4.0000	-2.0000
CCCF	0.5000	0.1000	0.4683	-11.5274	-1.7255
FCCF	-0.5000	95.4727	-0.2080	-4.8579	-1.7255
0CF0	4.0000	45.8264	0.9000	-4.0000	0.0000
0FF0	4.0000	45.8264	0.9000	-4.0000	0.0000

Table E.9: Constants used in the energy terms in ReaxFF.

Parameter	Description	Parameter	Description
r_σ	σ reference bond length	r_π	π reference bond length
$r_{\pi\pi}$	$\pi\pi$ reference bond length	val_i^e	number of valences electrons of atoms i
p_{bo1}	bond order parameter	p_{be1}	bond energy param
D_e^σ	σ bond energy param	D_e^π	π bond energy param
$D_e^{\pi\pi}$	$\pi\pi$ bond energy param	p_{lp1}	lone pair parameter
p_{lp2}	lone pair parameter	$n_{lp,opt}$	optimal nnumber of lone pairs
p_{val1}	valence angle param	p_{val2}	valence angle param
p_{3con1}	3-body conjugation param	p_{4con1}	4-body conjugation param
p_{tor1}	torsion parameter	p_{hb1}	hydrogen bond param
p_c	carbon triple bond param	V_1	torsion parameter
R_{cut}	Taper cutoff radius	p_{ovun1}	atom over/underb. param
γ_{ij}	Coulomb parameter	C	Coulomb parameter
p_{vdW}	vdW parameter	α_{ij}	vdW parameter
γ_ω	vdW parameter	D_{ij}	vdW parameter

The potential parameters used in this thesis can be found from the LAMMPS directory http://lammps.sandia.gov/:

1. lammps/potentials/BNC.tersoff
2. lammps/potentials/CH.airebo
3. lammps/potentials/ffield.reax.FC.

Bibliography

[1] K. S. Novoselov, A. K. Geim, S. V. Morozov, D. Jiang, Y. Zhang, S. V. Dubonos, I. V. Grigorieva, and A. A. Firsov, *Electric field effect in atomically thin carbon films.* Science **306**, 666 (2004).

[2] A. H. C. Neto, F. Guinea, N. M. R. Peres, K. S. Novoselov, and A. K. Geim, *The electronic properties of graphene.* Rev. Mod. Phys. **81**, 109 (2009).

[3] S. D. Sharma, S. Adam, E. H. Hwang, and E. Rossi, *Electronic transport in two-dimensional graphene.* Rev. Mod. Phys. **83**, 407 (2011).

[4] C. Lee, X. D. Wei, J. W. Kysar, and J. Hone, *Measurement of the elastic properties and intrinsic strength of monolayer graphene.* Science **321**, 385 (2008).

[5] A. A. Balandin, *Thermal properties of graphene and nanostructured carbon materials.* Nature Mater. **10**, 569 (2011).

[6] A. K. Geim and K. S. Novoselov, *The rise of graphene.* Nat. Mater. **6**, 183 (2007).

[7] (a) K. S. Novoselov, V. I. Falko, L. Colombo, P. R. Gellert, M. G. Schwab, and K. Kim, *A roadmap for graphene.* Nature **490**, 192 (2012). (b) V. Georgakilas, M. Otyepka, A. B. Bourlinos, V. Chandra, N. Kim, K. Christian Kemp, P. Hobza, R. Zboril, and K. S. Kim, *Functionalization of Graphene: Covalent and Non-Covalent Approaches, Derivatives and Applications.* Chem. Rev. **112**, 6156 (2012).

[8] Y. M. Lin, C. Dimitrakopoulos, K. A. Jenkins, D. B. Farmer, H. Y. Chiu, A. Grill, and P. Avouris, *100-GHz transistors from wafer-scale epitaxial graphene.* Science **327**, 662 (2010).

[9] M. Liu, X. B. Yin, E. Ulin-Avila, B. S. Geng, T. Zentgraf, L. Lu, F. Wang, and X. Zhang, *A graphene-based broadband optical modulator.* Nature **474**, 64 (2011).

[10] K. S. Kim, Y. Zhao, H. Jang, S. Y. Lee, J. M. Kim, K. S. Kim, J. Y. Ahn, P. Kim, J. Y. Choi, B. H. Hong, *Large-scale pattern growth of graphene films for stretchable transparent electrodes.* Nature **457**, 706 (2009).

[11] Y. W. Zhu, S. Murali, M. D. Stoller, K. J. Ganesh, W. W. Cai, P. J. Ferreira, A. Pirkle, R. M. Wallace, K. A. Cychosz, M. Thommes, D. Su, E. A. Stach, and R. S. Ruoff, *Carbon-Based Supercapacitors Produced by Activation of Graphene.* Science **332**, 1537 (2011).

[12] M. F. El-Kady, V. Strong, S. Dubin, and R. B. Kaner, *Laser Scribing of High-Performance and Flexible Graphene-Based Electrochemical Capacitors.* Science **335**, 6074 (2012).

[13] M. Terrones, A. R. Botello-Mendez, J. Campos-Delgado, F. Lypez-Urias, Y. I. Vega-Cantu, F. J. Rodriguez-Macias, A. L. Elias, E. Munoz-Sanoval, A. G. Cano-Marquez, J. C. Charlier, and H. Terrones, *Graphene and graphite nanoribbons: Morphology, properties, synthesis, defects and applications.* Nano Today **5**, 351 (2010).

[14] R. E. Peierls, Helv. Phys. Acta **7**, 81 (1934).

[15] R. E. Peierls, Ann. Inst. Henri Poincare **5**, 177 (1935).

[16] L. D. Landau, Phys. Z. Sowjetunion **11**, 26 (1937).

[17] L. D. Landau and E. M. Lifshitz, *Statistical Physics* part 1, Sections 137 and 138 (Pergamon, Oxford 1980).

[18] N. D. Mermin and H. Wagner, *Absence of Ferromagnetism or Antiferromagnetism in One- or Two-Dimensional Isotropic Heisenberg Models.* Phys. Rev. Lett. **17**, 1133 (1966).

[19] N. D. Mermin, *Crystalline Order in Two Dimensions.* Phys. Rev. **176**, 250 (1968).

[20] A. Fasolino, J. H. Los, and M. I. Katsnelson, *Intrinsic ripples in graphene.* Nat. Mater. **6**, 858 (2007).

[21] P. R. Wallace, *The Band Theory of Graphite.* Phys. Rev. **71**, 622 (1947).

[22] G. W. Semenoff, *Condensed Matter Simulation of a Three-dimensional Anomaly.* Phys. Rev. Lett. **53**, 2449 (1984).

[23] K. S. Novoselov, A. K. Geim, S. V. Morozov, D. Jiang, M. I. Katsnelson, I. V. Grigorieva, S. V. Dubonos, and A. A. Firsov, *Two-dimensional gas of massless Dirac fermions in graphene.* Nature **438**, 197 (2005).

[24] Y. Zhang, Y. -W. Tan, H. L. Stormer, and P. Kim, *Experimental observation of the quantum Hall effect and Berry's phase in graphene.* Nature **438**, 7065 (2005).

[25] H. -S. P. Wong, D. Akinwande, *Carbon Nanotubes and Graphene Devices Physics.* Cambridge University Press 2011, First Edition, ISBN 978-0-521-51905-2.

[26] J. Wu, W. Pisula, and K. Mullen, *Graphene as Potential Material for Electronics.* Chem. Rev. **107**, 718 (2007).

[27] L. Zhi and K. Mullens, *A bottom-up approach from molecular nanographenes to unconventional carbon materials.* J. Mat. Chem. **18**, 1472 (2008).

[28] M. Terrones, *Unzipped Nanotubes.* Nature (London) **458**, 845 (2009).

[29] J. M. Pereira Jr., P. Vasilopoulos, and F. M. Peeters, *Tunable Quantum Dots in Bilayer Graphene.* Nano Lett. **7**, 946 (2007).

[30] D. Abergel, V. Apalkov, J. Berashevich, K. Zieler, and T. Chakraborty, *Properties of Graphene: A Theoretical Perspective.* Adv. Phys. **59**, 261 (2010).

[31] M. R. Masir, P. Vasilopoulos, and F. M. Peeters, *Tunneling, conductance, and wavevector filtering through magnetic barriers in bilayer graphene.* Phys. Rev. B **79**, 035409 (2009).

[32] A. S. Barnard and I. K. Snook, *Thermal stability of graphene edge structure and graphene nanoflakes.* J. Chem. Phys. **128**, 094707 (2008).

[33] H. Zheng and W. Duley, *First-principles study of edge chemical modifications in graphene nanodots.* Phys. Rev. B **78**, 045421 (2008).

[34] W. L. Wang, S. Meng, and E. Kaxiras, *Graphene Nanoflakes with Large Spin.* Nano Lett. **8**, 241 (2008).

[35] O. V. Yazyev, W. L. Lang, S. Meng, and E. Kaxiras, *Comment on Graphene Nanoflakes with Large Spin: Broken-Symmetry States.* Nano Lett. **8**, 766 (2008).

[36] W. L. Wang, O. V. Yazyev, S. Meng, and E. Kaxiras, *Topological Frustration in Graphene Nanoflakes: Magnetic Order and Spin Logic Devices.* Phys. Rev. Lett. **102**, 157201 (2009).

[37] I. Snook and A. Barnard, *Physics and applications of graphene-theory*, edited by Sergey Mikhailov, (InTech, Croatia, 2011), Chap. 13.

[38] M. R. Lang, L. He, F. X. Xiu, X. X. Yu, J. X. Tang, Y. Wang, X. F. Kou, W. J. Jiang, A. V. Fedorov, and K. L. Wang, *Revelation of Topological Surface States in Bi_2Se_3 Thin Films by In Situ Al Passivation.* ACS Nano **6**, 295 (2012).

[39] H. B. Zhang, H. L. Yu, D. H. Bao, S. W. Li, C. X. Wang, and G. W. Yang, *Magnetoresistance Switch Effect of a Sn-Doped Bi_2Te_3 Topological Insulator.* Adv. Mater. **24**, 132 (2012).

[40] F. R. Gamble and B. G. Silbernagel, *Anisotropy of the proton spin-lattice relaxation time in the superconducting intercalation complex $TaS_2(NH_3)$: Structural and bonding implications.* J. Chem. Phys. **63**, 2544 (1975).

[41] X. F. Tang, W. J. Xie, H. Li, W. Y. Zhao, Q. J. Zhang, and M. Niino, *Preparation and thermoelectric transport properties of high-performance p-type Bi_2Te_3 with layered nanostructure.* Appl. Phys. Lett. **90**, 012102 (2007).

[42] K. Takeda and K. Shiraishi, *Theoretical possibility of stage corrugation in Si and Ge analogs of graphite.* Phys. Rev. B **50**, 14916 (1994).

[43] B. Aufray, A. Kara, S. Vizzini, H. Oughaddou, C. Léandri, B. Ealet, and G. Le Lay, *Graphene-like silicon nanoribbons on Ag(110): A possible formation of silicene.* Appl. Phys. Lett. **96**, 183102 (2010).

[44] S. Cahangirov, M. Topsakal, E. Aktürk, H. Şahin, and S. Ciraci, *Two- and One-Dimensional Honeycomb Structures of Silicon and Germanium.* Phys. Rev. Lett. **102**, 236804 (2009).

[45] B. Radisavljevic, A. Radenovic, J. Brivio, V. Giacometti, A. Kis, *Single-layer MoS_2 transistors.* Nat. Nanotechnol. **6**, 147 (2011).

[46] K. S. Novoselov, D. Jiang, F. Schedin, T. J. Booth, V. V. Khotkevich, S. V. Morozov, and A. K. Geim, *Two-dimensional atomic crystals.* P. Natl. Acad. Sci. USA **102**, 10451 (2005).

[47] M. Topsakal, E. Aktürk, and S. Ciraci, *First-principles study of two- and one-dimensional honeycomb structures of boron nitride.* Phys. Rev. B **79**, 115442 (2009).

[48] L. Wirtz, A. Rubio, R. A. de la Concha, and A. Loiseau, *Ab-initio calculations of the lattice dynamics of boron nitride nanotubes.* Phys. Rev. B **68**, 045425 (2003).

[49] H. Sahin, S. Cahangirov, M. Topsakal, E. Bekaroglu, E. Aktürk, R. T. Senger, and S. Ciraci, *Monolayer honeycomb structures of group-IV elements and III-V binary compounds: First-principles calculations.* Phys. Rev. B **80**, 155453 (2009).

[50] D. Golberg, Y. Bando, Y. Huang, T. Terao, M. Mitome, C. Tang, and C. Zhi, *Boron nitride nanotubes and nanosheets.* ACS Nano **4**, 2979 (2010).

[51] R. Arenal, X. Blase, and A. Loiseau, *Boron-nitride and boron-carbonitride nanotubes: synthesis, characterization and theory.* Adv. Phys. **59**, 101 (2010).

[52] L. Britnell, R. V. Gorbachev, R. Jalil, B. D. Belle, F. Schedin, A. Mishchenko, T. Georgiou, M. I. Katsnelson, L. Eaves, S. V. Morozov, N. M. R. Peres, J. Leist, A. K. Geim, K. S. Novoselov, and L. A. Ponomarenko, *Field-Effect Tunneling Transistor Based on Vertical Graphene Heterostructures.* Science **335**, 947 (2012).

[53] M. S. Bresnehan, M. J. Hollander, M. Wetherington, M. Labella, K. A. Trumbull, R. Cavalero, D. W. Snyder, and J. A. Robinson, *Integration of Hexagonal Boron Nitride with Quasi-freestanding Epitaxial Graphene: Toward Wafer-Scale, High-Performance Devices.* ACS Nano **6**, 5234 (2012).

[54] C. R. Dean, A. F. Young, I. Meric, C. Lee, L. Wang, S. Sorgenfrei, K. Watanabe, T. Taniguchi, P. Kim, K. L. Shepard, and J. Hone, *Boron nitride substrates for high-quality graphene electronics.* Nature Nanotechnol. **5**, 722 (2010).

[55] R. Liu and C. Cheng, *Ab-initio studies of possible magnetism in a BN sheet by non-magnetic impurities and vacancies.* Phys. Rev. B **76**, 014405 (2007).

[56] A. J. Du, S. C. Smith, and G. Q. Lu, *First-principle studies of electronic structure and C-doping effect in boron nitride nanoribbon.* Chem. Phys. Lett. **447**, 181 (2007).

[57] R. R. Nair, W. Ren, R. Jalil, I. Riaz, V. Kravets, L. Britnell, P. Blake, F. Schedin, A. Mayorov, S. Yuan, M. Katsnelson, H. Cheng, W. Strupinski, L. Bulusheva, A. Okotrub, I. Grigorieva, A. Grigorenko, K. Novoselov, and A. K. Geim, *Fluorographene: A Two-Dimensional Counterpart of Teflon.* Small **6**, 2877 (2010).

[58] R. Zboril, F. Karlicky, A. B. Bourlinos, T. A. Steriotis, A. K. Stubos, V. Georgakilas, K. Safárová, D. Jancík, C. Trapalis, and M. Otyepka, *Graphene Fluoride: A Stable Stoichiometric Graphene Derivative and its Chemical Conversion to Graphene.* Small, **6**, 2885 (2010).

[59] O. Leenaerts, H. Peelaers, A. D. Hernández-Nieves, B. Partoens, and F. M. Peeters, *First-principles investigation of graphene fluoride and graphane.* Phys. Rev. B **82**, 195436 (2010).

[60] K. J. Jeon, Z. Lee, E. Pollak, L. Moreschini, A. Bostwick, C. M. Park, R. Mendelsberg, V. Radmilovic, R. Kostecki, T. J. Richardson, and E. Rotenberg, *Fluorographene: A Wide Bandgap Semiconductor with Ultraviolet Luminescence.* ACS Nano **5**, 1042 (2011).

[61] T. L. Makarova, V. S. Zagaynova, G. Inan, A. V. Okotrub, G. N. Chekhova, D. V. Pinakov, and L. G. Bulusheva, *Structural Evolution and Magnetic Properties of Underfluorinated C_2F.* J. Supercond. Nov. Magn. **25**, 79 (2012).

[62] C. N. Contreras, H. H. Cocoletzi, and E. C. Anota, *Theoretical study of the electronic properties of fluorographene.* J. Mol. Model. **17**, 2093 (2011).

[63] G. K. Gueorguiev, C. Goyenola, S. Schmidt, and L. Hultman, *CF_x: A first-principles study of structural patterns arising during synthetic growth.* Chem. Phys. Lett. **516**, 62 (2011).

[64] D. K. Samarakoon, Z. F. Chen, C. Nicolas, and X. Q. Wang, *Structural and Electronic Properties of Fluorographene.* Small **7**, 965 (2011).

[65] M. A. Ribas, A. K. Singh, P. B. Sorokin, and B. I. Yakobson, *Patterning nanoroads and quantum dots on fluorinated graphene.* Nano Res. **4**, 143 (2011).

[66] S. Tang and S. Zhang, *Structural and Electronic Properties of Hybrid Fluorographene-Graphene Nanoribbons: Insight from First-Principles Calculations.* J. Phys. Chem. C **115**, 16644 (2011).

[67] A. Markevich, R. Jones, P. R. Briddon, *Doping of fluorographene by surface adsorbates.* Phys. Rev. B **84**, 115439 (2011).

[68] R. Singh and G. Bester, *Hydrofluorinated graphene: Two-dimensional analog of polyvinylidene fluoride.* Phys. Rev. B **84**, 155427 (2011).

[69] A. Ueta, Y. Tanimura, O. V. Prezhdo, *Infrared Spectral Signatures of Surface-Fluorinated Graphene: A Molecular Dynamics Study.* J. Phys. Chem. Lett. **3**, 246 (2012).

[70] X. Li, W. Cai, J. An, S. Kim, J. Nah, D. Yang, R. Piner, A. Velamakanni, I. Jung, E. Tutuc, S. K. Banerjee, L. Colombo, R. S. Ruoff, *Large-Area Synthesis of High-Quality and Uniform Graphene Films on Copper Foils.* Science **324**, 1312 (2009).

[71] S. Bae, H. Kim, Y. Lee, X. Xu, J. S. Park, Y. Zheng, J. Balakrishnan, T. Lei, H. R. Kim, Y. Song, Y. J. Kim, K. S. Kim, B. Özyilmaz, J. H. Ahn, B. H. Hong, and S. Iijima, *Roll-to-roll production of 30-inch graphene films for transparent electrodes.* Nature Nanotechnol. **5**, 574 (2010).

[72] S. Lee, K. Lee, and Z. Zhong, *Wafer scale homogeneous bilayer graphene films by chemical vapor deposition.* Nano Lett. **10**, 4702 (2010).

[73] I. Forbeaux, J. M. Themlin, and J. M. Debever, *Heteroepitaxial graphite on 6H-SiC(0001): interface formation through conduction-band electronic structure.* Phys. Rev. B **58**, 16396 (1998).

[74] C. Berger, Z. Song, T. Li, X. Li, A. Y. Ogbazghi, R. Feng, Z. Dai, A. N. Marchenkov, E. H. Conrad, P. N. First, and W. A. de Heer, *Ultrathin epitaxial graphite: 2D electron gas properties and a route toward graphene based nanoelectronics.* J. Phys. Chem. B **108**, 19912 (2004).

[75] T. Ohta, A. Bostwick, T. Seyller, K. Horn, E. Rotenberg, *Controlling the electronic structure of bilayer graphene.* Science **313**, 951 (2006).

[76] A. S. Mayorov, R. V. Gorbachev, S. V. Morozov, L. Britnell, R. Jalil, L. A. Ponomarenko, P. Blake, K. S. Novoselov, K. Watanabe, T. Taniguchi, and A. K. Geim, *Micrometer-Scale Ballistic Transport in Encapsulated Graphene at Room Temperature.* Nano Lett. **11**, 2396 (2011).

[77] R. R. Nair, P. Blake, A. N. Grigorenko, K. S. Novoselov, T. J. Booth, T. Stauber, N. M. R. Peres, and A. K. Geim, *Fine Structure Constant Defines Visual Transparency of Graphene.* Science **320**, 1308 (2008).

[78] J. S. Bunch, S. S. Verbridge, J. S. Alden, A. M. van der Zande, J. M. Parpia, H. G. Craighead and P. L. McEuen, *Impermeable Atomic Membranes from Graphene Sheets.* Nano Lett. **8**, 2458 (2008).

[79] K. V. Emtsev, A. Bostwick, K. Horn, J. Jobst, G. L. Kellogg, L. Ley, J. L. McChesney, T. Ohta, S. A. Reshanov, J. Röhrl, E. Rotenberg, A. K. Schmid, D. Waldmann, H. B. Weber, and T. Seyller, *Towards wafer-size graphene layers by atmospheric pressure graphitization of silicon carbide.* Nature Mater. **8**, 203 (2009).

[80] J. Moser, A. Barreiro, and A. Bachtold, *Current-induced cleaning of graphene.* Appl. Phys. Lett. **91**, 163513 (2007).

[81] J. Cai, P. Ruffieux, R. Jaafar, M. Bieri, T. Braun, S. Blankenburg, M. Muoth, A. P. Seitsonen, M. Saleh, X. Feng, K. Müllen, and R. Fasel, *Atomically precise bottom-up fabrication of graphene nanoribbons.* Nature **466**, 470 (2010).

[82] M. Y. Han, B. Ozyilmaz, Y. B. Zhang, and P. Kim, *Energy band-gap engineering of graphene nanoribbons.* Phys. Rev. Lett. **98**, 206805 (2007).

[83] L. A. Ponomarenko, F. Schedin, M. I. Katsnelson, R. Yang, E. W. Hill, K. S. Novoselov, and A. K. Geim, *Chaotic Dirac billiard in graphene quantumdots.* Science **320**, 356 (2008).

[84] C. Stampfer, E. Schurtenberger, F. Molitor, J. Güttinger, T. Ihn and K. Ensslin, *Tunable graphene single electron transistor.* Nano Lett. **8**, 2378 (2008).

[85] J. B. Oostinga, H. B. Heersche, X. L. Liu, A. F. Morpurgo, and L. M. K. Vandersypen, *Gate-induced insulating state in bilayer graphene devices.* Nature Mater. **7**, 151 (2008).

[86] D. C. Elias, R. R. Nair, T. M. G. Mohiuddin, S. V. Morozov, P. Blake, M. P. Halsall, A. C. Ferrari, D. W. Boukhvalov, M. I. Katsnelson, A. K. Geim, and K. S. Novoselov, *Control of Graphene's Properties by Reversible Hydrogenation: Evidence for Graphane.* Science **323**, 610 (2009).

[87] L. Liao, Y. C. Lin, M. Bao, R. Cheng, J. Bai, Y. Liu, Y. Qu, K. L. Wang, Y. Huang, and X. Duan, *High-speed graphene transistors with a self-aligned nanowire gate.* Nature **467**, 305 (2010).

[88] L. Liao, J. Bai, R. Cheng, Y. C. Lin, S. Jiang, Y. Qu, Y. Huang, and X. Duan, *Sub-100 nm Channel Length Graphene Transistors.* Nano Lett. **10**, 3952 (2010).

[89] E. W. Hill, A. Vijayaragahvan, K. Novoselov, *Graphene sensors.* IEEE Sensors J. **11**, 3161 (2011).

[90] T. O. Wehling, K. S. Novoselov, S. V. Morozov, E. E. Vdovin, M. I. Katsnelson, A. K. Geim, and A. I. Lichtenstein, *Molecular doping of graphene.* Nano Lett. **8**, 173 (2008).

[91] F. Fchedin, A. K. Geim, S. V. Morozov, E. W. Hill, P. Blake, M. I. Katsnelson, and K. S. Novoselov, *Detection of individual gas molecules absorbed on graphene.* Nat. Mater. **6**, 652 (2007).

[92] K. S. Novoselov, Z. Jiang, Y. Zhang, S. V. Morozov, H. L. Stormer, U. Zeitler, J. C. Maan, G. S. Boebinger, P. Kim, and A. K. Geim, *Room-Temperature Quantum Hall Effect in Graphene.* Science **315**, 1379 (2007).

[93] A. Tzalenchuk, S. Lara-Avila, A. Kalaboukhov, S. Paolillo, M. Syväjärvi, R. Yakimova, O. Kazakova, T. J. B. M. Janssen, V. Falko, and S. Kubatkin, *Towards a quantum resistance standard based on epitaxial graphene.* Nat. Nanotechnol. **5**, 186 (2010).

[94] T. J. B. M. Janssen, J. M. Williams, N. E. Fletcher, R. Goebel, A. Tzalenchuk, R. Yakimova, S. Lara-Avila, S. Kubatkin, V. I. Falko, *Precision comparison of the quantum Hall effect in graphene and gallium arsenide.* Metrologia **49**, 294 (2012).

[95] A. Abouimrane, O. C. Compton, K. Amine, S. B. T. Nguyen, *Non-annealed graphene paper as a binder-free anode for lithium-ion batteries.* J. Phys. Chem. C **114**, 12800 (2010).

[96] P. Simon and Y. Gogotsi, *Materials for electrochemical capacitors.* Nature Mater. **7**, 845 (2008).

[97] S. Mirsky, Scientific American Magazine **305**, 74 (2011).

[98] D. Lahiri, R. Dua, C. Zhang, I. D. Socarraz-Novoa, A. Bhat, S. Ramaswamy, A. Agarwal, *Graphene nanoplatelet-induced strengthening of ultrahigh molecular weight polyethylene and biocompatibility in vitro.* ACS Appl. Mater. Interfaces **4**, 2234 (2012).

[99] http://phys.org/news199365879.html, *First step toward electronic DNA sequencing: Translocation through graphene nanopores.*

[100] G. H. Lee, R. C. Cooper, S. J. An, S. Lee, A. van der Zande, N. Petrone, A. G. Hammerberg, C. Lee, B. Crawford, W. Oliver, J. W. Kysar, and J. Hone, *High-Strength Chemical-Vapor-Deposited Graphene and Grain Boundaries.* Science **340**, 1073 (2013).

[101] D. Cohen-Tanugi and J. C. Grossman, *Water Desalination across Nanoporous Graphene.* Nano Lett. **12**, 3602 (2012).

[102] H. Bao, Y. Pan and L. Li, *Recent advances in graphene-based nanomaterials for biomedical applications.* Nano Life **2**, 1230001 (2012).

[103] Y. -W. Son, M. L. Cohen, and S. G. Louie, *Half-metallic graphene nanoribbons.* Nature (London) **444**, 347 (2006).

[104] M. I. Katnelson and A. K. Geim, *Electron scattering on microscopic corrugations in graphene.* Phil. Trans. R. Soc. A **366**, 195 (2008).

[105] S. Costamagna, O. Hernandez, and A. Dobry, *Spectral gap induced by structural corrugation in armchair graphene nanoribbons.* Phys. Rev. B **81**, 115421 (2010).

[106] F. Ercolessi, *A molecular dynamics primer.* http://www.fisica.uniud.it/ercolessi/md/md/

[107] L. Verlet, *Computer "Experiments" on Classical Fluids. I. Thermodynamical Properties of Lennard-Jones Molecules.* Phys. Rev. **159**, 98 (1967).

[108] H. J. C. Berendsen, J. P. M. Postma, W. F. van Gunsteren, A. Dinola, and J. R. Haak, *Molecular dynamics with coupling to an external bath.* J. Chem. Phys. **81**, 3684 (1984).

[109] P. H. Hünenberger, *Thermostat Algorithms for Molecular Dynamics Simulations.* Adv. Polym. Sci. **173**, 105 (2005).

[110] G. Slotman, Master thesis (*Structure, stability and defects of single layer h- BN*), 2012.

[111] G. J. Martyna, D. J. Tobias, and M. L. Klein, *Constant pressure molecular dynamics algorithms.* J. Chem. Phys. **101**, 4177 (1994).

[112] T. Hammerschmidt and R. Drautz, *Bond-Order Potentials for Bridging the Electronic to Atomistic Modelling Hierarchies.* in: NIC Series 42 - Multiscale Simulation Methods in Molecular Science , edited by J. Grotendorst, N. Attig, S. Blügel and D. Marx. (Jülich Supercomputing Centre), 229 (2009).

[113] T. Liang, Y. K. Shin, Y. T. Cheng, D. E. Yilmaz, K. G. Vishnu, O. Verners, C. Zou, S. R. Phillpot, S. B. Sinnott, and A. C. T. van Duin, *Reactive potentials for advanced atomistic simulations.* Annu. Rev. Mater. Res. **43**, 12.1-12.21 (2013).

[114] J. Tersoff, *New empirical model for the structural properties of silicon.* Phys. Rev. Lett. **56**, 632 (1986).

[115] G. C. Abell, *Empirical chemical pseudopotential theory of molecular and metallic bonding.* Phys. Rev. B **31**, 6184 (1985).

[116] D. W. Brenner, O. A. Shenderova, J. A. Harrison, S. J. Stuart, B. Ni, and S. B. Sinnott, *A second-generation reactive empirical bond order (REBO) potential energy expression for hydrocarbons.* J. Phys.: Condens. Matter, **14**, 783 (2002).

[117] D. W. Brenner, *Empirical potential for hydrocarbons for use in simulating the chemical vapor deposition of diamond films.* Phys. Rev. B **42**, 9458 (1990).

[118] J. Tersoff, *New empirical approach for the structure and energy of covalent systems.* Phys. Rev. B **37**, 6991 (1988).

[119] A. C. T. van Duin, S. Dasgupta, F. Lorant, and W. A. Goddard III, *ReaxFF: A Reactive Force Field for Hydrocarbons.* J. Phys. Chem. A **105**, 9396 (2001).

[120] M. F. Russo Jr. and A. C. T. van Duin, *Atomistic-scale simulations of chemical reactions: Bridging from quantum chemistry to engineering.* Nucl. Instru. Meth. Phys. Res. B **269**, 1549 (2011).

[121] W. J. Mortier, S. K. Ghosh, and S. Shankar, *Electronegativity Equalization Method for the Calculation of Atomic Charges in Molecules.* J. Am. Chem. Soc. **108**, 4315 (1986).

[122] A. K. Rappe, W. A. Goddard III, *Charge Equilibration for Molecular Dynamics Simulations.* J. Phys. Chem. **95**, 3358 (1991).

[123] H. Hellmann, Deuticke, leipzig (1964).

[124] R. P. Feynman, *Forces in Molecules.* Phys. Rev. **56**, 340 (1939).

[125] M. C. Payne, M. P. Teter, D. C. Allan, T. A. Arias and J. D. Joannopoulos, *Iterative minimization techniques for ab-initio total-energy calculations: Molecular dynamics and conjugate gradients.* Rev. Mod. Phys. **64**, 1045 (1991).

[126] R. G. Parr and W. Yang, *Density-Functional Theory of Atoms and Molecules.* New York: Oxford University Press. ISBN: 0-19-509276-7 (1989).

[127] W. Koch and M. C. Holthausen, *A Chemist's Guide to Density Functional Theory.* Wiley-VCH. ISBN: 978-3-527-30422-6.

[128] R. M. Martin, *Electronic Structure: basic theory and practical methods.* Cambridge University Press. ISBN: 978-0521534406.

[129] P. Hohenberg and W. Kohn, *Inhomogeneous Electron gas.* Phys. Rev. **136**, B684 (1964).

[130] W. Kohn and L. J. Sham, *Self-Consistent Equations Including Exchange and Correlation Effects.* Phys. Rev. **140**, A1133 (1965).

[131] D. M. Ceperley and B. J. Alder, *Ground State of the Electron Gas by a Stochastic Method.* Phys. Rev. Lett. **45**, 566 (1980).

[132] J. Zimmermann, P. Pavone, and G. Cuniberti, *Vibrational modes and low-temperature thermal properties of graphene and carbon nanotubes: Minimal force-constant model.* Phys. Rev. B **78**, 045410 (2008).

[133] J. Maultzsch, S. Reich, C. Thomsen, H. Requardt, and P. Ordejón, *Phonon Dispersion in Graphite.* Phys. Rev. Lett. **92**, 075501 (2004).

[134] J. Zhou and J. Dong, *Vibrational property and Raman spectrum of carbon nanoribbon.* Appl. Phys. Lett. **91**, 173108 (2007).

[135] R. Gillen, M. Mohr, C. Thomsen, and J. Maultzsch, *Vibrational properties of graphene nanoribbons by first-principles calculations.* Phys. Rev. B **80**, 155418 (2009).

[136] G. Gao, T. Çağin, and W. A. Goddard III, *Energetics, structure, mechanical and vibrational properties of single-walled carbon nanotubes.* Nanotechnology **9**, 184 (1998).

[137] R. Saito, T. Takeya, T. Kimura, G. Dresselhaus, and M. S. Dresselhaus, *Raman intensity of single-wall carbon nanotubes.* Phys. Rev. B **57**, 4145 (1998).

[138] M. Menon, E. Richter, and K. R. Subbaswamy, *Structural and vibrational properties of fullerenes and nanotubes in a nonorthogonal tight-binding scheme.* J. Chem. Phys. **104**, 5875 (1996).

[139] B. Barszcz, B. Laskowska, A. Graja, E. Y. Park, T. Kim, and K. Lee, *Vibrational properties of two fullerene-thiophene-based dyads.* Synth. Met. **159**, 2539 (2009).

[140] S. Bera, A. Arnold, F. Evers, R. Narayanan, and P. Wölfle, *Elastic properties of graphene flakes: Boundary effects and lattice vibrations.* Phys. Rev. B **82**, 195445 (2010).

[141] B. K. Agrawal, S. Agrawal, and S. Singh, *Structural and vibrational properties of small carbon clusters.* J. Nanosci. Nanotechnol. **5**, 442 (2005).

[142] N. Breda, G. Onida, G. Benedek, G. Colò, and R. A. Broglia, *Bond-charge-model calculation of vibrational properties in small carbon aggregates: From spherical clusters to linear chains.* Phys. Rev. B **58**, 11000 (1998).

[143] R. Saito, M. Hofmann, G. Dresselhaus, A. Jorio, and M. S. Dresselhaus, *Raman Spectroscopy of Graphene and Carbon Nanotubes.* Adv. Phys. **60**, 413 (2011).

[144] A. Eckmann, A. Felten, A. Mishchenko, L. Britnell, R. Krupke, K. S. Novoselov, and C. Casiraghi, *Probing the Nature of Defects in Graphene by Raman Spectroscopy.* Nano Lett. **12**, 3925 (2012).

[145] A. M. Rao, E. Richter, S. Bandow, B. Chase, P. C. Eklund, K. A. Williams, S. Fang, K. R. Subbaswamy, M. Menon, A. Thess, R. E. Smalley, G. Dresselhaus, and M. S. Dresselhaus, *Diameter-Selective Raman Scattering from Vibrational Modes in Carbon Nanotubes.* Science **275**, 187 (1997).

[146] L. Venkataraman. Massachusetts Institute of Technology, PhD-thesis(1993).

[147] R. A. Jishi, L. Venkataraman, M. S. Dresselhaus, and G. Dresselhaus, *Phonon modes in carbon nanotubules.* Chem. Phys. Lett. **209**, 77 (1993).

[148] M. Tommasini, C. Castiglioni, and G. Zerbi, *Raman Scattering of Molecular Graphene.* Phys. Chem. Chem. Phys. **11**, 10185 (2009).

[149] M. A. Pimenta, G. Dresselhaus, M. S. Dresselhaus, L. G. Cançado, A. Jorio, and R. Saito, *Studying disorder in graphite-based systems by Raman spectroscopy.* Phys. Chem. Chem. Phys. **9**, 1276 (2007).

[150] A. G. Ryabenko, N. A. Kiselev, J. L. Hutchison, T. N. Moroz, S. S. Bukalov, L. A. Mikhalitsyn, R. O. Loutfy, and A. P. Moravsky, *Spectral properties of single-walled carbon nanotubes encapsulating fullerenes.* Carbon **45**, 1492 (2007).

[151] K. H. Michel and B. Verberck, *Theory of the evolution of phonon spectra and elastic constants from graphene to graphite.* Phys. Rev. B **78**, 085424 (2008).

[152] M. Mohr, J. Maultzsch, E. Dobardžić, S. Reich, I. Milošević, M. Damnjanović, A. Bosak, M. Krisch, and C. Thomsen, *Phonon dispersion of graphite by inelastic x-ray scattering.* Phys. Rev. B **76**, 035439 (2007).

[153] B. Partoens and F. M. Peeters, *From graphene to graphite: Electronic structure around the K point.* Phys. Rev. B **74**, 075404 (2006).

[154] N. Mounet and N. Marzari, *First-principles determination of the structural, vibrational and thermodynamic properties of diamond, graphite, and derivatives.* Phys. Rev. B **71**, 205214 (2005).

[155] W. An, Y. Gao, S. Bulusu, and X. C. Zeng, *Ab initio calculation of bowl, cage, and ring isomers of C_{20} and C_{20^-}.* J. Chem. Phys. **122**, 204109 (2005).

[156] D. P. Kosimov, A. A. Dzhurakhalov, and F. M. Peeters, *Carbon clusters: From ring structures to nanographene.* Phys. Rev. B **81**, 195414 (2010).

[157] D. P. Kosimov, A. A. Dzhurakhalov, and F. M. Peeters, *Theoretical study of the stable states of small carbon clusters C_n (n=2-10).* Phys. Rev. B **78**, 235433 (2008).

[158] A. Kuc, T. Heine, and G. Seifert, *Structural and electronic properties of graphene nanoflakes.* Phys. Rev. B **81**, 085430 (2010).

[159] M. Ezawa, *Metallic graphene nanodisks: electric and magnetic properties.* Phys. Rev. B **76**, 245415 (2007).

[160] J. Fernandez-Rossier and J. J. Palacios, *Magnetism in graphene nanoislands.* Phys. Rev. Lett. **99**, 177204 (2007).

[161] J. D. Louck, *Exact normal modes of oscillation of a linear chain of identicalatoms.* Am. J. Phys. **30**, 585 (1962).

[162] J. H. Eggert, *One-dimensional lattice dynamics with periodic boundary conditions: An analog demonstration.* Am. J. Phys. **65**, 108 (1997).

[163] T. Zhou, C. Xu, X. Zhang, C. Cheng, L. Chen, and Y. Xu, *A simple theoretical model for ring and nanotube radial breathing mode.* Acta Phys. -Chim. Sin. **24**, 1579 (2008).

[164] M. Vandescuren, P. Hermet, V. Meunier, L. Henrard, and Ph. Lambin, *Theoretical study of the vibrational edge modes in graphene nanoribbons.* Phys. Rev. B **78**, 195401 (2008).

[165] V. A. Schweigert and F. M. Peeters, *Spectral properties of classical two-dimensional clusters.* Phys. Rev. B **51**, 7700 (1995).

[166] L. X. Benedict, S. G. Louie, and M. L. Cohen, *Heat capacity of carbon nanotubes.* Solid State Commun. **100**, 177 (1996).

[167] A. A. Maradudin, E. W. Montroll, G. H. Weiss, and I. P. Ipatova, *Theory of the vibrational frequency spectra of solids.* In: H. E. Ehrenreich, F. Seitz, and D. Turnbull (ed.). Solid State Physics, Academic, New York, pp. 129-188 (1971).

[168] J. G. Dash, *History of the search for continuous melting.* Rev. Mod. Phys. **71**, 1737 (1999).

[169] K. Koga, T. Ikeshoji, and K. I. Sugawara, *Size- and Temperature-Dependent Structural Transitions in Gold Nanoparticles.* Phys. Rev. Lett. **92**, 115507 (2004).

[170] F. Ercolessi, W. Andreoni, and E. Tosatti, *Melting of small gold particles: Mechanism and size effects.* Phys. Rev. Lett. **66**, 911 (1991).

[171] L. J. Lewis, P. Jensen and J. L. Barrat, *Melting, freezing, and coalescence of gold nanoclusters.* Phys. Rev. B **56**, 2248 (1997).

[172] C. L. Cleveland, W. D. Luedtke, and U. Landman, *Melting of gold clusters.* Phys. Rev. B **60**, 5065 (1999).

[173] A. Rytkönen, H. Häkkinen, and M. Manninen, *Melting and Octupole Deformation of* Na_{40}. Phys. Rev. Lett. **80**, 3940 (1998).

[174] K. Joshi, D. G. Kanhere, and S. A. Blundell, *Abnormally high melting temperature of the* Sn_{10} *cluster.* Phys. Rev. B **66**, 155329 (2002).

[175] F. C. Chuang, C. Z. Wang, S. Ögüt, J. R. Chelikowsky, and K. M. Ho, *Melting of small Sn clusters by ab initio molecular dynamics simulations.* Phys. Rev. B **69**, 165408 (2004).

[176] T. L. Beck and R. S. Berry, *The interplay of structure and dynamics in the melting of small clusters.* J. Chem. Phys. **88**, 3910 (1988).

[177] B. S. Bas, M. J. Ford, and M. B. Cortie, *Melting in small gold clusters: a density functional molecular dynamics study.* J. Phys.: Condens. Matter **18**, 55 (2006).

[178] M. Schmidt, R. Kusche, W. Kronmüller, B. von Issendorff and H. Haberland, *Experimental Determination of the Melting Point and Heat Capacity for a Free Cluster of 139 Sodium Atoms.* Phys. Rev. Lett. **79**, 99 (1997).

[179] A. A. Shvartsburg and M. F. Jarrold, *Solid Clusters above the Bulk Melting Point.* Phys. Rev. Lett. **85**, 2530 (2000).

[180] G. A. Breaux, R. C. Benirschke, T. Sugai, B. S. Kinnear, and M. F. Jarrold, *Hot and Solid Gallium Clusters: Too Small to Melt.* Phys. Rev. Lett. **91**, 215508 (2003).

[181] C. Rey, L. J. Gallego, J. García-Rodeja, J. A. Alonso, and M. P. Iñiguez, *Molecular-dynamics study of the binding energy and melting of transition-metal clusters.* Phys. Rev. B **48**, 8253 (1993).

[182] J. García-Rodeja, C. Rey, L. J. Gallego and J. A. Alonso, *Molecular-dynamics study of the structures, binding energies, and melting of clusters of fcc transition and noble metals using the Voter and Chen version of the embedded-atom model.* Phys. Rev. B **49**, 8495 (1994).

[183] T. X. Li, Y. L. Ji, S. W. Yu and G. H. Wang, *Melting properties of noble metal clusters.* Solid State Commun. **116**, 547 (2000).

[184] N. Alem, R. Erni, C. Kisielowski, M. D. Rossell, W. Gannett, and A. Zettl, *Atomically thin hexagonal boron nitride probed by ultrahigh-resolution transmission electron microscopy.* Phys. Rev. B **80**, 155425 (2009).

[185] K. V. Zakharchenko, A. Fasolino, J. H. Los, and M. I. Katsnelson, *Melting of graphene: from two to one dimension.* J. Phys.: Condens. Matter **23**, 202202 (2011).

[186] K. Zhang, G. M. Stocks, and J. Zhong, *Melting and premelting of carbon nanotubes.* Nanotechnology **18**, 285703 (2007).

[187] G. D. Lee, C. Z. Wang, E. Yoon, N. M. Hwang, and K. M. Ho, *Reconstruction and evaporation at graphene nanoribbon edges.* Phys. Rev. B **81**, 195419 (2010).

[188] K. Raghavachari and J. S. Binkley, *Structure, stability, and fragmentation of small carbon clusters.* J. Chem. Phys. **87**, 2191 (1987).

[189] L. Rui, H. Yuan-Zhong, W. Hui, and Z. Yu-Jun, *Numerical distortion and effects of thermostat in molecular dynamics simulations of single-walled carbon nanotubes.* Chin. Phys. **17**, 4253 (2008).

[190] D. Porezag, T. Frauenheim, T. Kohler, G. Seifert, and R. Kaschner, *Construction of tight-binding-like potentials on the basis of density-functional theory: Application to carbon.* Phys. Rev. B **51**, 12947 (1995).

[191] M. Elstner, D. Porezag, G. Jungnickel, J. Elsner, M. Haugk, T. Frauenheim, S. Suhai, G. Seifert, *Self-consistent-charge density-functional tight-binding method for simulations of complex materials properties.* Phys. Rev. B **58**, 7260 (1998).

[192] T. Frauenheim, G. Seifert, M. Elstner, T. Niehaus, C. Kohler, M. Sternberg, Z. Hajnal, A. D. Carlo, S. Suhai, *Atomistic simulations of complex materials: ground-state and excited-state properties.* J. Phy.: Condens. Matter **14**, 3015 (2002).

[193] G. Zheng, S. Irle, K. Morokuma, *Performance of the DFTB method in comparison to DFT and semiempirical methods for geometries and energies of C_{20}-C_{86} fullerene isomers.* Chem. Phys. Lett. **412**, 210 (2005).

[194] A. Zobelli, V. Ivanovskaya, P. Wagner, I. Suarez-Martinez, A. Yaya, and C. P. Ewels, *A comparative study of density functional and density functional tight binding calculations of defects in graphene.* Phys. Status Solidi B **249**, 276 (2012).

[195] N. H. March and M. P. Tosi, *Introduction to Liquid State Physics* (World Scientific, Singapore, 2002).

[196] J. M. Ziman, *Principles of the Theory of Solids* (Cambridge University, Cambridge 1972).

[197] K. Sokolowski-Tinten, C. Blome, J. Blums, A. Cavalleri, C. Dietrich, A. Tarasevitch, I. Uschmann, E. Förster, M. Kammler, M. Horn-von-Hoegen, and D. von der Linde, *Femtosecond X-ray measurement of coherent lattice vibrations near the Lindemann stability limit.* Nature (London) **422**, 287 (2003).

[198] G. Shen, V. B. Prakapenka, M. L. Rivers, and S. R. Sutton, *Structure of Liquid Iron at Pressures up to 58 GPa.* Phys. Rev. Lett. **92**, 185701 (2004).

[199] E. C. Neyts and A. Bogaerts, *Numerical Study of the Size-Dependent Melting Mechanisms of Nickel Nanoclusters.* J. Phys. Chem. C **113**, 2771 (2009).

[200] Y. Zhou, M. Karplus, K. D. Ball, and R. S. Berry, *The distance fluctuation criterion for melting: Comparison of square-well and Morse potential models for clusters and homopolymers.* J. Chem. Phys. **116**, 2323 (2002).

[201] F. Ding, K. Bolton, and A. Rosen, *Molecular dynamics study of the surface melting of iron clusters.* Eur. Phys. J. D **34**, 275 (2005).

[202] F. A. Lindemann, *The calculation of molecular vibration frequencies.* Physik. Z. **11**, 609 (1910); H. Lowen, *Melting, freezing and colloidal suspensions.* Phys. Rep. **237**, 249 (1994); J. H. Bilgram, *Dynamics at the solid, liquid transition: experiments at the freezing point.* Phys. Rep. **153**, 1 (1987).

[203] P. J. Hsu, J. S. Luo, S. K. Lai, J. F. Wax, and J. -L. Bretonnet, *Melting scenario in metallic clusters.* J. Chem. Phys. **129**, 194302 (2008).

[204] B. Steele, R. Perriot, V. Zhakhovsky, and I. Oleynik, http://meetings.aps.org/link/BAPS.2012.MAR.W12.3.

[205] P. Koskinen, S. Malola, and H. Häkkinen, *Self-Passivating Edge Reconstructions of Graphene.* Phys. Rev. Lett. **101**, 115502 (2008).

[206] J. O. Sofo, A. S. Chaudhari, and G. D. Barber, *Graphane: A two-dimensional hydrocarbon.* Phys. Rev. B **75**, 153401 (2007).

[207] W. H. Lee, J. W. Suk, H. Chou, J. Lee, Y. Hao, Y. Wu, R. Piner, D. Akinwande, K. S. Kim, and R. S. Ruoff, *Selective-area fluorination of graphene with fluoropolymer and laser irradiation.* Nano Lett. **12**, 2374 (2012).

[208] J. T. Robinson, J. S. Burgess, C. E. Junkermeier, S. C. Badescu, T. L. Reinecke, F. K. Perkins, M. K. Zalautdniov, J. W. Baldwin, J. C. Culbertson, P. E. Sheehan, and E. S. Snow, *Properties of Fluorinated Graphene Films.* Nano Lett. **10**, 3001 (2010).

[209] F. Withers, M. Dubois, and A. K. Savchenko, *Electron properties of fluorinated single-layer graphene transistors.* Phys. Rev. B **82**, 073403 (2010).

[210] S. Costamagna, M. Neek-Amal, J. H. Los, and F. M. Peeters, *Thermal rippling behavior of graphane.* Phys. Rev. B **86**, 041408(R) (2012).

[211] S. K. Singh, S. G. Srinivasan, M. Neek-Amal, S. Costamagna, Adri C. T. van Duin, and F. M. Peeters, *Thermal properties of fluorinated graphene.* Phys. Rev. B **87**, 104114 (2013).

[212] R. Paupitz, P. A. S. Autreto, S. B. Legoas, S. Goverapet Srinivasan, A. C. T. van Duin, and D. S. Galvão, *Graphene to fluorographene and fluorographane: A theoretical study.* Nanotechnology **24**, 035706 (2013).

[213] S. H. Cheng, K. Zou, F. Okino, H. R. Gutierrez, A. Gupta, N. Shen, P. C. Eklund, J. O. Sofo, and J. Zhu, *Reversible fluorination of graphene: Evidence of a two-dimensional wide bandgap semiconductor.* Phys. Rev. B **81**, 205435 (2010).

[214] A. C. T. van Duin and J. S. S. Damsté, *Computational Chemical Investigation into Isorenieratene Cyclisation.* Org. Geochem. **34**, 515, 2003.

[215] K. Chenoweth, A. C. T. van Duin, and W. A. Goddard III, *ReaxFF Reactive Force Field for Molecular Dynamics Simulations of Hydrocarbon Oxidation.* J. Phys. Chem. A **112**, 1040 (2008).

[216] S. J. Plimpton, *Fast Parallel Algorithms for Short-Range Molecular Dynamics.* J. Comp. Phys. **117**, 1 (1995).

[217] W. G. Hoover, *Canonical Dynamics: Equilibrium Phase-Space Distributions.* Phys. Rev. A **31**, 1695 (1985); S. Nosé, *A Molecular Dynamics Method for Simulations in The Canonical Ensemble.* Mol. Phys. **52**, 255 (1984).

[218] C. E. Junkermeier, T. L. Reinecke, and S. C. Badescu, *Highly Fluorinated Graphene.* Condens. Matter. arxiv:1302.6878.

[219] V. M. Bedanov, G. V. Gadyak, and Yu. E. Lozovik, *On a Modified Lindemann-Like Criterion for 2D Melting.* Phys. Lett. A **109**, 289 (1985); V. M. Bedanov and F. M. Peeters, *Ordering and Phase Transitions of Charged Particles in A Classical Finite Two-Dimensional System.* Phys. Rev. B **49**, 2667 (1994).

[220] X. H. Zheng and J. G. Earnshaw, *On the Lindemann Criterion in 2D.* Europhys. Lett. **41**, 635 (1998).

[221] S. K. Singh, M. Neek-Amal, and F. M. Peeters, *Melting of graphene clusters.* Phys. Rev. B **87**, 134103 (2013).

[222] W. Zhang, L. Spinelle, M. Dubois, K. Guérin, H. Kharbache, F. Masin, A. P. Kharitonov, A. Hamwi, J. Brunet, C. Varenne, A. Pauly, P. Thomas, D. Himmel, and J. L. Mansot, *New Synthesis Methods for Fluorinated Carbon Nanofibres and Applications.* J. Fluorine Chem. **131**, 676 (2010).

[223] J. Giraudet, M. Dubois, K. Guérin, C. Delabarre, A. Hamwi, and F. Masin, *Solid-State NMR Study of The Post-Fluorination of $(C_{2.5}F)_n$ Fluorine-GIC.* J. Phys. Chem. B **111**, 14143 (2007).

[224] The small reduction in the potential energy curves E_F in the temperature range $1400 - 1700$ K is due to the appearance of a few large defects (i.e. big rings R10 and R14).

[225] M. Neek-Amal and F. M. Peeters, *Lattice thermal properties of graphane: Thermal contraction, roughness, and heat capacity.* Phys. Rev. B **83**, 235437 (2011).

[226] S. K. Singh, M. Neek-Amal, S. Costamagna, and F. M. Peeters, *Thermomechanical Properties of A Single Hexagonal Boron Nitride Sheet.* Phys. Rev. B **87**, 184106 (2013).

[227] S. Costamagna and A. Dobry, *From graphene sheets to graphene nanoribbons: Dimensional crossover signals in structural thermal fluctuations.* Phys. Rev. B **83**, 233401 (2011).

[228] X. Blase, A. Rubio, S. G. Louie, and M. L. Cohen, *Quasiparticle band structure of bulk hexagonal boron nitride and related systems.* Phys. Rev. B **51**, 6868 (1995).

[229] K. Watanabe, T. Taniguchi, and H. Kanda, *Direct-bandgap properties and evidence for ultraviolet lasing of hexagonal boron nitride single crystal.* Nat. Mater. **3**, 404 (2004).

[230] L. Britnell, R. V. Gorbachev, R. Jalil, B. D. Belle, F. Schedin, M. I. Katsnelson, L. Eaves, S. V. Morozov, A. S. Mayorov, N. M. R. Peres, A. H. Castro Neto, J. Leist, A. K. Geim, L. A. Ponomarenko, and K. S. Novoselov, *Electron Tunneling through Ultrathin Boron Nitride Crystalline Barriers.* Nano Lett. **12**, 1707 (2012).

[231] G. -H. Lee, Y. -J. Yu, C. Lee, C. Dean, K. L. Shepard, P. Kim, and J. Hone, *Electron tunneling through atomically flat and ultrathin hexagonal boron nitride.* Appl. Phys. Lett. **99**, 243114 (2011).

[232] J. Beheshtian, A. Sadeghi, M. Neek-Amal, K. Michel, and F. M. Peeters, *Induced polarization and electronic properties of carbon-doped boron nitride nanoribbons.* Phys. Rev. B **86**, 195433 (2012).

[233] J. C. Meyer, A. Geim, M. I. Katsnelson, K. S. Novoselov, T. J. Booth, and S. Roth, *The structure of suspended graphene sheets.* Nature (London) **446**, 60 (2007).

[234] D. A. Kirilenko, A. T. Dideykin, and G. Van Tendeloo, *Measuring the corrugation amplitude of suspended and supported graphene.* Phys. Rev. B **84**, 235417 (2011).

[235] J. Jung, Z. Qiao, Q. Niu, and A. H. MacDonald, *Transport Properties of Graphene Nanoroads in Boron Nitride Sheets.* Nano Letters, **12**, 2936 (2012).

[236] T. Ouyang, Y. Chen, Y. Xie, K. Yang, Z. Bao, and J. Zhong, *Thermal transport in hexagonal boron nitride nanoribbons.* Nanotechnology **21**, 245701 (2010).

[237] I. Savic, D. A. Stewart, and N. Mingo, *Thermal conduction mechanisms in boron nitride nanotubes: Few-shell versus all-shell conduction.* Phys. Rev. B **78**, 235434 (2008).

[238] D. A. Stewart, I. Savic, and N. Mingo, *First-principles calculation of the isotope effect on boron nitride nanotube thermal conductivity.* Nano Lett. **9**, 81 (2009).

[239] C. W. Chang, A. M. Fennimore, A. Afanasiev, D. Okawa, T. Ikuno, H. Garcia, D. Li, A. Majumdar, and A. Zettl, *Isotope Effect on the Thermal Conductivity of Boron Nitride Nanotubes.* Phys. Rev. Lett. **97**, 085901 (2006).

[240] H. Shen, *Thermal-conductivity and tensile-properties of BN, SiC and Ge nanotubes.* Comp. Mater. Sci. **47**, 220 (2009).

[241] Y. Xiao, X. H. Yan, J. X. Cao, J. W. Ding, Y. L. Mao, and J. Xiang, *Specific heat and quantized thermal conductance of single-walled boron nitride nanotubes.* Phys. Rev. B **69**, 205415 (2004).

[242] M. Sakurai, Y. Sakai, and S. Saito, *Electronic properties of graphene and boron-nitride based nanostructured materials.* J. Phys.: Conf. Ser. **302**, 012018 (2011).

[243] K. N. Kudin and G. E. Scuseria, and B. I. Yakobson, *C_2F, BN, and C nanoshell elasticity from ab initio computations.* Phys. Rev. B **64**, 235406 (2001).

[244] K. Albe and W. Möller, *Modelling of boron nitride: Atomic scale simulations on thin film growth.* Comput. Mater. Sci. **10**, 111 (1998).

[245] W. Sekkal, B. Bouhafs, H. Aourag, and M. Cartier, *Molecular-dynamics simulation of structural and thermodynamic properties of boron nitride.* J. Phys.: Condens. Matter **10**, 4975 (1998).

[246] K. Matsunaga, C. Fisher, and H. Matsubara, *Tersoff Potential Parameters for Simulating Cubic Boron Carbonitrides.* Japan J. Appl. Phys. **39**, 48 (2000).

[247] P. M. Kroll, PhD Thesis (Technische Hochschule Darmstadt, 1996).

[248] M. L. Liao, Y. C. Wang, S. P. Ju, T. W. Lien, and L. F. Huang, *Deformation behaviors of an armchair boron-nitride nanotube under axial tensile strains.* J. Appl. Phys. **110**, 054310 (2011).

[249] C. Sevik, A. Kinaci, J. B. Haskins, and T. Çağin, *Characterization of thermal transport in low-dimensional boron nitride nanostructures.* Phys. Rev. B **84**, 085409 (2011).

[250] D. Nelson, T. Piran and S. Weinberg, *Statistical Mechanics of Membranes and Surfaces* (Word Scientific, Singapore, 2004).

[251] http://lammps.sandia.gov

[252] S. J. Stuart, A. B. Tutein, and J. A. Harrison, *A reactive potential for hydrocarbons with intermolecular interactions.* J. Chem. Phys. **112**, 6472 (2000).

[253] J. H. Los, M. I. Katsnelson, O. V. Yazyev, K. V. Zakharchenko, and A. Fasolino, *Scaling properties of flexible membranes from atomistic simulations: Application to graphene.* Phys. Rev. B **80**, 121405 (2009).

[254] M. Neek-Amal and F. M. Peeters, *Graphene nanoribbons subjected to axial stress.* Phys. Rev. B **82**, 085432 (2010); *Defected graphene nanoribbons under axial compression.* Appl. Phys. Lett. **97**, 153118 (2010).

[255] M. Neek-Amal and F. M. Peeters, *Buckled circular monolayer graphene: a graphene nano-bowl.* J. Phys.: Condens. Matter **23**, 045002 (2011).

[256] A. Lajevardipour, M. Neek-Amal, and F. M. Peeters, *Thermomechanical properties of graphene: valence force field model approach.* J. Phys.: Condens. Matter **24**, 175303 (2012).

[257] K. H. Michel and B. Verbeck, *Theoretical phonon dispersions in monolayers and multilayers of hexagonal boron-nitride.* Phys. Status Solidi B **246**, 2802 (2009).

[258] K. H. Michel and B. Verbeck, *Phonon dispersions and piezoelectricity in bulk and multilayers of hexagonal boron nitride.* Phys. Rev. B **83**, 115328 (2011).

[259] L. J. Karssemeijer and A. Fasolino, *Phonons of graphene and graphitic materials derived from the empirical potential LCBOPII.* Surf. Sci. **605**, 1611 (2011).

[260] S. S. Han, J. K. Kang, H. M. Lee, A. C. T. van Duin, and W. A. Goddard, *The theoretical study on interaction of hydrogen with single-walled boron nitride nanotubes. I. The reactive force field ReaxFF$_{HBN}$ development.* J. Chem. Phys. **123**, 114703 (2005).

[261] P. L. Doussal and L. Radzihovsky, *Self-consistent theory of polymerized membranes.* Phys. Rev. Lett. **69**, 1209 (1992).

[262] G. Demazeau, *Growth of cubic boron nitride by chemical vapor deposition and high-pressure high-temperature synthesis.* Diam. Relat. Mater. **2**, 197 (1993).

[263] K. V. Zakharchenko, M. I. Katsnelson, and A. Fasolino, *Finite Temperature Lattice Properties of Graphene beyond the Quasiharmonic Approximation.* Phys. Rev. Lett. **102**, 046808 (2009).

[264] V. Perebeinos and J. Tersoff, *Valence force model for phonons in graphene and carbon nanotubes.* Phys. Rev. B **79**, 241409(R) (2009).

[265] T. M. G. Mohiuddin, A. Lombardo, R. R. Nair, A. Bonetti, G. Savini, R. Jalil, N. Bonini, D. M. Basko, C. Galiotis, N. Marzari, K. S. Novoselov, A. K. Geim, and A. C. Ferrari, *Uniaxial strain in graphene by Raman spectroscopy: G peak splitting, Grüneisen parameters, and sample orientation.* Phys. Rev. B **79**, 205433 (2009).

[266] M. Neek-Amal, *Comment on Irreversibility in Response to Forces Acting on Graphene Sheets.* Phys. Rev. Lett **106**, 209701 (2011).

[267] Q. Peng, W. Ji, and S. De, *Mechanical properties of the hexagonal boron nitride monolayer: Ab initio study.* Comp. Mat. Science **56**, 11 (2012).

[268] O. Frank, G. Tsoukleri, J. Parthenios, K. Papagelis, I. Riaz, R. Jalil, K. S. Novoselov, and C. Galiotis, *Compression Behavior of Single-Layer Graphenes.* ACS Nano **4**, 3131 (2010).

[269] G. Tsoukleri, J. Parthenios, K. Papagelis, R. Jalil, A. C. Ferrari, A. K. Geim , K. S. Novoselov, and C. Galiotis, *Subjecting a Graphene Monolayer to Tension and Compression.* Small **5**, 2397 (2009).

[270] J. Singer, J. Arbocz and T. Weller, *Experimental Methods in Buckling of Thin-Walled Structures* (Wiley, New York, 1998); R. M. Jones, *Buckling of Bars, Plates, and Shells* (Taylor and Francis, Philadelphia, 1999).

[271] B. I. Yakobson, C. J. Brabec, and J. Bernholc, *Nanomechanics of Carbon Tubes: Instabilities beyond Linear Response.* Phys. Rev. Lett. **76**, 2511 (1996).

[272] C. Berger, Z. Song, T. Li, A. Y. Ogbazghi, R. Feng, Z. Dai, A. N. Marchenkov, E. H. Conrad, P. N. First, and W. A. de Heer, *Electronic Confinement and Coherence in Patterned Epitaxial Graphene.* Science **312**, 1191 (2006).

[273] M. I. Katsnelson, K. S. Novoselov, and A. K. Geim, *Chiral tunnelling and the Klein paradox in graphene.* Nat. Phys. **2**, 620 (2006).

[274] H. Şahin, R. T. Senger, and S. Ciraci, *Spintronic properties of zigzag-edged triangular graphene flakes.* J. Appl. Phys. **108**, 074301 (2010).

[275] D. W. Boukhavalov, M. I. Katsnelson, and A. I. Lichtenstein, *Hydrogen on graphene: Electronic structure, total energy, structural distortions and magnetism from first-principles calculations.* Phys. Rev. B **77**, 035427 (2008).

[276] M. H. F. Sluiter and Y. Kawazoe, *Cluster expansion method for adsorption: Application to hydrogen chemisorption on graphene.* Phys. Rev. B **68**, 085410 (2003).

[277] H. Şahin, M. Topsakal, and S. Ciraci, *Structures of fluorinated graphene and their signatures.* Phys. Rev. B **83**, 115432 (2011).

[278] F. Withers, S. Russo, M. Dubois, and M. F. Craciun, *Tuning the electronic transport properties of graphene through functionalisation with fluorine.* Nanoscale Res. Lett. **6**, 526 (2011).

[279] K. V. Zakharchenko, J. H. Los, M. I. Katsnelson, and A. Fasolino, *Atomistic simulations of structural and thermodynamic properties of bilayer graphene.* Phys. Rev. B **81**, 235439 (2010).

[280] J. E. Mueller, A. C. T. van Duin, and W. A. Goddard III, *Development and Validation of ReaxFF Reactive Force Field for Hydrocarbon Chemistry Catalyzed by Nickel.* J. Phys. Chem. C **114**, 4939 (2010).

[281] Jaguar, version 7.8, Schrodinger, (LLC, New York, NY, 2011).

[282] R. Roldán, A. Fasolino, K. V. Zakharchenko, and M. I. Katsnelson, *Suppression of anharmonicities in crystalline membranes by external strain.* Phys. Rev. B **83**, 174104 (2011).

[283] J. H. Los, L. M. Ghiringhelli, E. J. Meijer, and A. Fasolino, *Improved long-range reactive bond-order potential for carbon. I. Construction* Phys. Rev. B **72**, 214102 (2005).

[284] H. Peelaers, A. D. Hernandez-Nieves, O. Leenaerts, B. Partoens, and F. M. Peeters, *Vibrational properties of graphene fluoride and graphane.* Appl. Phys. Lett. **98**, 051914 (2011).

[285] Y. Zheng, N. Wei, Z. Fan, L. Xu, and Z. Huang, *Mechanical properties of grafold: a demonstration of strengthened graphene.* Nanotechnology **22**, 405701 (2011).

[286] Q. Lu, W. Gao, and R. Huang, *Excess energy and deformation along free edges of graphene nanoribbons.* Phys. Rev. B **81**, 155410 (2010); *Atomistic simulation and continuum modeling of graphene nanoribbons under uniaxial tension.* J. Phys.: Condens. Matter **19**, 054006 (2011).

[287] L. Zhi and K. Mullens, *A bottom-up approach from molecular nanographenes to unconventional carbon materials.* J. Mater. Chem. **18**, 1472 (2008).

[288] S. Park and R. Ruoff, *Chemical methods for the production of graphenes.* Nature Nanotechnology **4**, 217 (2009).

[289] P. Potasz, A. D. Güçlü, O. Voznyy, J. A. Folk, and P. Hawrylak, *Electronic and magnetic properties of triangular graphene quantum rings.* Phys. Rev. B **83**, 174441 (2011).

[290] K. Chang and F. M. Peeters, *Spin-polarized ballistic transport in diluted magnetic semiconductor quantum wire systems.* Phys. Rev. B **68**, 205320 (2003).

[291] Y. -W. Son, M. L. Cohen, and S. G. Louie, *Energy Gaps in Graphene Nanoribbons.* Phys. Rev. Lett **97**, 216803 (2006).

[292] M. Ezawa, *Peculiar width dependence of the electronic properties of carbon nanoribbons.* Phys. Rev. B **73**, 045432 (2006).

[293] L. Brey and H. A. Fertig, *Electronic states of graphene nanoribbons studied with the Dirac equation.* Phys. Rev. B **73**, 235411 (2006).

[294] K. -I. Sasaki, S. Murakami, and R. Saito, *Gauge Field for Edge State in Graphene.* J. Phys. Soc. Jpn. **75**, 074713 (2006).

[295] S. Okada and A. Oshiyama, *Magnetic Ordering in Hexagonally Bonded Sheets with First-Row Elements.* Phys. Rev. Lett. **87**, 146803 (2001).

[296] H. Lee, Y. -W. Son, N. Park, S. Han, and J. Yu, *Magnetic ordering at the edges of graphitic fragments: Magnetic tail interactions between the edge-localized states.* Phys. Rev. B **72**, 174431 (2005).

[297] D. A. Abanin, P. A. Lee, L. S. Levitov, *Spin-Filtered Edge States and Quantum Hall Effect in Graphene.* Phys. Rev. Lett. **96**, 176803 (2006).

[298] A. D. Güçlü, P. Potasz, and P. Hawrylak, *Excitonic absorption in gate-controlled graphene quantum dots.* Phys. Rev. B **82**, 155445 (2010).

[299] X. Yan, X. Cui, B. Li, and L. -S. Li, *Large, Solution-Processable Graphene Quantum Dots as Light Absorbers for Photovoltaics.* Nano Lett. **10**, 1869 (2010).

[300] H. Zheng and W. Duley, *First-principles study of edge chemical modifications in graphene nanodots.* Phys. Rev. B **78**, 045421 (2008).

[301] O. Voznyy, A. D. Güçlü, P. Potasz, and P. Hawrylak, *Effect of edge reconstruction and passivation on zero-energy states and magnetism in triangular graphene quantum dots with zigzag edges.* Phys. Rev. B **83**, 165417 (2011).

[302] A. D. Güçlü, P. Potasz, and P. Hawrylak, *Electric-field controlled spin in bilayer triangular graphene quantum dots.* Phys. Rev. B **84**, 035425 (2011).

[303] M. J. Frisch et al., GAUSSIAN 09, Revision A.1, Gaussian, Inc., Wallingford CT, 2009.

[304] A. D. Becke, *Density-functional thermochemistry. III. The role of exact exchange.* J. Chem. Phys. **98**, 5648 (1993).

[305] E. Rudberg, P. Salek, and Y. Luo, *Nonlocal Exchange Interaction Removes Half-Metallicity in Graphene Nanoribbons.* Nano Lett. **7**, 2211 (2007).

[306] M. A. Akhukov, A. Fasolino, Y. N. Gornostyrev, and M. I. Katsnelson, *Dangling bonds and magnetism of grain boundaries in graphene.* Phys. Rev. B **85**, 115407 (2012).

[307] Z. Z. Zhang, K. Chang, and F. M. Peeters, *Tuning of energy levels and optical properties of graphene quantum dots.* Phys. Rev. B **77**, 235411 (2008).

[308] K. A. Ritter and J. W. Lyding, *The influence of edge structure on the electronic properties of graphene quantum dots and nanoribbons.* Nature Mater. **8**, 235 (2009).

[309] A. C. Ferrari and D. M. Basko, *Raman spectroscopy as a versatile tool for studying the properties of graphene.* Nat. Nano. **8**, 235 (2013); M. S. Dresselhaus and P. C. Eklund, *Phonons in carbon nanotubes.* Adv. Phys. **49**, 705 (2000); S. Reich and C. Thomsen, *Raman spectroscopy of graphite.* Philos. Trans. R. Soc. London, Ser. A **362**, 2271 (2004).

[310] S. B. Bon, L. Valentini, R. Verdejo, J. L. G. Fierro, L. Peponi, M. A. Lopez-manchado, and J. M. Kenny, *Plasma Fluorination of Chemically Derived Graphene Sheets and Subsequent Modification With Butylamine.* Chem. Mater. **21**, 3433 (2009).

[311] J. Demaison and G. Wlodarczak, *The equilibrium C-H bond length.* Struct. Chem. **5**, 57 (1994).

[312] A. W. Castleman Jr., S. N. Khanna, A. Sen, A. C. Reber, M. Qian, K. M. Davis, S. J. Peppernick, A. Ugrinov, M. D. Merritt, *From designer clusters to synthetic crystalline nanoassemblies.* Nano Lett. **7**, 2734 (2007).

[313] A. F. Oliveira, G. Seifert, T. Heine, and H. A. Duarte, *Density-functional based tight-binding: an approximate DFT method.* J. Braz. Chem. Soc. **20**, 1193 (2009).

[314] M. Elstner, T. Frauenheim, J. McKelvey, and G. Seifert, *Density Functional Tight Binding: Contributions from the American Chemical Society Symposium.* J. Phys. Chem. A **111**, 26 (2007).

[315] http://www.dftb.org

[316] *"Publisher's note: Sir John A. Pople, 1925-2004".* J. Comput. Chem. **25 (9)**, v-vii (2004).

[317] K. V. Zakharchenko, R. Roldán, A. Fasolino, and M. I. Katsnelson, *Self-consistent screening approximation for flexible membranes: Application to graphene.* Phys. Rev. B **82**, 125435 (2010).

[318] J. -P. Kownacki and D. Mouhanna, *Crumpling transition and flat phase of polymerized phantom membranes.* Phys. Rev. E **79**, 040101 (2009).

[319] M. I. Katsnelson, *Graphene: Carbon in Two Dimensions.* Cambridge university press, New York, 2012.

Curriculum Vitae

Name: **Sandeep Kumar Singh**

Born: 15/03/1984, Aligarh, India

Contact: U 206, Groenenborgerlaan 171
2020, Antwerp, Belgium

Email: san2007iit@gmail.com

Phone: +32-488-383042

Education:

2010-2014: **PhD** Department of physics, University of Antwerp, Belgium.

2007-2009: **M. Tech** Department of mathematics, IIT Madras, Chennai, India.

2003-2006: **MSc** Department of physics, Aligarh Muslim University, Aligarh, India.

2000-2003: **BSc** Department of physics, Aligarh Muslim University, Aligarh, India.

List of Publications:

- **Sandeep Kumar Singh**, S. Costamagna, M. Neek-Amal, and F. M. Peeters, *Melting of partially fluorinated graphene: from detachment of fluorine atoms to large defects and random coils*, J. Phys. Chem. C **118**, 4460 (2014).
- **Sandeep Kumar Singh**, M. Neek-Amal, and F. M. Peeters, *Electronic properties of graphene nano-flakes: Energy gap, permanent dipole, termination effect and Raman spectroscopy*, J. Chem. Phys. **140**, 074304 (2014).
- **Sandeep Kumar Singh**, M. Neek-Amal, S. Costamagna, and F. M. Peeters, *Thermomechanical properties of a single hexagonal boron nitride sheet*, Phys. Rev. B **87**, 184106 (2013).
- **Sandeep Kumar Singh**, M. Neek-Amal, and F. M. Peeters, *Melting of graphene clusters*, Phys. Rev. B **87**, 134103 (2013).
- **Sandeep Kumar Singh**, S. Goverapet Srinivasan, M. Neek-Amal, S. Costamagna, Adri C. T. van Duin, and F. M. Peeters, *Thermal properties of fluorinated graphene*, Phys. Rev. B **87**, 104114 (2013).
- M. Neek-Amal, J. Beheshtian, F. Shayeganfar, **S. K. Singh**, J. H. Los, and F. M. Peeters, *Spiral graphone and one-sided fluorographene nanoribbons*, Phys. Rev. B **87**, 075448 (2013).
- **Sandeep Kumar Singh** and F. M. Peeters, *Vibrational properties of nanographene*, Nanoscale Systems: Mathematical Modeling, Theory and Applications **2**, 10 (2013).

Other Publications:

- T. Basak, S. Roy, **S. K. Singh**, I. Pop, *Analysis of mixed convection in a lid-driven porous square cavity with linearly heated side wall(s)*, Int. J. Heat Mass Trans. **53 (9)** , 1819 (2010).
- T. Basak, S. Roy, **S. K. Singh**, I. Pop, *Finite element simulation of natural convection within porous trapezoidal enclosures for various inclination angles: Effect of various wall heating*, Int. J. Heat Mass Trans. **52 (19)** , 4135 (2009).

Conferences and Workshops

- EuroMagNET summer school: *Science in High Magnetic Fields*, 5^{th}-11^{th} Sep. 2010, Ameland, Netherlands.-Poster
- School on Computational Modeling of Materials, 2^{nd}-3^{rd} Dec. 2010, University of Antwerp, Belgium.
- CCP5 Summer School in Molecular Simulation, 17^{th}-26^{th} July 2011, Queen's University, Belfast, UK.-Poster
- Belgian Physical Society, 30^{th} May 2012, Vrije Universiteit Brussel, Belgium.-Poster
- Graphene Week 2012 international conference, 4^{th}-8^{th} June 2012, University of Delft, Netherlands.-Poster
- Summer school on atomistic simulation techniques, 23^{th}-24^{th} Sep. 2013, University of Antwerp, Belgium.

Research Interests

- Spectral and electronic properties of graphene nanostructures.
- Thermo-mechanical properties of graphene and other 2-dimensional material.
- Multiscale modeling.

Computer Skills

Operating systems:	Windows, Linux
Office:	Word, Excel, PowerPoint
Programming languages:	C/C++, Fortran, Java
Mathematical software:	Mathematica, MATLAB, Origin, Latex, CorelDraw
DFT and MD Package:	Gaussian 09, DFTB+, Lammps (ReaxFF, Airebo, Tersoff)

Language Proficiency

- Hindi (Native), English (Fluent).

Awards and Honors

- Qualified GATE (Graduate Aptitude Test in Engineering), conducted by Ministry of Human Resources and Development (M.H.R.D.), New Delhi (India), with a percentile of 99.52, ranked 25^{th} in 2007.
- Awarded Junior Research fellowship by Indian University Grants Commission in 2007-2009.
- Qualified Joint CSIR-UGC (NET) Examination conducted by Council of Scientific and Industrial Research (C.S.I.R.). This is an eligibility test for the post of professorship in any University (India) in December 2006.
- Worked as placement coordinator at the Indian Institute of Technology Madras, India in 2008-2009.